Quantitative Characterization of Multi-Variable Human Ankle Mechanical Impedance

by

Hyunglae Lee

Master of Science in Mechanical Engineering
Seoul National University, South Korea, 2004

Bachelor of Science in Mechanical Engineering
Seoul National University, South Korea, 2002

Submitted to the Department of Mechanical Engineering
in Partial Fulfillment of the Requirements for the Degree of

Doctor of Philosophy

at the

Massachusetts Institute of Technology

June 2013

Signature of Author: ....
Department of Mechanical Engineering
May 10, 2013

Certified by: ....
Neville Hogan
Professor of Mechanical Engineering and Brain and Cognitive Sciences
Thesis Supervisor

Accepted by: ....
David E. Hardt
Professor of Mechanical Engineering
Chairman, Department Committee on Graduate Students

Quantitative Characterization of Multi-Variable Human Ankle Mechanical Impedance

by

Hyunglae Lee

Submitted to the Department of Mechanical Engineering on May 10, 2013
in Partial Fulfillment of the Requirements for the Degree of
Doctor of Philosophy in Mechanical Engineering

Abstract

Ankle mechanical impedance, which is a dynamic relationship between angular displacement and the corresponding torque at the ankle joint, plays a key role in natural interaction of the lower-extremity with the environment. The human ankle is a biomechanically complex joint consisting of three bones with non-intersecting anatomical axes, and its motions under normal motor control and function are predominantly in multiple degrees-of-freedom (DOF). This thesis provides a quantitative characterization of multi-variable ankle mechanical impedance of young healthy subjects in two DOF, both in the sagittal and the frontal planes. Multi-variable studies provide several important characteristics of the human ankle, unavailable from single DOF studies, which have mostly been in the sagittal plane. Three characterization methods were developed to study ankle mechanical impedance in different conditions: 1) *steady-state static*, 2) *steady-state dynamic*, and 3) *transient dynamic*.

First, *steady-state static ankle mechanical impedance*, which is a non-linear torque and angle relationship at the ankle, was characterized in two coupled DOFs over the normal range of motion. Robust vector field approximation methods based on thin-plate spline smoothing with generalized cross validation showed that static ankle impedance is highly direction dependent, being weak in the inversion-eversion direction. Activating a single muscle or co-contracting antagonistic muscles significantly increased static ankle impedance in all directions but more in the dorsiflexion-plantarflexion direction than the inversion-eversion. Static ankle behavior in both relaxed and active muscles was close to that of a passive elastic system.

Second, *steady-state dynamic ankle mechanical impedance* was characterized based on linear time-invariant multi-input multi-output stochastic system identification methods. A highly linear relationship between muscle activation and ankle impedance was identified in all movement directions in the sagittal and frontal planes. Furthermore, small coupling between 2 DOF and energetic passivity were observed at different levels of muscle activation and over a wide frequency range.

Third, *transient dynamic ankle mechanical impedance* was characterized during walking on a treadmill, across the gait cycle from the end of stance phase through swing and to early stance phase. Modified linear time-varying ensemble based system identification methods enabled reliable identification of transient behavior of the ankle. In both DOF, damping and stiffness decreased at the end of stance phase before the toe-off, remained relatively constant during the whole swing phase, and substantially increased around the heel-strike.

Quantitative characterization of multi-variable ankle mechanical impedance of young healthy subjects will shed light on its roles in lower-extremity motor function. It will serve as a baseline for clinical studies in patients, especially those with neurological disorders, as well as studies of elderly subjects, whose biomechanical and neurological properties may be altered due to impairments and/or aging. Finally, the methods presented in this thesis are intended to be sufficiently general to be applicable to any multi-joint system or single joint having multiple DOF.

Thesis Supervisor: Neville Hogan
Title: Professor, Department of Mechanical Engineering
Professor, Department of Brain and Cognitive Sciences

Acknowledgements

First of all, I must express my deepest appreciation to my advisor Prof. Neville Hogan. I would not have made it this far without his guidance, support, encouragement, and praise. He has always encouraged me to tackle new challenges and has provided me invaluable advice whenever I was in need. His keen physical insight and ability to capture core issues in a complicated problem are always inspiring and changed my perspective on engineering. I have tried hard to learn from him in my quest for a Ph.D and will continue to try to emulate his abilities. He has also been a great counselor and consultant for my personal concerns, especially my future plans. I also would like to thank him for his generosity and kind consideration for my situation as a father of two children. I was truly privileged to have him as my advisor and mentor.

Next, I am also grateful to my superb committee members, Dr. Hermano Igo Krebs, Prof. Harry Asada, and Prof. Dagmar Sternad. Dr. Krebs has been a great help to me throughout my years in the Newman Lab. His expertise in robot-aided rehabilitation helped me significantly to improve my work. In addition, he has provided me many chances to collaborate with great researchers at other institutions. Many thanks also go to Prof. Asada, who has brought up important issues to be addressed in system identification for the course of this thesis. His invaluable feedback and suggestions helped me to polish the thesis as it is now. I am also indebted to Prof. Dagmar Sternad, who generously agreed to be my thesis committee member and provided precious comments and suggestions on data analysis and interpretation of experimental results.

I'd like to thank all of past and current members of the Newman Lab. Especially, Jooeun Ahn and Yunseong Song have been always a great help to me in many aspects. They were always beneficial partners for intensive discussions and good friends for making my life at MIT more enjoyable. Next, without the help of the members of the Anklebot project, Patrick Ho, Mohammad Rastgaar, and Dan Klenk, I would not have made my thesis work as it is. I should also mention my two UROP students, Shuo Wang and Emma Feshbach, who were excellent assistants in much of the experimental work. I also have enjoyed my doctoral study in the Newman Lab thanks to Tyler Susko and Will Bosworth, with whom I shared concerns in my doctoral study. Panagiotis artemiadis, Konstantinos Michmizos, Laura Dipietro, Fabrizio Sergi, Seungjae Kim, Hiroaki Hirai, Glauco Caurin, and Steven Charles gave me fruitful feedback on my thesis work. I also deeply appreciate Marjorie Joss and Leslie Regan for their lightning fast administrative support throughout my life at MIT.

Last, but certainly not least, I'd like to express my deepest appreciation to all my family in Korea. Many, many thanks to my mom and dad for their support, encouragement, and untiring love. Now the long journey of Ph.D study is finally done, and I am sure they are as happy as I am. My deep gratitude is also extended to my father- and mother-in-law, who have been great supporters in many aspects, too.

Most importantly, this work would not have been made possible without my adorable son and daughter, Seungmin and Yoonji, as well as my beloved wife, Jooyeon. Seungmin and Yoonji always have made me smile and laugh, even when I was having a rough day and tired. They have kept me sane and moving forward for the past few years. Jooyeon has experienced every joy and pain with me throughout my Ph.D study. I express my deep appreciation and would like to give credit to her tremendous love, support, encouragement, praise, sacrifice, and unwavering belief in me. For that I owe everything. Thank you again Jooyeon!

This work was supported in part by Toyota Motor Corporation's Partner Robot Division, by DARPA's Warrior Web program, BAA-11-72, and by a Samsung Scholarship.

To my wife, Jooyeon,

my daughter, Jennifer Yoonji,

and my son, Joshua Seungmin

And

To my parents and parents-in-law

Table of Contents

List of Figures

List of Tables

Chapter 1

Introduction

1.1 Statement of Purpose

While all joints in the kinematic chain between foot and trunk (ankle, knee, and hip) participate in lower-extremity functions, the contribution of the ankle is significant for healthy people [1-4] as well as for those with neurological disorders [5-7]. Ankle mechanical impedance plays a key role in natural interaction of the lower-extremity with the environment, including postural stabilization during standing as well as propulsion, energy-absorption, and lower limb joint coordination during locomotion.

The goal of this thesis is to provide a quantitative characterization of multi-variable human ankle mechanical impedance, paving the way to better understand its roles in lower-extremity function, and suggesting a baseline for clinical studies in patients, especially those with neurological disorders.

More specifically, the primary goal of this thesis is to develop methods for characterizing human joint mechanical impedance in multiple degrees-of-freedom (DOFs), possibly time-varying and nonlinear. The methods are intended to be sufficiently general to be applicable to any multi-joint system or single joint having multi-DOFs.

The second goal is to identify, through application of these methods, human ankle mechanical impedance in different muscle active conditions and both under stationary and transient conditions: steady-state static, steady-state dynamic, and transient dynamic ankle mechanical impedance.

The strategy to realize these two goals involves use of a wearable ankle robot and several different system identification methods.

1.2 Background

1.2.1 Definition of Mechanical Impedance

It is important to clarify the definition of mechanical impedance, used throughout this thesis. Strictly speaking, by analogy with electrical engineering usage, impedance is a functional that maps any velocity time-history onto a corresponding force time-history, $v(t) \rightarrow f(t)$, where f and v are dual or conjugate interaction-port variables such that power (P) into the interaction port (positive inward by convention) is determined by their product, $P = f \cdot v$. However, the analogy between electrical and mechanical systems has been debated for decades [8].

Mechanical impedance could be defined to map force onto velocity or vice-versa but neither definition would reflect the profound role of geometry and kinematics in all aspects of mechanical system dynamics. For example, finite rotations, which are common in human movements, do not commute in addition (final orientation of the body differs according to the sequence of rotations) [9]. Thus, we may lose important displacement information from integration of velocity. On the other hand, velocity can be derived from differentiation of displacement.

In this thesis, the term "mechanical impedance (Z)" is defined to be a dynamic operator that maps a time-history of displacement onto the corresponding force time-history, where the force and displacement vectors are energetically conjugate such that they may define mechanical work ((Eq. (1.1)):

$$Z : \boldsymbol{x}(t) \rightarrow \boldsymbol{f}(t) \qquad (1.1)$$

$$dW = \boldsymbol{f}^T d\boldsymbol{x}$$

This might be termed a "dynamic stiffness function" but stiffness connotes a locally linear approximation to a displacement-force function, and an assumption of linearity is neither necessary nor desirable for mechanical impedance.

Following the definition, ankle mechanical impedance is defined as a dynamic relationship between angular displacement ($\boldsymbol{\theta}$) and the corresponding torque ($\boldsymbol{\tau}$) at the ankle joint ((Eq. (1.2)), where $\boldsymbol{\theta}$ and $\boldsymbol{\tau}$ are not confined to single DOF.

$$Z : \boldsymbol{\theta}(t) \rightarrow \boldsymbol{\tau}(t) \qquad (1.2)$$

$$dW = \boldsymbol{\tau}^T d\boldsymbol{\theta}$$

For the remaining part of the thesis, the term "ankle impedance" is used synonymously with "ankle mechanical impedance" for brevity.

1.2.2 Importance of Characterization of Mechanical Impedance

Why is characterization of joint mechanical impedance important? Mechanical impedance is a fundamental medium between the limb and the environment enabling natural dynamic interaction. Proper modulation of joint impedance permits effective regulation and control of desired postural and movement behaviors [10, 11]. Thus, we can investigate how human central nervous system (CNS) and biomechanical systems of the body controls interaction with its mechanical environment through the study of impedance of the neuro-muscular system.

Besides the importance in the neuro-motorcontrol aspect, study of joint impedance can provide valuable information in clinical aspects. Improper regulation of joint impedance can lead to injuries to the soft tissue of joints, such as tendons, ligaments, and muscles, when the achieved joint impedance is mismatched to the task, causing undesired, unexpected or excessive movement or velocity at the joint. For example, ankle sprains frequently occur when we walk on uneven terrain or stairs. Given the accurate characterization of joint impedance for each individual person, we may suggest a customized strategy to prevent possible orthopedic injuries. In addition, impedance characterization can serve as an assessment tool to follow up patients' recovery from injuries.

Characterization of joint impedance has great importance not only in orthopedic but also in neurological applications. As the number of patients with neurological disorders, such as strokes, multiple sclerosis (MS), spinal cord injuries (SCI), cerebral palsy (CP) etc., is increasing apace with the aging society, the demand for neuro-rehabilitation is also growing [12]. Most neurological diseases induce alterations of mechanical properties of joints, which results in abnormal motor behaviors [13-15]. Thus, characterization of joint impedance of patients and investigation of how it may deviate from the norm as a result of disorders is expected to help better diagnose of pathological behaviors of the joint. Furthermore, a regular inspection of this property can be used to quantitatively assess the progress of neuro-rehabilitation.

Last but not least, characterization of human joint impedance can provide new opportunities in the robotics field facilitating advancement of physical human-robot interaction. While various types of wearable devices, such as powered exoskeletons and active orthoses, have been developed for different purposes [16], controllers for those devices are still yet to be perfected. One of the main reasons is the lack of understanding on how human joint impedance changes during physical human-robot interaction. Once joint impedance is fully quantified, this can be utilized in designing an impedance controller for each joint of the robot, whose impedance value is determined based on the characterized human joint impedance.

1.2.3 Importance of Multi-variable Study

Human motor behavior generally involves multi-joint motions and/or single-joint multi-DOF motions, and therefore multi-variable study of joint impedance in multiple DOFs promises deeper understanding of its roles in motor control and function.

Characterization of the human ankle joint impedance also falls into this category. The human ankle is a biomechanically complex joint including three bones: the tibia, the fibular, and the talus. These bones all come together to allow movements in multiple DOFs, both in the sagittal and the frontal planes. Although ankle motions are often described about a medial-lateral axis (perpendicular to the sagittal plane) and anterior-posterior axis (perpendicular to the frontal plane), respectively, the anatomical axes of the joint do not intersect, are far from orthogonal, and change with ankle movement [17, 18]. These complexities could introduce a biomechanical coupling between 2 DOFs. Furthermore, single degree-of-freedom (DOF) movements are uncommon under natural conditions; for example, even in normal human walking, frontal plane motions of the ankle are substantial as well as sagittal plane motions. Thus, the control of multiple ankle DOFs may present unique challenges, and quantitative characterization of multi-variable ankle impedance promises better understanding of the functional role of the ankle and may afford unique insight about its special vulnerabilities.

1.3 Related Work

1.3.1 Upper-Extremity Study

Multi-variable and multi-joint, upper-extremity mechanical impedance has been extensively studied ever since interactive arm robots, such as MIT-MANUS [19], were introduced. Earlier multi-variable studies provided richer information on multi-joint limb control and opened a new research area in neuro-motorcontrol, unavailable from single DOF studies [10, 11, 20-22]. Most of earlier studies used transient position disturbance to retrieve stiffness ellipse.

More recently, different research groups employed system identification methods, which find a relationship between perturbation inputs and the corresponding outputs at joints, to determine the dynamic properties of multi-joint arm impedance [23-26], elbow joint impedance [27-29]. In addition, a wrist robot was used to experimentally characterize the wrist stiffness in flexion-extension, radial-ulnar deviation, and combinations of the two under relaxed muscles condition [30, 31].

1.3.2 Lower-Extremity Study

For the lower-extremity, many studies examined ankle stiffness [32-34] or knee stiffness [35-37] by calculating the slope of the torque-angle curve. However, this cannot explain the instantaneous joint stiffness or impedance [38], and often described as quasi-stiffness [39].

To directly measure stiffness or impedance, external energy input to perturb the joint of interest is essential. Several system identification methods, both parametric and non-parametric methods, have been widely used. While few studies on knee [40, 41] and hip impedance [42] have been reported, a considerable number of studies on ankle impedance, both simulation and experimental work, have been published.

Hunter and Kearney [43-45] and Weiss et al. [46, 47] used stochastic system identification techniques to examine elastic, viscous and inertial terms of the ankle joint. They investigated effects of mean ankle torque, mean ankle position, and input displacement amplitude, on ankle impedance. Intrinsic and reflex component of ankle impedance was also extensively studied based on nonlinear system identification methods [48, 49]. Time-varying behavior of the ankle was also investigated in simulation [50, 51], goal directed imposed movement conditions [52, 53], and experimentally during stance phase of human walking [54].

Besides studies in healthy people, there have been several studies characterizing ankle impedance of patients with neurological disorders, such as stroke [14, 55-57], MS [13], and SCI [15], to better understand pathological behavior of the human ankle.

While all of the above ankle studies have investigated ankle impedance in the sagittal plane, i.e., dorsiflexion-plantarflexion (DP) direction, only a few studies measured ankle impedance in the frontal plane, inversion-eversion (IE) direction [58-60]. Multi-DOF studies are even less. Roy et al. measured ankle stiffness in both IE and DP directions but did not assess coupling between these DOFs [61, 62].

1.4 Overview of Remaining Chapters

In Chapter 2, *steady-state static ankle mechanical impedance*, which is a non-linear torque and angle relationship, is characterized as a first step to study multi-variable ankle impedance in 2 coupled DOFs, both in the sagittal and frontal planes. Robust vector field approximation methods are introduced to quantify the anisotropy and "spring-like" property of static ankle impedance under relaxed and active muscles.

In Chapter 3, characterization is extended to the frequency domain, and *steady-state dynamic ankle mechanical impedance* is characterized based on linear time-invariant multi-input multi-output stochastic system identification methods. Anisotropy of the impedance and its relationship to muscle activation levels is investigated. The energetic passivity of the ankle is also quantified as a function of frequency and muscle activation levels.

In Chapter 4, *transient dynamic ankle mechanical impedance* is characterized during walking on a treadmill. Modified linear time-varying ensemble based system identification methods are used to investigate how damping and stiffness of the ankle in 2 DOFs change across gait cycle between the end of stance phase to the early stance phase. Close investigation around the heel-strike and toe-off events is also provided.

In Chapter 5, a brief comparison between three different characterization methods presented in previous chapters (Chapter 2~4). On-going work, future applications, and the relevance of this study to other fields of study are discussed.

Formal licenses were obtained from publishers to reuse any portion (e.g., figure, graph, table, or textual material) of copyrighted papers [63-69].

Chapter 2

Multi-Variable Steady-State Static Ankle Mechanical Impedance

2.1 Summary

This chapter presents quantification of multi-variable static ankle mechanical impedance. An experimental protocol using a wearable therapeutic robot enabled reliable measurement of torque and angle data in multiple degrees-of-freedom simultaneously, a combination of inversion-eversion and dorsiflexion-plantarflexion.

The measured nonlinear torque-angle relation was represented as a vector field, and approximated using a method based on thin-plate spline smoothing with generalized cross validation. A robust approximation method provided a reliable estimate of static ankle mechanical impedance even in the (inevitable) presence of noisy data.

The vector field enabled assessment of several important characteristics of static component of ankle mechanical impedance that are not available from prior single degree-of-freedom studies: the directional variation of ankle mechanical impedance, the extent to which the ankle behaves as a spring, and evidence of uniquely neural contributions.

Experiments with young unimpaired subjects quantified the behavior of the human ankle under maximally-relaxed muscles and voluntary contraction of ankle muscles either singly or antagonistically. Under fully relaxed ankle muscles, ankle mechanical impedance is spring-like but strongly direction-dependent, being weakest in inversion, exhibiting a characteristic “peanut” shape.

Predominantly activating a single muscle or co-contracting antagonistic muscles (10% of maximum voluntary contraction) significantly increased ankle stiffness in all directions but it increased more in the sagittal plane than in the frontal plane, accentuating the relative weakness of the ankle in the inversion-eversion direction. Remarkably, the observed increase was not consistent with simple superposition of muscle-generated stiffness.

Static ankle behavior in active muscles was close to that of a passive elastic system, although statistically significant non-zero curl components were observed. This externally simple behavior would help to ensure stable dynamic interaction with the environment.

2.2 Introduction

While a considerable number of single DOF studies and a few of uncoupled 2 DOF studies on ankle impedance have been reported, to the best of my knowledge, no one has investigated ankle impedance in the coupled DOFs. As stressed in Chapter 1, multi-variable studies in coupled DOFs of the ankle will provide richer information in many aspects.

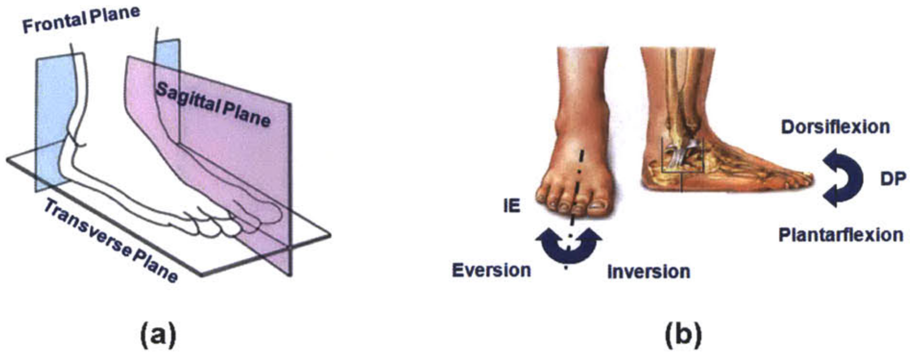

Figure 2.1: Planes of interest and the corresponding ankle motions. (a): Sagittal and frontal planes. (b): Dorsiflexion-plantarflexion.

In this chapter, a nonlinear torque-angle relationship at the ankle, which is defined as static ankle mechanical impedance, was studied as a first step to characterize ankle impedance in 2 coupled DOFs, a combination of IE and DP (Figure 2.1).

Static ankle impedance was characterized under fully relaxed muscles and active muscles, either singly or antagonistically at 10% maximum voluntary contraction (MVC) levels.

In the following sections, an experimental setup, especially a wearable ankle robot, is described in detail. Next, a vector field approximation method to quantify static ankle impedance is explained. Characterization results on young healthy subjects under relaxed and active muscles follow.

2.3 Experimental Setup


(a) (b)

Figure 2.2: A wearable ankle robot, Anklebot.
(a): Anklebot actuator. (b): Anklebot connected to the knee brace and the shoe

A wearable ankle robot, Anklebot (Interactive Motion Technologies, Inc.) [62], was used as the center piece to characterize ankle impedance (Figure 2.2 (a)). The most salient features of this robot are that it is highly back-drivable with very low intrinsic mechanical impedance, and has two active DOFs and a third passive DOF which prevents imposing any inadvertent kinematic constraints on the motion of the ankle. This design minimally interferes with normal motion of the foot relative to the shank, and allows the maximum range of motion (ROM) required for the typical gait of healthy or pathological subjects [2]. The robot can provide actively controllable torque up to 23 Nm in the sagittal plane for dorsiflexion-plantarflexion (DP) and 15 Nm in the frontal plane for inversion-eversion (IE) motions. The robot was mounted to a knee brace and end effectors of the robot were connected to a U-shape bracket attached to a custom designed shoe (Figure 2.2 (b)).

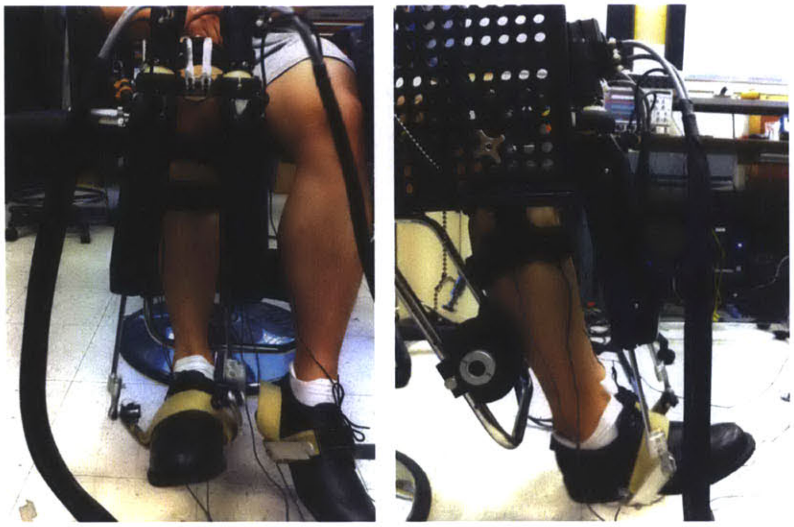

Figure 2.3: Subject wearing the Anklebot in a seated posture.

Subjects wore the brace and shoe, and seated with their ankle held by the robot clear of the ground in a neutral position with the sole at a right angle to the tibia. The knee brace was securely fastened to the chair to support the weight of the robot and the leg and to ensure that measurements were made in a repeatable posture (Figure 2.3). In addition, to prevent foot slippage inside the shoe, a proper shoe size was selected for each subject, the foot was tightly fastened with shoe laces, and a wide Velcro strap was secured over the laces.

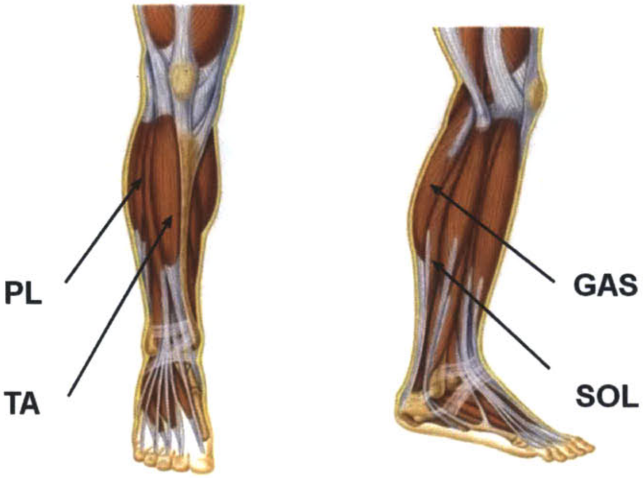

Figure 2.4: Four major ankle muscles.

To monitor muscle activation levels, electromyographic (EMG) signals were recorded using differential surface electrodes with built-in pre-amplifiers (Delsys Inc.). They were placed on the bellies of major muscles related to ankle movement: tibialis anterior (TA), peroneus longus (PL), soleus (SOL), and medial gastrocnemius (GAS) (Figure 2.4). EMG signals, band pass filtered between 20 Hz and 450 Hz, were sampled at 1 kHz and their amplitudes were estimated using a root-mean-square (RMS) filter with a moving window of 200 *ms* after removing any DC component of the signal.

2.4 Methods

2.4.1 Vector Field Approximation Method

In general, ankle mechanical impedance is a dynamic operator that maps a time-history of angular displacement onto a corresponding time-history of torque. Its time-invariant, static component is a relation between angle and torque, possibly nonlinear, and can be represented as a vector field (Eq. (2.1)).

$$(\tau_{IE}, \tau_{DP}) = V(\theta_{IE}, \theta_{DP}) \tag{2.1}$$

where θ_{IE} and θ_{DP} are angular displacements in the IE and DP directions, respectively, and τ_{IE} and τ_{DP} are the corresponding applied torques. In this study, I decomposed the vector field approximation (V) problem into two scalar function estimation problems (Eq. (2.2)).

$$\begin{aligned} \tau_{IE} &= \phi_1(\theta_{IE}, \theta_{DP}) \\ \tau_{DP} &= \phi_2(\theta_{IE}, \theta_{DP}) \end{aligned} \tag{2.2}$$

For scalar function estimation, I used Thin-Plate Spline (TPS) [70] smoothing with Generalized Cross Validation (GCV) [71]. TPS smoothing provides a surface approximation for each scalar function. With the application of GCV, each scalar function (ϕ_1 and ϕ_2) is uniquely determined in the form of a TPS, and the total vector field (V) can be defined accordingly.

In detail, given a set of n data points ($P_i = (x_i, y_i), i = 1,2,...,n$) in $\Re^2$ and n vectors $z = (z_1, z_2, ..., z_n)$, where z_i corresponds to the z value at point P_i, a weighted combination of TPS centered about each data point together with an affine transformation gives the interpolation function (f) that passes through the points exactly (Eq. (2.3)).

$$f(x,y) = a_0 + a_1 x + a_2 y + \sum_{i=1}^{n} w_i U(|P_i - (x,y)|)$$

$$U(r) = r^2 \log r^2, \quad U(0) = 0 \tag{2.3}$$

Noise reduction by smoothing is very important for robust data analysis, since biological experimental data contain considerable noise. Smoothing TPS is a regularization problem with a smoothing parameter (λ). For a fixed smoothing parameter (λ), the function for TPS (f_λ) is the minimizer of E_{tps} (Eq. (2.4)).

$$f_\lambda = \arg\min_{f} \; E_{tps}$$

$$E_{tps} = \frac{1}{n} \sum_{i=1}^{n} (z_i - f(x_i, y_i)) + \lambda \iint_{\Re^2} \left(\left(\frac{\partial^2 f}{\partial x^2} \right)^2 + 2 \left(\frac{\partial^2 f}{\partial x \partial y} \right) + \left(\frac{\partial^2 f}{\partial y^2} \right)^2 \right) dxdy \tag{2.4}$$

As λ runs from 0 to ∞, the smoothing surface changes from an interpolation to a flat surface in a least squares sense. The challenge in TPS smoothing is to find the optimal smoothing parameter (λ^*) that creates functions that pass, as closely as possible, to all data points while maximizing smoothness. In other words, the challenge is to determine the best tradeoff between fidelity to the data and roughness of the surface.

For this purpose, we adopted the GCV approach which provides an excellent estimate of the optimal smoothing parameter even when the amount of noise is unknown [71]. Finding the optimal smoothing parameter (λ^*) is a nonlinear regression problem of minimizing mean squared error $R(\lambda)$ between the estimate (f_λ) and the underlying function (f) (Eq. (2.5)).

$$z_i = f(x_i, y_i) + \varepsilon_i$$

$$R(\lambda) = \frac{1}{n}\sum_{i=1}^{n}(f_\lambda(x_i, y_i) - f(x_i, y_i))^2$$

$$\lambda^* = \underset{\lambda}{\operatorname{argmin}} R(\lambda) \tag{2.5}$$

where z_i are measured data, $f(x_i, y_i)$ an underlying smooth surface, $f_\lambda(x_i, y_i)$ an estimate, and ε_i a white noise process. Details of calculating optimal smoothing parameters and description of TPS smoothing with GCV in a matrix form are provided in Appendix A.

2.4.2 Anisotropy of Static Ankle Mechanical Impedance

To quantify the anisotropy or directional variation of ankle mechanical impedance, the effective ankle stiffness was evaluated from the friction-compensated nonlinear vector field for each direction of movement by computing the slope of a least squares linear fit to the displacement and torque data in that direction, and the variation of ankle stiffness with direction in IE−DP space was constructed accordingly. This representation of stiffness ignores all components orthogonal to the displacement.

Although stiffness can be calculated at any point of interest in the displacement field, in this study, to estimate the predominant behavior of the ankle, stiffness was calculated as the average slope of data points between the neutral and target positions. Its slope represented the effective stiffness opposing displacement in that direction.

2.4.3 Vector Field Decomposition

The nonlinear vector field approximation was also decomposed into a conservative (symmetric) component and a rotational (anti-symmetric) component. Although a vector field may be nonlinear for large displacements, it is approximately linear for small deviations about any point in the displacement field as long as the field is sufficiently smooth around that point. Therefore, the torque-angular displacement relationship around a point of interest can be expressed as a Taylor series expansion (Eq. (2.6)):

$$\delta\tau_{IE} = \frac{\partial \tau_{IE}}{\partial \theta_{IE}}(\theta_{IE0},\theta_{DP0})\delta\theta_{IE} + \frac{\partial \tau_{IE}}{\partial \theta_{DP}}(\theta_{IE0},\theta_{DP0})\delta\theta_{DP} + higher\,order\,terms$$

$$\delta\tau_{DP} = \frac{\partial \tau_{DP}}{\partial \theta_{IE}}(\theta_{IE0},\theta_{DP0})\delta\theta_{IE} + \frac{\partial \tau_{DP}}{\partial \theta_{DP}}(\theta_{IE0},\theta_{DP0})\delta\theta_{DP} + higher\,order\,terms \qquad (2.6)$$

For sufficiently small displacements from the point of interest, the higher order terms may be neglected, and the torque-angular displacement relation is linear to a first-order approximation, yielding in matrix notation (Eq. (2.7)):

$$\begin{bmatrix}\delta\tau_{IE}\\ \delta\tau_{DP}\end{bmatrix} = \begin{bmatrix}K_{11} & K_{12}\\ K_{21} & K_{22}\end{bmatrix}\begin{bmatrix}\delta\theta_{IE}\\ \delta\theta_{DP}\end{bmatrix}$$

$$K_{11} = \frac{\partial \tau_{IE}}{\partial \theta_{IE}} \qquad K_{12} = \frac{\partial \tau_{IE}}{\partial \theta_{DP}}$$

$$K_{21} = \frac{\partial \tau_{DP}}{\partial \theta_{IE}} \qquad K_{22} = \frac{\partial \tau_{DP}}{\partial \theta_{DP}}$$

$$\boldsymbol{\delta\tau} = \boldsymbol{K\delta\theta} \qquad (2.7)$$

The locally linearized stiffness matrix $\boldsymbol{K}$ can be further decomposed into its symmetric ($\boldsymbol{K}_s$) and anti-symmetric ($\boldsymbol{K}_a$) components (Eq. (2.8)):

$$\boldsymbol{K} = \boldsymbol{K}_s + \boldsymbol{K}_a$$

$$\boldsymbol{K}_s = \frac{\boldsymbol{K} + \boldsymbol{K}^T}{2} = \begin{bmatrix} K_{11} & (K_{12} + K_{21})/2 \\ (K_{12} + K_{21})/2 & K_{22} \end{bmatrix}$$

$$\boldsymbol{K}_a = \frac{\boldsymbol{K} - \boldsymbol{K}^T}{2} = \begin{bmatrix} 0 & (K_{12} - K_{21})/2 \\ (K_{21} - K_{12})/2 & 0 \end{bmatrix} \tag{2.8}$$

where superscript T denotes the transpose operation. The symmetric component is conservative, having zero curl but non-zero divergence, while the anti-symmetric component is non-conservative, having zero divergence but non-zero curl.

The conservative component is spring-like. Here, a set of muscles is defined as spring-like if the torque vector is an integrable function of displacement so that a potential function analogous to the elastic energy stored in a spring may be determined [10]. In that case, the torque vector is the gradient of a potential function and, as a result, the curl of the torque field must be identically zero. Spring-like behavior is passive, since no energy is generated or removed by cyclic displacements. On the other hand, the rotational component is active because cyclic displacements may add or remove energy. Thus we can quantify how spring-like the ankle is by comparing the size of the rotational (curl) component of the field with its conservative component. A detailed definition of "spring-like" is provided in Appendix B.

The comparison of the relative magnitudes of $\boldsymbol{K}_s$ and $\boldsymbol{K}_a$ enabled quantification of the extent to which the ankle is passive, more specifically spring-like. The ratio of the square roots of the determinants of the anti-symmetric ($\boldsymbol{K}_a$) and symmetric ($\boldsymbol{K}_s$) parts of the stiffness matrix was calculated to assess the importance of non-zero curl components in the rotational field (Eq. (2.9)).

$$\sqrt{K_{ratio}} = \sqrt{\det(\boldsymbol{K}_a)} / \sqrt{\det(\boldsymbol{K}_s)} \tag{2.9}$$

When the rotational field has no curl, i.e., $\det(\boldsymbol{K}_a) = 0$ and $\sqrt{K_{ratio}} = 0$ accordingly, the torque field can be derived from a potential function, meaning that the system is fundamentally spring-like.

2.5 Validation of Analysis Methods

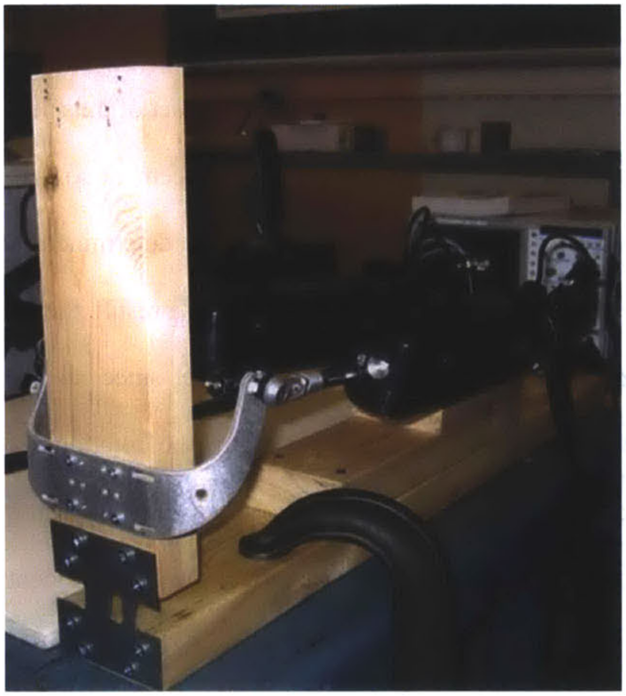

Figure 2.5: A physical mockup consisting of passive elements.

To validate our methods, the procedure was tested using a simple physical "mock-up", loosely resembling the human foot-ankle-shank complex. It consisted of two wooden blocks joined by a flexible steel plate and connected to the Anklebot in the same way as the shoe and knee brace (Figure 2.5). To allow for the robot torque limits and prevent plastic deformation of the steel plate, the nominal angular displacement of this “mock-up” was set as 3°, and the torque-angle data were recorded for movements in 24 directions.

Although the mockup did not display the same torque-angle relation as the human ankle, it provided a challenging test of our methods because (i) by design it had strongly direction-dependent behavior and (ii) its torque-angle relation had zero curl, because we know from physical principles that any collection of passive elements (elastic, inertial or frictional) however connected, cannot generate non-zero curl.

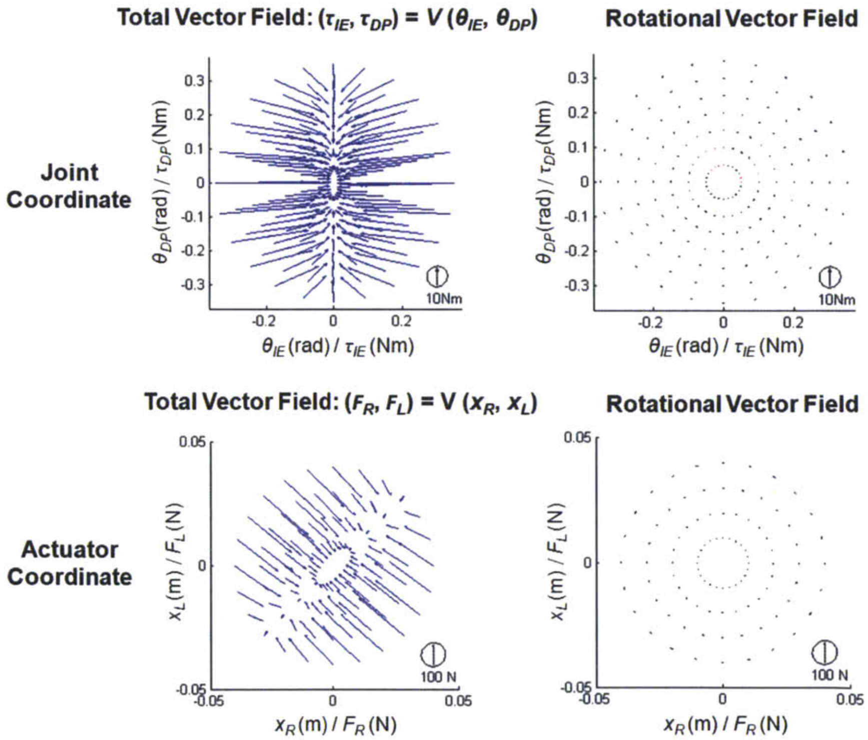

Figure 2.6: Validation of the vector field approximation methods using a physical mockup. Top: joint coordinates, bottom: actuator coordinates, left: total field, right: rotational field.

The total vector field measured from the physical mock-up is shown in Figure 2.6. As expected from the geometry of the thin steel plate connecting the blocks, it was substantially stiffer in IE than DP, and this was reflected in the pattern of the vector field. In addition, whether the torque-angle relation is linear or nonlinear, because the mock-up was a passive mechanical structure, the vector field must be conservative. Decomposition of the measured vector field showed that its curl components were not significantly different from zero (Figure 2.6).

If curl is zero in one coordinate frame, it should be zero in all coordinate frames. We verified this by computing the curl in joint coordinates and in actuator coordinates, first transforming the raw data between the two frames through the nonlinear kinematic relations due to the mechanical connection of the Anklebot to the limb [62] then applying the vector field fitting procedure. Although the shape of the total vector field was changed by this coordinate transformation, the curl value remained zero (Figure 2.6).

These results showed that analysis methods correctly identified curl when it was absent. To test whether the method correctly identified curl when it was present, we simulated a torque field with non-zero curl and noise comparable to our experimental data and applied our method to analyze it. The results (detailed in Appendix C) verified that curl was also correctly identified when it was present.

2.6 Steady-State Static Ankle Mechanical Impedance in Relaxed Muscle

2.6.1 Subjects

Eight unimpaired young human subjects with no reported history of biomechanical or neuromuscular disorders (4 males, 4 females; age 22 to 31; height 1.62 m to 1.90 m; weight 59.0 kg to 84.8 kg) were recruited for this study. Participants gave written informed consent to participate as approved by MIT's Committee on the Use of Humans as Experimental Subjects (COUHES).

2.6.2 Experimental Protocol

Subjects were instructed to relax while Anklebot applied terminated ramp perturbations to the ankle with a slow velocity (5°/sec), selected to avoid evoking spindle-mediated stretch reflexes and maintain quasi-static conditions. Anklebot moved the ankle along a commanded trajectory, and held the foot for 0.1 seconds at the starting and ending positions.

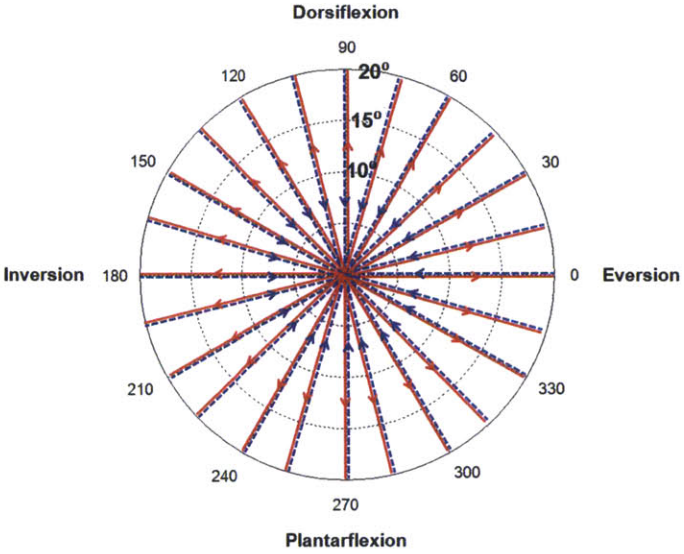

Figure 2.7: The displacement profile in IE–DP space. Solid red lines denote outbound movements, and dotted blue lines represent inbound movements.

The complete protocol consisted of 48 movements total along 24 equally-spaced directions in IE–DP space, once outbound and once inbound per direction, with a nominal displacement amplitude of 20° in each direction (Figure 2.7). Perturbations began with pure eversion (0°), rotated by 15° on each subsequent perturbation (45° corresponded to equal perturbations in eversion and dorsiflexion) and ended at 345°.

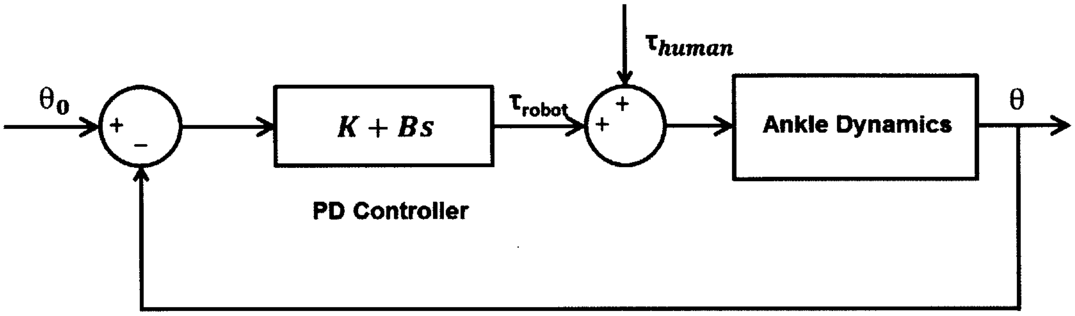

Figure 2.8: Schematic representation of a simple impedance controller. θ_o and θ are the reference ankle angle and measured angle from the neutral position, respectively.

A simple impedance controller was implemented to move the ankle along the commanded trajectory (Figure 2.8). A PD controller for joint angle with proportional gain $K = 100 Nm/rad$ and derivative gain $B = 2 Nms/rad$ guaranteed safe, stable, and highly compliant operations in human–robot interactions.

Applied torque and actual angular displacement in both DOFs as well as EMG data were sampled at 200 Hz. The complete set of measurements took a little over 3 minutes.

Any torque components required to overcome the inertia and friction of the actuators were measured by 10 repetitions of the experimental protocol explained above but with no human subject. The average of these measurements was expressed as a multi-variable relation between torque and angle and subtracted from the recorded torque. Furthermore, data points around the neutral and target positions were discarded to avoid possible errors due to initial lengthening and shortening of muscle fibers [72].

2.6.3 Reliability of Field Approximation

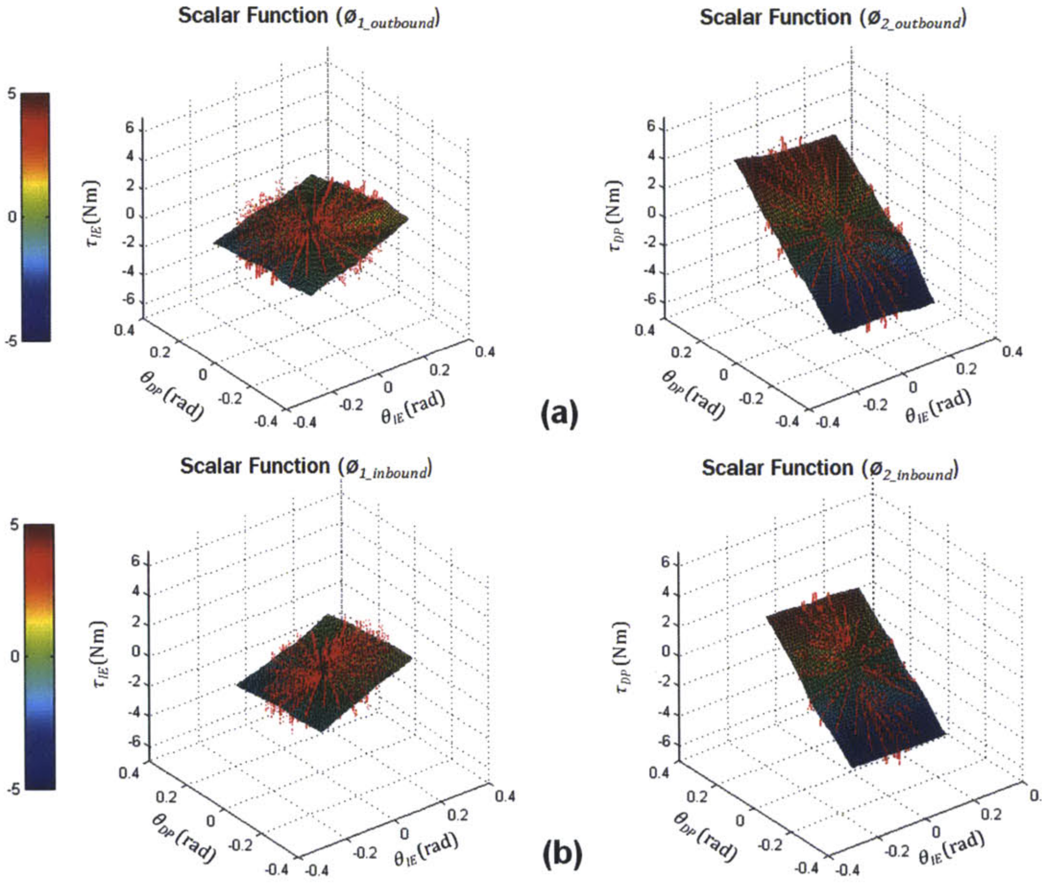

Figure 2.9: Representative friction-compensated measurements and the corresponding vector field. Measurements are depicted as point sets in 24 directions, and the vector field consists of 2 TPS surface estimates. (a): Outbound, (b): Inbound

Outbound and inbound torque and angular displacement data were approximated separately (Figure 2.9). The data points distributed in 24 directions are the friction-compensated measurements. The surfaces are estimates of the two torque components obtained by TPS approximation with an optimal smoothing parameter determined by GCV. The actual displacement amplitude was about 15° (mean value across 24 directions of all subjects data is 15.33° with standard deviation 1.54°), and all data except points near the starting position (0~1°) of each movement direction were used for scalar function estimation. The mean deviation between measurements and estimates was less than 0.005 Nm with standard deviation (SD) 0.380 Nm, from which we defined zero deviation as –0.740 to 0.750 Nm with 95% confidence. Because of the substantial smoothing effect of the surface fitting procedure used to identify the vector field, this error was substantially smaller than the apparatus measurement error range, ±1 Nm [62].

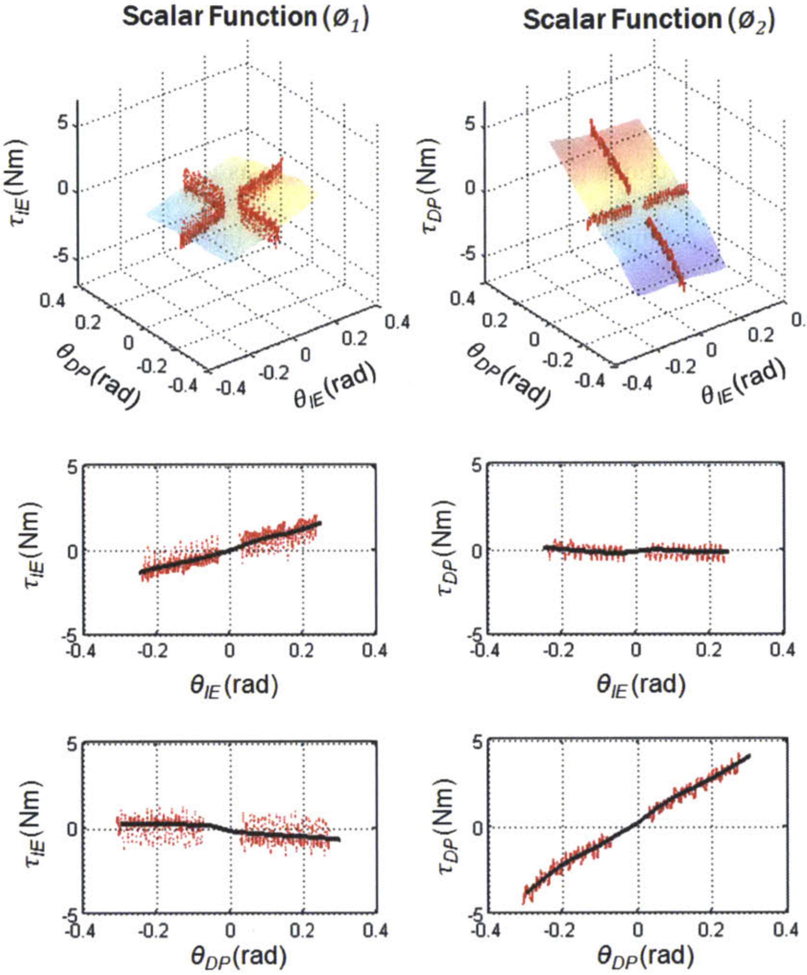

Figure 2.10: Representative 2D slices of the vector field in 4 major directions (inversion, eversion, dorsiflexion, and plantarflexion). Measurements in 4 major directions and the fitted field (top), projected 2D data in inversion-eversion (mid) and dorsiflexion-plantarflexion (bottom).

Representative 2D-slices of the vector field in 4 major directions (inversion, eversion, dorsiflexion and plantarfelxion) show how well the field fit the observed data (Figure 2.10).

2.6.4 Anisotropy of Static Ankle Mechanical Impedance and Hysteresis in Relaxed Muscles

For all subjects, the effective ankle stiffness was calculated from the estimated vector field in 48 movement directions (24 outbound, 24 inbound) as detailed above. To check the validity of this stiffness estimate, we quantified how well this linearized approximation fit the nonlinear torque field by calculating an R^2 value. The lowest R^2 value was 0.88 and most subjects showed R^2 values higher than 0.90, indicating that the linearized stiffness accounted for at least 90% of the variance.

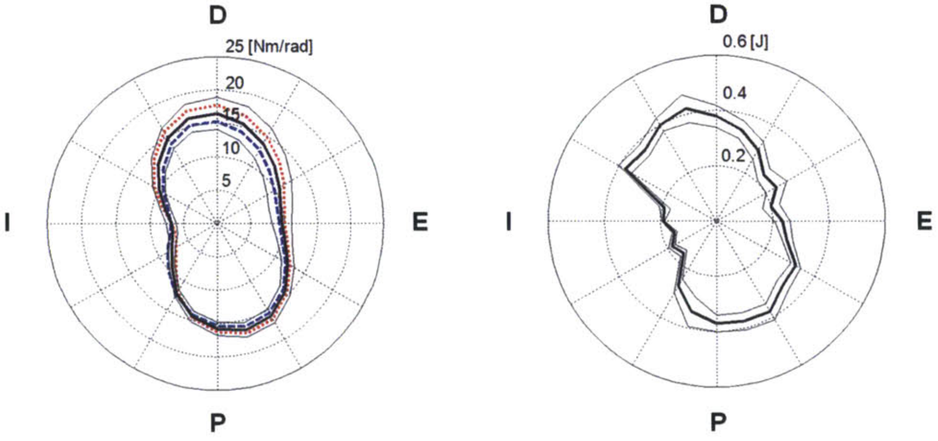

(a) (b)

Figure 2.11: Anisotropy of static ankle mechanical impedance and hysteresis. Directional variation of (a) ankle stiffness (Dark solid band: Mean value of outbound and inbound data, Light solid bands: Mean±SE, Dotted band: Mean of outbound data, Dashed band: Mean of inbound data) and (b) hysteresis (Dark solid band: Mean value, Light solid bands: Mean±SE) in IE−DP space.

The averaged stiffness estimation results of all subjects but one (subject #6) are plotted in polar coordinates in (Figure 2.11 (a)). Ankle stiffness varied significantly with direction in IE−DP space and was consistently lower in the IE direction than in the DP direction, resulting in a “peanut” shape, pinched in the IE direction. Subject #6, who was excluded from the means presented in Figure 2.11 (a) had an unusually low dorsiflexion impedance (9.86 Nm/rad) and an unusually high plantarflexion impedance (33.15 Nm/rad) compared to the mean values of all other subjects (16.99 Nm/rad for dorsiflexion and 15.71 Nm/rad for plantarflexion).

The torque required for outbound (loading) movements was consistently greater than for inbound (unloading) movements, even after static torques due to Anklebot friction were subtracted from the measurements. In all 24 directions, this torque was statistically different from zero ($p<0.05$). The resulting energy dissipation was quantified by the area enclosed within the “hysteresis” loop formed by the compensated outbound and inbound curves of the raw data. The result is graphically depicted in IE–DP space in (Figure 2.11 (b)). Hysteresis was highly correlated with stiffness ($R^2 = 0.88$) and larger in DP than IE, exhibiting a pinched “peanut” shape.

2.6.5 “Spring-like” Property of Static Ankle Mechanical Impedance

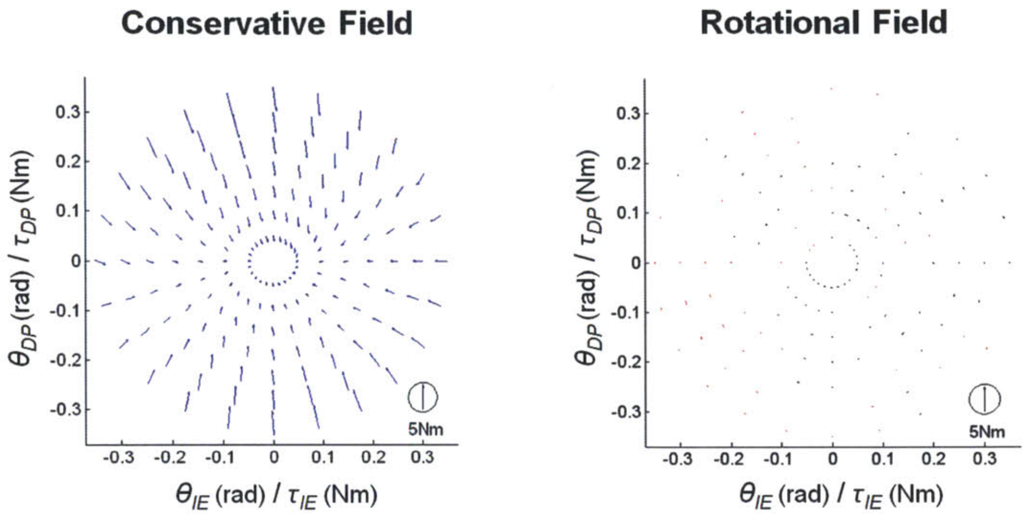

Figure 2.12: Decomposition of a representative vector field. The torque vector is represented by an arrow drawn with its tail at the tip of the angular displacement vector (Red: positive curl, Black: negative curl).

Decomposition of the vector field into a conservative field (with zero curl) and a rotational field (with zero divergence) showed that, in general, the rotational components were much smaller than the conservative components (Figure 2.12).

The mean magnitude of curl and the ratio of the determinants of the anti-symmetric and symmetric parts of the stiffness matrix ($\sqrt{K_{ratio}}$) were computed. Excluding one subject (subject #3, discussed below), the average magnitude of curl was 0.22 Nm with SD 0.19 Nm, which was statistically indistinguishable from zero. The mean value of $\sqrt{K_{ratio}}$ for the same 7 subjects was 0.13 (see Table 2.1 for details). The ankle joint is predominantly spring-like in the fully relaxed condition.

Table 2.1: Rotational components and effective stiffness in major directions for all subjects.

OUTBOUND Subject	Mean curl magnitude (Nm)	Curl std. dev. (Nm)	$\sqrt{K_{ratio}}$	Stiffness in major directions (Nm/rad)			
				Inversion	Eversion	Dorsiflexion	Plantarflexion
1	0.17	0.13	0.11	5.35	7.06	12.33	14.26
2	0.13	0.1	0.09	8.28	8.85	16.25	15.41
3	0.35	0.4	0.20	11.26	10.39	24.46	18.21
4	0.22	0.18	0.09	9.91	15.4	29.65	15.47
5	0.29	0.19	0.15	5.26	11.51	19.72	21.11
6	0.28	0.24	0.17	6.69	11.67	9.33	34.11
7	0.23	0.21	0.10	7.83	13.21	21.02	11.86
8	0.22	0.24	0.15	4.28	4.66	7.32	19.74
INBOUND Subject	Mean curl magnitude (Nm)	Curl std. dev. (Nm)	$\sqrt{K_{ratio}}$	Stiffness in major directions (Nm/rad)			
				Inversion	Eversion	Dorsiflexion	Plantarflexion
1	0.19	0.15	0.13	5.35	6.73	11.39	13.45
2	0.14	0.13	0.11	6.1	8.09	14.29	14.47
3	0.41	0.36	0.26	9.71	8.57	15.44	11.68
4	0.29	0.24	0.13	9	12.65	20.15	18.51
5	0.26	0.21	0.14	6.98	11.63	16.57	15.87
6	0.27	0.22	0.15	7.23	9.98	10.38	32.18
7	0.24	0.18	0.11	8.99	11.5	19.97	13.17
8	0.2	0.19	0.15	4.72	4.82	9.23	16.69

One subject (subject #3) exhibited undesired muscle activation during the protocol, apparently being unable to relax fully. This subject significantly activated tibialis anterior (evident as a large magnitude of EMG, ~ 0.02 mV) during movements in directions between 255 ° and 345 °. For comparison, the mean EMG magnitude for each of four fully relaxed muscles was lower than 0.002 mV.

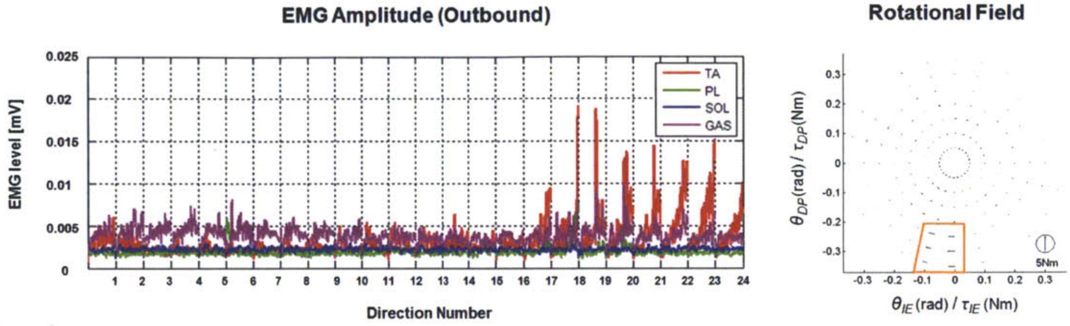

Figure 2.13: Non-zero curl components (right panel, color code as in Figure 2.12) due to undesired muscle activation (left panel). (Red: TA, Green: PL, Blue: SOL, Pink: GAS)

This subject's muscle activation was accompanied by non-zero rotational components, notably in the 255° and 270° directions (the highlighted region in the right panel of Figure 2.13).

Another interesting subject (subject #2) who fell asleep during the measurement protocol exhibited an average magnitude curl of 0.13 Nm with SD 0.1 Nm. These were the smallest values recorded among all subjects.

2.6.7 Discussion

Identifying a vector field by treating each vector component as a scalar field has been challenged by who pointed out that the details of a scalar approximation (e.g. using Gaussian radial basis functions) vary with the coordinates chosen by the experimenter, potentially rendering the structure of the estimated vector field sensitive to an investigator's arbitrary choices [73]. I validated the suggested method experimentally using a simple physical "mock-up" consisting of wooden blocks and a steel plate. From physical considerations we know that the rotational component (curl) of the vector torque-angle relation for the mock-up must be identically zero, and measurements confirmed this. In addition, I showed that the conclusion that curl was zero did not depend on the coordinate frame used to represent the data. Although the detailed shape of the total vector field may change when it is represented in different coordinates (Figure 2.6), certain physical properties (such as whether the field is energetically conservative, with zero curl) must be independent of coordinates. I verified that the observation of zero curl was invariant even under nonlinear coordinate transformations.

A plot of stiffness vs. direction exhibited a characteristic "peanut" shape, pinched in the IE direction. Although ankle stiffness is highly variable even within a group of young healthy subjects, on average, ankle stiffness in the DP direction was higher than in the IE direction by about a factor of 2. The orientation of this "peanut" shape was not precisely aligned with the axes of joint coordinates, the maximum-stiffness direction being consistently tilted slightly from the DP axis in a counterclockwise (CCW) direction. These are clinically meaningful results and indicate the direction of rotation in which the ankle is most vulnerable. Lower frontal-plane stiffness indicates a greater tendency for the foot to roll, especially in inversion. Perturbations, e.g. from uneven ground, may evoke excessive displacement and possibly injury of the ankle. This is consistent with the observation that most ankle-related injuries occur in the frontal plane rather than in the sagittal plane [74].

I also found that the torque evoked by displacement away from the equilibrium posture (outbound) was typically greater than the torque corresponding to the same displacement as the foot returned towards equilibrium (inbound). As positive net work was required to displace the ankle and return it to equilibrium, the presence of some dissipative phenomenon is indicated, similarly observed in the wrist [75]. As forces due to static friction or other non-ideal behavior of the Anklebot were measured prior to the experiments and subtracted from the recorded data, and the phenomenon varied with direction similarly to ankle stiffness, it appears to be a characteristic of muscle. Further study seems warranted.

Analysis of the estimated multi-variable vector field provided a precise quantification of the extent to which the ankle is "spring-like". Across almost all subjects, curl was indistinguishable from zero both for outbound and inbound fields with friction and hysteresis compensation; the ankle was spring-like. Because muscles were relaxed, this may seem unsurprising. The force-length relation for each individual muscle resembles a spring (albeit possibly nonlinear) and any arbitrary connection of spring-like muscles to the skeleton will yield a spring-like joint behavior (again possibly nonlinear). However, neural feedback (e.g. from spindles and Golgi tendon organs) may also contribute to static ankle mechanical impedance. If it does, then inter-muscular feedback between muscles which act on different degrees of freedom may introduce a deviation from spring-like behavior [10]. If curl is zero while inter-muscular feedback is non-zero, then the feedback gains must be exactly balanced; a dorsi-plantar flexion torque evoked by an inversion-eversion displacement must be identical to the inversion-eversion torque evoked by a comparable dorsi-plantar flexion displacement. Conversely, with constant muscle activity, non-zero curl can only be due to unbalanced inter-muscular feedback. Spring-like behavior (zero curl) in the presence of non-zero inter-muscular feedback is important because it would indicate that although the neuromuscular system is internally complex, it apparently exhibits an externally simple behavior. Spring-like behavior is consistent with dynamically passive ankle mechanical impedance which would help to ensure stable interaction with a dynamically passive environment [76].

Remarkably, I observed non-zero curl in one alert subject. This subject showed a small but significantly non-zero activation of TA and a small but significantly non-zero curl when the foot was displaced towards plantar flexion, stretching the TA. Movement in other directions evoked zero curl and EMG was silent, showing that this subject was able to relax fully under our experimental manipulation. The activation of TA when it was stretched suggests an involuntary action of neural feedback. If so, the observation of non-zero curl may be due to unbalanced inter-muscular feedback. Conversely, our most relaxed subject (who fell asleep during the measurement procedure) exhibited the smallest curl measured in all subjects. Taken together, these observations show that vector field approximation based on scalar methods using TPS smoothing with GCV works well−sufficiently precise to detect the subtle differences in structure due to small changes in muscle activation.

2.7 Steady-State Static Ankle Mechanical Impedance in Active Muscle

2.7.1 Subjects

The participants in this study were 10 unimpaired young human subjects with no reported history of biomechanical or neuromuscular disorders (7 males, 3 females; age 19 to 31; height 1.55 m to 1.80 m; weight 55.8 kg to 81.6 kg). Approval for this study was obtained from COUHES and participants gave written informed consent to participate as approved by COUHES.

2.7.2 Experimental Protocol

As a first step for active studies, the MVC of each muscle was measured while subjects stood upright. In detail, subjects were asked to activate each to their maximum level and maintain it for 5 seconds while the robot provided high restoring torques to hold the ankle near the neutral position. Measurements were repeated 3 times for each muscle with enough rest time between measurements to minimize fatigue. Amplitudes of measurements were estimated and the MVC level was determined as the maximum of 3 measurements.

The target EMG level was set as 10% of MVC. I set the target to a constant level of muscle activity, rather than constant torque, to better understand the role of "muscle stiffness" and "kinematic stiffness" in joint stiffness changes. In detail, joint stiffness is determined not only by muscle stiffness but also by the nonlinear kinematics due to the variation of muscle moment arms and their derivatives.

Subjects were seated with their ankle held by the robot in a neutral position with the sole at a right angle to the tibia. As a baseline for active studies, passive ankle impedance was first measured with muscles fully relaxed. For active studies, a graphical user interface was provided to subjects, showing real-time EMG amplitudes of TA and SOL along with the corresponding target levels (10% MVC) subjects were to maintain. EMG amplitudes were estimated as described above and normalized to the MVC level.

Subjects were first instructed to activate a specific muscle and maintain it at the target level. When the activation level reached the target level, the robot applied terminated ramp perturbations to the ankle with a slow velocity (10°/sec) selected to maintain quasi-static conditions (no contribution of inertia and minimal effect of viscosity) and minimize the involvement of spindle mediated stretch reflexes [77]. During measurements, subjects were instructed not to resist robot perturbations voluntarily.

Three types of active study were performed: in two of them subjects were instructed to activate only a single muscle (TA or SOL) against a resisting torque exerted by the robot.

Especially, SOL was selected for the plantarflexor active study over the GAS, since GAS is a bi-articular muscle that crosses both the ankle joint and the knee joint, which may induce motions at the knee. In the third, subjects were instructed to co-contract both TA and SOL while maintaining each at a level comparable to that when nominally acting alone.

To minimize any possible effects due to inconstant muscle activation, four repetitive measurements were performed for each study.

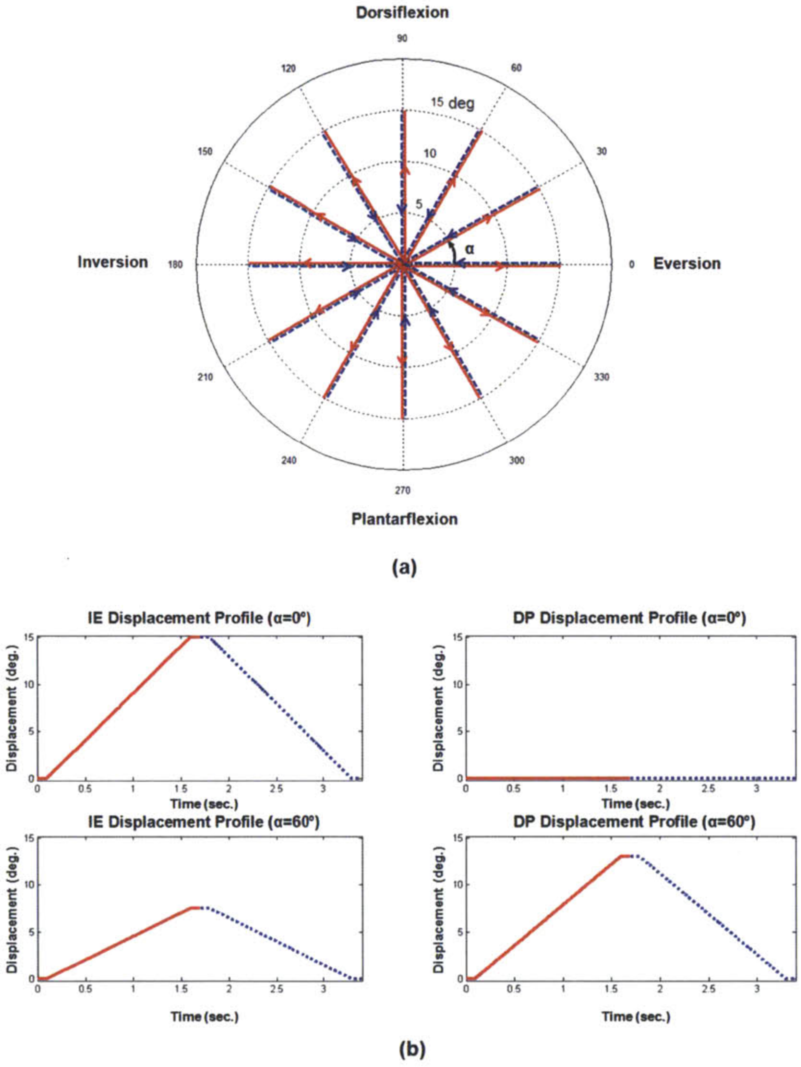

Figure 2.14: (a): The displacement profile in active studies. (b) Representative IE−DP displacement profiles. Solid red lines denote outbound movements, and dotted blue lines represent inbound movements.

Each measurement consisted of a total of 24 movements along 12 equally-spaced directions in IE–DP space, once outbound and once inbound per direction (Figure 2.14 (a)). Measurements with a decreased number of movement directions from 48 in relaxed muscles to 24 minimized was to prevent muscle fatigue during the four repeated measurements. The robot moved the ankle along a commanded trajectory with a nominal displacement amplitude of 15° to cover the normal ROM of the ankle, and held the foot for 0.1 seconds at the starting and ending positions.

The same impedance controller described in section 2.6.2 was used, but with different gain settings ($K = 200 Nm/rad$ and $B = 1 Nms/rad$) to guarantee safe and stable data capture even when muscles were highly activated.

As in the relaxed study, any torque components required to overcome the friction of the actuators were subtracted from the measured torque prior to further analysis. Examples of IE and DP displacement profiles are presented in (Figure 2.14 (b)). The applied torque and actual angular displacement in both DOFs (IE and DP) were recorded at 200 Hz. To avoid fatigue, a 3 minute rest period was given between measurements.

2.7.3 EMG Analysis

The ratio of EMG amplitudes with muscles active to their corresponding MVC levels satisfied the normality condition ($p>>0.05$ according to MATLAB's *jbtest* function) justifying comparison using paired t-tests (MATLAB's *ttest2* function).

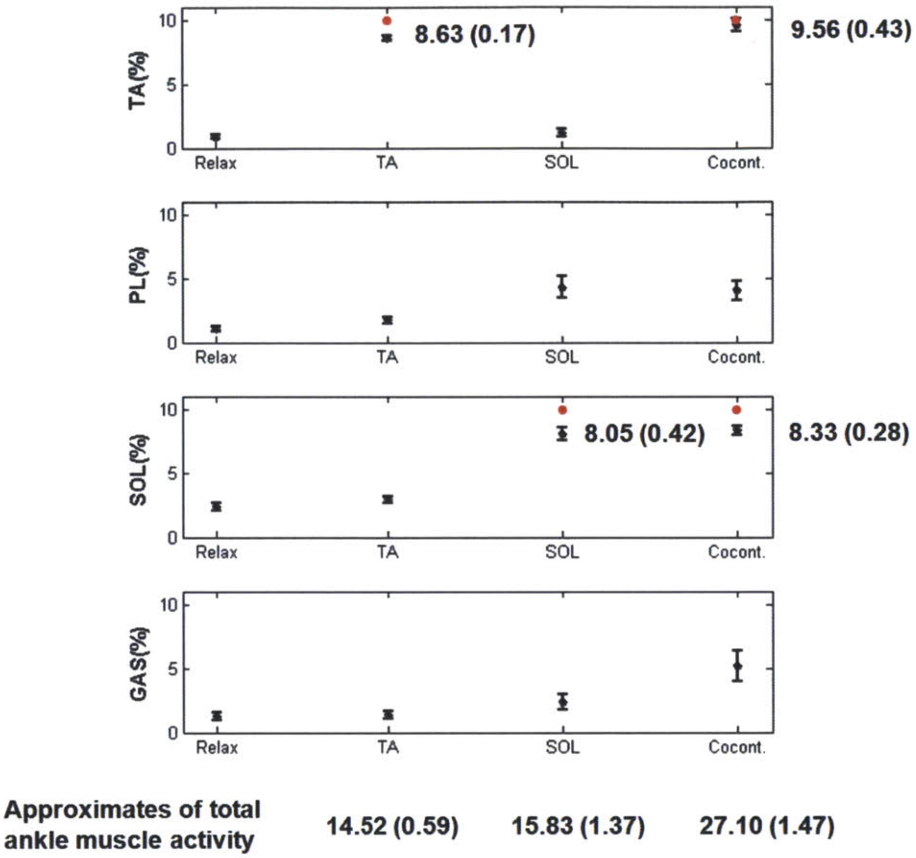

Figure 2.15: The ratio of EMG amplitudes with muscles active. The x-axis represents the type of study and the y-axis presents each muscle's activation level as a percentage of the corresponding MVC level. Target muscle activation levels (10% MVC) are depicted as red dots. The mean ± SE of all analyzed subjects are illustrated as an asterisk and bars, respectively. For each study, total ankle muscle activity was approximated by summing normalized EMG amplitude of all measured muscles, and represented at the bottom of the figure.

They demonstrated that all 10 subjects could follow instructions (Figure 2.15). In general, subjects were able to maintain TA activation around the target level, 10% MVC, quite well: the mean of all subjects was 8.63% (0.17%) for the TA active study, and 9.56% (0.43%) for the co-contraction study. The value in parentheses is the standard error (SE) over all subjects. Activation levels of the SOL were slightly lower than the target level: the mean of all subjects was 8.05% (0.42%) for the SOL active study, and 8.33% (0.28%) for the co-contraction study. In both studies, activation levels of TA and SOL muscles in the co-contraction study were comparable to those when nominally acting alone ($p>0.05$).

In addition, total ankle muscle activity was approximated by summing normalized EMG amplitudes of all measured muscles. For the TA and SOL active studies, estimates were 14.52 (0.59) and 15.83 (1.37), respectively. The estimate for the co-contraction study was 27.10 (1.47) (Figure 2.15).

2.7.4 Reliability of Repetitive Measurements and Field Approximation

Four repetitions of measurements in the 24 directions (a total of 96 movements) were approximated as 8 separate fields (4 outbound and 4 inbound), and averaged into an estimate of a single continuous vector field for outbound and inbound movement.

One subject (#1) from the SOL active study and another (#6) from the co-contraction study exceeded the torque limit of the hardware. Data exceeding the limit were excluded from subsequent analysis. The mean error between the friction-compensated measurements and surface approximates obtained by the TPS smoothing with GCV was less than 0.02 Nm, which is substantially smaller than the measurement error range, ± 1 Nm [62]. This validates the accuracy of the field approximation.

To investigate the variability of repetitive measurements, the mean and SD of absolute error between the approximated field from each of four repeated measurements and their average as a single field were calculated for each subject separately, and averaged across all subjects (Table. 2.2).

Table 2.2: Variability of repeated measurements.

		Scalar Function (Φ_1)		Scalar Function (Φ_2)	
Direction	**Study**	**Mean of Error**	**SD of Error**	**Mean of Error**	**SD of Error**
Outbound	**Relaxed**	0.10 (<0.01)	0.02 (<0.01)	0.15 (0.01)	0.03 (0.01)
	TA Active	0.20 (0.03)	0.05 (0.01)	0.51 (0.06)	0.14 (0.03)
	SOL Active	0.25 (0.08)	0.08 (0.04)	0.52 (0.08)	0.17 (0.07)
	Co-contraction	0.25 (0.01)	0.06 (0.01)	0.64 (0.05)	0.18 (0.04)
Inbound	**Relaxed**	0.11 (<0.01)	0.02 (<0.01)	0.15 (0.01)	0.03 (0.01)
	TA Active	0.20 (0.02)	0.05 (0.01)	0.54 (0.04)	0.12 (0.02)
	SOL Active	0.23 (0.04)	0.06 (0.01)	0.59 (0.07)	0.13 (0.02)
	Co-contraction	0.28 (0.03)	0.06 (0.01)	0.63 (0.04)	0.17 (0.02)

The mean and SD of absolute error in Nm between the field derived from each measurement and the single field averaged from four measurements were calculated for each subject separately. The mean and SE (in parentheses) across all analyzed subjects are presented in the table.

The mean and SD for the scalar function ϕ_2 were greater than for the scalar function ϕ_1. In addition, the mean and SD with muscles active were greater than when relaxed. In all study conditions both for outbound and inbound data, the mean error was less than 0.28 Nm and 0.64 Nm for ϕ_1 and ϕ_2, respectively. The SD was even smaller, less than 0.08 Nm and 0.18 Nm for ϕ_1 and ϕ_2, respectively.

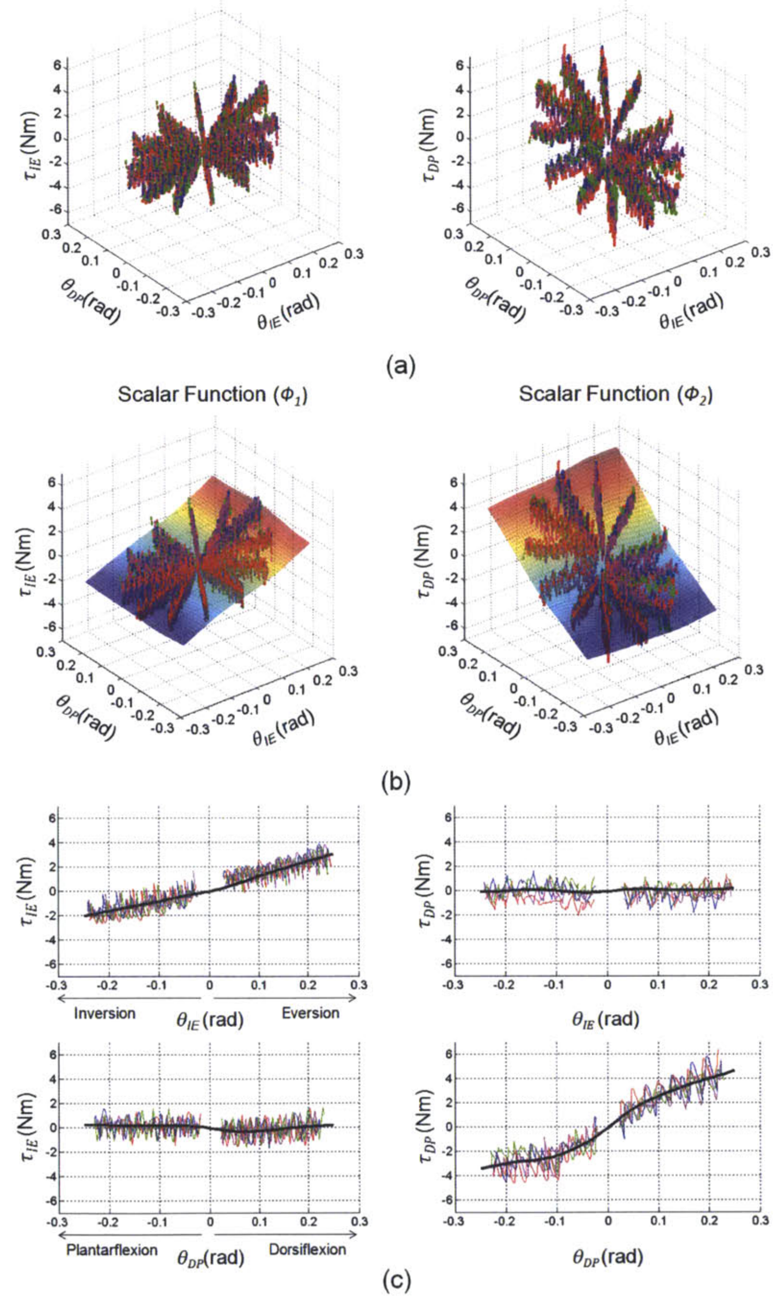

Figure 2.16: Representative measurements and the resultant vector field. (a) Friction compensated measurements of a representative subject (subject #1 outbound data). Each color corresponds to each of four repeated measurements. (b) Four measurements and the fitted field (ϕ_1, ϕ_2). (c) 2D slices of the vector field in four major directions (IE (top) and DP (bottom)).

Figure 2.16 shows raw data and the resultant single vector field of a representative subject (subject #1) and 2D-slices in four major directions (inversion, eversion, dorsiflexion, and plantarflexion) to demonstrate how well the field fit the measurements and how small the variability of repetitive measurements was.

2.7.5 Anisotropy of Static Ankle Mechanical Impedance in Active Muscles

For each subject, the directional variation of ankle stiffness was identified. The effective ankle stiffness was evaluated from the averaged single vector field for each direction of movement by computing the slope of a least squares linear fit to the displacement and torque data in that direction (data between nominal displacements of 1° to 14° were used for fitting), and the variation of ankle stiffness with direction in IE−DP space was constructed accordingly.

To evaluate the effective resolution of stiffness estimation, we calculated the minimum difference of stiffness values between two adjacent directions among 36 directions for each study and for each subject separately. When averaged across all subjects, the resolution was substantially smaller than the stiffness values in all study conditions, verifying that our approach was sensitive enough to detect small stiffness changes in different movement directions (Table 2.3).

Table 2.3: Effective resolution for stiffness estimation.

Direction \ Study	Relaxed	TA Active	SOL Active	Co-contraction
Outbound	0.04 (0.01)	0.06 (0.02)	0.11 (0.03)	0.13 (0.04)
Inbound	0.05 (0.01)	0.06 (0.02)	0.13 (0.05)	0.13 (0.04)

Parentheses denote SE. The unit is Nm/rad.

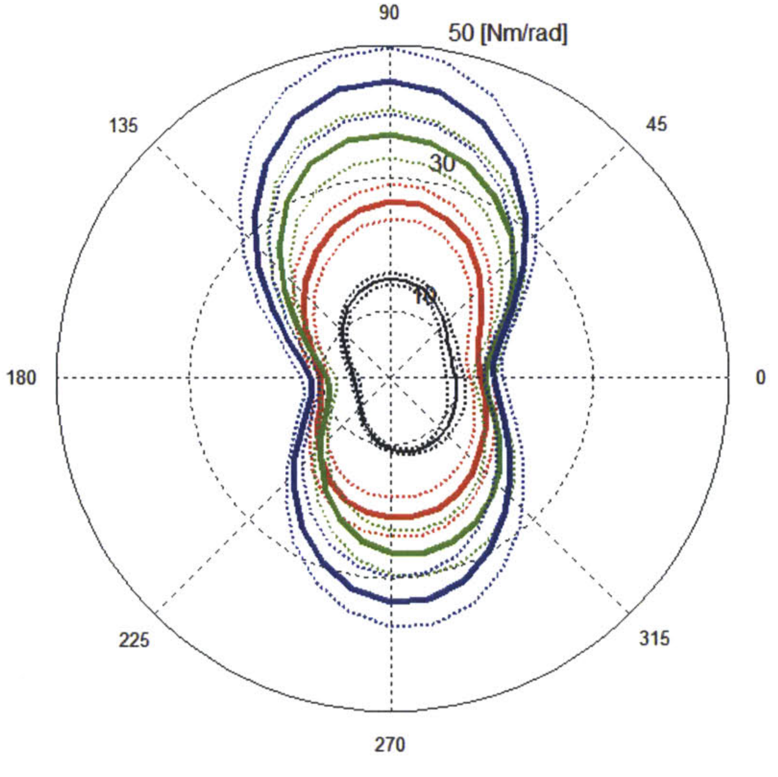

Figure 2.17: Anisotropy of ankle stiffness. Stiffness increases significantly in all movement directions with active muscles ($p<<0.05$). Black: relaxed, Red: TA active, Green: SOL active, Blue: Co-contraction Solid line: mean value of all analyzed subjects, Dashed: mean ± SE.

Results were represented in a polar plot (Figure 2.17), where outbound and inbound results were averaged, and the means and SE for all analyzed subjects in all conditions, 3 active and 1 relaxed, are presented. Absolute stiffness values did not satisfy the normality condition, so comparisons were performed using Wilcoxon signed-rank tests. Predominantly activating a single muscle or co-contracting antagonistic muscles significantly increased ankle stiffness in all directions ($p<0.05$). However, stiffness increased more in the sagittal plane (DP direction) than in the frontal plane (IE direction) in all active studies, substantially accentuating the "peanut" shape, pinched in the IE direction. The ratio of active stiffness to maximally-relaxed stiffness satisfied the normality condition ($p>0.05$). Its values in the four principal directions (inversion, eversion, dorsiflexion, plantarflexion) and the average for all directions are presented in (Table 2.4).

Table 2.4: Ratio of active stiffness to relaxed stiffness.

Direction Study	Inversion	Eversion	Dorsiflexion	Plantarflexion	All directions
TA Active	2.00 (0.24)	1.45 (0.13)	1.85 (0.23)	1.98 (0.26)	1.87 (0.21)
SOL Active	1.85 (0.20)	1.55 (0.12)	2.60 (0.40)	2.62 (0.29)	2.22 (0.23)
Co-contraction	2.30 (0.22)	1.69 (0.12)	3.12 (0.42)	3.14 (0.35)	2.65 (0.24)

Parentheses denote SE. The unit is Nm/rad.

All subjects except one (#4) showed the greatest DP stiffness increase when co-contracting antagonistic muscles.

2.7.6 Passive Property of the Ankle in Active Muscles

Passive/non-passive behavior of the ankle was identified from curl analysis on the averaged single vector field. For the curl analysis, I first defined a criterion for zero curl from four repetitive measurements using the same experimental protocol but without a human subject. Rotational field of these measurements should be zero ideally, since the robot with the suggested controller was implemented as a passive system. Any non-zero curl identified from the friction compensated vector field was regarded as artifactual curl arising due to the precision limit of measurements or numerical errors in differentiation. The identified artifactual curl components followed normal distribution ($p>0.05$). The mean was 0.012 Nm with SD 0.369 Nm, which implied that any value outside the range -0.719 to 0.728 Nm was significantly different from zero with 95% confidence.

Following the vector field decomposition method described in 2.4.3, a rotational field containing curl components was calculated.

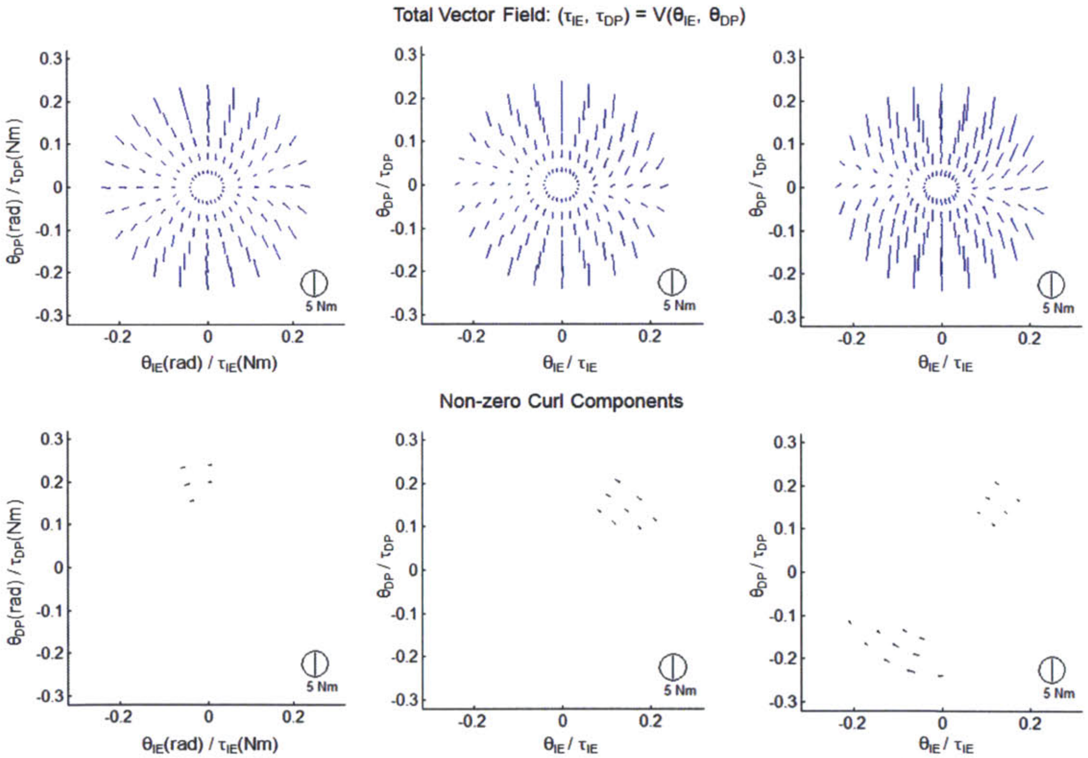

Figure 2.18: An example (subject #5) of vector field analysis. 1st, 2nd and 3rd column: TA active, SOL active, and Co-contraction studies. 1st and 2nd row: total field and rotational field (curl components statistically non-zero are shown).

A representative example (#5) of a total vector field and its rotational (curl) component is shown (Figure 2.18). As reported in the relaxed study, curl components in the maximally-relaxed were not statistically significantly different from zero. In contrast, significant non-zero curl components were observed when muscles were active.

The mean and SD of the curl components in the rotational field are summarized in (Table 2.5).

Table 2.5: Curl components and $\sqrt{K_{ratio}}$ for all data analyzed.

Subject	Mean (SD) of curl components [Nm]				Mean of $\sqrt{K_{ratio}}$			
	Relaxed	TA	SOL	COC	Relaxed	TA	SOL	COC
1	-0.033 (0.164)	-0.238 (0.356)*	N/A	-0.179 (0.543)*	0.083	0.118*	N/A	0.104*
2	-0.022 (0.131)	-0.017 (0.200)	-0.265 (0.388)*	-0.189 (0.281)*	0.079	0.093	0.176*	0.085
3	-0.041 (0.106)	-0.173 (0.277)*	-0.052 (0.255)	-0.067 (0.294)*	0.080	0.117*	0.110*	0.113*
4	-0.010 (0.140)	0.006 (0.316)*	-0.150 (0.398)*	-0.132 (0.365)*	0.096	0.101*	0.148*	0.137*
5	-0.042 (0.112)	-0.149 (0.283)*	-0.224 (0.282)*	-0.254 (0.345)*	0.074	0.135*	0.160*	0.172*
6	-0.036 (0.109)	-0.085 (0.317)*	-0.170 (0.431)*	N/A	0.083	0.150*	0.158*	N/A
7	-0.012 (0.108)	0.034 (0.257)	-0.224 (0.268)*	-0.082 (0.348)*	0.096	0.115	0.114*	0.121*
8	-0.045 (0.233)	-0.194 (0.448)*	-0.146 (0.347)*	-0.007 (0.711)*	0.091	0.132*	0.172*	0.137*
9	-0.043 (0.134)	-0.086 (0.423)*	-0.096 (0.330)*	-0.052 (0.385)*	0.099	0.091*	0.109*	0.091
10	-0.048 (0.208)	-0.087 (0.265)	-0.173 (0.405)*	0.040 (0.318)*	0.087	0.097*	0.090	0.056**
Average	**-0.033 (0.144)**	**-0.099 (0.314)**	**-0.167 (0.345)**	**-0.083 (0.399)**	**0.087**	**0.115**	**0.137**	**0.113**

Asterisks (*) denote significant difference from the relaxed study ($p<0.05$). Double asterisks (**) indicate significantly lower $\sqrt{K_{ratio}}$ than relaxed. Lower $\sqrt{K_{ratio}}$ values are due to greater increase of conservative components with activation than rotational components.

Outbound and inbound results were averaged since no significant difference was found between them ($p>0.05$). Averaged over the entire rotational field, the mean of the curl components was not statistically different from zero.

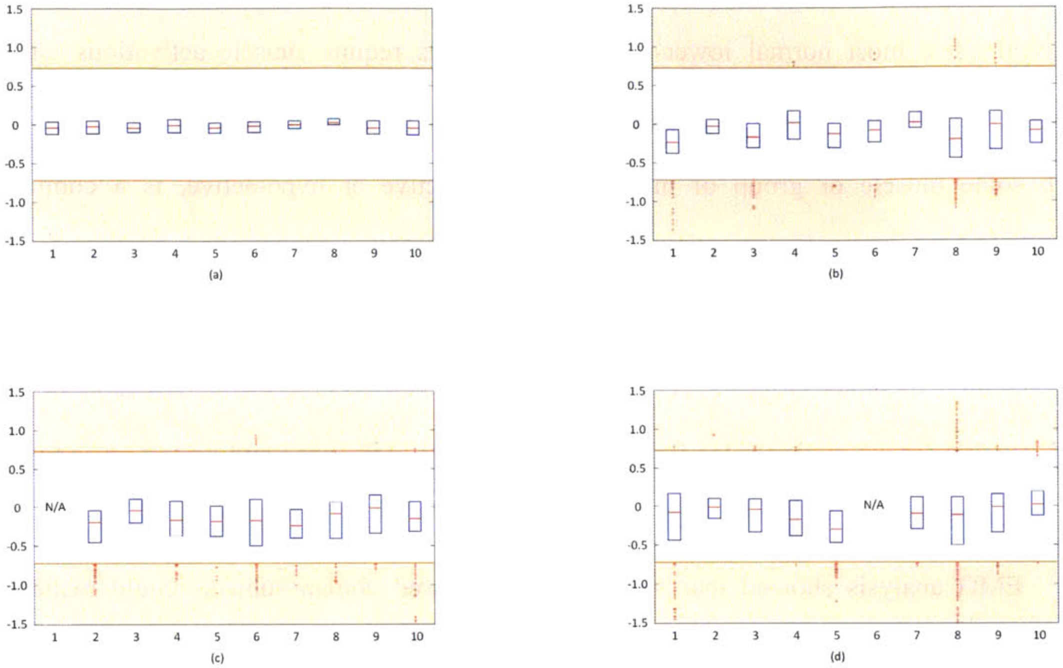

Figure 2.19: Curl component analysis for all data analyzed. (a) Relaxed, (b) TA active, (c) SOL active, (d) Co-contraction. The x-axis is subject number and the y-axis the curl value in [Nm]. In each box, the central mark is the median and the edges of the box are the 25th and 75th percentiles of all curl values. Significantly non-zero curl values (outside the range of -0.719 to 0.728 Nm (shaded region)) are plotted individually with red crosses (+).

However, significant non-zero curl components were observed in some regions: in 7 out of 10 subjects for the TA active study, 8 out of 9 subjects for the SOL active study, and in all 9 subjects for the co-contraction study (Figure 2.19). Calculating $\sqrt{K_{ratio}}$ showed that non-spring-like behavior increased with muscle activation, though the rotational component averaged over all subjects was less than 14 % of the corresponding conservative component (Table 2.5). However, we found no common patterns in the rotational field across subjects.

2.7.7 Discussion

An accurate characterization of ankle mechanical impedance with active muscles is important since most normal lower-extremity functions require muscle activations either singly, synergistically, or antagonistically. Furthermore, abnormal muscle tone, a condition in which some muscle or group of muscles is hyper-active or hypo-active, is a common consequence of neurological disorder [14, 55, 61].

Repetitive measurements using a wearable robot combined with robust function-approximation methods based on TPS with GCV enabled reliable characterization of the multi-variable torque-angle vector field at the ankle in IE–DP space and how it varied with muscle activation.

EMG analysis showed that our young unimpaired human subjects could maintain substantially constant muscle contraction under the given experimental conditions. However, despite instructions, most subjects had difficulty activating only one muscle exclusively (Figure 2.15). This is consistent with a growing body of evidence that the central nervous system addresses muscles in functional groups called synergies, and not individually [78, 79]. In addition, most subjects could voluntarily activate SOL more easily than GAS, and appeared to be especially incapable of focusing voluntary control on PL, at least in the context of this experiment.

Under voluntary contraction of ankle muscles at 10% MVC either singly or antagonistically, the variability of repeated measurements was significantly smaller than the measurement error of our apparatus (Table 2.2), although it was higher than when muscles were relaxed. This is consistent with previous studies showing increased variability of force with voluntary contraction [80].

In general, ankle stiffness increased in all directions with activation of a single muscle or co-contraction of antagonistic muscles (Table 2.4, Figure 2.17). Ankle stiffness was highly direction-dependent whether muscles were maximally relaxed or active. In all cases, the directional variation of stiffness exhibited a characteristic "peanut" shape, pinched in the IE direction. This might be expected, as normal locomotor progression is predominantly in the sagittal plane. However, the effect of muscle activation was not simply to scale stiffness magnitude as observed in the upper extremity [11]. The shapes observed with co-contraction or predominant TA or SOL activation were not scaled-up copies of relaxed behavior. Instead, contraction or co-contraction of the major dorsi- and plantar-flexors contributed much less to increase IE stiffness (Table 2.4), which means the ankle remains relatively more vulnerable to frontal plane perturbations even with voluntary contraction of these muscles.

What might account for these results? One possible explanation is a different contribution of "passive" and "active" stiffness to the different movement directions. Passive stiffness adds to active muscle stiffness as a bias or offset from zero which was greater in DP than IE. If active muscles contributed more to DP than IE and their ratio was greater than the ratio of passive contributions to DP and IE, the total stiffness would increase more in DP than IE, as we observed. To clarify with a hypothetical example, a muscle that was aligned to contribute exclusively to DP torque and stiffness, with zero contribution to IE torque and stiffness, would add to DP stiffness but not IE stiffness. This explanation is consistent with the preponderance of potentially synergistic muscles contributing to DP but not IE: only 5 out of 13 ankle muscles contribute to inversion-eversion, while 12 out of 13 muscles contribute to dorsiflexion-plantarflexion.

Interestingly, the joint stiffness when antagonistic muscles were co-contracted was less than the sum of what was observed in the TA and SOL active studies (passive stiffness was included just once in summing the stiffness of TA and SOL active studies): 2.00 vs. 2.43 for the IE direction, 3.13 vs. 3.53 for the DP direction, and 2.65 vs. 3.09 for all directions (Table 2.4). This may have been due, in part, to the fact that the TA and SOL active studies also evoked a degree of co-contraction due to synergies. However, estimated total muscle activity in the co-contraction study exceeded that of the TA active study by 87% while the co-contraction joint stiffness exceeded that of the TA active study by only 64% in the DP direction, 16% in the IE directions and 42% averaged over all directions (Table 2.6).

Table 2.6: The effect of muscle activation was not simply to scale stiffness magnitude.

Increase Ratio in Co-contraction Study / Reference Study	Total muscle activation	Stiffness		
		DP Direction	IE direction	All Direction
TA Active	1.87	1.64	1.16	1.42
SOL Active	1.71	1.20	1.17	1.19

The ratios of total muscle activation and stiffness in the co-contraction study to their values in the single-muscle-active studies were calculated. Mean values for all subjects analyzed are presented.

Comparing the co-contraction study to the SOL active study, the discrepancy was even more marked: estimated total muscle activity in the co-contraction study exceeded that of the SOL active study by 71% while the co-contraction joint stiffness exceeded that of the SOL active study by only 20% in the DP direction, 17% in the IE direction and 19% averaged over all directions (Table 2.6). In both studies, the joint stiffness increase ratios in DP, IE and all directions were significantly lower than the corresponding increase ratios of estimated total muscle activity ($p<<0.05$).

Several possibilities might explain these experimental observations. First, it is known that, with fatigue, a greater amplitude of EMG is required to maintain a constant force. To the extent that subjects maintained constant levels of EMG, if they fatigued, the force (and presumably stiffness) they generated would have declined. However, the experimental protocol was specifically designed to avoid fatigue. Compared with previous experiments on ankle muscle fatigue [81], contractions at 10% MVC for 40 seconds with intervening 3-minute rest periods seem very unlikely to have induced fatigue.

A second possibility arises from nonlinear musculo-tendon kinematics. The derivatives of muscle length with respect to joint angle define muscle moment arms which, in general, vary with joint angle [82, 83]. The nominal ankle positions in the TA and SOL active studies were slightly dorsiflexed and plantarflexed from the neutral position, respectively, while the nominal ankle position in the co-contraction study was close to the neutral position. This difference of nominal ankle position might have influenced the measured ankle stiffness. To explore this possibility, the stiffness in each study was evaluated based on shifted displacements. However, the effect of different initial ankle positions was negligible, not enough to explain our experimental observation.

A third possibility is also related to nonlinear musculo-tendon kinematics. Because humans have an endo-skeleton, if tendon tension is non-zero, that leads to a negative joint stiffness of purely kinematic origin [84, 85]. Any relation between intrinsic muscle stiffness and tension will vary between muscles; longer muscles of lower cross-sectional area may be expected to contribute more tension with less stiffness. Thus contraction (or co-contraction) of longer, slenderer muscles may, in principle, reduce joint stiffness. However, both the positive (intrinsic) and negative (kinematic) contributions of any muscle contribute linearly to net joint stiffness. Therefore, if muscle activity in the co-contraction study was the simple sum of muscle activities in the TA and SOL active studies, the stiffnesses should also have added; but they did not.

A fourth possibility may arise from possible contributions of unmonitored muscles. We monitored 4 superficial muscles but 8 out of 13 ankle muscles are deep and were not monitored. Those muscles might have contributed positively or negatively to ankle stiffness. If they contributed positively, it might be that these deep muscles were comparably active in all three studies. As a result, their activity in the co-contraction study would not have been the sum of their activities in the TA and SOL active studies. That would result in our observation that co-contraction stiffness was not the sum of TA and SOL active stiffnesses. In contrast, deep muscles tend to be more slender than superficial muscles (such as gastrocnemius) and might contribute negatively to joint stiffness. If they were more active in the co-contraction study, they would result in our observation that co-contraction stiffness was not the sum of TA and SOL active stiffnesses.

Interestingly, one subject (#4) exhibited lower DP stiffness when co-contracting antagonistic muscles than when activating single muscles, even though muscle activation levels were comparable in all cases and this cannot be dismissed as imprecision of our measurement (Table. 2.7).

Table 2.7: Stiffness may not increase with co-contraction.

Ratio of active stiffness to relaxed stiffness				EMG amplitude levels normalized to MVC					
Direction / Study	Dorsi-flexion	Plantar-flexion	DP	Muscle / Study	TA	SOL	PL	GAS	Approximates of total muscle activity
TA Active	1.86	2.74	2.30	TA Active	8.27	3.10	1.30	1.42	14.09
SOL Active	2.65	2.28	2.47	SOL Active	1.23	7.55	4.45	1.86	15.09
Co-contraction	2.23	2.20	2.22	Co-contraction	8.83	8.33	3.55	1.93	Љ2.64

One subject (#4) exhibited *lower* DP stiffness during co-contraction than with single muscles active despite comparable or greater levels of activation.

In detail, when all normalized EMG amplitudes were summed as an approximate estimate of total ankle muscle activity of this subject, the co-contraction study showed 50% to 60% greater total activation: TA active sum was 14.09; SOL active sum was 15.09; Co-contraction sum was 22.64 (Table 2.7). In the absence of nonlinear kinematic effects, impedances add and we should expect a greater increase of impedance with co-contraction [86]. However, in the dorsiflexion direction, the stiffness increase in the co-contraction study was only 18.8% compared to TA active study and decreased compared to the SOL active study by -16.6%. In the plantarflexion direction, the difference was even more compelling: -24.6% compared to the TA active study and -3.6% compared to the SOL active study. The average of both directions was -3.6% and -11.3% compared to the TA active and SOL active studies, respectively, substantially smaller than the 50% to 60% increase expected from the sum of muscle electrical activities.

Of the possible explanations we considered above, the only one that appears to be compatible with this observation is that unmonitored deep muscles contributed negative joint stiffness (consistent with their slenderness) and were more active in the co-contraction study.

However, only one subject out of 10 clearly displayed this phenomenon and further study is required to understand this observation. Nevertheless, even this single subject emphasizes that there is no guarantee that joint stiffness will increase in proportion to muscle activation.

Consequently, our observation that, averaging over all subjects, net ankle stiffness increased with muscle activation–by as much as a factor of 2 to 3 with co-contraction (Table 2.4)–is not a-priori obvious. It suggests that impedance modulation by antagonist muscle co-contraction–despite its substantial cost in metabolic energy consumption–serves an important function; and that function is sufficiently important that muscle may have co-evolved with musculo-skeletal kinematics so that its stiffness increased sufficiently rapidly with force to ensure stability [87]. In fact, a recent study showed that the limits of upper-extremity force production were determined by the need to stabilize the joints [88] rather than by muscle strength.

The musculo-skeletal anatomy of the ankle is highly variable in humans [89] and that implies a comparable variability in the effect of muscle activity on joint stiffness; as we observed, increasing muscle activity may not always increase joint stiffness. Moreover, biomechanical injury to the passive tissues of the ankle may permanently change the relation between muscle activity and joint stiffness, and the full range of ankle stiffness (and in particular, joint stability) that was available pre-injury may no longer be accessible post-injury. Further experimental study is required to quantify these possibilities.

Investigation of passive/non-passive behavior of the joint is very important, since this may affect stability of the neuromuscular system in interaction with the environment. More specifically, the necessary and sufficient condition for a system such as a robot or a human limb to be stable when coupled to any stable and passive object is that its driving point impedance should be passive [90]. Coupled stability for the robot interacting with the environment has been well addressed by impedance control [91-93]. On the other hand, we cannot make a priori assumption that human joints are fundamentally passive, since the central nervous system of human, from the spinal cord to the cortex, plays a significant role in movement controls, and passive behavior of joint impedance can be affected by muscle activation and changes in inter-muscular feedback (e.g. from muscle spindles or Golgi Tendon Organ). Especially, when interactions due to inter-muscular feedback are unbalanced, non-zero curl is introduced, which is non-passive.

The suggested vector field approximation methods based on TPS smoothing with GCV enabled reliable characterization of multi-variable torque-angle vector field at the ankle in the 2D-space consisting of sagittal and frontal planes. Passive/non-passive behavior of the ankle joint was identified from curl analysis on the approximated vector field, in different muscle active conditions. Note that this analysis was previously not available in the single DOF studies, because curl analysis requires the determination of the influence of displacements in one DOF on the forces generated in another DOF.

The static behavior of the fully-relaxed ankle was that of a passive elastic system, i.e., spring-like. In contrast, generating a steady ankle torque or voluntarily co-contracting antagonist muscles evoked statistically significantly non-passive static behavior, i.e. non-zero curl, which may arise from unbalanced inter-muscular feedback between IE and DP muscle groups. Non-zero curl due to failure to maintain constant muscle activation cannot be completely ruled out, though to minimize this possibility we averaged four repeated measurements. To investigate the source of non-zero curl more thoroughly, we compared EMG levels and their variation in regions with non-zero curl with their values in regions with zero curl. If the level and variation of EMG in the two regions were statistically indistinguishable, it is more likely that the non-spring-like behavior (non-zero curl) was due to unbalanced neural feedback rather than non-constant muscle activation. To test the equality of two variances and means, F-tests and paired t-tests were used with a significance level 0.05. In fact, we found no statistical difference ($p>0.05$) in EMG variation between regions of non-zero curl and zero curl in all active studies, except in one region for one subject (subject #1) in the TA active study. In addition, EMG levels in the majority of non-zero curl regions were not statistically different ($p>0.05$) from the levels in zero curl regions: statistical differences ($p<0.05$) were found in only 14.3 % of curl regions from the TA study, 19.2 % from the SOL study, and 14.7 % from the COC. From these results, we infer that the observed non-zero curl originated more from unbalanced neural feedback than non-constant muscle activation due to changes of voluntary descending drive.

Compared to relaxed muscles, active muscles, either singly, synergistically or antagonistically, exhibited significantly greater mean magnitude and SD of curl components as well as $\sqrt{K_{ratio}}$ in general (Table 2.5). However, we found that $\sqrt{K_{ratio}}$ of the co-contraction study was lower than the single muscle active studies. This is because the conservative components increased more than the rotational components, when co-contract antagonistic muscles.

We found no common patterns in the rotational field across subjects. That may reflect imperfect tuning of spinal feedback circuits. If the central nervous system had evolved towards maintaining ankle impedance to resemble a passive system even when muscles were active, this would require any heteronymous feedback loops (from the sensors of one DOF to the muscles of another DOF) to be perfectly balanced. But perfection is rare in biological systems. If the biological system had evolved to approximate passivity, though imperfectly, we might expect individuals to differ in this departure from perfection due to different motor ability, sensory acuity, genetic factors, or other causes.

Whatever its origin, the non-passive static behavior of the ankle with active muscles was modest in the unimpaired young subjects we studied—a $\sqrt{K_{ratio}}$ value of 0.087 in the relaxed condition and $\sqrt{K_{ratio}}$ values less than 0.140 in all active conditions can be interpreted as relatively small non-passive behavior (Table 2.5).

Chapter 3

Multi-Variable Steady-State Dynamic Ankle Mechanical Impedance

3.1 Summary

While a nonlinear torque-angle relationship at the ankle was described in Chapter 2, the characterization was limited to the static component of ankle mechanical impedance. This chapter presents quantitative characterization of multi-variable dynamic ankle mechanical impedance.

Measurements using the Anklebot combined with linear time-invariant multi-input multi-output stochastic system identification methods enabled reliable identification of dynamic ankle mechanical impedance in two degrees-of-freedom simultaneously, both in the sagittal and frontal planes. In addition to the identification in two major planes, directional variation (anisotropy) of ankle impedance in the 2D-space formed by the two planes, and energetic passivity of the ankle were identified under maximally-relaxed muscles and voluntary contraction of ankle muscles. Impedance matrix and its ellipse representation were also provided for their widespread use in the field of biomechanics and motor control.

Experiments with young healthy subjects with no reported history of biomechanical or neuromuscular disorders successfully quantified the dynamic behavior of the ankle over a wide frequency range and in different muscle activation levels.

Ankle impedance in joint coordinates showed responses more or less consistent with a 2nd order system with inertia, damping, and stiffness, although slight mid-frequency transitions were observed both under relaxed and active muscles, which may be due to the contribution of muscle mass as well as non-negligible couplings between 2 degrees-of-freedom. While inertia was relatively constant, stiffness and damping increased with the higher level of muscle activation. Especially, low- (<2 Hz) and mid-frequency (5~8 Hz) impedance increased linearly with muscle activation in both degrees-of-freedom.

Ankle impedance increased linearly with muscle activation in all directions in the 2D-space but more in the sagittal than in the frontal plane, resulting in an accentuated "peanut shape" both in the TA active and SOL active studies. The peanut shape was slightly tilted in the counter-clockwise direction, which can be well explained with anatomical axes of rotations of the ankle.

The ankle of young healthy subjects was energetically passive under relaxed muscles. Non-passive behavior was observed in some subjects with active muscles, but its contribution was modest, and most subjects satisfied the passivity condition.

The highly linear relationship between muscle activation and multi-variable impedance, the small coupling between 2 degrees-of-freedom, and the energetic passivity of the ankle will all together help the construction of a simple model of multi-variable ankle impedance for young healthy subjects.

3.2 Introduction

The study of multi-variable static ankle mechanical impedance provides biomechanically and neurologically valuable information about the ankle joint, not available from previous single DOF studies. Although this study sheds lights on quantitative characterization of ankle impedance, it may not be directly used in more general situations, since the ankle operates in different frequency regions for different lower-extremity functions. For example, the frequency content of normal human walking is considerably higher than 10 Hz [94, 95].

Along the same line of the previous static study, I quantified the directional variation of ankle impedance and the energetic passivity of the ankle over a wide range of frequency. The same experimental setup, Anklebot and the EMG system used in the static study, was also used in this study.

In the following sections, linear time-invariant (LTI) multi-input multi-output (MIMO) stochastic system identification methods and subsequent analysis methods are explained. Characterization results on young healthy subjects under relaxed and active muscles follow.

3.3 Methods

3.3.1 Multi-Variable Dynamic Ankle Mechanical Impedance in Joint Coordinates

Anklebot actuates left (L) and right (R) linear drives in actuator coordinates, which in turn applies perturbations to the ankle joint, in both IE and DP directions. The IE and DP directions define joint coordinates, and torques and angular displacements in the joint coordinates are obtained by transforming actuator forces and linear displacements through the nonlinear kinematics of the Anklebot [62].

Multi-variable ankle impedance in joint coordinates can be identified by applying a standard non-parametric MIMO stochastic identification method on recorded time history of torque and displacement data [25, 96]. This method is preferred to other parametric system identification approaches because it requires no a-priori assumption about the dynamic structure of joint mechanical impedance, and can provide a chance to investigate its complex higher order dynamics, if exists. In addition, the use of mild random white noise as inputs rather than transient inputs, such as impulse, step, or ramp, is preferred, since it minimizes the possibility of subjects' voluntary reactions to perturbations.

Mechanical admittance ($\boldsymbol{Y}$) was identified first, since we applied torque input and recorded displacement output (Eq. (3.1)):

$$\boldsymbol{\theta} = \boldsymbol{Y}\boldsymbol{\tau}\,, \qquad \boldsymbol{\theta} = (\theta_{IE}, \theta_{DP})\,, \qquad \boldsymbol{\tau} = (\tau_{IE}, \tau_{DP}) \tag{3.1}$$

$$\begin{bmatrix} \theta_{IE} \\ \theta_{DP} \end{bmatrix} = \begin{bmatrix} Y_{11}(f) & Y_{12}(f) \\ Y_{21}(f) & Y_{22}(f) \end{bmatrix} \begin{bmatrix} \tau_{IE} \\ \tau_{DP} \end{bmatrix}, \qquad \boldsymbol{Y} = \begin{bmatrix} Y_{11}(f) & Y_{12}(f) \\ Y_{21}(f) & Y_{22}(f) \end{bmatrix}$$

A brief description of MIMO stochastic identification methods based on spectral analysis to obtain each element of $\boldsymbol{Y}$ is provided in Appendix D.

To calculate auto- and cross-power spectral density, Welch's periodogram approach (MATLAB's *cpsd* function) was used [97]. This method splits the data of finite length into overlapping sections, computes modified periodograms of the sections, and averages the resulting periodograms. An appropriate window size should be selected to reduce both bias errors and variance as well as to provide a fine spectral resolution. When the window size is large, periodograms are calculated with the fine spectral resolution (lowest/smallest resolvable frequency), and bias errors decrease. However, due to the reduced number of average, the variance of estimation increases. So there exists trade-off between the periodograms resolution, bias errors, and variance. In this study, the sampling rate was 1 kHz, and the number of FFT points was set as 4000, yielding a spectral resolution of 0.25 Hz. A periodic Hamming window was used to provide 50% overlap of the window size.

In the linear system, mechanical impedance ($\boldsymbol{Z}$) can be calculated from the inverse of mechanical admittance ($\boldsymbol{Y}$), if positive definite condition of $\boldsymbol{Y}$ is satisfied (Eq. (3.2)):

$$\boldsymbol{\tau} = \boldsymbol{Y}^{-1}\boldsymbol{\theta} = \boldsymbol{Z}\boldsymbol{\theta}, \qquad \boldsymbol{Z} = \begin{bmatrix} Z_{11}(f) & Z_{12}(f) \\ Z_{21}(f) & Z_{22}(f) \end{bmatrix} \tag{3.2}$$

Here, a portion of the recorded angular displacements resulted from the robot dynamics. To compensate for the contribution of the robot dynamics, impedance of the robot ($\boldsymbol{Z}_{Abot}$) should be identified first, and then subtracted from the measured impedance ($\boldsymbol{Z}_{Ankle+Abot}$) (Eq. (3.3)):

$$\begin{aligned} \boldsymbol{Z}_{Ankle}(f) &= \boldsymbol{Z}_{Ankle+Abot}(f) - \boldsymbol{Z}_{Abot}(f) \\ &= \frac{\boldsymbol{\tau}(f)}{\boldsymbol{\theta}(f)}_{Ankle+Abot} - \frac{\boldsymbol{\tau}(f)}{\boldsymbol{\theta}(f)}_{Abot} \end{aligned} \tag{3.3}$$

This is the case when the system is open-loop (Figure 3.1).

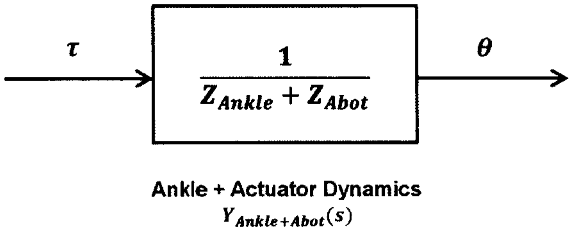

Figure 3.1: Open-loop system identification.

In fact, a closed-loop system identification was used in this study for ankle impedance identification, and details of this method will be described in section 3.4.

Next, from the analysis of partial coherence, which indicates linear dependency between input and output after removing the effects of other inputs, we investigated the linearity of each element of $\boldsymbol{Z}_{ankle}$ and the amount of coupling between the 2 DOFs. A method to calculate partial coherence based on spectral analysis is also provided in Appendix E.

Within high coherences ranges, we can investigate the impedance in the major directions (diagonal terms of $\boldsymbol{Z}_{ankle}$) and interactions among them (off-diagonal terms of $\boldsymbol{Z}_{ankle}$). Frequency response of ankle impedance is represented as a Bode plot.

3.3.2 Anisotropy of Dynamic Ankle Mechanical Impedance

In addition to impedance identification in joint coordinates (θ_{IE}, θ_{DP}), we can characterize directional variation of ankle impedance in the coupled 2 DOFs. With a rotational transformation ($\boldsymbol{R}$), new coordinates ($\boldsymbol{\theta}'$) can be defined (Eq. (3.4)):

$$\boldsymbol{\theta}' = \boldsymbol{R}\boldsymbol{\theta}, \qquad \boldsymbol{\tau}' = \boldsymbol{R}\boldsymbol{\tau}, \qquad \boldsymbol{R} = \begin{bmatrix} \cos\alpha & \sin\alpha \\ -\sin\alpha & \cos\alpha \end{bmatrix} \tag{3.4}$$

$$\boldsymbol{\theta}' = (\theta_{IE}', \theta_{DP}'), \qquad \boldsymbol{\tau}' = (\tau_{IE}', \tau_{DP}')$$

where α is the angle defined as a CCW direction from the axis for the direction of θ_{IE} (Figure 3.2).

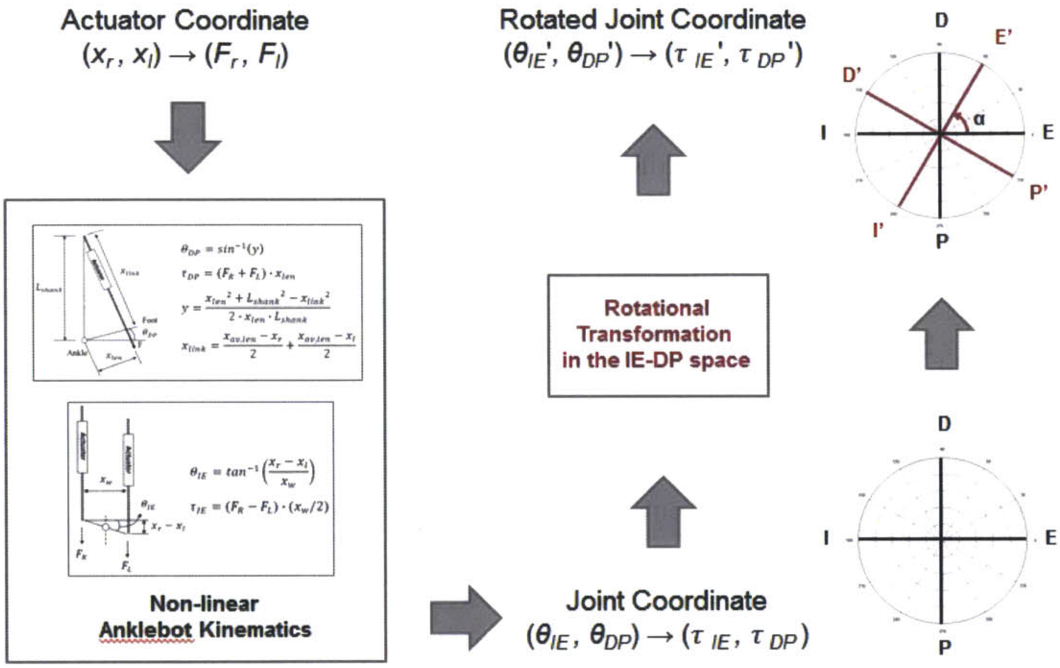

Figure 3.2: Impedance identification in rotated joint coordinates ($\boldsymbol{\theta}' = (\theta_{IE}', \theta_{DP}')$).

For example when $\alpha = 45°$, θ_{IE}' and θ_{DP}' correspond to the directions in the middle of θ_{IE} and θ_{DP} directions. By applying the same impedance identification procedure (Eq. (3.1) ~ (3.3)) to the transformed data ($\boldsymbol{\theta}'$ and $\boldsymbol{\tau}'$), and changing the angle α from $0°$ to $90°$, ankle impedance in any direction in the 2D-space can be calculated. One thing to check is whether mild random perturbations applied to each actuator provide enough power to excite the ankle in the rotated joint coordinates of any α.

Representation of a directional variation of ankle impedance or an isotropy of ankle impedance, can be also obtained by calculating the magnitude of impedance for each movement direction in the 2D-space and plotting them in polar coordinates. Compared to the static study, this study provides how directional variation of impedance changes as a function of frequency.

3.3.3 Ellipse Representation and Impedance Matrix

The representation of the directional variation of impedance in polar coordinates (direction dependent map) is different from a widely used "stiffness ellipse", a linear representation of stiffness matrix [11]. In detail, the direction dependent map explains torques that oppose motions in a particular direction, i.e., magnitude of impedance for each movement direction in the IE–DP space. On the other hand, the ellipse representation describes the trajectory of restoring torque vectors when the joint is displaced along the unit circle in the IE–DP space.

Although the ellipse representation cannot provide direct information of the magnitude of impedance in a particular movement direction, considering its widespread use, I also provide ellipse representation of ankle impedance together with the direction dependent map. In fact, the ellipse representation can be directly derived from the direction dependent map. In addition, directions of maximum and minimum impedance magnitude in the direction dependent map correspond to the major and minor principal axes of the impedance ellipse.

Once the ellipse representation is determined, a 2-by-2 impedance matrix ($\boldsymbol{Z}$) is further calculated based on energy conservation between different coordinates (Figure 3.3 and Eq. (3.5)).

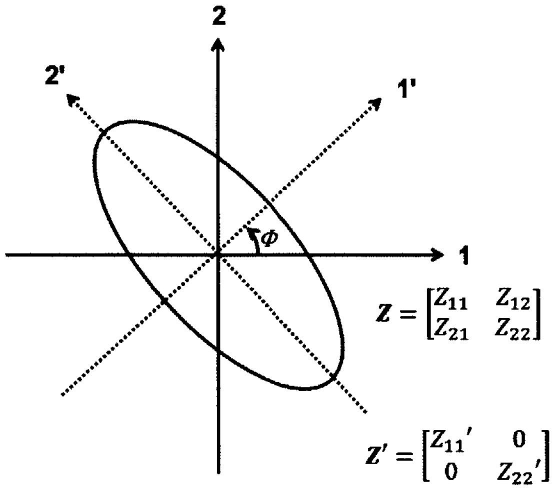

Figure 3.3: Ellipse representations in different coordinates. Axes 1 and 2 define the original coordinate system (IE–DP), and axes 1' and 2' define directions of minor and major principal axes of the ellipse. The angle between the axis of the original coordinate frame and the minor principal axis is defined as Φ.

When the rotational transformation between two frames is defined as $\boldsymbol{R}$, $\boldsymbol{Z}$ is calculated as Eq. (3.5).

$$\boldsymbol{\theta}' = \boldsymbol{R}\boldsymbol{\theta}, \qquad \boldsymbol{\tau}' = \boldsymbol{R}\boldsymbol{\tau}$$

$$\boldsymbol{R} = \begin{bmatrix} \cos\Phi & \sin\Phi \\ -\sin\Phi & \cos\Phi \end{bmatrix}$$

$$\boldsymbol{\tau}' = \boldsymbol{Z}'\boldsymbol{\theta}' = \boldsymbol{Z}'\boldsymbol{R}\boldsymbol{\theta}$$

$$\boldsymbol{\tau} = \boldsymbol{R}^T\boldsymbol{\tau}' = \boldsymbol{R}^T\boldsymbol{Z}'\boldsymbol{R}\boldsymbol{\theta} = \boldsymbol{Z}\boldsymbol{\theta}$$

$$\boldsymbol{Z} = \boldsymbol{R}^T\boldsymbol{Z}'\boldsymbol{R} = \begin{bmatrix} \cos\Phi & -\sin\Phi \\ \sin\Phi & \cos\Phi \end{bmatrix} \begin{bmatrix} Z_{11}' & 0 \\ 0 & Z_{22}' \end{bmatrix} \begin{bmatrix} \cos\Phi & \sin\Phi \\ -\sin\Phi & \cos\Phi \end{bmatrix}$$

$$\boldsymbol{Z} = \begin{bmatrix} Z_{11} & Z_{12} \\ Z_{21} & Z_{22} \end{bmatrix} = \begin{bmatrix} Z_{11}'cos^2\Phi + Z_{22}'sin^2\Phi & (Z_{11}'-Z_{22}')sin\Phi cos\Phi \\ (Z_{11}'-Z_{22}')sin\Phi cos\Phi & Z_{11}'sin^2\Phi + Z_{22}'cos^2\Phi \end{bmatrix} \tag{3.5}$$

As representative characteristics of the ellipse representation, three parameters defining the orientation, shape, and size of the ellipse were calculated: the angle between the minor principal axis and the axis defining the IE direction (Φ), the ratio of Z_{22}'/Z_{11}', and the determinant of $\boldsymbol{Z}$.

Simple examples comparing the direction dependent map and the ellipse representation are provided in Appendix E.

3.3.4 Energetic Passivity of the Ankle Joint

To validate the use of the direction dependent map and the ellipse representation described in previous sections, energetic passivity should be checked. If the passivity condition is not satisfied, at least one of four variables of the impedance matrix is discarded. Investigation of energetic passivity of the joint is also important to understand coupled stability of physical interaction and the contribution of neural feedback to the joint. It has been known that two physically coupled systems with energetically passive port functions guarantee coupled stability [98]. But the passive property of the ankle may change, since many lower-extremity functions accompany changes of limb kinematics, muscle activities, and reflex actions. In addition, if there is unbalanced inter-muscular reflex feedback around the ankle joint, this can act as active components, i.e., energy source [10]. Hence we must check whether the ankle is passive to be able to state anything about coupled stability.

A passivity analysis was performed following the procedure described in [99, 100]. In brief, the passivity criterion for the linear system is described as Eq. (3.6), where matrix $\boldsymbol{H}$ is a 2x2 transfer matrix relating inputs ($\boldsymbol{u}$) and outputs ($\boldsymbol{y}$) to the system, and $\boldsymbol{u}$ and $\boldsymbol{y}$ are dual or conjugate interaction-port variables:

$$\forall w \geq 0,\ \boldsymbol{T}(jw) = \boldsymbol{H}(jw) + \boldsymbol{H}(-jw)^T \geq 0 \tag{3.6}$$

$$\boldsymbol{y}(jw) = \boldsymbol{H}(jw)\boldsymbol{u}(jw)$$

Inputs and outputs were selected in rotated joint coordinates (IE'–DP' where $\alpha = 45°$) as follows: $\boldsymbol{u} = \boldsymbol{\tau}' = (\tau_{IE'}, \tau_{DP'})$ and $\boldsymbol{y} = \boldsymbol{\omega}' = (\omega_{IE'}, \omega_{DP'})$ where $\boldsymbol{\tau}'$ denotes torques (Nm) in the rotated joint coordinates after compensating the contribution of actuator dynamics, and $\boldsymbol{\omega}'$ represents the corresponding angular velocities (rad/s). The compensation was performed in a similar way as we did for impedance identification (Eq. (3.3)). When the positive definite condition (Eq. (3.7)) of $\boldsymbol{T}(jw)$ is satisfied, the ankle is dissipative, or strictly passive.

$$\forall w \geq 0,\ \boldsymbol{T}(jw) = \boldsymbol{H}(jw) + \boldsymbol{H}(-jw)^T > 0 \tag{3.7}$$

Detailed descriptions for the analysis method are provided in [94, 95].

3.4 Closed-loop Mechanical Impedance Identification

With an open-loop system identification explained in chapter 3.3, we cannot prevent actuators from drifting from initial positions. In ankle impedance identification, keeping the foot around the initial neutral position against gravity is required for reliable identification. A closed-loop system identification with a simple proportional-derivative (PD) controller can be a good solution.

3.4.1 Closed-loop Identification of Anklebot Mechanical Impedance

Before running human experiments, impedance of Anklebot (Z_{robot}) was identified first, which will be used to compensate for the contribution of the robot dynamics in subsequent analyses. Identification results were also used to validate analysis methods and experimental procedures.

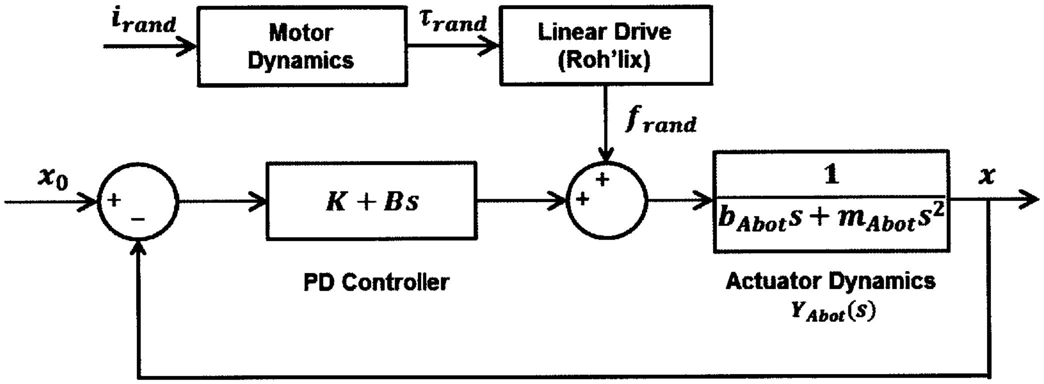

Figure 3.4: Controller for the identification of Anklebot impedance. The same controller was implemented for each of left and right actuators independently. Intrinsic inertia and damping of the actuator are denoted as m_{act} and b_{act}, and programmed stiffness (P gain) and damping (D gain) as K and B.

A simple PD controller was integrated with random input perturbations for the system identification (Figure 3.4). Gains of the controllers were set as $K = 500\,N/m$ and $B = 0\,Ns/m$, and Anklebot was unconstrained by anything. The initial position of actuator x_0 was set as 0. Two uncorrelated mild random perturbations (band-limited white Gaussian noise with stop frequency 100 Hz) were applied to each actuator for 60 seconds.

The closed-loop transfer function ($Y_{CL}(s) = Z^{-1}{}_{CL}(s)$) between random force perturbations to the actuator (f_{rand}) and the corresponding linear displacement (x) was represented as Eq. (3.8):

$$Y_{CL}(s) = Z^{-1}{}_{CL}(s) = \left.\frac{x(s)}{f_{rand}(s)}\right|_{CL} = \frac{Y_{Abot}(s)}{1+(K+Bs)Y_{Abot}(s)} = \frac{1}{I_{Abot}s^2 + B_{Abot}s + K} \tag{3.8}$$

$$Z_{Abot}(s) = I_{Abot}s^2 + B_{Abot}s$$

$$Z_{CL}(s) = Z_{Abot}(s) + K$$

Frequency responses of $Z_{CL}(s)$ in 2 coupled DOFs were estimated based on the previously explained MIMO system identification. Magnitude and phase responses were calculated and represented as Bode plots, and partial coherences plots were also provided.

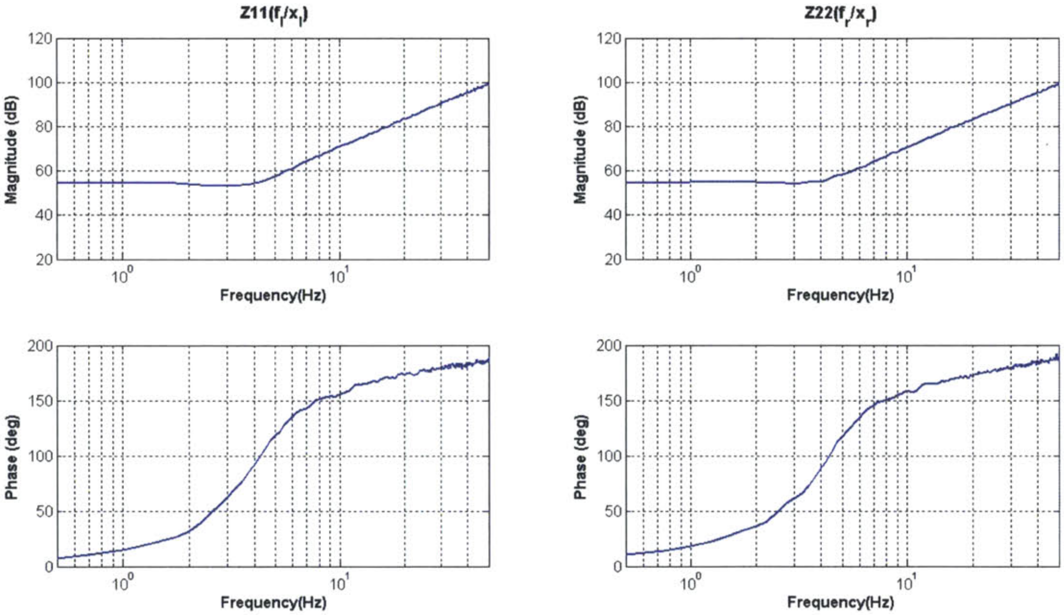

Figure 3.5: Closed-loop impedance $Z_{CL}(s)$ in actuator coordinates.

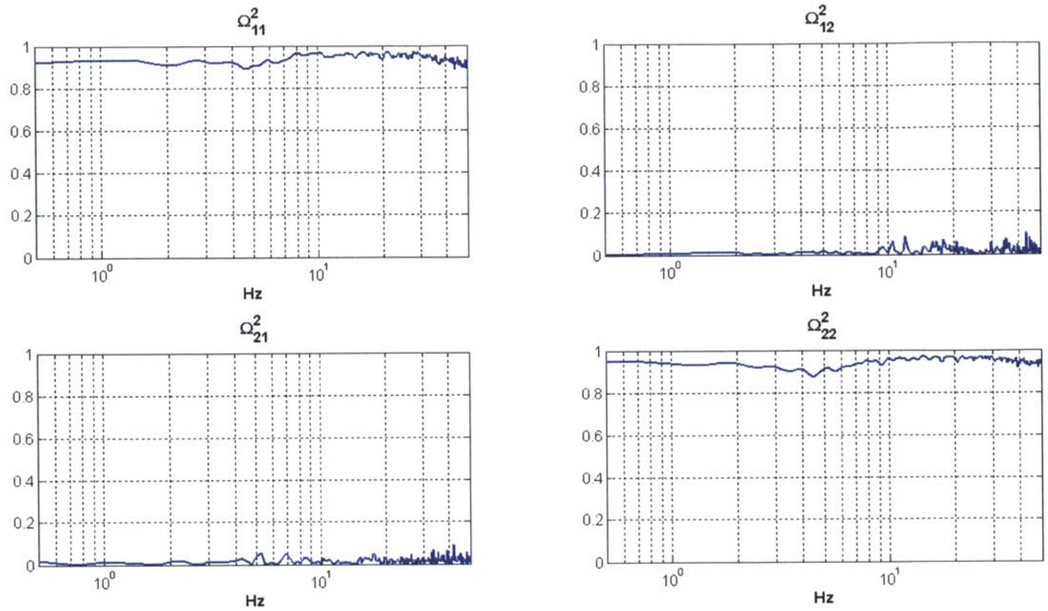

Figure 3.6: Partial coherence plots in actuator coordinates. Subscript 11, 12, 21, and 22 denote partial coherence relating x_l and f_l, x_r and f_l, x_l and f_r, and x_r and f_r.

Identification results in actuator coordinates and partial coherence plots are presented in Figure 3.5 and Figure 3.6. Partial coherences of diagonal terms were very high (>0.9) over the wide frequency range up to 50 Hz, implying that mechanical impedance of each actuator can be well explained with a linear model. On the other hand, coherences of off-diagonal terms were close to zero across all frequency regions, indicating no coupling or interaction between the left and right actuators. This is because the controller for each actuator was implemented independently.

Both magnitude and phase plots for diagonal terms showed clear frequency response of a 2nd order system, which was expected from Eq. (3.8). Stiffness was dominant in the low frequency region approximately below 2 Hz with a zero magnitude slope. In the high frequency region over about 4 Hz, inertia was dominant with a magnitude slope 40 dB/decade (dec). Negligible phase lag at low frequencies and the 180° phase lag of at high frequencies, also matched well with that of a 2nd order system.

Estimated programmed stiffness (K), calculated by averaging the impedance magnitude below 2 Hz, was 498.1 N/m and 506.9 N/m for the left and right actuator, respectively. This corresponds to the estimation error less than 0.4% and 1.4% of the commanded value (500 N/m), validating the experimental setup, protocol and analysis methods. In addition, frequency responses of left and right actuators were almost identical. The best-fit inertia and damping were 0.81 kg and 0.79 kg, and 20.2 Ns/m and 20.8 Ns/m for left and right actuators, respectively.

Identification results in joint coordinates through nonlinear kinematic transformation from the actuator coordinates to the joint coordinates, and the corresponding partial coherence plots are also presented in Figure 3.7 and Figure 3.8.

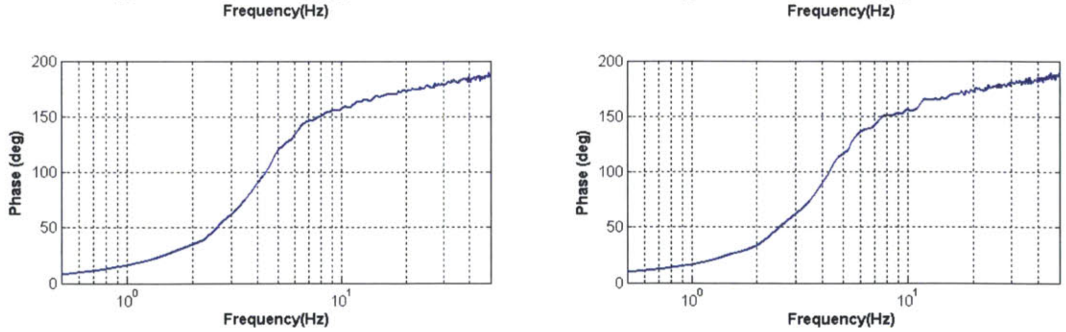

Figure 3.7: Anklebot impedance in joint coordinates.

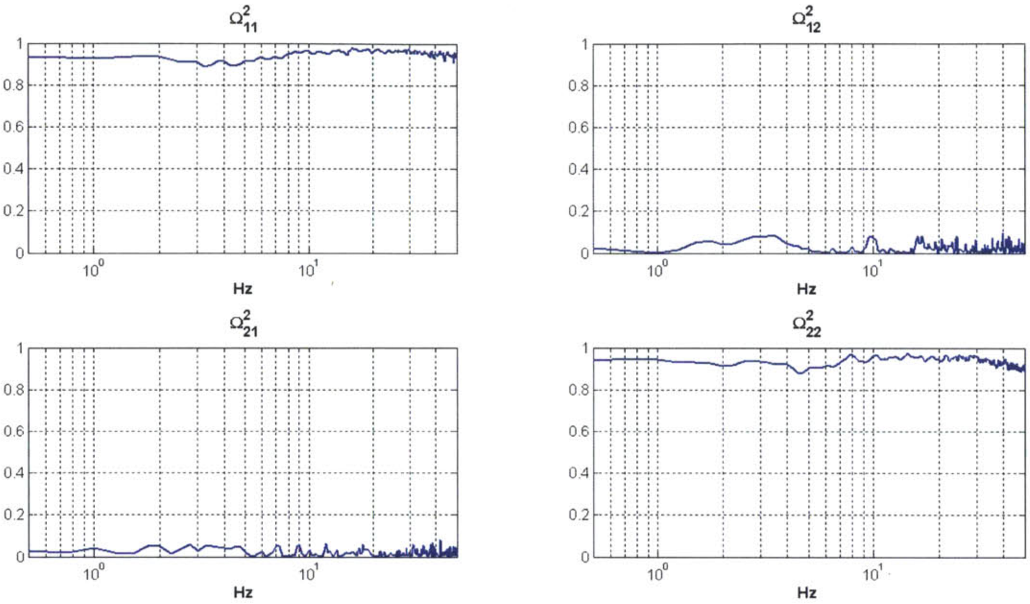

Figure 3.8: Partial coherence plots in joint coordinates. Subscript 11, 12, 21, and 22 denote partial coherence relating θ_{IE} and τ_{IE} , θ_{DP} and τ_{IE} , θ_{IE} and τ_{DP} , and θ_{DP} and τ_{DP} .

3.4.2 Closed-loop Identification of Ankle Mechanical Impedance

When the human ankle was connect to end effectors of the Anklebot, the control loop (Figure 3.4) changes to Figure 3.9.

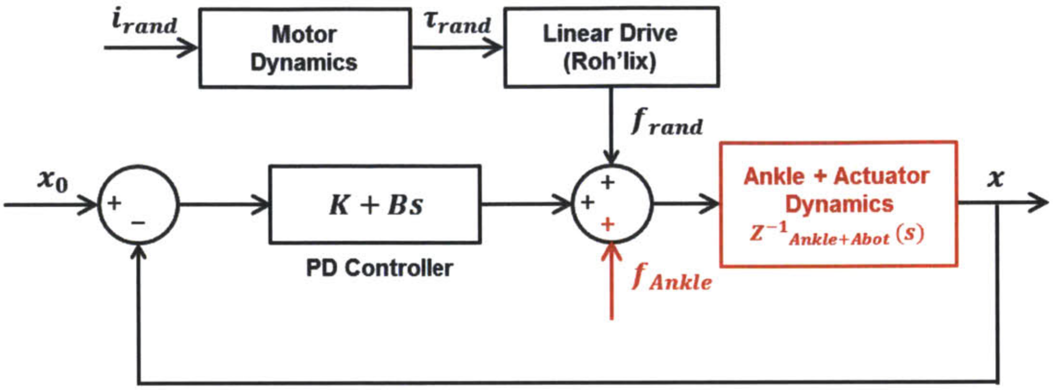

Figure 3.9: Control block diagram when human ankle is connected to the Anklebot. The same controller was implemented for each of left and right actuators independently. External ankle force is denoted as f_{Ankle}.

The closed-loop transfer function ($Y_{Ankle\_CL}(s) = Z^{-1}{}_{Ankle\_CL}(s)$) between random force perturbations to the actuator (f_{rand}) and the corresponding linear displacement (x) was represented as Eq. (3.9):

$$Y_{Ankle\_CL}(s) = Z^{-1}{}_{Ankle\_CL}(s) = \left.\frac{x(s)}{f_{rand}(s)}\right|_{Ankle\_CL} = \frac{Y_{Ankle+Abot}(s)}{1+(K+Bs)Y_{Ankle+Abot}(s)} \quad (3.9)$$

Since the ankle and Anklebot share the same displacement, they are modeled as parallel impedance elements (Eq. (3.10)):

$$Z_{Ankle+Abot}(s) = Y^{-1}{}_{Ankle+Abot}(s) = Z_{Ankle}(s) + Z_{Abot}(s) \quad (3.10)$$

Finally, ankle impedance (Z_{Ankle}) is obtained by subtracting Anklebot dynamics (Z_{Abot}) and programmed Anklebot stiffness (K) from the closed-loop impedance ($Z_{Ankle\_CL}(s)$) (Eq. (3.11)):

$$Z_{Ankle}(s) = Z_{Ankle\_CL}(s) - Z_{Abot}(s) - K \tag{3.11}$$

3.5 Steady-State Dynamic Ankle Mechanical Impedance in Relaxed Muscle

3.5.1 Subjects

Ten unimpaired young human subjects (5 males, 5 females; all right footed) with no reported history of neuromuscular or biomechanical disorders participated in this study. Subjects were between the ages of 21–37, the heights of 1.58 m–1.90 m, and the weights 48.0 kg–80.0 kg. Following procedures approved by the ethics committee (institutional review board), MIT's Committee on the Use of Humans as Experimental Subjects, informed consent was obtained from all subjects.

3.5.2 Experimental Protocol

MVC level of each muscle was first measured in the standing posture in the same way as described in the static study (section 2.7.2).

Each MVC level was used as a reference to calculate normalized EMG amplitudes. Next, a neutral position of the ankle in 2 DOFs was measured while subjects stood upright.

Relaxed ankle impedance was measured in two different postures to investigate its posture dependent property: standing (knee stretched) and seated (knee flexed).

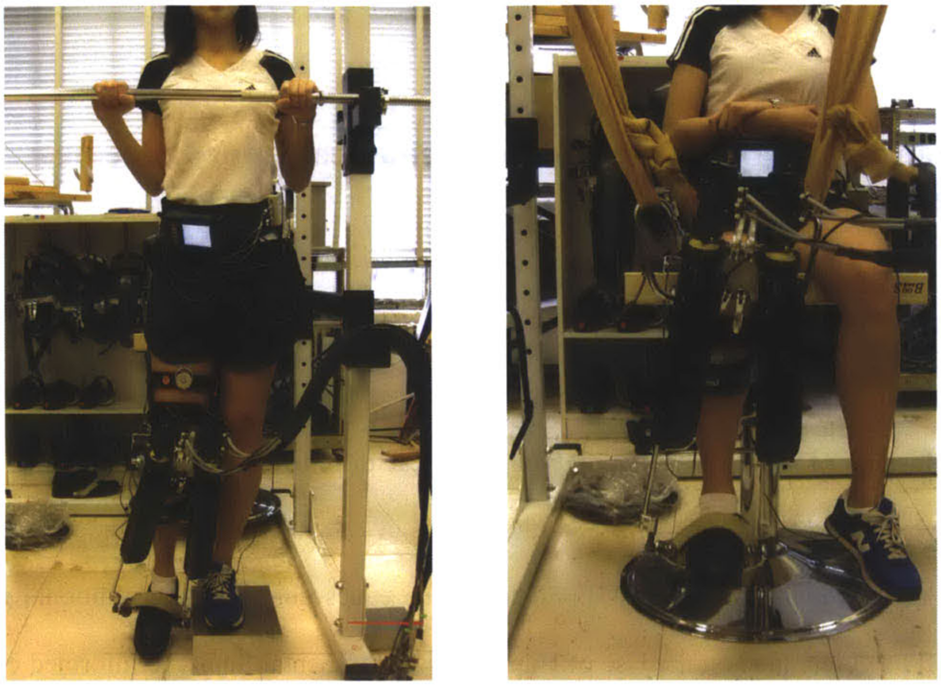

Figure 3.10: Impedance measurements in two different postures. Left: standing (knee stretched), Right: seated (knee flexed)

For the standing measurement, subjects were instructed to place the left foot on the block to provide a clearance between the right foot and the ground. Subjects were allowed to hold a bar in front of them and asked to relax their ankle muscles (Figure 3.10 (left)).

For the seated measurement, the weight of the robot was supported through elastic bands, and a right angle between the thigh and shank was maintained (Figure 3.10 (right)). Elastic bands were used instead of the rigid mounting device used in the static study, mainly to decouple dynamics of the chair from measurements.

Two uncorrelated mild random perturbations (Gaussian white noise with bandwidth 100 Hz) were applied to each actuator for 40 seconds. The same PD controller, used for the identification of Anklebot impedance, was used. Force–displacement in actuator coordinates, torque–angular displacement in joint coordinates, and EMG data were sampled at 1 kHz. EMG amplitudes were calculated from the sampled raw signal using a root-mean-square filter with a moving window of 200 *ms*.

3.5.3 EMG Analysis

Both in standing and seated measurements, all subjects well maintained relaxed muscle condition. When EMG amplitudes were normalized to their corresponding MVC levels, activation levels were under 1.3% MVC when averaged across all subjects, and even the maximum activation level for each muscle was always less than 4.3% MVC for each subject (Table 3.1).

Table 3.1: EMG amplitudes normalized to their corresponding MVC levels.

Muscle / Posture	TA	PL	SOL	GAS
Seated	0.28 (0.42)	0.08 (0.06)	0.21 (0.14)	0.15 (0.12)
Standing	0.88 (0.82)	0.67 (0.52)	1.28 (1.00)	0.65 (0.58)

The mean and SE (value in parentheses) over all subjects are presented. (Unit: %MVC)

3.5.4 Dynamic Ankle Impedance in Joint Coordinates

Ankle impedance has been known that it varies with mean displacement amplitude [44]. Thus, it is important to note ranges of torque input perturbations and the corresponding output displacements in this experiment (Table 3.2).

Table 3.2: Ranges of commanded torque inputs and recorded angular displacements.

	Input (Nm)				Output (Deg.)			
Direction	IE		DP		IE		DP	
Posture	RMS	Min/Max	RMS	Min/Max	RMS	Min/Max	RMS	Min/Max
Seated	2.23	-5.25/5.25	3.29	-7.74/7.74	2.20 (0.08)	-9.45/8.57 (0.47)/(0.34)	1.48 (0.09)	-5.35/5.29 (0.15)/(0.16)
Standing					2.17 (0.06)	-9.31/8.06 (0.34)/(0.27)	1.54 (0.04)	-4.86/5.19 (0.15)/(0.54)

The mean and SE (in parentheses) across all subjects are presented in the table. The same torque inputs were used across all subjects. Parentheses denote SE.

For the mild torque perturbations, RMS and maximum values of displacement in joint coordinates (IE and DP directions) were less than about 2.2° and 1.5° and less than about 9.2° and 5.4°, respectively.

Diagonal components of the partial coherence matrix were very high (>0.8) up to 50 Hz, indicating that ankle impedance in IE and DP directions can be well explained with linear models under the given experimental conditions (Figure 3.11). On the other hand, off-diagonal components of the partial coherence matrix were lower than 0.3, which explains that coupling between different DOFs (IE and DP directions) were substantially small (Figure 3.11).

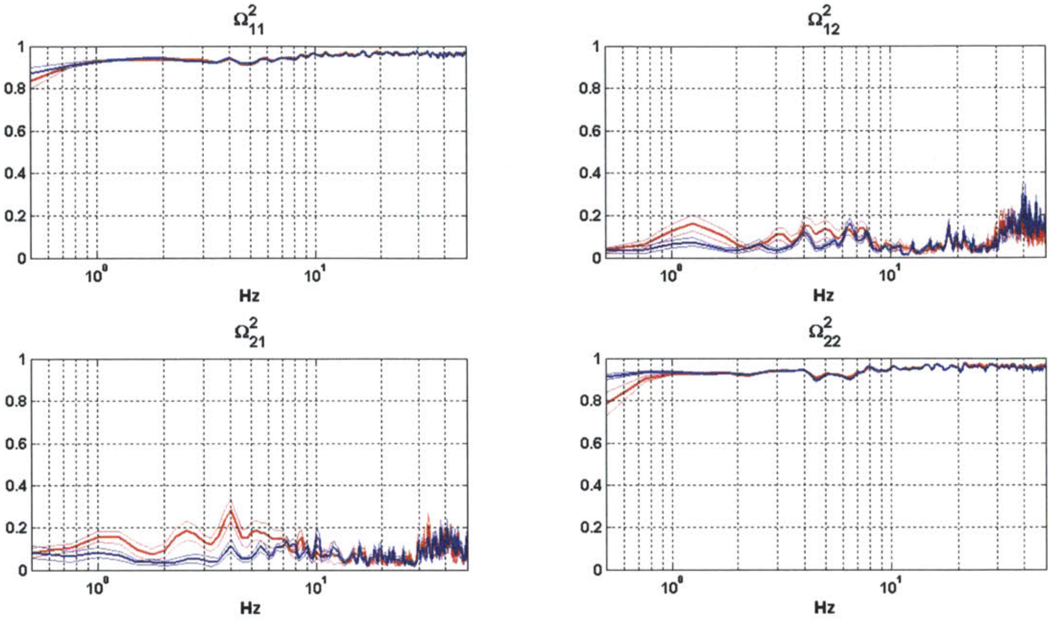

Figure 3.11: Partial coherences in joint coordinates. Red and blue lines denote standing (knee stretched) and seated (knee flexed), respectively. Thick and thin lines represent the mean and mean±1 SE of all subjects, respectively.

Diagonal components of ankle impedance, i.e, IE and DP impedance, were represented as Bode plots to show magnitude and phase responses of impedance in the frequency domain (Figure 3.12). In average of all subjects, inertia was dominant (magnitude increase at ~40 dB/dec) in a high frequency region over about 8~10 Hz for both directions and both postures. For the DP direction, break frequency was higher in the standing than the seated. Stiffness was dominant (zero magnitude slope) below this region, although slight deviations from the zero slope were observed between 2 Hz and 5 Hz. Resonance and anti-resonance behaviors over about 20~30 Hz, which is more evident in DP impedance, was due to vibration modes of the bracket attached to the bottom of a shoe. The same behavior was observed from mechanical impedance of a physical mockup having the same shoe bracket. Details are provided in Appendix F.

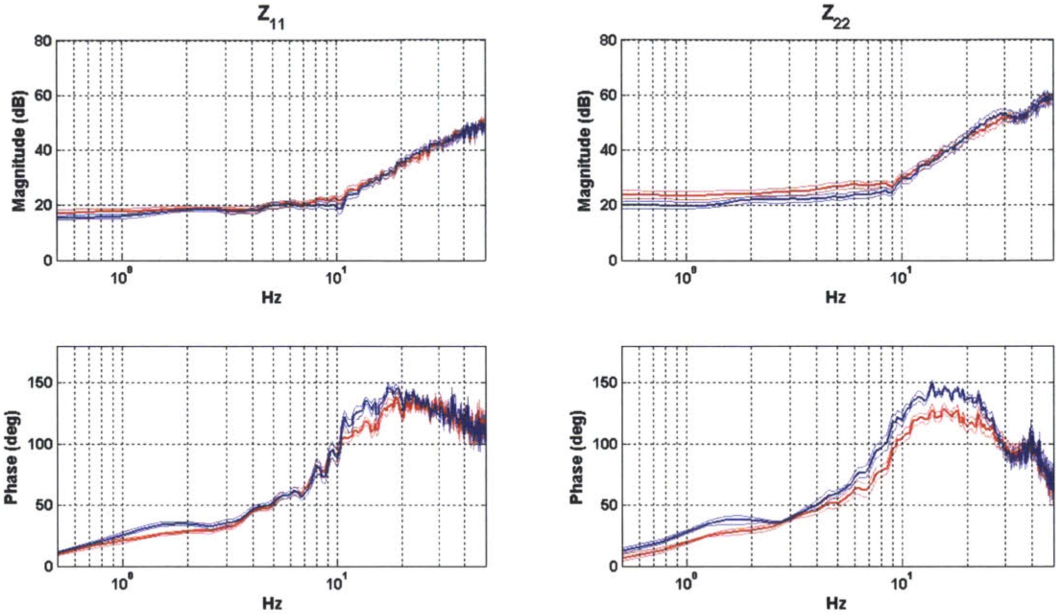

Figure 3.12: Ankle mechanical impedance in joint coordinates. Left: IE impedance (Z_{11}), Right: DP impedance (Z_{22}). Top: magnitude responses, Bottom: phase responses, respectively. The same color codes as in Figure 3.11.

The magnitude of impedance was calculated in two different frequency regions, which I defined the low-frequency region as below 2 Hz and the mid-frequency region between 5 Hz and 8 Hz.

Impedance magnitude in different DOFs (Z_{11} vs. Z_{22}), different knee configurations (knee stretched vs. knee flexed), and different frequency ranges (low-frequency vs. mid-frequency) were calculated and compared (Table 3.3). When pooling all subjects together for each condition, impedance magnitude satisfies normality conditions ($p>0.05$). Paired t-tests were performed to investigate statistical difference between groups. Results are illustrated in Figure 3.13 ~ 3.14.

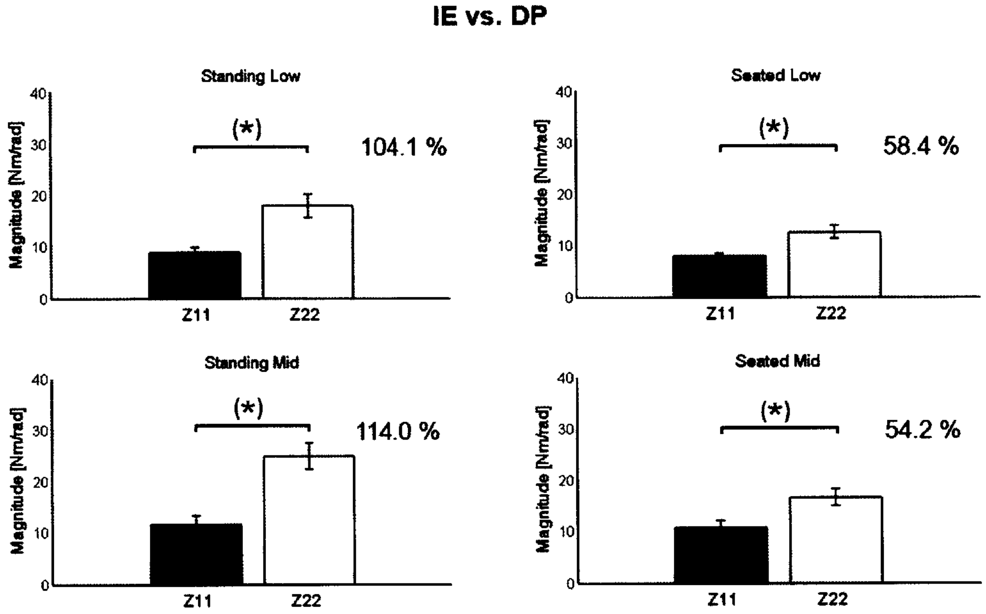

Figure 3.13: IE impedance (Z_{11}) vs. DP impedance (Z_{22}). The mean and mean±1 SE of all subjects are illustrated. Asterisks (*) denote significant difference between groups

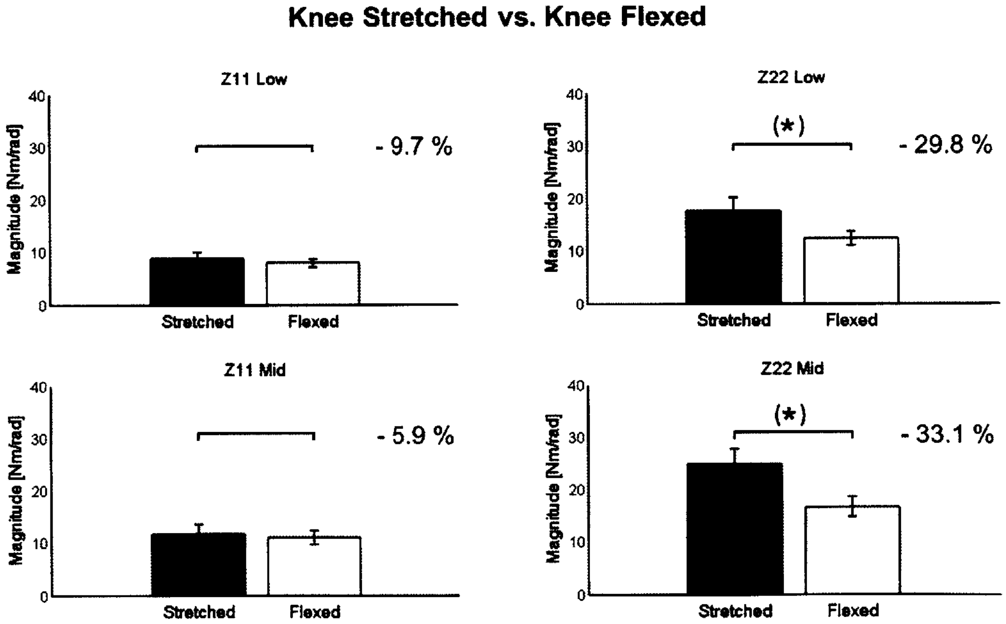

Figure 3.14: Impedance in standing posture (knee stretched) vs. Impedance in seated posture (knee flexed).

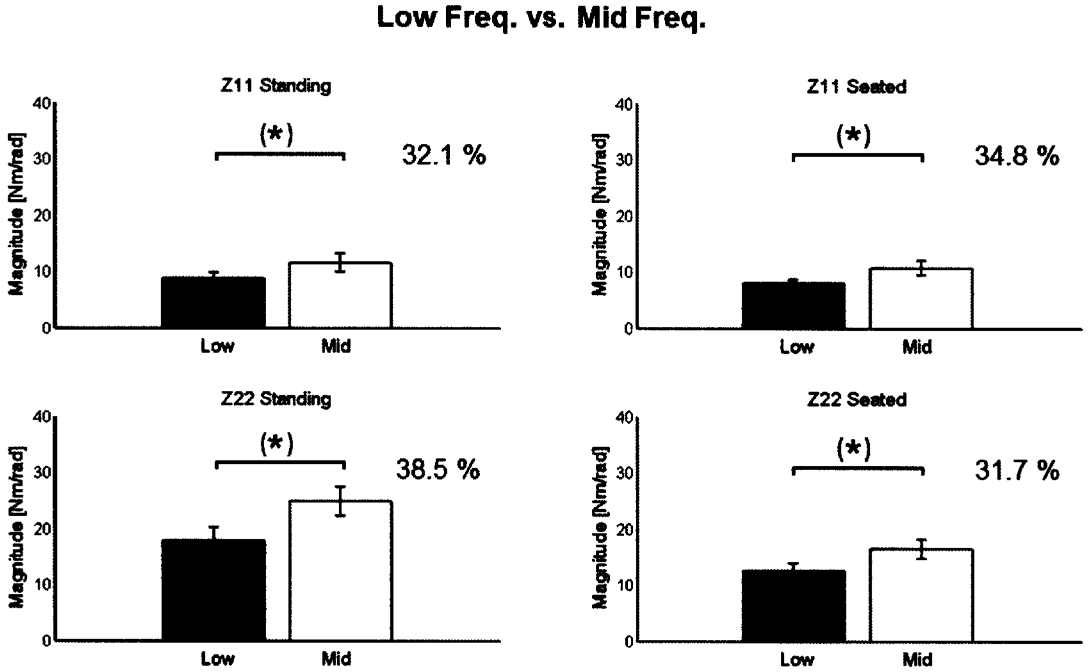

Figure 3.15: Low frequency impedance vs. Mid frequency impedance.

Table 3.3: Impedance magnitude in different DOFs, knee configurations, and frequency ranges.

Directions	IE (Z_{11})		DP (Z_{22})	
Frequency Region / Posture	Low	Mid	Low	Mid
Seated	7.96 (0.62)	10.73 (1.27)	12.61 (1.27)	16.54 (1.69)
Standing	8.79 (1.06)	11.62 (1.58)	17.94 (2.27)	24.85 (2.50)

The mean and SE (in parentheses) across all subjects are presented in the table. (Unit: Nm/rad)

Impedance in the IE direction was always lower than the DP direction for both frequency regions and postures ($p<0.01$ for all conditions). For each condition, the increase of DP impedance in reference to the corresponding IE impedance was calculated. The increase was greater in the standing than in the seated posture, due to higher DP impedance in the standing posture (Figure 3.13).

When impedance in standing (knee stretched) and seated (knee flexed) was compared, no statistical difference was observed for IE impedance ($p>0.20$), while significant difference was found for DP impedance ($p<0.01$). About 30% of impedance decrease was observed when the knee was flexed than when stretched (Figure 3.14).

Mid frequency impedance was about 30~40% greater than low frequency impedance in all conditions ($p<0.01$) (Figure 3.15).

3.5.6 Energetic Passivity of the Ankle Joint in Relaxed Muscles

Energetic passivity of the ankle was tested by evaluating positive semi-definite condition of $\boldsymbol{T}(jw) = [T_{11}\, T_{12}; T_{21}\, T_{22}]$ (Eq. (3.6)). In detail, the passivity condition was satisfied when all of the leading principal minors of $\boldsymbol{T}$ (T_{11} and $|\boldsymbol{T}|$) were equal or greater than zero. Since the order of inputs and outputs can be arbitrarily selected, i.e., IE' first and DP' next or vice versa, we should check both T_{22} as well as T_{11}. In both seated and standing measurements, T_{11} are T_{22} were strictly positive and $|\boldsymbol{T}|$ was equal or greater than zero up to 50 Hz. This condition was satisfied for all subjects, and average results were shown in Figure 3.16.

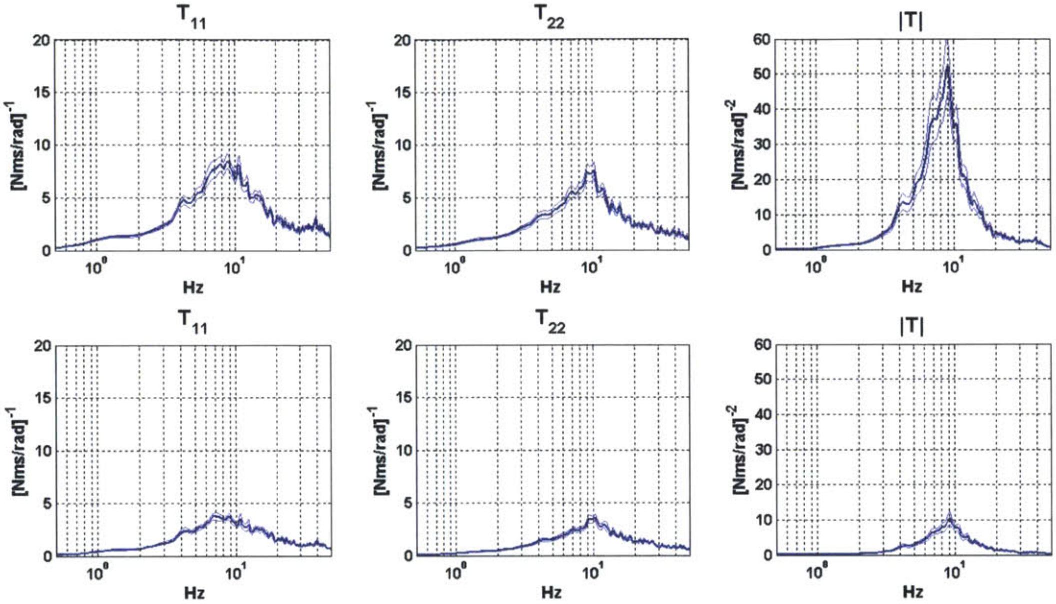

Figure 3.16: Energetic passivity of the relaxed ankle in seated (top row) and standing (bottom row) postures. Thick and thin lines represent the mean and mean±1 SE of all subjects, respectively.

3.5.7 Anisotropy of Dynamic Ankle Impedance in Relaxed Muscles

The directional variation of dynamic ankle impedance was identified based on calculations in rotated coordinates. The increment of the rotation angle (α) for the rotational transformation ($\boldsymbol{R}$) in Eq. (3.4) was set as $10°$ ($\alpha = 0°, 10°, ..., 80°$).

Input power spectral density (PSD) was first estimated in the rotated coordinates. PSD of τ_{IE}' and τ_{DP}' were flat up to 100 Hz for any α, validating that ankle impedance can be reliably estimated in all directions in the IE−DP space based on spectral analysis (Figure 3.17).

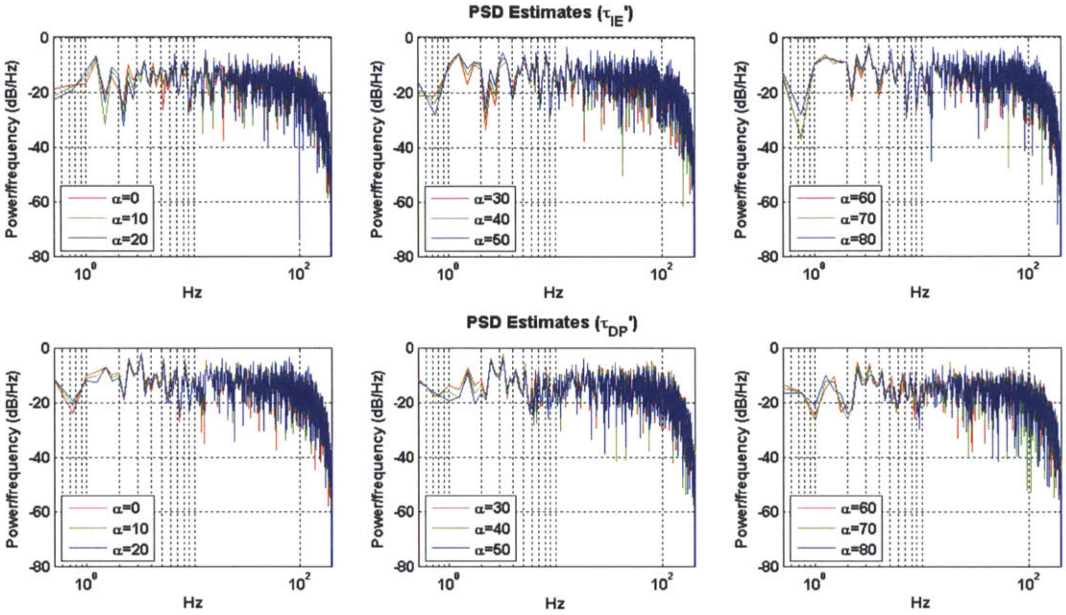

Figure 3.17: Input power spectral density in the rotated joint coordinates ($\alpha = 0°, 10°, ..., 80°$). Top: PSD of τ_{IE}', bottom: PSD of τ_{DP}'.

The directional variation of impedance was depicted in polar coordinates, where the angle corresponds to each movement direction in the 2D-space, and the radius corresponds to the magnitude of impedance in that direction. As in the representation of directional variation of static ankle impedance (section 2.6.4), directions of $0°, 90°, 180°$ and $270°$ in the polar coordinates represent eversion, dorsiflexion, inversion and plantarflexion, respectively.

Average results of all subjects in the low-frequency and mid-frequency regions under seated and standing postures are shown in Figure 3.18. Results of individual subject are provided in Appendix G.

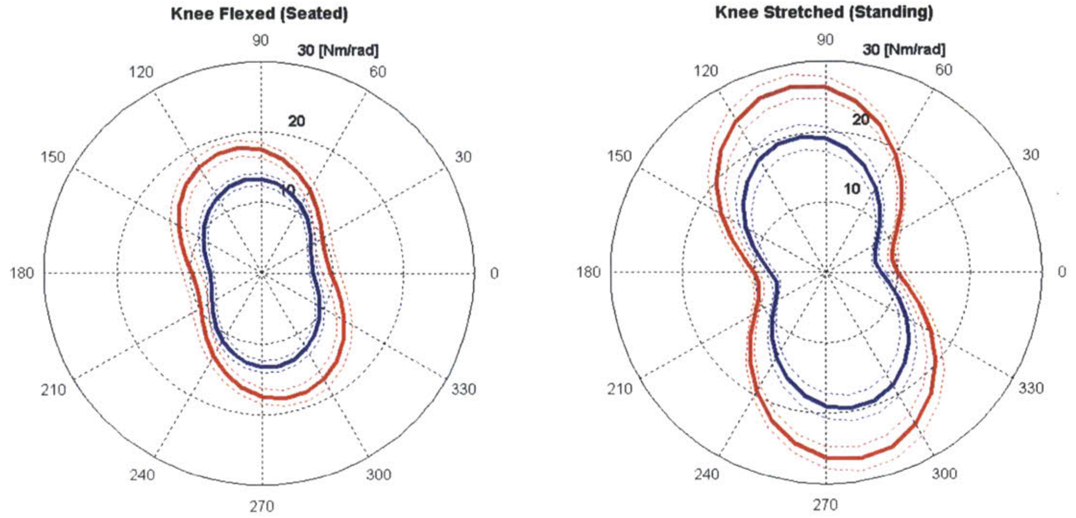

Figure 3.18: Anisotropy of dynamic ankle impedance in seated and standing postures. Thick and thin lines represent the mean and mean±1 SE of all subjects, respectively. Blue and red lines represent low- and mid-frequency impedance, respectively.

In average across all subjects, impedance in the mid-frequency region was greater than in the low-frequency region in all movement directions ($p<0.05$) in the standing posture, and in all movement directions except the directions $0° \leq \alpha \leq 60°$ and $180° \leq \alpha \leq 240°$ in the seated posture. In addition, impedance in the standing measurement was greater than in the seated measurement in the directions $70° \leq \alpha \leq 150°$ and $250° \leq \alpha \leq 330°$ for the low frequency and $50° \leq \alpha \leq 140°$ and $230° \leq \alpha \leq 320°$ for the mid frequency ($p<0.05$), otherwise statistically not significantly different ($p>0.05$).

Directions of highest and lowest impedance magnitude, which I defined as a major principal axis and a minor principal axis, respectively, were tilted in the CCW direction from the original joint coordinates. Directions of major and minor principal axes and the corresponding impedance magnitude are summarized in Table 3.4.

Table 3.4: Direction of major and minor axes and the corresponding impedance magnitude.

	Direction of Principal Axes		Impedance in the Major Principal Axis Direction		Impedance in the Minor Principal Axis Direction	
Frequency Region / Posture	**Low-Freq.**	**Mid-Freq.**	**Low-Freq.**	**Mid-Freq.**	**Low**	**Mid**
Seated	6.0 (3.1)	14.5 (2.7)	13.5 (0.9)	18.1 (1.2)	7.0 (0.6)	9.1 (1.2)
Standing	14.0 (1.7)	10.0 (1.6)	19.6 (1.8)	26.9 (1.7)	7.0 (0.6)	9.4 (0.7)

The direction of major and minor axis and minor axis are defined from the axis for the direction of IE and DP, respectively, in the CCW direction (Unit of direction: °, unit of magnitude: Nm/rad). The mean and SE (value in parentheses) over all subjects are presented.

3.5.8 Ellipse Representation and Impedance Matrix in Relaxed Muscles

Following the description in section 3.3.3, the directional variation of dynamic ankle impedance was represented as an ellipse. Average results of all subjects in the low-frequency and mid-frequency regions under seated and standing postures are shown in Figure 3.19. Results of individual subject are provided in Appendix G.

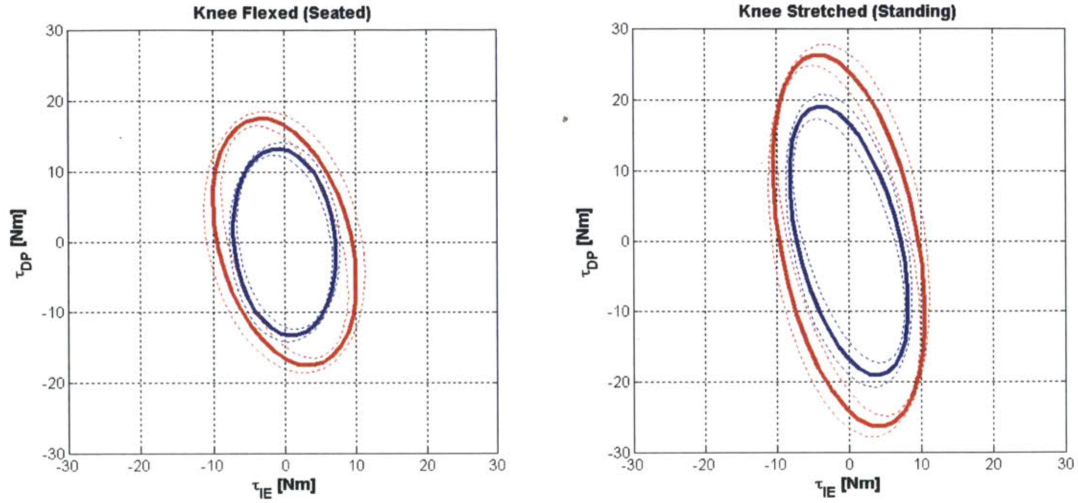

Figure 3.19: Ellipse representation of dynamic ankle impedance in seated and standing postures. The same format as in Figure 3.18.

2-by-2 impedance matrix was calculated for each posture and for each subject separately according to Eq. (3.5), and the mean ± 1 SE is presented below:

$$\boldsymbol{Z}_{seated\_low} = \begin{bmatrix} 7.25 & -0.63 \\ -0.63 & 13.28 \end{bmatrix} \pm \begin{bmatrix} 0.59 & 0.36 \\ 0.36 & 0.89 \end{bmatrix}$$

$$\boldsymbol{Z}_{seated\_mid} = \begin{bmatrix} 9.86 & -2.13 \\ -2.13 & 17.41 \end{bmatrix} \pm \begin{bmatrix} 1.30 & 0.45 \\ 0.45 & 1.12 \end{bmatrix}$$

$$\boldsymbol{Z}_{s\tan ding\_low} = \begin{bmatrix} 7.73 & -2.82 \\ -2.82 & 18.87 \end{bmatrix} \pm \begin{bmatrix} 0.66 & 0.33 \\ 0.33 & 1.81 \end{bmatrix}$$

$$\boldsymbol{Z}_{s\tan ding\_mid} = \begin{bmatrix} 10.92 & -3.04 \\ -3.04 & 26.17 \end{bmatrix} \pm \begin{bmatrix} 0.89 & 0.69 \\ 0.69 & 1.54 \end{bmatrix}$$

Average results of three parameters defining the orientation (Φ), shape (Z_{22}'/Z_{11}'), and size of the ellipse ($|\boldsymbol{Z}|$) are also presented in Table 3.5.

Table 3.5: Orientation, shape, and size of the impedance ellipse.

Parameters	**Orientation (Φ)**		**Shape (Z_{22}'/Z_{11}')**		**Size ($\|\mathbf{Z}\|$)**	
Frequency Region / Posture	**Low-Freq.**	**Mid-Freq.**	**Low-Freq.**	**Mid-Freq.**	**Low**	**Mid**
Seated	6.0	14.5	1.97	2.14	98.0	175.9
	(3.1)	(2.7)	(0.12)	(0.16)	(12.9)	(33.7)
Standing	14.0	10.0	2.86	2.91	142.6	259.8
	(1.7)	(1.6)	(0.20)	(0.16)	(24.3)	(35.7)

The mean and SE (value in parentheses) over all subjects are presented. Unit of orientation: °, unit of size: $[\mathrm{Nm/rad}]^2$.

The orientation Φ exactly matched with the direction of minor principal axis of the direction dependent map. The ratio between the largest and smallest impedance magnitude was between 2 and 3. The size of impedance ellipse was bigger in the mid frequency region than in the low frequency, and the size in the standing was larger than in the seated measurement.

To investigate the variability across subjects, coefficient of variation (CV=standard deviation/mean) was calculated for each parameter and summarized in Table 3.6.

Table 3.6: Coefficient of variation of parameters for impedance ellipse.

Parameters	**Orientation (Φ)**		**Shape (Z_{22}'/Z_{11}')**		**Size ($\|\mathbf{Z}\|$)**	
Frequency Region / Posture	**Low-Freq.**	**Mid-Freq.**	**Low-Freq.**	**Mid-Freq.**	**Low**	**Mid**
Seated	1.55	0.56	0.18	0.22	0.39	0.57
Standing	0.36	0.48	0.21	0.16	0.51	0.41

The same units as in Table 3.5.

In general, the CV of shape was smaller than that of orientation or size. However, care is needed for this interpretation, because orientation can be very sensitive to numerical error. For example, high value of the CV for the orientation in low-frequency of the seated measurement is due to one outlier subject (subject #3) showing orientation tilted in opposite direction (clockwise (CW) for the DP direction).

3.5.9 Discussion

The analysis of partial coherences showed that ankle impedance in relaxed muscles can be well investigated from linear system identifications in both IE and DP directions. However, coupling between different DOFs in the joint coordinates were substantially small; in other words, activations of major muscles for DP (IE) barely introduced motions in IE (DP) direction.

When muscles were relaxed, both IE and DP impedances showed clear inertia dominant behavior over about 8~10 Hz. Low- and mid-frequency responses below the inertia dominant region were more or less consistent with stiffness, although slight deviations were observed. As a result, impedance magnitude in the mid-frequency was significantly (about 30~40%) higher than in the low-frequency. The transition behavior in this frequency region is practically important, since operating conditions of the ankle during fast walking or running may fall into this region.

In all subjects, DP impedance was greater than IE impedance both in the seated and standing measurements, which was consistent with previous observations in the static study [64]. In addition, the magnitude of DP impedance in the standing posture was consistently higher than in the seated posture across all subjects. This can be explained with the stretch of gastrocnemius, which is a bi-articular muscle running from its two heads just above the knee to the heel. When the knee was stretched in the standing posture, gastrocnemius also stretched more than in the knee flexed posture causing higher passive stiffness. This effect was negligible in IE impedance, since gastrocnemius is a plantarflexor acting only in the sagittal plane.

Ankle impedance was highly direction dependent, being weak in the IE direction, resulting in a "peanut" shape structure. The impedance structure in the mid-frequency region was bigger than that in the low-frequency region, but the characteristic "peanut" structure was maintained. This feature is consistent with prevalent ankle injuries in the IE direction, observed in various unconstrained situations accompanying ankle motions in different frequency regions [74, 101]. In addition, directions of principal axes well match with anatomical axes of rotations of the ankle. It has been reported that the axes of rotation for IE and DP motions are slightly tilted in the CCW and CW directions with respect to the axes perpendicular to the frontal and sagittal planes, respectively [17].

Ankle impedance was also simply represented as a 2-by-2 impedance matrix, and three parameters defining the orientation, shape, and size of impedance were calculated. Under relaxed muscles, variation of the shape across subjects was relatively small compare to that of the orientation and the size of impedance, implying that the ratio of impedance magnitude between major and minor principal axis directions is relatively invariant, even when absolute impedance values across subjects are highly variable.

The passivity analysis showed that the relaxed ankle of young healthy subjects is fundamentally passive ($|\boldsymbol{T}|=0$) in the low-frequency region where stiffness was dominant. This result is consistent with previous finding in the static study: zero curl under relaxed muscle condition for young healthy subjects [64]. The ankle was dissipative (strictly passive) where damping was dominant, and almost passive in the inertia dominant high frequency region.

3.6 Steady-State Dynamic Ankle Mechanical Impedance in Active Muscle

3.6.1 Experimental Protocol

The same 10 unimpaired young human subjects (5 males, 5 females; all right footed) described in section 3.5.1 participated in this study. To investigate effects of muscle activation, ankle impedance was measured in different muscle active levels. TA and SOL were selected as target muscles for dorsiflexor and plantarflexor active studies, respectively. Ankle impedance was measured at 5 different activation levels, from 10% to 30% of MVC level in increments of 5% MVC. As a baseline for active studies, passive ankle impedance was also measured with muscles fully relaxed. To prevent muscle fatigue, a 3 minute rest period was given to each subject between measurements.

During measurements, subjects were seated with their ankle held by the robot in a neutral position with the sole at a right angle to the tibia (Figure 3.10 (right)). A visual display showing current and target activation levels were provided to subjects. Subjects were first instructed to activate a specific muscle and maintain it at the target level. When the activation level reached the target level, the robot applied two uncorrelated mild random perturbations (Gaussian white noise with bandwidth 100 Hz) to the ankle for 40 seconds. The same PD controller in the relaxed study was used (Figure 3.9), except different gain settings. The Anklebot stiffness or P-gain in the controller was set to 2000 N/m for active studies.

Force–displacement in actuator coordinates, torque–angular displacement in joint coordinates, and EMG data were sampled at 1 kHz. EMG amplitudes were calculated from the sampled raw signal using a root-mean-square filter with a moving window of 200 *ms*.

3.6.2 EMG Analysis

First, activation levels under relaxed muscles were under 0.3% MVC, when averaged across all subjects. To ensure that each subject was able to maintain target muscle activation levels, the mean EMG amplitude for each measurement was calculated and its ratio to the MVC level was compared with the corresponding target level (10~30% MVC). The linearity of actual activation levels was measured by calculating the correlation coefficient (R^2). Linearly increasing activation levels of TA and SOL were observed in all subjects with very high R^2 (Table 3.7).

In addition, total ankle muscle activity was approximated by summing normalized EMG amplitudes of all measured muscles, and its linearity was calculated. This is important because subjects could not solely activate a single muscle, but evoked a degree of co-activation of other muscles due to synergies (Figure 3.20). For example, in the SOL active study, all platarflexors (SOL, PL, and GAS) were activated in the same pattern, while TA activation was very low. Linearity of total muscle activation levels was also very high for both studies (Table 3.7), validating the suggested experimental protocol to investigate the effect of muscle activation on ankle impedance.

Table 3.7: Linearity of Muscle Activation.

Study	TA Active		SOL Active	
Muscle Type / Subject	Target (TA)	Total	Target (SOL)	Total
1	1.000	0.985	0.988	0.983
2	0.994	0.980	0.978	0.912
3	0.998	0.916	0.987	0.987
4	0.995	0.946	0.996	0.930
5	0.999	0.983	0.993	0.959
6	0.999	0.993	0.995	0.955
7	0.998	0.958	0.999	0.998
8	0.997	0.897	0.999	0.959
9	0.999	0.971	1.000	0.985
10	0.999	0.994	0.996	0.974
Mean	**0.998**	**0.962**	**0.993**	**0.964**
(SE)	**(0.0002)**	**(0.004)**	**(0.001)**	**(0.003)**

The correlation coefficient (R^2) was calculated for each subject and presented in the table.

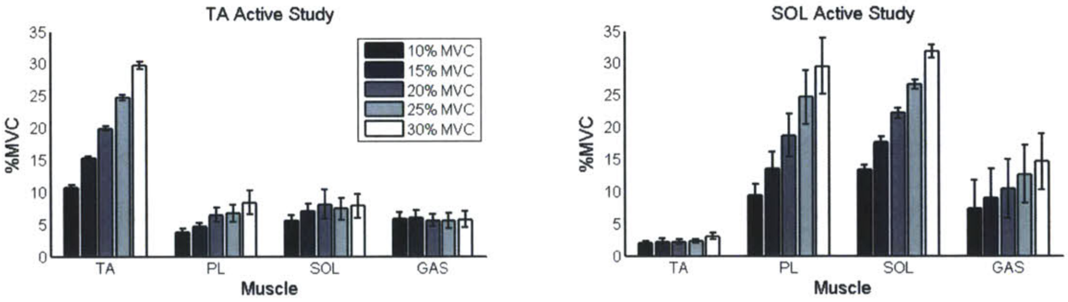

Figure 3.20: Activation levels of all measured muscles in two active studies. The y-axis presents each muscle's activation level as a percentage of the corresponding MVC level. The mean ± SE of all subjects are illustrated.

Average results of all subjects are shown in Figure 3.21. Target levels in the TA active study were well maintained, while activation levels of SOL were slightly higher than the target levels. The level of total muscle activations was significantly higher in the SOL active study than the TA active study.

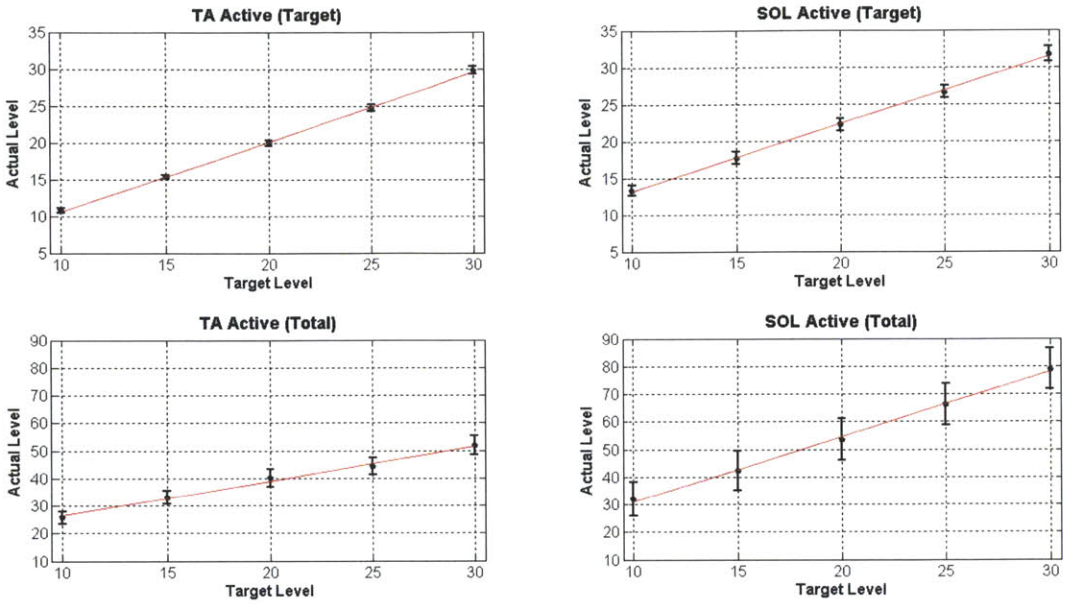

Figure 3.21: Linearity of muscle activation levels. Top: target muscle activation, bottom: total muscle activation. The mean ± SE of all subjects are illustrated as asterisks and bars. Red lines are linear regression fits to measurements.

3.6.3 Dynamic Ankle Impedance in Joint Coordinates

Different mean ankle positions are expected for different levels of muscle activation. Ankle impedance has been known that it varies with mean ankle position [46]. Thus, it is important to note ranges of ankle positions measured in this experiment (Figure 3.22).

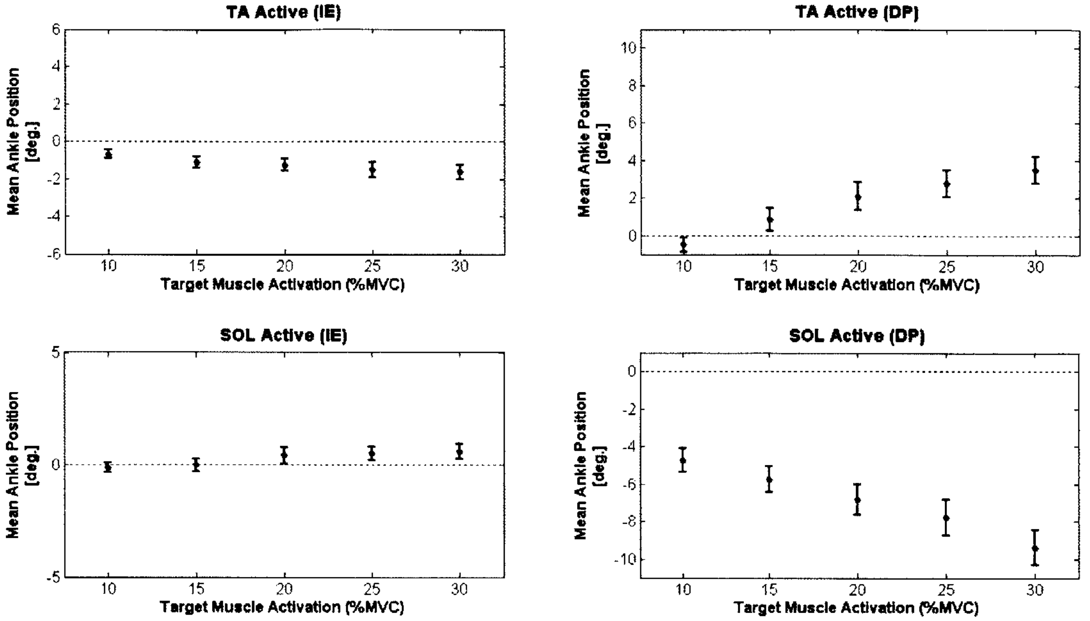

Figure 3.22: The mean ankle position in active muscle studies. Positive (negative) values denote dorsiflexion (plantarflexion) and eversion (inversion) in the sagittal and the frontal planes, respectively. The mean ± SE of all subjects are illustrated as asterisks and bars.

In the TA active study, the ankle was more inverted and dorsiflexed with increased muscle activation, since TA is a major dorsiflexor and an inverter. In the SOL active study, the ankle was plantarflexed due to the activation of major plantarflexors. Among plantarflexors, PL is a main everter, and the activation of this muscle introduced slight eversion.

Across all muscle activation conditions, the ankle was constrained in a small ROM due to high restoring torques by the Anklebot in both DOFs: −1.6° ~ −0.7° (IE) and −0.5° ~ 3.5° (DP) for the TA active study, and −0.1° ~ 0.6° (IE) and −9.4° ~ −4.7° (DP) for the SOL active study.

Diagonal components of the partial coherence matrix were high in all muscle activation conditions up to 50 Hz, except the low frequency region below 1~2 Hz. In this region, partial coherences decreased as muscle activation increased. Off-diagonal components were substantially low even with muscle activations, although not negligible.

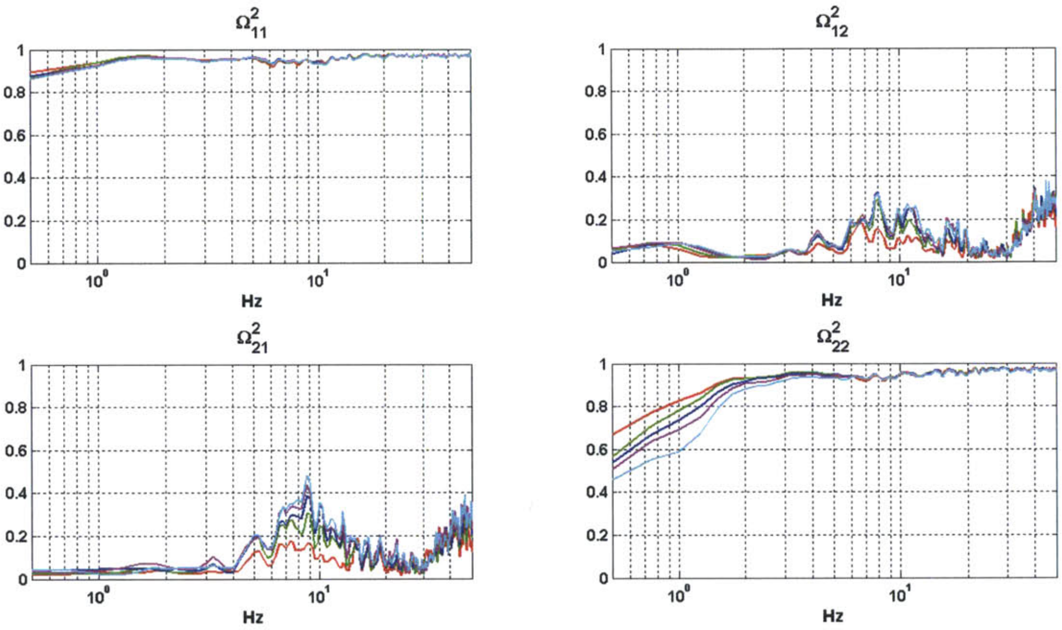

Figure 3.23: Partial coherences in the TA active study. Red, green, blue, magenta, and cyan colors denote 10%, 15%, 20%, 25%, and 30% MVC, respectively. The means of all subjects are presented.

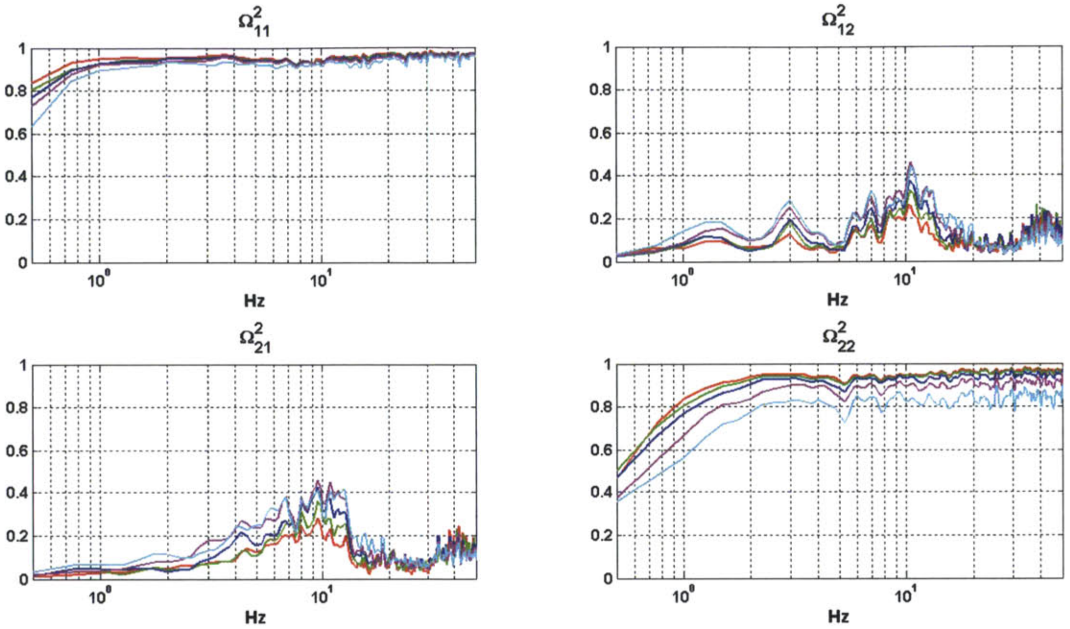

Figure 3.24: Partial coherences in the SOL active study. The same format as in Figure 3.23.

Diagonal components of ankle impedance in the TA active and SOL active studies are shown as Bode plots in Figure 3.25 and Figure 3.26, respectively. Both studies showed response more or less consistent with a 2nd order system with inertia, damping, and stiffness. When averaged across all subjects, inertia was dominant in the high frequency region over about 10~20 Hz depending on muscle activations. Below inertia dominant regions, the magnitude of impedance increased with the increase of muscle activation either TA or SOL. Phase transitions around break frequencies were smoother with higher muscle activation. In addition, phase transitions of IE impedance were more rapid than DP impedance.

The similar resonance and anti-resonance behaviors over about 20~30 Hz explained in the relaxed study were also observed.

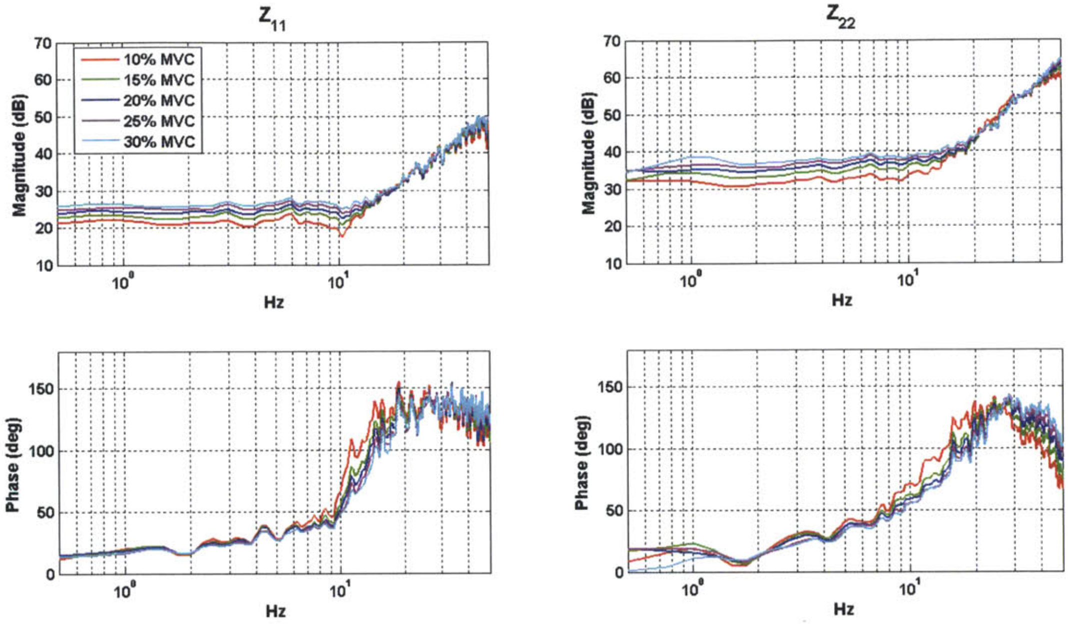

Figure 3.25: Ankle mechanical impedance in the TA active study. Left: IE impedance (Z_{11}), Right: DP impedance (Z_{22}). Top: magnitude responses, Bottom: phase responses, respectively. The same color codes as in Figure 3.23.

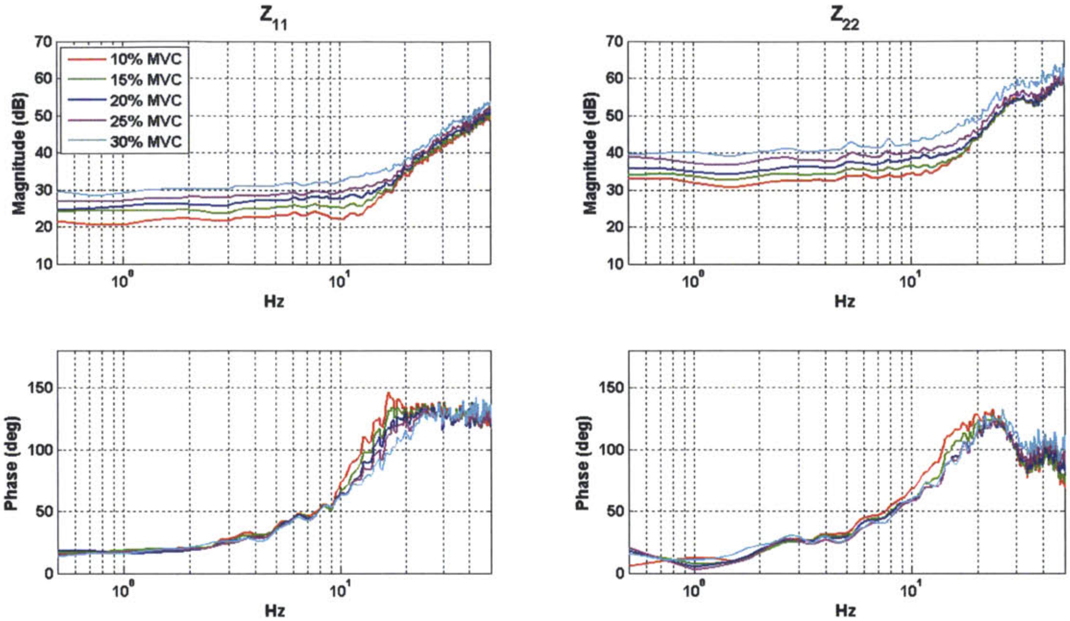

Figure 3.26: Ankle mechanical impedance in the SOL active study. The same format as in Figure 3.23.

The magnitude of impedance in the low-frequency region (1~2 Hz) and mid-frequency region (5~8 Hz) were calculated, and the relationship between muscle activation and impedance was investigated for each subject separately. Impedance value below 1 Hz was not considered due to low partial coherence values.

Most subjects showed a highly linear trend between muscle activation levels and the corresponding impedance magnitude in both TA active and SOL active studies. Only one subject (subject #6) in the SOL active study showed substantially low R^2 values in all conditions. When the mean for the SOL active study was re-calculated except this outlier subject, R^2 value was 0.90, 0.90, 0.92, and 0.92 for low-frequency IE, mid-frequency DP, low-frequency DP, and mid-frequency DP impedance.

Table 3.8: Actual muscle activation level vs. Ankle impedance.

Study	**TA Active**				**SOL Active**			
Direction	**IE**		**DP**		**IE**		**DP**	
Freq. Region / **Subject**	**Low Freq.**	**Mid Freq.**	**Low Freq.**	**Mid Freq.**	**Low Freq.**	**Mid Freq.**	**Low Freq.**	**Mid Freq.**
1	0.98	0.96	0.98	0.95	0.93	0.91	1.00	0.99
2	0.95	0.97	0.87	0.96	0.96	0.94	0.97	0.98
3	0.90	0.94	0.90	0.93	0.78	0.85	1.00	0.99
4	0.93	0.96	0.95	0.79	0.96	0.95	0.91	0.88
5	0.89	0.92	0.84	0.89	0.95	0.95	0.89	0.93
6	0.93	0.95	0.94	0.96	0.51	0.39	0.61	0.37
7	0.94	0.84	0.98	0.90	0.88	0.85	0.94	0.94
8	0.97	0.98	0.95	0.91	0.97	0.95	0.92	0.89
9	0.98	0.97	0.80	0.90	0.88	0.85	0.78	0.70
10	0.97	0.97	0.95	0.98	0.78	0.84	0.90	0.90
Mean (SE)	**0.94 (0.01)**	**0.95 (0.01)**	**0.92 (0.02)**	**0.92 (0.02)**	**0.86 (0.05)**	**0.85 (0.06)**	**0.89 (0.04)**	**0.86 (0.06)**

The correlation coefficient (R^2) was calculated for each subject and presented in the table.

When the linearity was calculated based on the pooled data from all 10 subjects, R^2 value was very high closed to 1 (Table 3.9 and Figure 3.27).

Table 3.9: Actual muscle activation level vs. Ankle impedance based on the pooled data.

Study	**TA Active**				**SOL Active**			
Direction	**IE**		**DP**		**IE**		**DP**	
Freq. Region	**Low Freq.**	**Mid Freq.**	**Low Freq.**	**Mid Freq.**	**Low Freq.**	**Mid Freq.**	**Low Freq.**	**Mid Freq.**
R^2	0.993	0.985	0.997	0.975	0.985	0.978	0.959	0.963
Slope	0.43	0.52	1.89	2.10	1.03	1.22	3.48	4.30

The unit of slope is Nm/rad/%MVC.

The slope of linear fit was calculated. Slopes in the IE direction were lower than in the DP direction, and slopes in the SOL active study were higher than the corresponding values in the TA study.

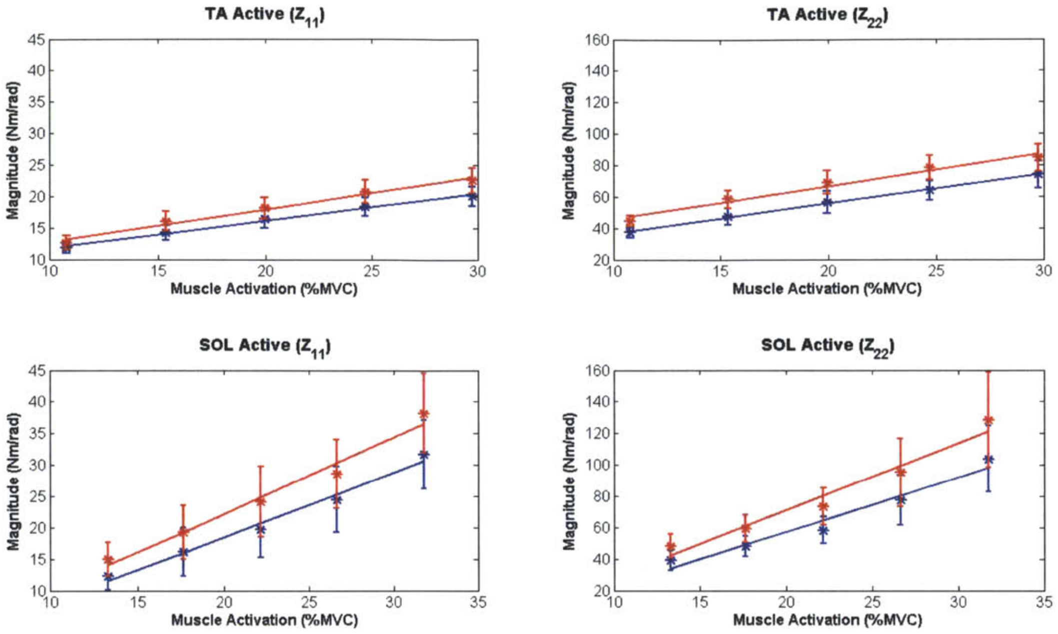

Figure 3.27: Actual muscle activation level vs. Ankle impedance based on the pooled data. Top row: TA active study, bottom row: SOL active study, left column: IE impedance, right column: DP impedance. Low- and mid-frequency impedance is illustrated as blue and red colors, respectively. The mean ± SE of all subjects are illustrated as asterisks and bars.

For the same target muscle activation level, low- and mid-frequency impedance for the TA study and SOL study were compared. The ratio between impedance in the TA study and the SOL study was summarized in Table 3.10. In average across all subjects, impedance in the SOL study was greater than in the TA study, and the discrepancy became more marked with the increased muscle activation.

Table 3.10: The ratio of impedance in the SOL study to the TA study.

Freq. Region	Low-Freq.		Mid-Freq.	
Direction Target Activation Level	IE	DP	IE	DP
10% MVC	1.04	1.05	1.18	1.08
15% MVC	1.13	1.01	1.20	1.01
20% MVC	1.20	1.03	1.33	1.07
25% MVC	1.33	1.21	1.38	1.22
30% MVC	1.58	1.40	1.69	1.52

The ratio was calculated based on pooled data from all subjects.

Mid-frequency impedance was consistently higher than low-frequency impedance for both IE and DP directions in all muscle activation levels. The ratio between low- and mid-frequency was summarized in Table 3.11.

Table 3.11: The ratio of mid-frequency impedance to low-frequency impedance.

Study	TA Active		SOL Active	
Direction Target Activation Level	IE	DP	IE	DP
10% MVC	1.07	1.19	1.22	1.23
15% MVC	1.13	1.23	1.19	1.23
20% MVC	1.11	1.22	1.23	1.26
25% MVC	1.13	1.22	1.17	1.23
30% MVC	1.13	1.14	1.21	1.24
Mean **(SD)**	1.11 (0.03)	1.20 (0.04)	1.20 (0.02)	1.24 (0.01)

The ratio was calculated based on pooled data from all subjects.

3.6.4 Energetic Passivity of the Ankle Joint in Active Muscles

Energetic passivity of the ankle in active muscles was investigated by evaluating positive semi-definite condition of $\boldsymbol{T}(jw) = \left[T_{11}\,T_{12}; T_{21}\,T_{22}\right]$ (Eq. (3.6)). Most subjects (9 out of 10 for the TA study and 7 out of 10 for the SOL study) satisfied the positive semi-definite condition of $\boldsymbol{T}$ in all muscle activation conditions up to the frequency region of our interest (<30 Hz). Average results of all subjects are shown in Figure 3.28.

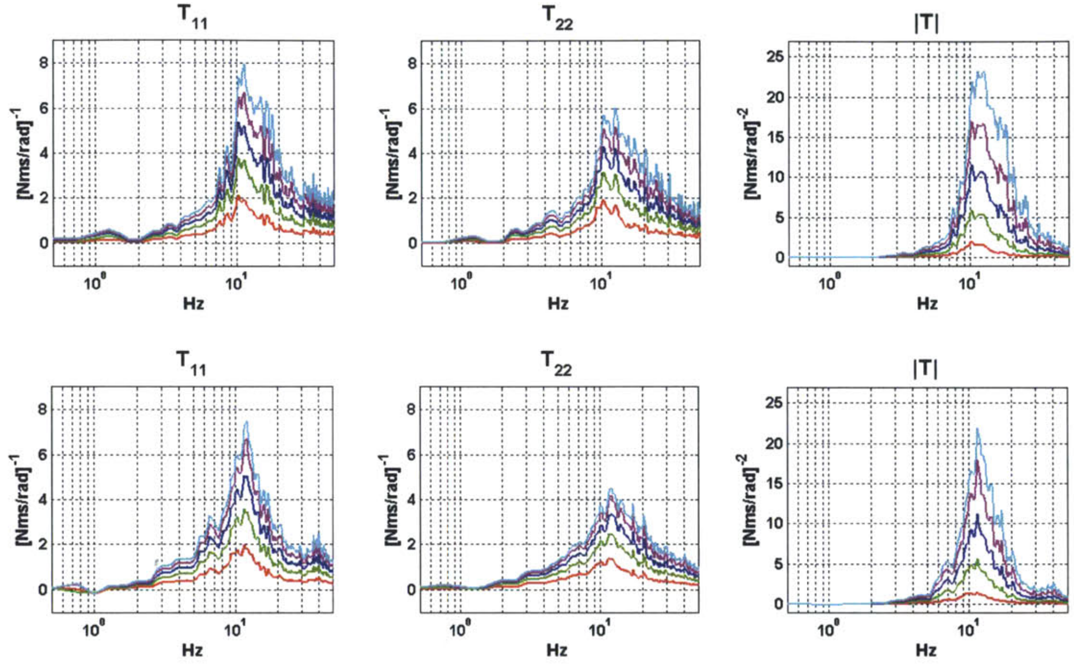

Figure 3.28: Energetic passivity of the ankle in active studies. Top: TA study, bottom: SOL study. The mean of all subjects are presented. Black: relaxed, red: 10% MVC, green: 15% MVC, blue: 20% MVC, magenta: 25% MVC, cyan: 30% MVC.

The ankle of young healthy subjects under active muscles is fundamentally passive in the low-frequency region where stiffness was dominant ($|\boldsymbol{T}| = 0$), and almost passive in the high-frequency region where foot inertia contributed. The passivity condition was strictly positive where damping was dominant.

Interestingly, several subjects didn't satisfy the passivity condition in the low-frequency region below 2 Hz: one subject (subject #1) in the TA study and 3 subjects (subject #2, #5, #9) in the SOL active study showed non-passive behavior. To evaluate how significant the non-passive behavior of these subjects is, impedance matrix was calculated in the frequency region where the passivity condition was not satisfied, and the ratio of the square roots of the determinants of the anti-symmetric ($\boldsymbol{Z}_a$) and symmetric ($\boldsymbol{Z}_s$) parts of the impedance matrix was calculated ($\sqrt{\boldsymbol{Z}_{ratio}} = \sqrt{\det(\boldsymbol{Z}_a)} / \sqrt{\det(\boldsymbol{Z}_s)}$). Results are summarized in Table 3.12, and the result of one subject (#5) was excluded in the evaluation due to low partial coherence (<0.3) in this frequency region.

Table 3.12: $\sqrt{Z_{ratio}}$ for subjects showing non-passive behavior.

Target Activation Level \ Subject	TA Study #1	SOL Study #2	SOL Study #9
10% MVC	0.11	0.02	0.02
15% MVC	0.08	0.04	0.01
20% MVC	0.10	0.05	0.01
25% MVC	0.08	0.08	0.04
30% MVC	0.10	0.08	0.10

In all muscle activation levels, the contribution of the anti-symmetric component was less than about 10% of the corresponding symmetric component.

3.6.5 Anisotropy of Dynamic Ankle Impedance in Active Muscles

The directional variation of dynamic ankle impedance was identified in active muscles based on the same method used in the relaxed study. Average results of all subjects are shown in Figure 3.29 and Figure 3.30 for the TA study and SOL study, respectively.

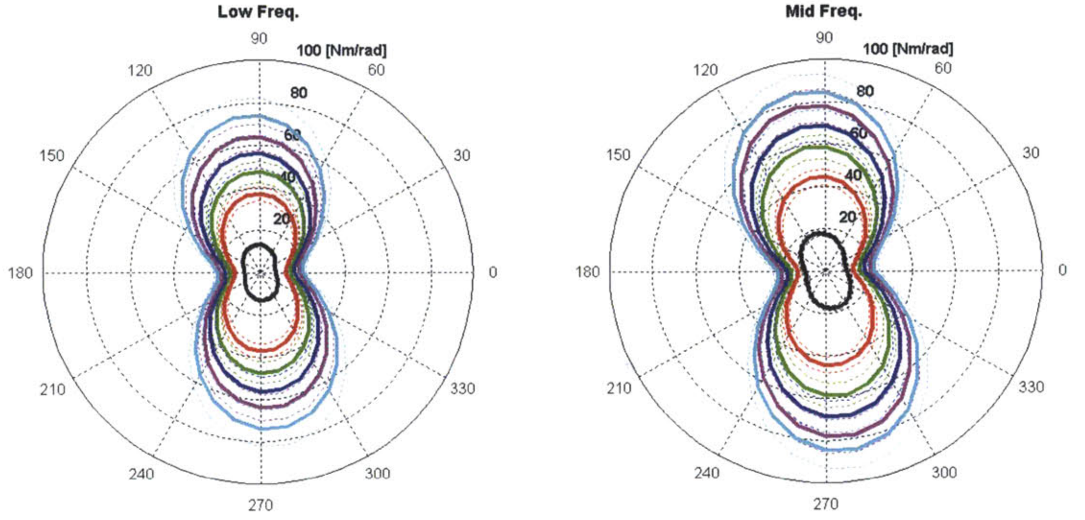

Figure 3.29: Anisotropy of dynamic ankle impedance in the TA active study. Left: low-frequency impedance, right: mid-frequency impedance. Thick and thin lines represent the mean and mean±1 SE of all subjects, respectively. The same color codes as in Figure 3.28.

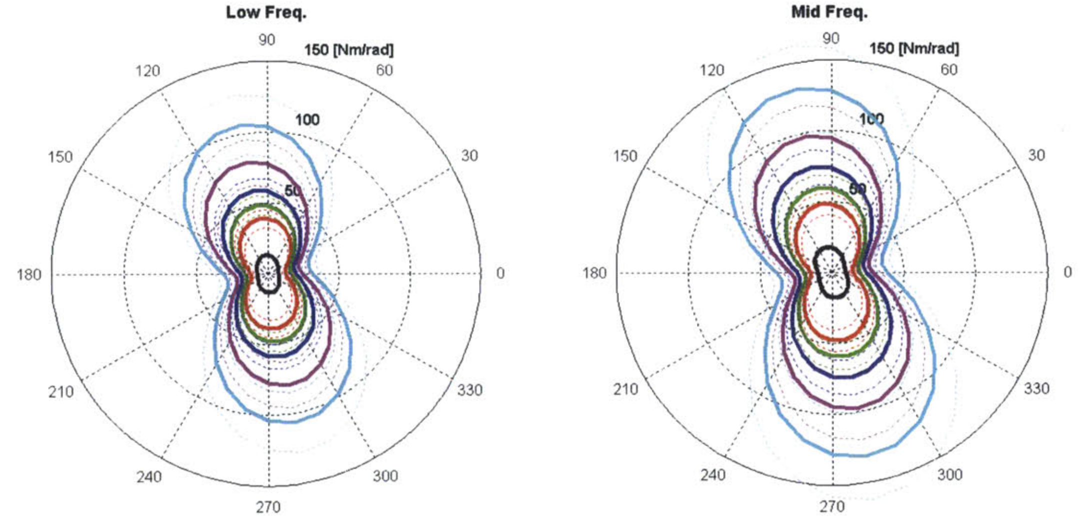

Figure 3.30: Anisotropy of dynamic ankle impedance in the SOL active study. The same format as in Figure 3.28.

Activating muscles significantly increased ankle impedance in all directions in the IE–DP space, but it increased more in the sagittal plane (DP direction) than in the frontal plane (IE direction), accentuating the "peanut" shape, pinched in the IE direction. The ratio of active impedance to maximally-relaxed (passive) impedance was calculated for each movement direction, and results in the IE direction, DP direction, and the mean of all 36 directions are summarized in Table 3.13. The ratio for the DP direction was substantially higher than the IE direction.

Table 3.13: The ratio of active impedance to relaxed impedance.

Freq. Region		Low-Freq.			Mid-Freq.		
Direction Target Activation Level		IE	DP	All	IE	DP	All
TA Study	10% MVC	1.63 (0.12)	2.81 (0.25)	2.31 (0.20)	1.74 (0.15)	3.35 (0.28)	2.66 (0.22)
	15% MVC	1.96 (0.16)	3.58 (0.39)	2.89 (0.29)	2.21 (0.22)	4.42 (0.42)	3.47 (0.33)
	20% MVC	2.25 (0.20)	4.25 (0.52)	3.40 (0.38)	2.50 (0.23)	5.19 (0.56)	4.04 (0.42)
	25% MVC	2.52 (0.20)	4.82 (0.46)	3.84 (0.35)	2.86 (0.25)	5.88 (0.58)	4.59 (0.44)
	30% MVC	2.76 (0.22)	5.57 (0.64)	4.37 (0.45)	3.11 (0.27)	6.38 (0.64)	4.97 (0.48)
SOL Study	10% MVC	1.69 (0.30)	2.94 (0.46)	2.40 (0.38)	2.06 (0.37)	3.62 (0.57)	2.95 (0.46)
	15% MVC	2.22 (0.53)	3.63 (0.50)	3.01 (0.50)	2.64 (0.59)	4.47 (0.68)	3.68 (0.61)
	20% MVC	2.70 (0.62)	4.38 (0.65)	3.65 (0.62)	3.31 (0.77)	5.53 (0.90)	4.56 (0.81)
	25% MVC	3.36 (0.72)	5.84 (1.20)	4.75 (0.95)	3.93 (0.75)	7.16 (1.61)	5.75 (1.20)
	30% MVC	4.35 (0.76)	7.82 (1.59)	6.31 (1.21)	5.25 (0.86)	9.68 (2.26)	7.76 (1.64)

The ratio was calculated for each subject separately, and averaged across all subjects. The mean and SE (in parentheses) across all subjects are presented in the table. All direction implies the mean of all 36 directions.

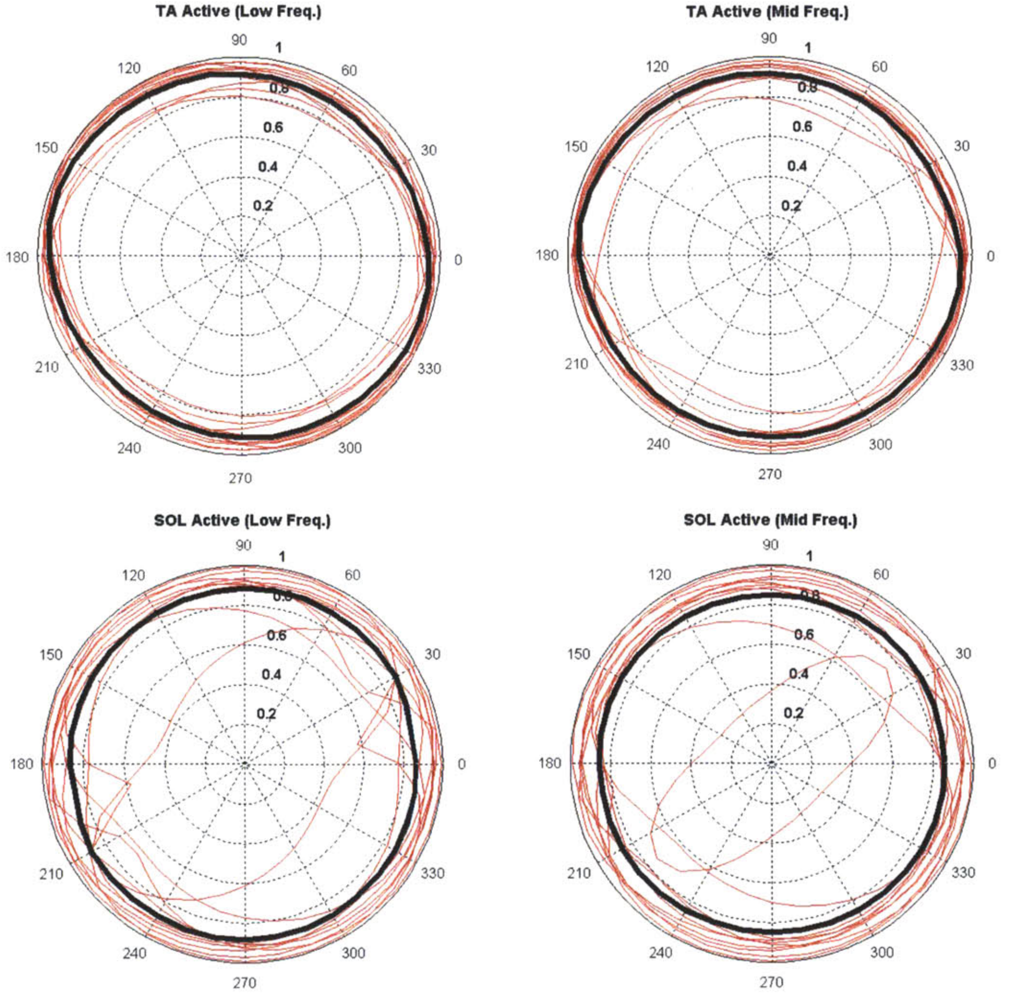

Figure 3.31: Linearity between muscle activation level and ankle impedance in IE−DP space. The correlation coefficient (R^2) for each movement direction was presented in polar coordinates. Each thin red line represents the result of individual subject, and the thick black line represents the mean of all subjects. Top row: TA active study, bottom row: SOL active study, left column: low-frequency impedance, right column: mid-frequency impedance.

The correlation coefficient (R^2) between the level of muscle activation and the magnitude of ankle impedance for each of 36 movement directions was calculated for each subject and presented in Figure 3.31. In average across all subjects, R^2 value for the TA study was very high (>0.90) for all directions. For the SOL study, the averaged R^2 value was still high (>0.85), although two subjects (#6 and #9) showed an outlier behavior.

Both in the TA active and SOL active studies, major and minor principal axes were slightly tilted in the CCW direction from the original joint coordinates in all muscle activation conditions (Table 3.14).

Table 3.14: Direction of major and minor axes of dynamic ankle impedance and the corresponding impedance magnitude in the TA active and SOL active studies.

Study Type	Target Activation Level	Direction of Principal Axis		Impedance in the Major Principal Axis Direction		Impedance in the Minor Principal Axis Direction	
		Low-Freq.	Mid-Freq.	Low-Freq.	Mid-Freq.	Low-Freq.	Mid-Freq.
TA Study	10% MVC	0.5 (0.1)	4.0 (0.2)	37.3 (3.4)	44.6 (3.7)	11.8 (0.8)	12.4 (1.0)
	15% MVC	1.0 (0.1)	6.0 (0.2)	47.6 (5.1)	59.1 (5.6)	14.2 (1.2)	15.6 (1.6)
	20% MVC	2.5 (0.1)	6.5 (0.2)	56.5 (6.9)	69.3 (7.6)	16.3 (1.5)	17.7 (1.8)
	25% MVC	4.0 (0.2)	6.5 (0.2)	64.1 (6.2)	78.7 (7.9)	18.1 (1.4)	20.1 (1.8)
	30% MVC	4.0 (0.2)	6.5 (0.2)	74.2 (8.6)	85.3 (8.6)	19.8 (1.6)	21.9 (1.9)
SOL Study	10% MVC	6.0 (0.2)	7.0 (0.4)	39.6 (6.3)	49.0 (7.7)	11.7 (2.0)	14.0 (2.2)
	15% MVC	8.5 (0.3)	11.0 (0.3)	49.9 (7.1)	61.1 (9.5)	14.3 (2.6)	17.4 (3.1)
	20% MVC	10.0 (0.3)	11.0 (0.3)	60.1 (9.1)	76.5 (12.9)	17.6 (3.4)	21.0 (3.7)
	25% MVC	14.0 (0.2)	12.5 (0.2)	80.6 (16.2)	98.4 (21.8)	21.3 (4.1)	25.2 (4.4)
	30% MVC	12.0 (0.3)	13.0 (0.3)	107.4 (21.3)	132.8 (30.5)	28.1 (4.9)	33.9 (5.4)

The direction of major and minor axis and minor axis are defined from the axis for the direction of IE and DP, respectively, in the CCW direction (Unit of direction: °, unit of magnitude: Nm/rad). The mean and SE (value in parentheses) over all subjects are presented.

Directions of principal axes were more tilted in the CCW direction in the SOL study than in the TA study. The variability across subjects was very small (SE less than 0.4°) in all muscle activation conditions. As expected from Figure 3.29 and Figure 3.30, the magnitude of impedance in the major axis direction was substantially larger than in the minor axis direction, more than 3 times in average across all subjects.

3.6.6 Ellipse Representation and Impedance Matrix in Active Muscles

Ellipse representations of dynamic ankle impedance in the TA active and SOL active studies were shown in Figure 3.32 and Figure 3.33.

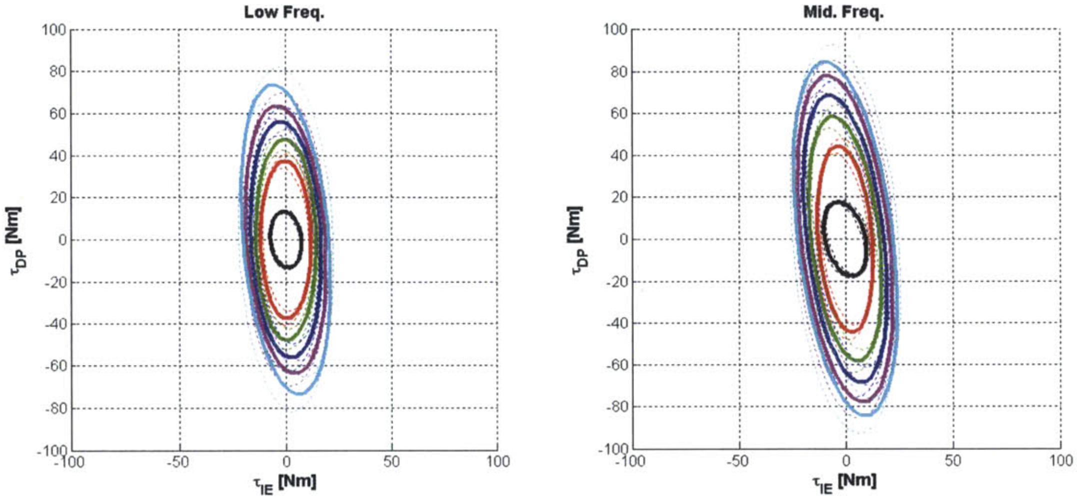

Figure 3.32: Ellipse representation of dynamic ankle impedance in the TA study. The same format as in Figure 3.28.

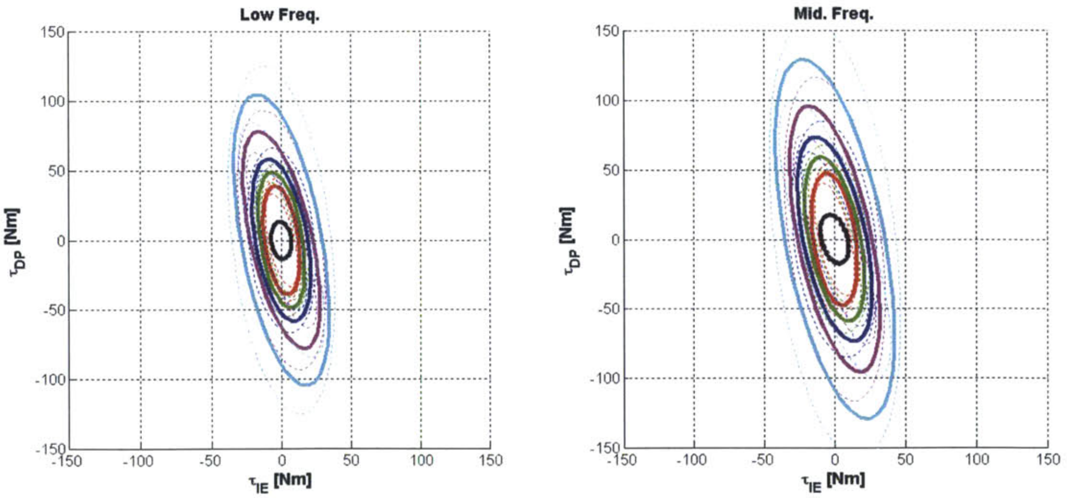

Figure 3.33: Ellipse representation of dynamic ankle impedance in the SOL study. The same format as in Figure 3.28.

Impedance matrix was calculated for each study and for each subject separately, and the mean ± 1 SE of all subjects is presented in Table 3.15:

Table 3.15: Impedance matrix for ankle impedance in active studies.

Freq. Region		Low-Freq.			Mid-Freq.		
Target Activation Level / Impedance Element		Z_{11}	Z_{22}	Z_{12} (or Z_{21})	Z_{11}	Z_{22}	Z_{12} (or Z_{21})
TA Study	10% MVC	11.9 (0.9)	37.2 (3.3)	-0.35 (0.7)	12.8 (1.1)	44.3 (3.6)	-2.4 (1.0)
	15% MVC	14.3 (1.2)	47.5 (5.1)	-0.41 (0.4)	16.4 (1.6)	58.3 (5.6)	-4.5 (1.4)
	20% MVC	16.6 (1.5)	56.2 (6.9)	-1.83 (1.0)	18.7 (1.9)	68.3 (7.3)	-5.8 (1.8)
	25% MVC	18.6 (1.5)	63.6 (6.1)	-3.24 (1.5)	21.3 (2.0)	77.6 (7.7)	-6.7 (2.0)
	30% MVC	20.7 (1.8)	73.4 (8.3)	-4.7 (2.2)	23.1 (2.1)	84.1 (8.4)	-7.3 (2.2)
SOL Study	10% MVC	12.5 (2.3)	38.8 (6.0)	-3.5 (1.4)	15.5 (2.9)	47.5 (7.5)	-4.2 (2.1)
	15% MVC	16.0 (3.5)	48.2 (6.6)	-5.1 (2.1)	19.7 (4.2)	58.8 (8.9)	-7.7 (2.3)
	20% MVC	19.9 (4.5)	57.9 (8.5)	-6.8 (2.5)	24.4 (5.4)	73.1 (11.9)	-10.2 (3.7)
	25% MVC	24.9 (4.9)	77.0 (15.9)	-12.6 (2.4)	28.8 (5.4)	94.8 (21.3)	-14.0 (3.4)
	30% MVC	31.4 (5.4)	104.0 (21.1)	-13.5 (3.2)	38.5 (6.0)	128.1 (30.1)	-17.8 (4.6)

2-by-2 impedance matrix is represented as $Z = [Z_{11}\ Z_{12};\ Z_{21}\ Z_{22}]$ and each element is presented in the table.

Average results of three parameters defining the orientation (Φ), shape (Z_{22}'/Z_{11}'), and size of the impedance ellipse ($|Z|$) are also presented in Table 3.16.

Table 3.16: Orientation, shape, and size of the impedance ellipse in active studies.

Freq. Region		Low-Freq.			Mid-Freq.		
Target Activation Level \ Impedance Element		Orientation (Φ)	Shape (Z_{22}'/Z_{11}')	Size ($\lvert Z\rvert$)	Orientation (Φ)	Shape (Z_{22}'/Z_{11}')	Size ($\lvert Z\rvert$)
TA Study	10% MVC	0.5 (0.1)	3.2 (0.1)	458.9 (65.6)	4.0 (0.2)	3.7 (0.2)	575.8 (80.9)
	15% MVC	1.0 (0.1)	3.3 (0.2)	718.1 (125.2)	6.0 (0.2)	3.9 (0.2)	981.1 (166.1)
	20% MVC	2.5 (0.1)	3.4 (0.2)	994.2 (198.4)	6.5 (0.2)	4.0 (0.3)	1312.9 (228.9)
	25% MVC	4.0 (0.2)	3.5 (0.2)	1223.2 (201.3)	6.5 (0.2)	4.0 (0.3)	1668.4 (284.9)
	30% MVC	4.0 (0.2)	3.7 (0.3)	1551.2(304.8)	6.5 (0.2)	3.9 (0.3)	1963.2 (358.5)
SOL Study	10% MVC	6.0 (0.2)	3.6 (0.4)	537.1 (165.0)	7.0 (0.4)	3.7 (0.5)	774.4 (215.3)
	15% MVC	8.5 (0.3)	3.8 (0.4)	839.8 (272.4)	11.0 (0.3)	3.7 (0.4)	1234.9 (382.1)
	20% MVC	10.0 (0.3)	3.9 (0.6)	1277.0 (443.8)	11.0 (0.3)	3.8 (0.5)	1925.0 (638.3)
	25% MVC	14.0 (0.2)	4.1 (0.6)	2173.2 (902.1)	12.5 (0.2)	4.0 (0.5)	3080.8 (1159.4)
	30% MVC	12.0 (0.3)	4.1 (0.6)	3716.3 (1466.7)	13.0 (0.3)	3.9 (0.5)	5567.1 (2144.0)

The mean and SE (value in parentheses) over all subjects are presented. Unit of orientation: °, unit of size: [Nm/rad]^2.

In addition, to investigate the variability of three parameters across subjects, the CV was calculated for each parameter and summarized in Table 3.17. In general, the CV of shape was less than the CV of orientation or size. As mentioned in section 3.5.8, care is needed for this interpretation, because orientation can be very sensitive to numerical error.

Table 3.17: Coefficient of variation of parameters for impedance ellipse in active studies.

Freq. Region		Low-Freq.			Mid-Freq.		
Target Activation Level \ Impedance Element		Orientation (Φ)	Shape (Z_{22}'/Z_{11}')	Size ($\lvert Z\rvert$)	Orientation (Φ)	Shape (Z_{22}'/Z_{11}')	Size ($\lvert Z\rvert$)
TA Study	10% MVC	7.4	0.1	0.4	1.1	0.2	0.4
	15% MVC	3.2	0.1	0.5	0.9	0.2	0.5
	20% MVC	1.7	0.2	0.6	0.7	0.2	0.5
	25% MVC	1.3	0.1	0.5	0.7	0.2	0.5
	30% MVC	1.3	0.2	0.6	0.7	0.2	0.5
SOL Study	10% MVC	1.2	0.3	0.9	1.7	0.4	0.8
	15% MVC	1.0	0.3	1.0	0.8	0.3	0.9
	20% MVC	0.9	0.4	1.0	0.8	0.4	1.0
	25% MVC	0.5	0.5	1.2	0.6	0.4	1.1
	30% MVC	0.7	0.4	1.2	0.6	0.4	1.2

3.6.7 Discussion

Measurements using the Anklebot with LTI MIMO stochastic system identification methods enabled reliable characterization of steady-state dynamic behavior of the ankle in 2 DOFs simultaneously under active muscles.

Results of partial coherence analysis verified that mild random perturbations used in this study were powerful enough to reliably estimate ankle impedance in 2 DOFs (Figure 3.23 and 3.24). Partial coherences of diagonal terms were very high over the wide frequency range up to 50 Hz, even at the high muscle activation level of 30% MVC. Coherence drops were observed at the low frequency region below 1~2 Hz in both TA active and SOL active studies. Coherence drops may be due to insufficient input power, measurement noise, contribution of unmeasured inputs, and/or nonlinear input-output relationship. In this study, the most likely cause was the increased nonlinearity due to coupling to the human subject. Especially, the higher the muscle activation, the lower the partial coherence in this region. Partial coherences below 1 Hz were lower than 0.8. Hence measurements below 1 Hz were not considered in calculating the magnitude of low-frequency impedance. Partial coherences of off-diagonal terms were still very low (<0.2) in most frequency regions, except the region about 5~15 Hz. In this region, coherences were higher than those in the relax study, and increased with muscle activation, which implied non-negligible coupling between 2 DOFs. However, the highest coherence value was still low (~0.4).

A closed-loop control with a high proportional gain for the actuator (2000 N/m) constrained the ankle in a small ROM: less than 0.9° and 0.7° for the IE direction and less than 4.0° and 4.7° for the DP direction in the TA active and SOL active studies, respectively, when averaged across all subjects (Figure 3.22). This minimized position dependence of ankle dynamics, and enabled a clear investigation of the relation between muscle activation and ankle impedance.

All subjects could successfully activate TA or SOL around 5 different target activation levels, from 10% to 30% MVC levels in increments of 5% MVC. The linearity of measured activation levels was very high, close to R^2 value 1, and even the lowest R^2 value was 0.9 (Table 3.7). Total ankle muscle activity was also estimated, since activation of other ankle muscles besides the target muscle (TA or SOL) can contribute ankle joint impedance. Rough estimates of total muscle activity, calculated by summing normalized EMG amplitudes of 4 measured muscles, also showed a highly linear trend (Figure 3.21).

High partial coherences, constrained ankle positions in all muscle activation levels, and the high linearity of muscle activation validate the suggested experimental setup and protocol to investigate the effect of muscle activation on ankle impedance.

Magnitude and phase responses of IE and DP impedance under active muscles, either dorsiflexors or plantarflexors, were close to those of a 2nd order system with stiffness, damping, and inertia components (Figure 3.25 and 3.26). Responses over the break frequency were relatively invariant in all measurement conditions, consistent with the same inertia of the foot and ankle complex across measurements.

Responses around the break frequency were explained by the damping of ankle. In general, phase transitions in the DP direction were smoother than the IE direction, suggesting more damped behavior of the ankle in the sagittal plane than in the frontal plane. In addition, damped behavior became more salient when muscles were more active. From this result, it is anticipated that increased viscosity of the ankle with muscle activation will make an essential contribution to shock-absorption during lower-extremity functions to maintain the stability in the aspect of energy dissipation.

In the frequency region below the break frequency, the magnitude of impedance was relatively constant, although slight deviation from the zero slope were observed. The magnitude of impedance in the mid-frequency was about 10~25% higher than in the low-frequency (Table 3.10). This is significantly smaller than the increase ratio observed in the relaxed muscles, which was about 30~40% increase. Further study seems warranted to investigate the biomechanical origin of this transient behavior.

Magnitude of impedance increased with muscle activation. Especially, all subjects except one (subject #6 in the SOL active study) showed a very highly linear relationship between the level of muscle activation and the magnitude of impedance in both IE and DP directions in the TA active and SOL active studies (Figure 3.27). While linear trends were observed in both directions, impedance increased more in the DP than IE direction with increased muscle activation, which is expected due to the fact that most ankle muscles (12 out of 13) contribute to DP, while only 5 out of 13 muscles contribute to IE. In addition, impedance increased more in the SOL study than in the TA study (Table 3.9). As a result, for the same target muscle activation level, impedance in the SOL study was greater than in the TA study, and the discrepancy increased with the increasing muscle activation (Table 3.10). This is because most subjects accompanied activation of GAS and PL due to muscle synergy in the SOL active study, and the total muscle activation in the SOL study was substantially greater than in the TA study.

In general, joint stiffness is determined by muscle generated stiffness and kinematic stiffness due to nonlinear musculo-tendon kinematics. Detailed descriptions are provided in

Appendix H. In this study, ankle positions under the given experimental conditions were tightly constrained and the variation of muscle moment arms was expected to be very small, while derivatives of muscle moment arms, which determine the kinematic stiffness, need not be. Even with this confounding factor, ankle impedance could be accurately predicted solely from activation of ankle muscles. This expectation was well verified by the highly linear relationship between muscle activation and ankle impedance in all movement directions in the IE–DP space (Figure 3.31).

Interestingly, subject #6 exhibited no impedance increase at activation levels higher than 20% MVC, contrary to the clear linear increasing trend observed between 10% and 20% MVC. To investigate this experimental observation, muscle activation levels and impedance magnitudes at 25% and 30% MVC were compared with values at 20% MVC (Table 3.18).

Table 3.18: Impedance may not increase with muscle activation.

	Impedance Magnitude				**Muscle Activation**	
Freq. Region	Low-Freq.		Mid-Freq.		Target Muscle (SOL)	Total Muscle
Direction / Target Level	IE	DP	IE	DP		
25% MVC	1.02	0.95	0.85	0.82	1.18	1.06
30% MVC	0.96	0.94	0.85	0.82	1.41	1.14

The ratio of the impedance magnitude and muscle activation level in reference to the corresponding value at 20 %MVC was calculated.

Muscle activation showed a linearly increasing trend for SOL as well as for the sum of normalized EMG amplitudes of all 4 measured muscles. However, impedances at 25% and 30% MVC were comparable each other and lower than those at 20% MVC, except the low-frequency IE impedance. Lower impedance at higher muscle activation is due to the contribution of negative kinematic stiffness as explained in Appendix H. However, we might expect even lower impedances at 30% MVC than 25% MVC, because the effect of negative kinematic stiffness can become more noticeable with increased muscle activation.

In fact, mean ankle positions in two measurements were almost same (difference between two measurements was less than 0.2° and 0.6° for IE and DP directions, respectively), and moment arms and their derivatives were expected to be almost same, accordingly. Under this condition, we should expect more contribution of negative kinematic stiffness with increased muscle activation, but it was not. So what might account for the experimental observation?

One plausible explanation is the positive contribution of unmonitored muscles. As mentioned in section 2.7.7, only 4 superficial muscles were monitored but 8 out of 13 ankle muscles are deep and were not monitored, which might have contributed positively or negatively to ankle impedance. If they contributed positively, this would compensate the increased contribution of negative kinematic stiffness at higher activation level, resulting in the experimental observation that ankle impedance at 30% MVC was comparable to that at 25% MVC.

In general, ankle impedance substantially increased with muscle activation in all directions in the 2D-space consisting of sagittal and frontal planes, but highly direction dependent as observed in the relaxed study (Figure 3.29 and 3.30). Actually, more impedance increase in the DP direction than the IE direction resulted in an accentuated "peanut shape" both in the TA active and SOL active studies (Table 3.13). Although IE impedance in active muscles was relatively weak compared to DP impedance, activation of ankle muscles could effectively increase IE impedance a few times higher than the passive impedance. Thus for healthy subjects, activation of ankle muscles can be a good strategy to help lateral stability in lower-extremity functions. However, this strategy may not be possible for neurologically impaired patients, if they are unable to modulate ankle muscles, either voluntarily or reflexively.

Ellipse representation of ankle impedance and impedance matrix were also provided for their prevalent use in the field of biomechanics and neuro-motorcontrol. The major and minor principal axes of the impedance ellipse were slightly tilted in the CCW direction to the joint coordinates (IE and DP directions). The tilt angle was less when TA was active than SOL active, which may be due to the contribution of TA (main inverter) in the frontal plane. The direction of principal axis changed depending on muscle activation levels, although the variability was small (Table 3.13). Different nominal ankle positions with different muscle activations may partly explain this observation. In addition, directions of principal axis were not exactly matched for low- and mid-frequency regions. To better understand whether this is a true property of human ankle or variations due to numerical calculations, further study is required to investigate the direction of principal axis as a function of frequency. The ratio of impedance magnitude between directions of principal major and minor axes was relatively constant across different muscle activation levels (Table 3.16). As a result, the shape of impedance ellipse was much less variable than the size.

Most subjects satisfied the passivity condition under substantial activation of ankle muscles. In addition, even subjects not satisfying the passivity condition exhibited mild non-passive dynamic behavior of the ankle (less than about 10% of passive behavior). This finding was comparable with curl analysis results of static ankle impedance with active muscles (Table 2.5).

Chapter 4

Multi-Variable Transient Dynamic Ankle Mechanical Impedance

4.1 Summary

Steady-state static and dynamic ankle mechanical impedance were quantified in Chapter 2 and 3, respectively. This chapter presents the characterization of transient or time-varying dynamic ankle mechanical impedance during human walking.

Multiple realizations of stride data were successfully obtained from 13 minutes of walking with the Anklebot and foot-switches. Since the robot is highly backdrivable and most of its inertia is concentrated on the knee, young healthy subjects could walk with the robot without discomfort or muscle fatigue.

The negligible effect of mild random perturbations on muscle activity during walking, the low variability of stride, stance, and swing durations, and no significant effect of time-scaling of realizations all together supported the use of the ensemble-based approach to identify transient ankle impedance.

Two ensemble sets, the stance and the swing, were constructed after normalizing all realizations to the length of the mean stance or the swing duration and removing outliers

based on spatial, temporal, and neurophysiological criteria. Time series of random torque perturbations were used for inputs of ensemble sets, and the corresponding angular displacements at the ankle were used for outputs, after compensating the effect of actuator dynamics.

Impulse response functions were accurately estimated with the correlation-based system identification method, from pre-swing phase through swing phase to early-stance phase before the toe-down. This interval corresponds to the period when either heel or toe or both heel and toe are off the ground. Estimated impulse response functions were reliably approximated with a 2^{nd} order model consisting of inertia, damping, and stiffness for both degrees-of-freedom.

Several noticeable time-varying behaviors of ankle impedance were found. Damping and stiffness significantly decreased at the end of stance phase before toe-off, remained rather constant during swing phase and substantially increased around heel-strike. In general, damping and stiffness in the IE direction and damping in the DP direction increased even before heel-strike.

Impedance increase after heel-strike was greater in the IE direction which cannot be solely explained by co-contraction of antagonistic muscles in the frontal plane. A kinematic constraint due to the "lock" of the ankle in the frontal plane after the heel-strike as well as the compression of soft tissue at the ankle joint may well explain the observed ankle behavior.

High impedance after the heel-strike in both the sagittal and frontal planes will help the stability of the lower-limb from the moment of heel-strike to the loading response. It is expected that healthy human subjects can easily maintain the lateral stability when the foot first contacts the ground by landing with the heel not with the toe.

4.2 Introduction

A study of multi-variable static ankle impedance provided quantification of nonlinear torque-angle relationship at the ankle over the normal ROM in 2 DOFs, a combination of IE and DP. In addition, a study of steady-state dynamic ankle impedance enabled characterization of multi-variable ankle impedance over a wide range of frequency.

While investigation of steady-state ankle behavior is a very important first step to characterize ankle impedance, we could better understand its roles in motor control and function, if transient or time-varying behavior of the ankle can be additionally identified. Characterization methods suggested in previous chapters were limited to time-invariant conditions, preventing their application to time-varying situations, such as during human locomotion.

In fact, several different time-varying system identification methods, such as a regressive technique [22, 102], temporal expansion method [103, 104], time-frequency method [105, 106], and ensemble-based method [50-53], have been developed to investigate transient behavior of biological systems. Among them, the ensemble-based identification method outperforms others for the following reasons: it requires no a priori assumption on the structure of the system to identify, can capture very fast time-varying behavior of the system, and is robust to noisy measurements.

A few previous studies have investigated time-varying behavior of the human ankle in simulations [50, 51] or imposed movement environments [52, 53]. However, to the best of our knowledge, there is only one study which experimentally identified ankle mechanical impedance during walking [54]. That study utilized a robotic platform applying an angular perturbation to the ankle during stance phase. Ankle impedance, approximated as a 2^{nd} order model with inertia, damping, and stiffness, was reliably estimated at four timing points between 13% and 63% of the stance phase, showing that stiffness and damping values increased throughout this period. Although we acknowledge the importance of impedance identification during the mid-stance phase, we may better understand human locomotion if we can measure ankle impedance in other sub-phases of the gait cycle, especially at heel-strike (HS) and toe-off (TO) which are important reference points for the transition from the swing to the stance phase or vice versa.

In this chapter, time-varying ankle impedance was studied during human walking on a treadmill, focusing on swing phase and initial and final stages of stance phase. As with previous steady-state studies, I aimed at identification of time-varying ankle mechanical impedance in 2 DOFs simultaneously, both in the sagittal and frontal planes. The Anklebot and a modified ensemble-based linear time-varying system identification method were used for this purpose.

In the following sections, an experimental procedure, a modified linear time-varying (LTV) ensemble-based system identification, and subsequent analysis methods are explained. Characterization results on young healthy subjects under normal walking on a treadmill follow.

4.3 Experiments

4.3.1 Experimental Setup

The Anklebot was used as the centerpiece to measure multi-variable ankle impedance during walking. The total mass of the robot is about 3.6 kg, but most of that mass is concentrated at the knee, not the ankle or shank. This design is intended to minimize the effect of the device on normal human walking, and one recent work verified this [107].

Subjects wore the brace and custom designed shoe, and the robot was attached in the same way as described in steady-state studies (Chapter 2.3). A shoulder strap, running up around the shoulder and neck, was additionally connected to the knee brace to prevent slippage of the Anklebot and the knee brace.

Two footswitches (Delsys Inc.) were used to detect the moment of HS and TO, from which the stance and the swing phase of the gait were defined. One sensor was attached to the heel and the other to the big toe. The same EMG setup and analysis method were used to estimate the amplitude of muscle activation during walking.

The torque exerted by the Anklebot, the resulting kinematics of the ankle in 2 DOFs were recorded at 500 Hz in one computer, and footswitch and EMG data were sampled at 1 kHz in another computer. To synchronize data from 2 different computers, a single triggering step signal (0 to 5 V) was recorded by both computers before running the walking experiment. The whole experimental setup is shown in Figure 4.1.

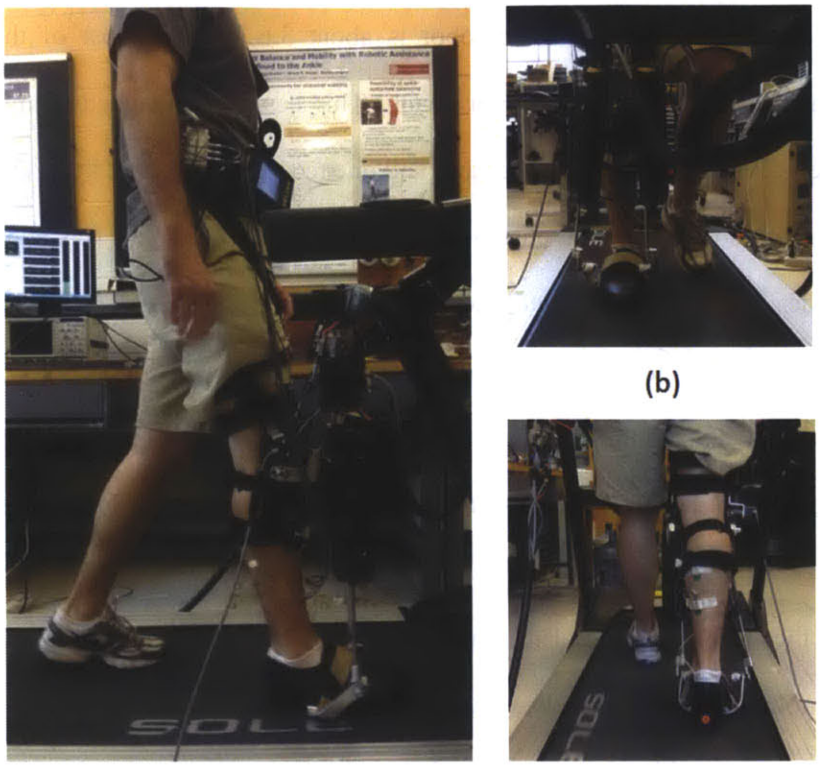

(a) (b) (c)

Figure 4.1: Experimental setup for walking on a treadmill. (a): side view, (b): front view, (c): rear view.

4.3.2 Experimental Protocol

First, MVC level of each muscle was measured in the standing posture in the same way as described in the static study (section 2.7.2).

After the MVC measurement, subjects walked on a treadmill for a few minutes without actuation of the robot to familiarize themselves with the experimental setup. Then they were asked to select a preferred walking speed (PWS) by themselves, which was comfortable enough to maintain for the duration of the experiment with the added mass of the Anklebot and other apparatus. Next, subjects were instructed to walk comfortably on the treadmill with their selected PWS. After one minute of walking, mild random torque perturbations were applied to the ankle for 13 minutes for data collection.

Two uncorrelated mild random perturbations (band-limited white Gaussian noise with stop frequency 100 Hz) were applied to each actuator to produce random torque perturbations at the ankle joint in 2 DOFs. To prevent excessive deviations from the nominal trajectory of ankle displacement due to perturbations, stiffness of the Anklebot (P-gain) was set as 500 N/m. The ranges of the applied torques (peak-to-peak torques) were ±7.7 Nm and ±5.3 Nm for DP and IE, respectively. This magnitude of perturbations was low enough not to disturb natural walking, but strong enough to perturb the ankle throughout the gait cycle except during the middle and terminal stance phases, when the foot is flat on the ground (about 10~50% of the gait cycle).

4.4 Methods

4.4.1 Linear Time-Varying (LTV) Ensemble-based System Identification

The LTV ensemble-based system identification used in this study was based on the correlation approach presented in [50, 53].

For each sampling time i, the relationship between the noise-free input ($u_r(i)$) and the corresponding noisy output ($z_r(i) = y_r(i) + n_r(i)$, where $y_r(i)$ is the true output and $n_r(i)$ is additive white noise) for the r^{th} realization of the ensemble data, can be represented as a discrete convolution equation (Eq. (4.1)):

$$z_r(i) = \Delta t \sum_{j=0}^{M} \hat{h}(i,j) u_r(i-j) \qquad (4.1)$$

where $\hat{h}(i,j)$ is an impulse response function (IRF) estimate with a finite lag length $L = M+1$ ($\hat{h}(i,j) = 0$ for $j > M$), which is often called finite impulse response. By multiplying both sides of Eq. (4.1) with $u_r(i-k)$ and summing over all realizations and dividing them with the number of realizations (R), we get the Wiener-Hopf equations (Eq. (4.2)):

$$\frac{1}{R}\sum_{r=1}^{R} z_r(i)u_r(i-k) = \Delta t\sum_{j=0}^{M}\hat{h}(i,j)\frac{1}{R}\sum_{r=1}^{R}u_r(i-j)u_r(i-k) \tag{4.2}$$

In fact, Eq. (4.2) can be written simply as (Eq. (4.3)) with an input-output cross-correlation function estimate ($\hat{\phi}_{zu}$) and an input auto-correlation function estimate ($\hat{\phi}_{uu}$):

$$\hat{\phi}_{zu}(i,-k) = \Delta t\sum_{j=0}^{M}\hat{h}(i,j)\hat{\phi}_{uu}(i-k,k-j) \tag{4.3}$$

We can get a matrix equation (Eq. (4.4)) by changing the lag index k from 0 to M, where $\hat{\mathbf{\Phi}}_{uu}(i)$ is a $L \times L$ matrix and $\hat{\mathbf{\Phi}}_{zu}(i)$ and $\hat{\mathbf{h}}(i)$ are $L \times 1$ vectors:

$$\hat{\mathbf{\Phi}}_{zu}(i) = \Delta t\hat{\mathbf{\Phi}}_{uu}(i)\hat{\mathbf{h}}(i) \tag{4.4}$$

$$\hat{\mathbf{h}}(i) = \frac{1}{\Delta t}\hat{\mathbf{\Phi}}_{uu}(i)^{-1}\hat{\mathbf{\Phi}}_{zu}(i) \tag{4.5}$$

The IRF estimate ($\hat{\mathbf{h}}(i)$) is obtained from an inverse matrix operation (Eq. (4.5)). In this study, the lag length L was selected long enough for the IRF estimate settle down close to zero.

4.4.2 Solutions for the Limitations of the Original Ensemble-based Method

A fundamental assumption of the ensemble-based method is that every realization experiences the same time-varying behavior. This assumption may hold for simulations or in a limited experimental condition. However, it is not valid in many practical measurements, such as real human locomotion. Even in walking on a treadmill at a fixed speed, stride duration, step length, and joint kinematics may vary significantly on each gait cycle. This violates the fundamental assumption of the ensemble-based method, and we cannot directly apply the method described in the previous section. To address this problem, two solutions were considered: time-scaling (normalization) of each realization and rejection of highly variable realizations.

Two ensemble sets were constructed in this study: one set for stance data and the other for swing data. However, the length of each realization is not the same, preventing direct application of the identification method. As a remedy, all realizations of the stance ensemble set were normalized to the length of mean stance duration, and the swing ensemble set to the length of mean swing duration. The effect of time-scaling (normalization) on the distortion of impedance should be addressed (see the section 4.6).

In addition, highly variable realizations were discarded to construct ensemble data sets. Three criteria were used to reject outliers: temporal, spatial, and neurophysiological criteria. First, deviation of the stance duration from the mean stance duration of all realizations and deviation of the swing duration from the mean swing duration were used as temporal criteria. Second, deviation of the DP angle from the averaged DP angle across one gait cycle of all realizations was selected as a spatial criterion. Third, deviation of the EMG level of TA and triceps surae (TS: SOL and GAS) from the corresponding nominal activation profile was considered as a neurophysiological criterion. For each of criteria, the outermost 5% of all realizations were discarded.

4.4.3 Transient Dynamic Ankle Mechanical Impedance in Joint Coordinates

Diagonal components of the impedance matrix, i.e, IE and DP impedance, were identified based on the modified LTV ensemble-based identification method, which was explained above sections.

One important thing to note is to clearly define input ($u_r(i)$) and output ($z_r(i)$) to be used for the system identification. To identify ankle impedance during walking, we need to find the displacement profile purely due to input torque perturbations. However, the measured displacement ($z_m(i)$) contains two components: one due to the input torque perturbations and the other one simply as a result of walking, which I called a nominal trajectory ($z_o(i)$). The output $z_r(i)$ was obtained by subtracting $z_o(i)$ from $z_m(i)$.

The nominal trajectory was determined by averaging all selected realizations. This approach of calculating $z_n(i)$ is valid, since averaging of considerable number of realizations removes the effect of random perturbations.

The IRF estimate ($\hat{\mathbf{h}}(i)$) was obtained at every 2 *ms*, since the measurement rate in this study was set as 500 Hz. In the calculation of $\hat{\mathbf{h}}(i)$ in Eq. (4.5), $\hat{\mathbf{\Phi}}_{uu}(i)$ satisfied the positive definite condition (tested with MATLAB's *chol* function).

Assuming that human ankle behavior does not change significantly within w, a smoothed IRF ($\hat{\mathbf{h}}_s(i)$) was calculated by averaging the $\hat{\mathbf{h}}(i)$ with a moving window having the size of w (Eq. (4.6)), where N_w is the number of $\hat{\mathbf{h}}(i)$ inside the window between $i - w/2$ and $i + w/2$.

$$\hat{\mathbf{h}}_s(i) = \frac{1}{N_w} \sum_{j=i-w/2}^{j=i+w/2} \hat{\mathbf{h}}(j) \tag{4.6}$$

According to [94], 98% of power in normal human walking is contained below 10 Hz and 99% below 15 Hz. It has been also known that the reflex loop delay is greater than 40 *ms*, which means that feedback cannot contribute impedance changes within this period [48, 49, 108]. Based on these reported values, I set the moving average window size as $w = 40$ *ms*.

In the steady-state dynamic study, responses of ankle impedance in joint coordinates in different muscle activation conditions were close to a 2^{nd} order system. In addition, ankle impedance during stance phase was successfully approximated as a 2^{nd} order system [54]. So the smoothed IRFs ($\hat{\mathbf{h}}_s(i)$) were approximated with inertia ($I(i)$), damping ($B(i)$), and stiffness ($K(i)$) components, and its goodness-of-fit was calculated. The best fit parameters ($I^*(i), B^*(i), K^*(i)$) were estimated by minimizing the mean squared error between IRF of the model ($\mathbf{h}_{\mathrm{mod}}(i)$) constructed by $I(i), B(i), K(i)$ and the smoothed IRF ($\hat{\mathbf{h}}_s(i)$). Here, the optimal parameters $I^*(i), B^*(i), K^*(i)$ include the contribution from the Anklebot dynamics in ankle joint coordinates. As impedance of Anklebot ($I_{Abot}, B_{Abot}, K_{Abot}$) was also accurately approximated as a 2^{nd} order system (Figure 3.7), ankle parameters ($I_{Ankle}, B_{Ankle}, K_{Ankle}$) can be obtained as Eq. (4.7):

$$\begin{aligned} I_{Ankle} &= I^* - I_{Abot} \\ B_{Ankle} &= B^* - B_{Abot} \end{aligned} \tag{4.7}$$

$$K_{Ankle} = K^* - K_{Abot}$$

However in this study, I_{Ankle} was not considered since $I_{Abot} >> I_{Ankle}$ and small errors in I_{Abot} can cause substantial variations of I_{Ankle}.

The reliability of IRF estimation was evaluated by calculating the variance accounted for (VAF) between $z_r(i)$ and $\hat{z}_r(i)$ (the output predicted by the convolution of $\mathbf{h}_{\text{mod}}(i)$ and $u_r(i)$) for each realization (Eq. (4.8)):

$$VAF_{output}(r) = 100 \times (1 - \frac{\text{var}(z_r(i) - \hat{z}_r(i))}{\text{var}(z_r(i))}) \tag{4.8}$$

Absolute output error between $z_r(i)$ and $\hat{z}_r(i)$ was also calculated for each realization (Eq. (4.9)):

$$e_{output}(r) = \frac{1}{N}\sum_{i=1}^{N} | z_r(i) - \hat{z}_r(i) | \tag{4.9}$$

In addition, to assess the goodness of fit of 2nd order model approximation, the VAF between $\mathbf{h}_{\text{mod}}(i)$ and $\hat{\mathbf{h}}_{\mathbf{s}}(i)$ was calculated for each sampling step (Eq. (4.10)):

$$VAF_{IRF}(i) = 100 \times (1 - \frac{\text{var}(\hat{\mathbf{h}}_{\mathbf{s}}(i) - \mathbf{h}_{\text{mod}}(i))}{\text{var}(\hat{\mathbf{h}}_{\mathbf{s}}(i))}) \tag{4.10}$$

4.4.4 Ankle Parameters in Sub-Gait Phases

In this study, mild random perturbations were used not to disturb natural walking, but at the same time, the power of perturbations was not strong enough to properly actuate the ankle during a weight-bearing stance. So ankle parameters were identified throughout the gait cycle except when the foot is flat on the ground. In the stance phase, only early and late stages were considered, which was defined as early stance phase (EST) and pre-swing phase (PSW): EST begins with HS (initial contact) and ends at toe contact, and PSW begins with contralateral HS and ends at TO. The swing phase was evenly divided into 3 periods: initial swing phase (ISW), mid-swing phase (MSW), and terminal swing phase (TSW). The 5 sub-gait phases are illustrated in Figure 4.2.

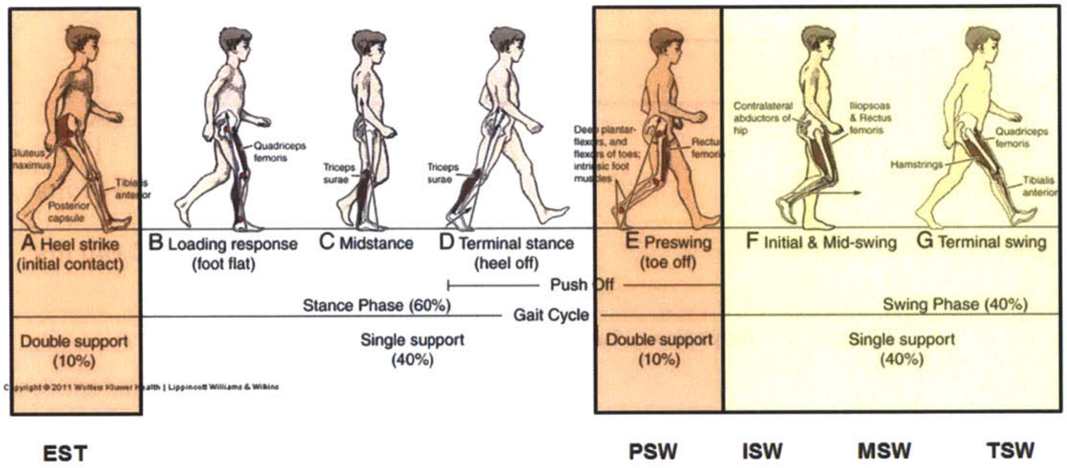

Figure 4.2: The gait cycle and 5 sub-phases for impedance identification. Impedance was identified in EST, PSW, MSW, and TSW, but not in the loading response, mid-stance, and terminal stance. Copyright: Wolters Kluwer Health | Lippincott Williams & Wilkins

Although IRF estimates and ankle parameters were identified at every 40 *ms* from PSW to EST, I also calculated representative parameter values for each sub-gait phase to more clearly see how ankle parameters change across the gait cycle. Identification results within each sub-gait phase were averaged into a single representative value for each parameter.

In addition, parameter changes around HS and TO were closely investigated. Three data sets were compared for each case (Figure 4.3): parameter values at 40 *ms* before and after HS (HS^- and HS^+) were compared with the mean value within a period between the start of TSW and 40 *ms* before HS, and parameter values at 40 *ms* before and after TO (TO^- and TO^+) were compared with the mean value within a period between the start of PSW and 40 *ms* before TO.

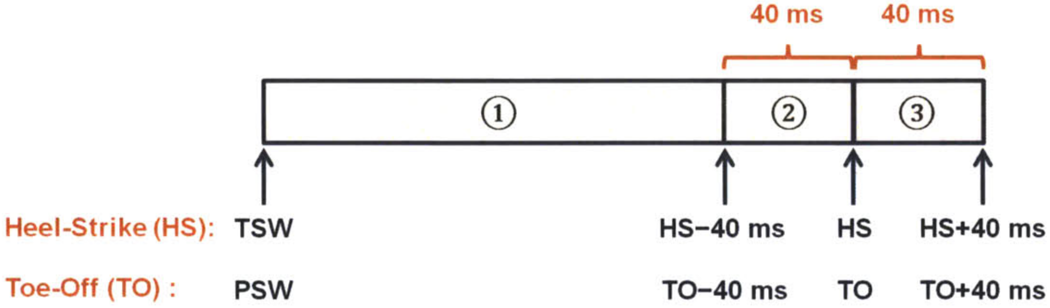

Figure 4.3: Comparison of ankle parameters around HS and TO.

4.5 Effect of Random Perturbations on Muscle Activity

Mild random perturbations were applied to the ankle for 13 minutes during walking on a treadmill. Although the amount of torque was selected as low not to disturb natural human walking, it may affect reflex activity of ankle muscles.

In fact, Stein and Kearney assessed the influence of random perturbations on the reflex torque and EMG, showing that reflex responses decreased with application of the random perturbations under isometric contraction of TA and GAS in a supine posture [109]. However, properties (amplitude and bandwidth) of perturbation and experimental conditions in this paper are not same as I performed.

On the other hand Ritzmann et al. has shown that vibratory motions at the ankle can evoke substantial stretch reflex [110]. Thus, it is important to investigate the effect of random perturbations on muscle activity under the same experimental condition described in section 4.3.

4.5.1 Subjects

Ten young healthy subjects (age 18 to 24; height 1.60 m to 1.90 m; weight 47.7 kg to 81.8 kg) with no reported history of biomechanical or neuromuscular disorders participated. Approval for this study was obtained from COUHES and participants gave written informed consent.

4.5.2 Experimental Protocol

The same experimental setup described in section 4.3.1 was used in this study. After MVC measurements, subjects were asked to walk with their own PWS on a treadmill. After one minute of walking, the same mild random torque perturbations used for impedance identification were applied to the ankle for 10 minutes, but the perturbations were turned on and off every 30 seconds. As a result, 20 segments of walking data were collected, 10 with perturbations and another 10 without perturbations.

4.5.3 Results

EMG amplitudes of all measured muscles were calculated using a root-mean-square filter with a moving window of 200 *ms*, and representative mean values were calculated for each of 20 segments. Two data sets, one set with perturbations and another without perturbations, were compared to investigate how random perturbations changed EMG levels.

Both data sets of individual subject satisfied the normality condition for all muscles ($p>>0.05$) justifying statistical comparison using paired t-tests. Paired t-tests were performed to compare two data sets with and without perturbations. In addition, the increase ratio of EMG amplitudes with perturbations to without perturbations as well as the absolute increase amount of EMG amplitudes (in %MVC) was calculated.

EMG records of a representative subject are shown in Figure 4.4, and analysis results of all subjects are summarized in Table 4.1.

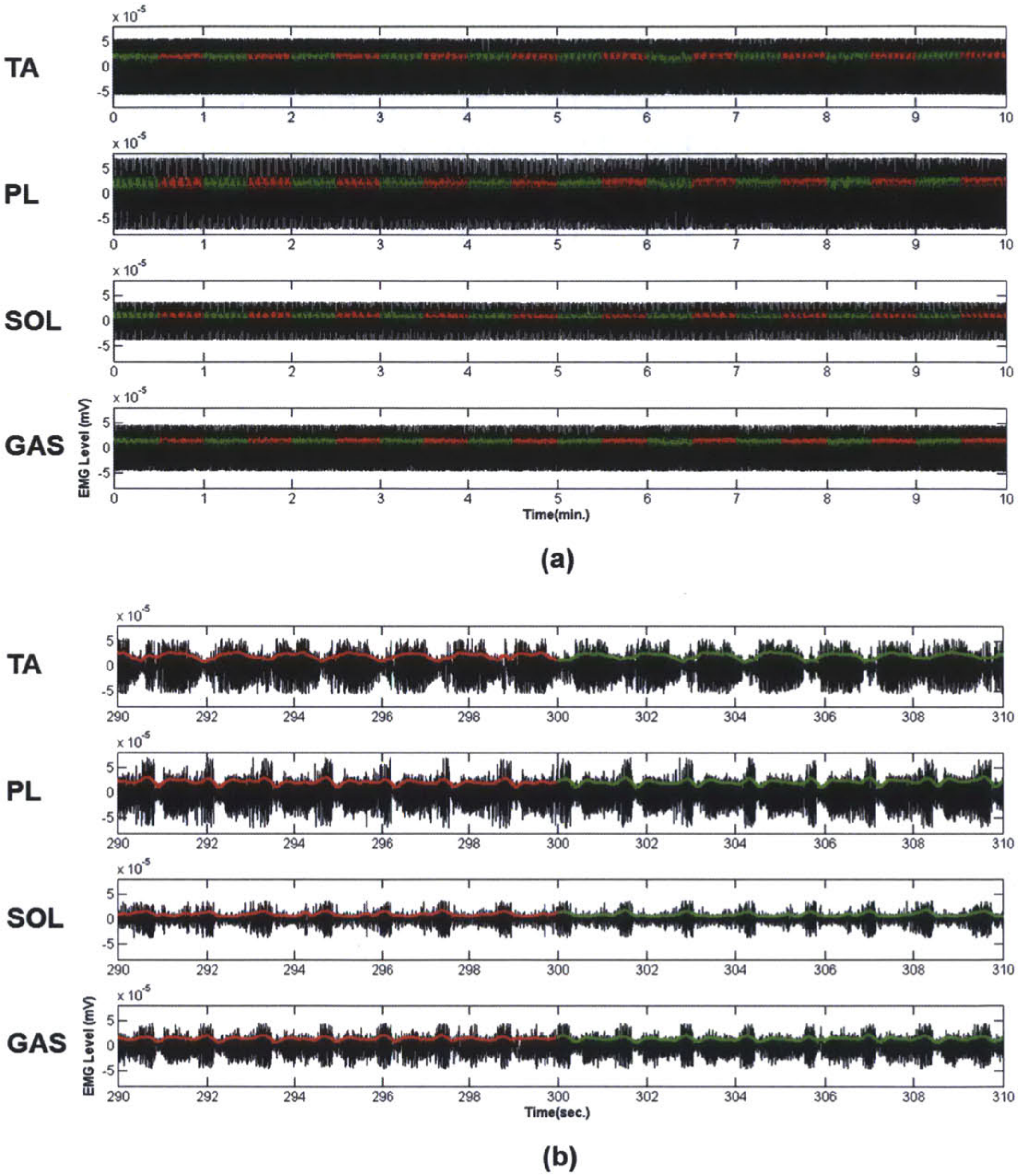

Figure 4.4: EMG records 4 muscles of a representative subject. Black lines denote raw EMG data. Red and green lines represent EMG amplitudes with and without perturbations, respectively. (a): Whole data set (10 minutes), (b): Sampled data set around 5 minutes (20 seconds).

Table 4.1: The increase ratio and increase amount of EMG amplitude with perturbations.

Muscles **Subject**	TA		PL		SOL		GAS	
	Increase Ratio (%)	Increase Amount	Increase Ratio (%)	Increase Amount	Increase Ratio (%)	Increase Amount	Increase Ratio (%)	Increase Amount
1	6.24*	0.50	8.59*	0.36	2.76	0.24	11.41*	0.66
2	2.05	0.28	6.78*	0.87	1.71	0.21	3.57*	0.16
3	0.27	0.02	1.28	0.05	2.72	0.13	0.68	0.06
4	4.23*	0.61	5.17	0.92	4.75	0.45	5.11*	0.28
5	4.63*	0.43	11.84*	0.49	4.98	0.95	7.09	0.74
6	7.51	0.91	-1.55	-0.16	12.07*	1.87	1.02	0.01
7	12.30*	1.12	6.66*	0.90	0.42	0.05	1.74	0.04
8	4.58*	0.28	2.88	0.24	-1.56	-0.09	0.59	0.01
9	2.87	0.35	10.03*	0.68	9.92*	0.64	9.28	0.15
10	2.08	0.18	-1.62	-0.11	-0.83	-0.13	5.41	0.74
Mean	**4.68**	**0.47**	**5.01**	**0.43**	**3.70**	**0.43**	**4.59**	**0.28**
(SE)	**(0.34)**	**(0.03)**	**(0.47)**	**(0.04)**	**(0.44)**	**(0.06)**	**(0.38)**	**(0.03)**

Asterisks (*) denote significant difference from 0 ($p<0.05$). The unit for the increase amount is % MVC.

In general, most subjects showed increased EMG amplitudes in all muscles when random perturbations were applied to the ankle. However, many of them were statistically insignificant, or very small even when significant. In average across all subjects, all 4 muscles showed less than about 5% increase of activations with perturbations, which corresponds to the increase amount less than about 0.5% MVC. In conclusion, the effect of random perturbations on muscle activity during walking experiment for impedance identification is expected to be minimal.

4.6 Effect of Time-Scaling on Impedance Estimation

To investigate the effect of time scaling of realizations (normalization) on impedance estimation and to verify the validity of the normalization process in this study, simple simulations were performed with several 2nd order models having different time-varying parameters $I(i), B(i), K(i)$ (Figure 4.5).

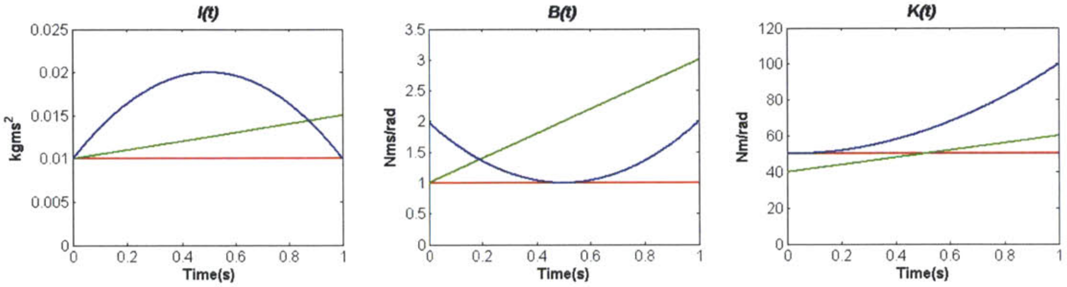

Figure 4.5: Simulations with 3 different 2nd order models. Red: parameters with constant values, green: parameters change linearly, blue: parameters change non-linearly. Plausible ranges were set for each parameter.

For each simulation condition, an ensemble set of 500 realizations ($R = 500$) having different lengths was constructed. Random inputs were generated by using a random number generator (MATLAB's *normrnd* function), so that the distribution of the length (duration) of input realizations had a normal distribution with the mean of 1 second and different SDs. Several different SDs were tested to investigate how the different amount of distortion affects the error in impedance estimation.

Outputs of the ensemble set were constructed by the convolution of generated inputs and time-varying IRFs ($\boldsymbol{h}(t)$) obtained by $I(i), B(i), K(i)$. Thus, each pair of input and output realizations had the same length. The lag length for IRFs was set as 200 *ms*, the same length used in the analysis of experimental data. Next, all realizations of inputs and outputs having different lengths ($L(r)$) were normalized to the mean of all realizations ($\overline{L}_R$), which is 1 second. The mean of distortion ratio due to the normalization was calculated as Eq. (4.11):

$$distortion\ \ ratio = \frac{1}{R}\sum_{r=1}^{R}\left|\frac{L(r)-\overline{L}_R}{\overline{L}_R}\right| \tag{4.11}$$

By applying the same LTV ensemble based system identification method on the normalized ensemble set, new time-varying IRFs ($\boldsymbol{h}_{distort}(i)$) and the corresponding parameters ($I_{distort}(i), B_{distort}(i), K_{distort}(i)$) were obtained.

The estimation error due to time-scaling was evaluated as Eq. (4.12):

$$p_{error}\,(\%) = \frac{1}{N_T}\sum_{i=0}^{T}\left|\frac{p_{distort}(i)-p(i)}{p(i)}\right| \times 100 \tag{4.12}$$

where p can be either I, B or K, and N_T is the number of evaluation points between time 0 and T.

Simulations were repeated 10 times for each model, and the mean and SE of repetitions are shown in Figure 4.6.

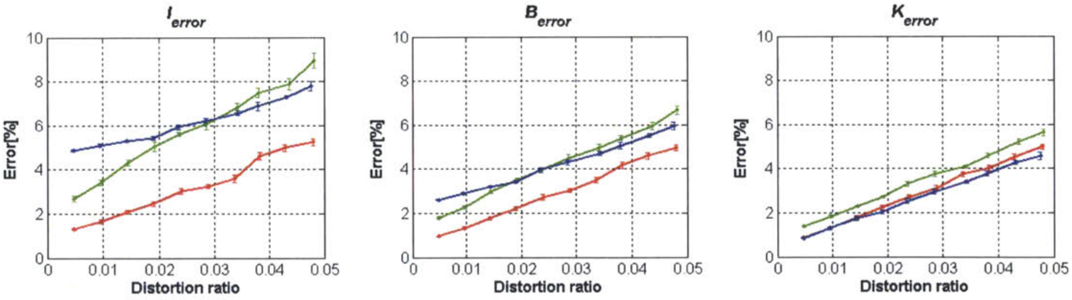

Figure 4.6: Parameter estimation error vs. Distortion ratio. The mean and SE of 10 iterations are presented as points and bars, respectively. The same color codes as in Figure 4.5.

The variability due to different random inputs was negligible. The parameter estimation error increased with the higher level of distortion ratio. Except the condition with constant parameters (red lines in Figure 4.5 and 4.6), the estimation error for K is lower than that for B, and B lower than I. Based on simulation results, less than 6% and 4% errors for B and K are expected from the average distortion ratio of 0.02 and 0.04, respectively.

4.7 Transient Dynamic Ankle Mechanical Impedance in Human Walking

4.7.1 Subjects

Ten young healthy male subjects (age 26 to 34; height 1.71 m to 1.91 m; weight 61.0 kg to 90.0 kg) with no reported history of biomechanical or neuromuscular disorders participated. Approval for this study was obtained from COUHES and participants gave written informed consent.

4.7.2 Ensemble Set Construction

All 10 subjects walked on a treadmill for 14 minutes (1 minute of walking without perturbations and subsequent 13 minute walking with perturbations) successfully with their own PWS. Selected PWS was lower than the normal human walking speed (about 4 km/h), probably due to the added mass of the robot and other apparatus. The ratio of the mean swing duration to the mean stride duration was close to the reported value of normal human walking (about 0.4).

As a first step to construct ensemble sets (a stance ensemble set and a swing ensemble set), stride data were identified by two successive heel-strikes. The moment of TO divided each stride data into a pair of stance and swing data, each of them became one realization for the corresponding ensemble set. The number of realizations generated from 13 minutes of walking was more than 500. Samples of foot-switches (toe and heel sensors), knee and ankle angles in the sagittal plane of a representative subject (subject #1) are shown in Figure 4.7.

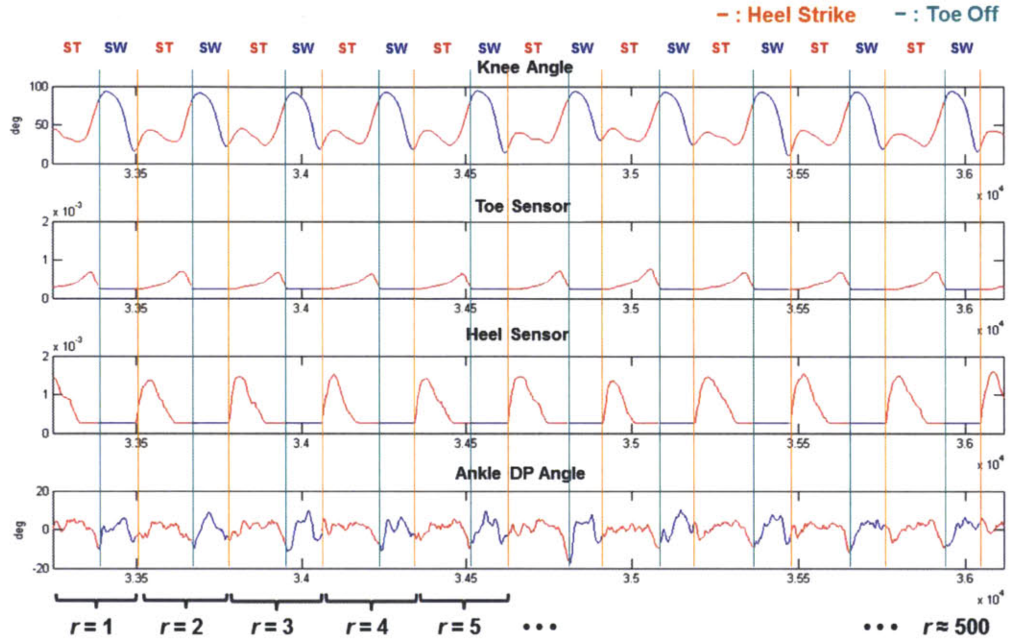

Figure 4.7: Samples of stance and swing data for ensemble set construction. Stance phase (ST) begins with HS and ends at TO, and swing phase (SW) begins with TO and ends at next HS. Orange and green lines define the moment of HS and TO, respectively. X-axis represents number of sample measured at 500 Hz.

Data distributions of the stride duration, stance duration, and swing duration were close to normal. Histograms of all subjects are provided in Appendix I. In addition, the CV of the stride, stance, and swing durations were small, supporting the application of ensemble-based approach.

The mean stance duration ($\overline{L_{ST}}$) and mean swing duration ($\overline{L_{SW}}$) of all realizations were calculated. The stance and swing durations of all realizations were compared with $\overline{L_{ST}}$ and $\overline{L_{SW}}$, and 5% outermost realizations were discarded for each case.

All selected realizations in the stance and swing ensemble sets were then normalized to have the length of $\overline{L_{ST}}$ and $\overline{L_{SW}}$. For each subject, distortion ratios for stance and swing were calculated as Eq. (4.13):

$$distortion\ ratio_{ST} = \frac{1}{R}\sum_{r=1}^{R}\left|\frac{L_{ST}(r)-\overline{L}_{ST}}{\overline{L}_{ST}}\right| \qquad (4.13)$$

$$distortion\ ratio_{SW} = \frac{1}{R}\sum_{r=1}^{R}\left|\frac{L_{SW}(r)-\overline{L}_{SW}}{\overline{L}_{SW}}\right|$$

where $L_{ST}(r)$ and $L_{SW}(r)$ are original length of stance and swing data of realization r, and R is the number of selected realizations.

In average of all subjects, distortion ratios due to time scaling were about 0.024 and 0.041 for the stance and swing ensemble sets, respectively. The distortion ratio for the swing was greater than the stance because $\overline{L}_{SW} < \overline{L}_{ST}$.

Once all realizations of the stance and swing ensemble sets were normalized, outlier realizations were further discarded based on additional 2 selection criteria (spatial and neurophysiological) explained in section 4.4.2. About 16% of all realizations were discarded. The summary of the walking experiment is provided in Table 4.2.

Table 4.2: Summary of the walking experiment.

Subject	Walking Speed (km/h)	Total Stride Number	Rejection Ratio by 3 Criteria	Stride Duration CV	Stance Duration CV	Swing Duration CV	Distortion Ratio (Stance)	Distortion Ratio (Swing)	Swing/ Stride
1	2.9	557	0.15	0.022	0.026	0.043	0.018	0.032	0.40
2	2.9	544	0.16	0.013	0.016	0.033	0.012	0.024	0.38
3	2.6	529	0.16	0.026	0.027	0.057	0.020	0.042	0.36
4	2.6	522	0.14	0.037	0.052	0.072	0.033	0.049	0.37
5	1.9	606	0.15	0.029	0.043	0.061	0.030	0.042	0.40
6	3.2	544	0.15	0.030	0.030	0.063	0.022	0.046	0.42
7	2.4	536	0.16	0.028	0.039	0.049	0.028	0.035	0.41
8	2.4	536	0.16	0.032	0.041	0.065	0.029	0.047	0.35
9	3.2	522	0.17	0.018	0.039	0.070	0.029	0.052	0.40
10	3.2	553	0.16	0.029	0.030	0.054	0.022	0.040	0.41
Mean (SD)	**2.7 (0.4)**	**544.9 (24.5)**	**0.16 (0.01)**	**0.026 (0.007)**	**0.034 (0.010)**	**0.057 (0.012)**	**0.024 (0.007)**	**0.041 (0.009)**	**0.39 (0.02)**

Finally, ensemble sets of input (u_r) and output (z_r) pairs were saved for the system identification. Outputs due to input perturbations (z_r) were obtained by subtracting z_o from z_m. Samples of u_r, z_m, and z_r for both IE and DP directions are shown in Figure 4.8.

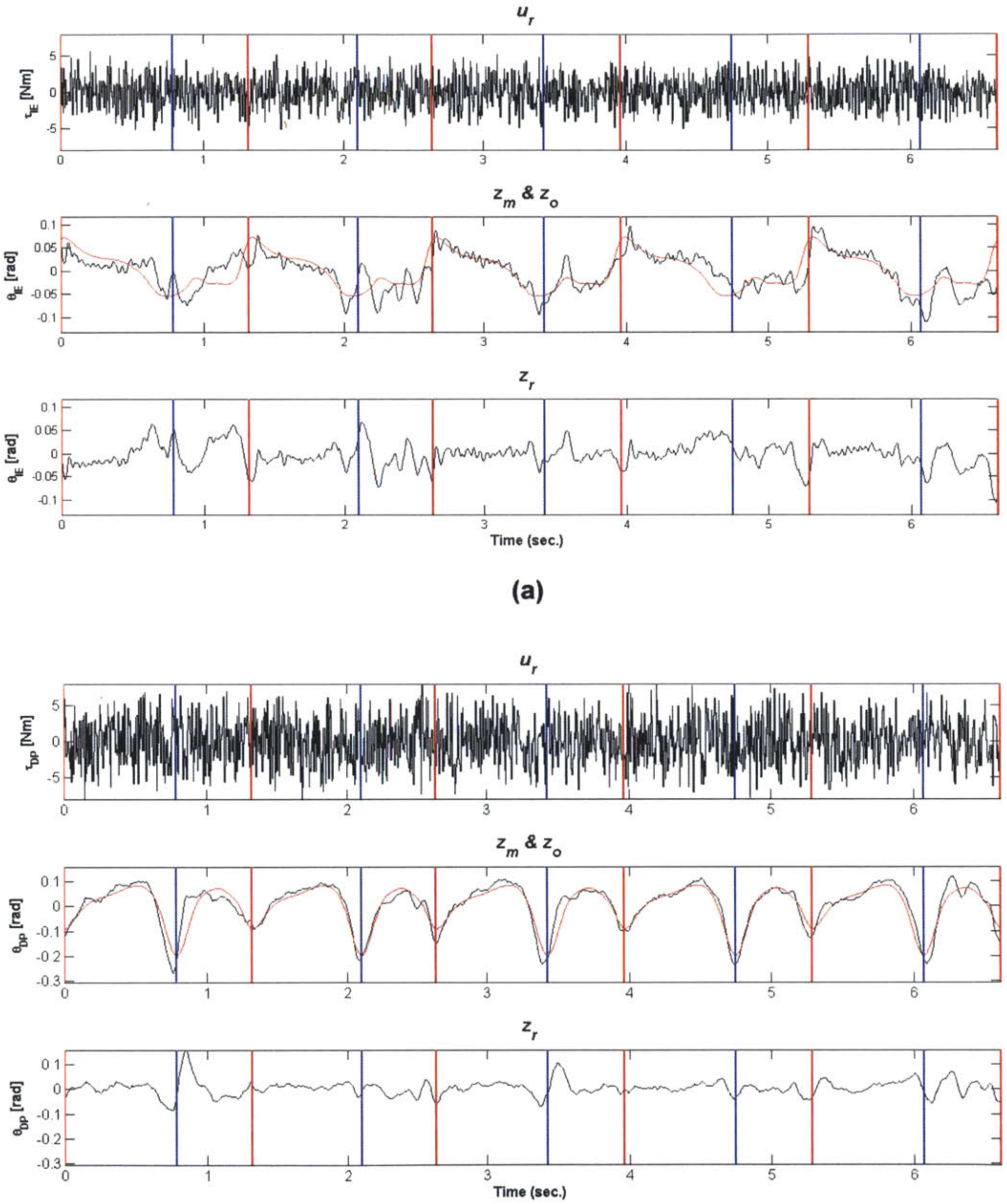

Figure 4.8: Samples of u_r, z_m, and z_r in 2 DOFs. (a): IE direction, (b): DP direction. Red and blue bars represent the timing of HS and TO, respectively.

4.7.3 Ankle Kinematics and EMG Records

Ankle angular trajectories in 2 DOFs for one gait cycle were calculated from the normalized ensemble sets (Figure 4.9 and 4.10).

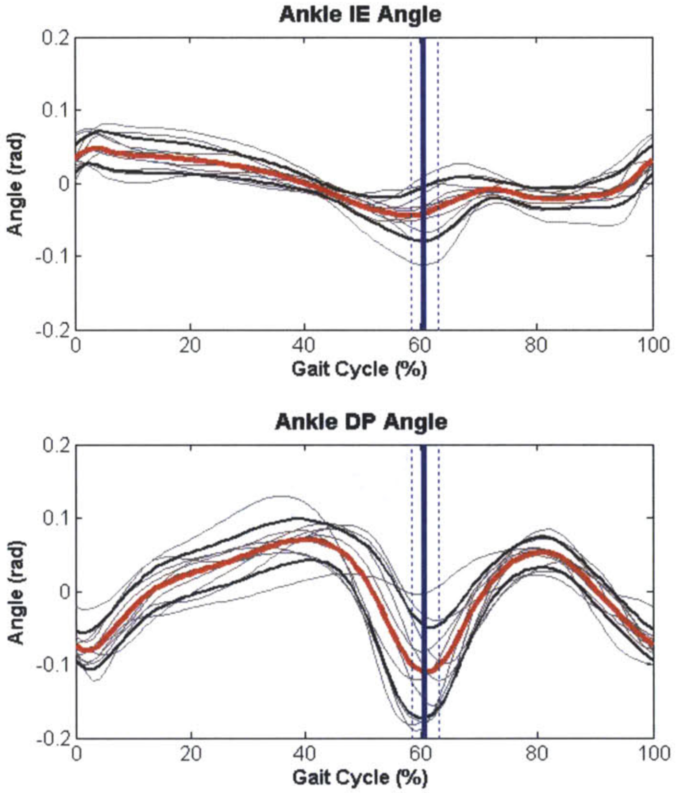

Figure 4.9: Ankle angular trajectories in 2 DOFs. Each thin gray line represents the result of individual subject, and the thick red and black lines represent the mean and mean±1SD of all subjects. Solid blue and dotted blue lines represent the timing of TO, the mean and mean±1SD, respectively.

Although, the ROMs for IE and DP angles were less than those of normal human walking probably due to non-zero stiffness of the robot, the shape of trajectories was qualitatively similar:

EMG trajectories of 4 muscles (TA, PL, SOL, and GAS) for one gait cycle were also obtained from the normalized ensemble sets (Figure 4.8). Plantarflexors (SOL, GAS, and PL) were turned off at the end of stance phase, while TA started to activate from PSW. TA continued to increase until right after TO, and started to decrease from ISW until it became active again just before HS. Plantarflexors were rather inactive across entire swing phase. After HS, antagonistic muscles for inversion (TA) and eversion (PL) were co-contracted.

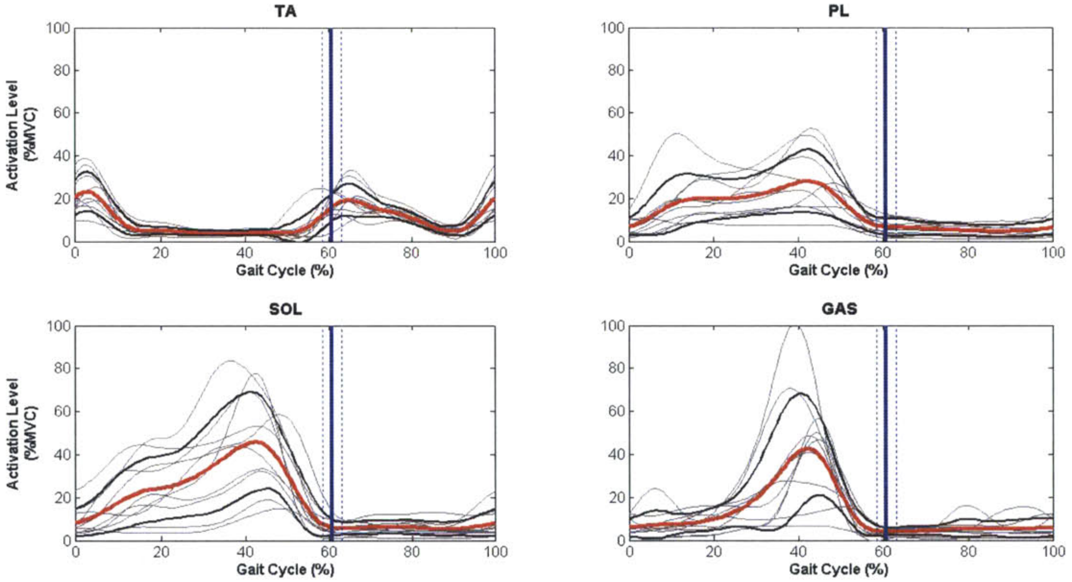

Figure 4.10: EMG trajectories of 4 muscles (TA, PL, SOL, and GAS) in one gait cycle. The same color codes as in Figure 4.6.

4.7.4 IRF Estimation and 2^nd^ Order Model Approximation

IRFs were estimated at every 2 *ms* and smoothed with a moving average window of 40 *ms* as explained in section 4.4.3. However, the moving average operation was not applied to the boundary between TSW and EST to better understand a discrete event at HS. Once IRFs were estimated, they were approximated with a 2^{nd} order model.

A representative result of IRF estimation and 2nd order model approximation (subject #1) is provided in Figure 4.11.

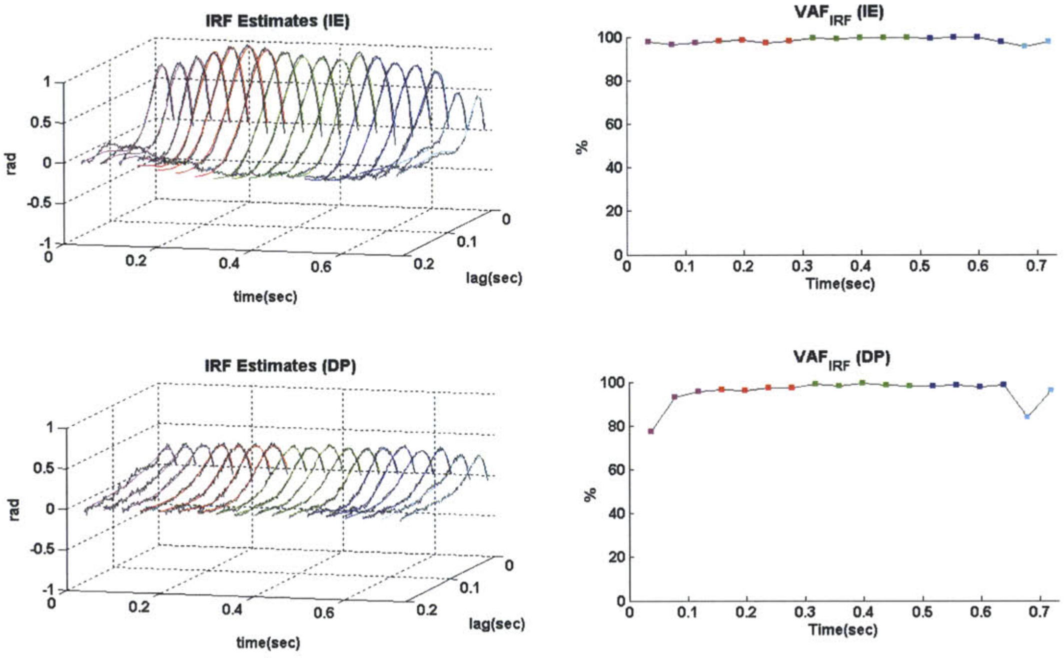

Figure 4.11: IRF estimation and the reliability of a second-order model approximation. 1st row: IE direction, 2nd row: DP direction. 1st column: IRF estimates with the suggested method (gray) and the best-fit 2nd order response (magenta: PSW, red: ISW, green: MSW, blue: TSW, cyan: EST). 2nd column: Model goodness of fit by Eq. (4.10). The start of PSW is set as zero time, and time step between estimates is 40 *ms*.

Samples of measured outputs and reconstructed outputs from the convolution of inputs and IRF estimates are also provided in Figure 4.12.

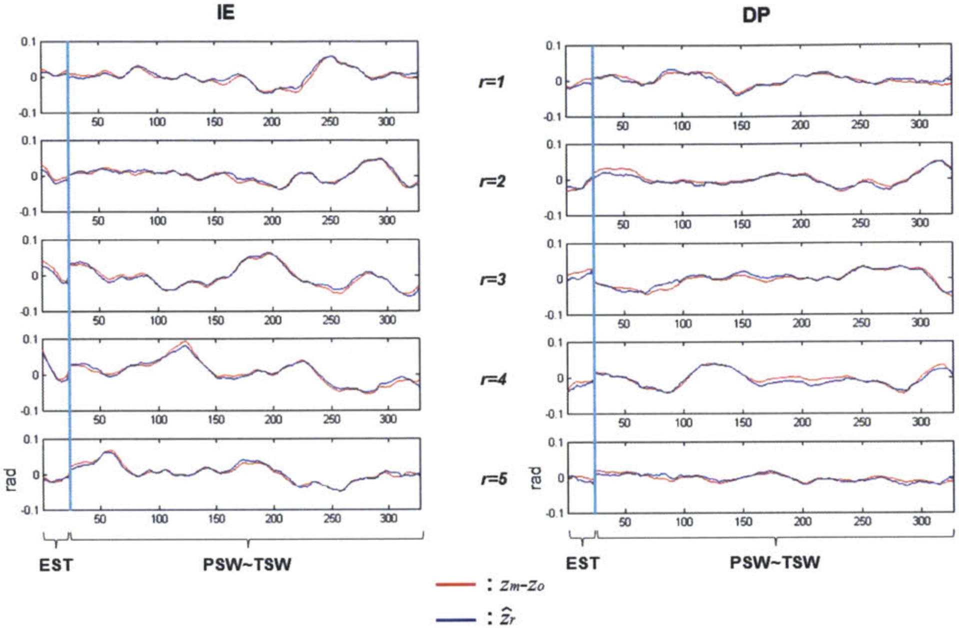

Figure 4.12: Samples of measured outputs vs. reconstructed outputs. Left: IE direction, Right: DP direction, Red lines: measured outputs after subtracting the nominal trajectory, blue lines: predicted outputs based on estimated IRFs.

The reliability of IRF estimation and 2nd order model approximation was evaluated by calculating VAF_{output}, e_{output}, and VAF_{IRF}. The mean and SE of reliability measures of all subjects are summarized in Table 4.3.

Table 4.3: Reliability measures for IRF estimation and 2nd order model approximation.

Reliability Measures		VAF_{IRF}					VAF_{output}	e_{output}
Dir.	**Phase Subject**	**PSW**	**ISW**	**MSW**	**TSW**	**EST**		
IE	**1**	97.1	97.9	99.2	98.8	96.3	87.4	0.69
	2	95.3	96.8	99.1	99.0	95.4	94.6	0.77
	3	94.1	95.9	99.1	98.8	91.8	88.3	0.80
	4	96.7	96.6	99.2	99.3	95.3	89.2	0.64
	5	93.7	96.7	97.7	98.9	92.1	89.2	0.54
	6	96.5	95.6	99.1	98.8	93.5	85.4	0.70
	7	95.7	96.1	98.8	97.9	95.1	83.8	0.72
	8	95.7	97.8	99.1	98.0	82.9	86.5	0.84
	9	96.7	96.9	99.2	98.7	96.5	88.1	0.67
	10	92.5	97.7	98.7	96.3	85.5	87.0	0.88
	Mean (SE)	**95.4 (0.5)**	**96.8 (0.3)**	**98.9 (0.1)**	**98.4 (0.3)**	**92.4 (0.5)**	**87.9 (0.9)**	**0.72 (0.03)**
DP	**1**	88.7	96.9	98.7	98.0	89.9	86.6	1.12
	2	79.7	93.2	98.9	98.2	94.9	90.2	1.17
	3	87.8	94.4	99.1	97.7	96.3	97.3	1.07
	4	91.4	97.0	99.0	98.2	96.8	88.6	0.89
	5	92.9	96.6	99.0	99.1	95.2	91.3	0.69
	6	86.4	96.1	98.8	98.6	95.7	91.7	0.99
	7	90.7	94.9	99.1	97.3	95.5	88.1	1.06
	8	88.6	97.2	97.7	96.8	93.8	85.9	1.11
	9	83.5	96.3	98.7	98.6	97.1	94.9	0.88
	10	92.7	94.6	99.1	98.1	86.1	93.0	1.00
	Mean (SE)	**88.2 (1.3)**	**95.7 (0.4)**	**98.8 (0.1)**	**98.1 (0.2)**	**94.1 (1.1)**	**89.8 (0.9)**	**1.00 (0.08)**

The unit for VAF_{IRF} and VAF_{output} is %, and e_{output} is degree.

In general, all subjects showed very high VAF_{output} and small e_{output}, verifying the reliability of IRF estimation based on the modified ensemble-based method. In addition, high VAF_{IRF} in all sub-gait phases between PSW and EST supported the validity of 2^{nd} order model approximation.

Identified parameters ($I_{Ankle+Abot}, B_{Ankle}, K_{Ankle}$) of all subjects are plotted in Figure 4.13.

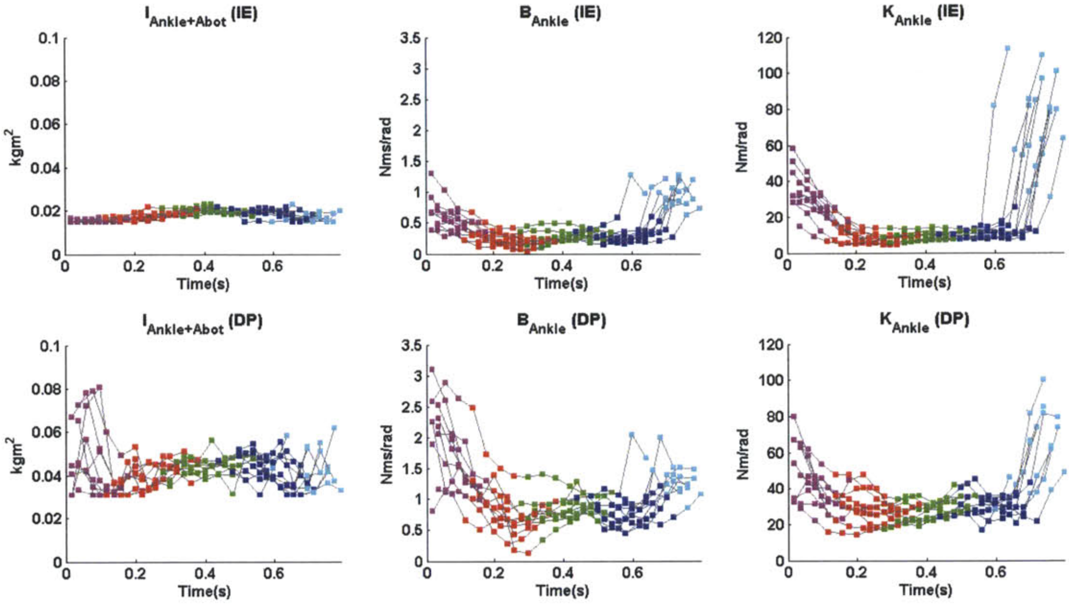

Figure 4.13: Time-varying ankle parameters of all subjects. 1st row: IE direction, 2nd row: DP direction. 1st column: inertia ($I_{Ankle+Abot}$). 2nd column: damping (B_{Ankle}), 3rd column: stiffness (K_{Ankle}). The start of PSW is set as zero time, and time step between estimates is 40 *ms*. The same color code as Figure 4.11.

In both DOFs, several noticeable time-varying behaviors of the ankle were found.

First, the variability of $I_{Ankle+Abot}$ was substantially lower than B_{Ankle} and K_{Ankle} across sub-gait phases for both directions. The SD and CV of $I_{Ankle+Abot}$, B_{Ankle}, and K_{Ankle} were summarized in Table 4.4.

Table 4.4: The variability of parameters

Measures	SD			CV		
Parameter / Direction	$I_{Ankle+Abot}$	B_{Ankle}	K_{Ankle}	$I_{Ankle+Abot}$	B_{Ankle}	K_{Ankle}
IE	0.002 (0.0001)	0.32 (0.02)	27.3 (2.22)	0.11 (0.01)	0.69 (0.04)	1.06 (0.06)
DP	0.005 (0.001)	0.46 (0.04)	14.41 (1.94)	0.12 (0.02)	0.40 (0.03)	0.38 (0.04)

The mean and SE (in parentheses) across all subjects are presented in the table.

Second, B_{Ankle} decreased at the end of stance (PSW) and remained relatively constant throughout swing phase, and increased again in TSW, and continued to increase after HS in EST. Third, K_{Ankle} showed the similar patterns as B_{Ankle}. Interestingly, K_{Ankle} started to increase in TSW (just before HS) and substantially increase in EST, especially in the frontal plane. In general, B_{Ankle} and K_{Ankle} were higher in the sagittal plane than in the frontal plane, except EST. In EST, K_{Ankle} in the IE direction is comparable to or higher than that of the DP direction.

4.7.5 Time-Varying Ankle Parameters in Sub-Gait Phases

Results of IRF estimates, 2nd order model approximates, and identified ankle parameters within each of 5 sub-gait phases were averaged into representative values. The mean and SE of all subjects are shown in Figure 4.14 and 4.15, and results of individual subject are provided in Appendix J.

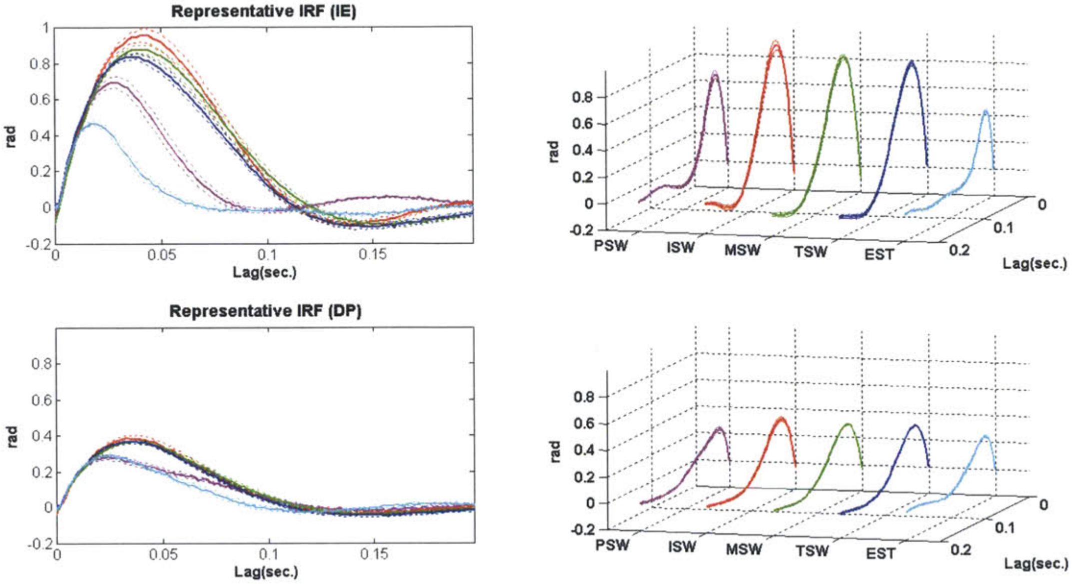

Figure 4.14: Representative IRF estimates. 1st row: IE direction, 2nd row: DP direction. 1st column: 2D representation. 2nd column: 3D representation. Thick solid and thin dotted lines represent the mean and mean±1 SE of all subjects, respectively. The same color code as Figure 4.11.

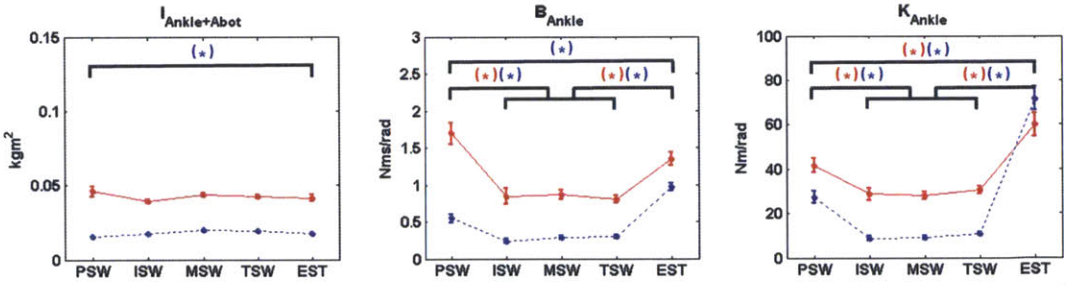

Figure 4.15: Representative time-varying ankle parameters in sub-gait phases. Solid red line: DP direction, dotted blue line: IE direction.

Statistical analyses were performed to compare ankle parameters in the IE and DP directions, and investigate changes across sub-gait phases from PSW to EST. When pooling all subjects together for each sub-gait phase, each parameter satisfied normality conditions ($p>0.05$).

First, paired t-tests were performed for each parameter and for each sub-gait phase to investigate difference between IE and DP directions. There was significant statistical difference between 2 directions ($p<<0.05$) in all conditions except stiffness (K_{Ankle}) at EST ($p=0.14$).

Next, one-way ANOVA (MATLAB's *anova1* function) was performed for each parameter and for each direction to examine differences between PSW and EST. Furthermore, Tukey's honestly significant difference (HSD) test (MATLAB's *multcompare* function) was used to find pairs that differed significantly from each other. In all statistical analyses, significance level of 0.05 was used.

No statistical difference was found for $I_{Ankle+Abot}$ in the DP direction. However, several pairs for $I_{Ankle+Abot}$ in the IE direction were statistically significantly different ($p<0.05$). This is because the variability of $I_{Ankle+Abot}$ in the IE direction was very small for each sub-gait phase (substantially smaller than the one in the DP direction).

For both directions, B_{Ankle} decreased from PSW to ISW and remained relatively constant throughout the swing phase, and increased again in EST. B_{Ankle} in the IE direction at EST was significantly higher than PSW. On the other hand, the value in the DP direction was higher in PSW than in EST, although statistically insignificant. K_{Ankle} showed the same time-varying trend as B_{Ankle} in both directions, except an observation that the value in EST was significantly higher than in PSW.

4.7.6 Impedance around Heel-Strike and Toe-Off

To investigate any significant changes of B_{Ankle} and K_{Ankle} around two important transition events from the swing phase to the stance phase and vice versa, identified ankle parameters around HS and TO were more closely investigated following the description in section 4.4.4.

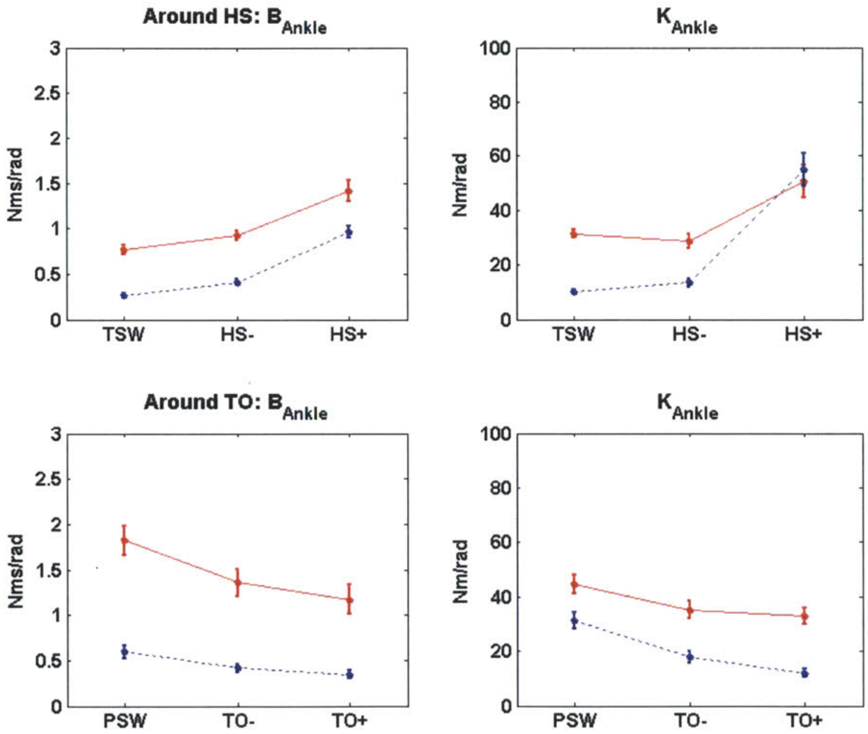

Figure 4.16: Ankle parameter changes around HS and TO. 1st row: around HS, 2nd row: around TO. Solid red line: DP direction, dotted blue line: IE direction. The mean and mean±1 SE of all subjects are illustrated as asterisks and bars, respectively.

First, two general trends were observed around HS for both DOFs: B_{Ankle} increased at the end of swing (HS^-) and continued to increase after HS (HS^+), while K_{Ankle} significantly increased right after HS (HS^{+}). Second, substantial decrease of B_{Ankle} and K_{Ankle} was observed around TO for both DOFs.

Statistical analysis using absolute values may mislead interpretation, when pooling all subject data together. So the increase ratio around HS (or TO) (section ② and ③ in Figure 4.3) in reference to the value at TSW (or PSW) (section ① in Figure 4.3) was used for the statistical analysis. Since, normalized values of the section ② and ③ did not satisfy the normality condition, Wilcoxon-rank tests (MATLAB's *signrank* function) were performed to check any statistical difference between normalized ② and 1 (reference value) as well as between normalized ② and normalized ③. Significance level of 0.05 was used.

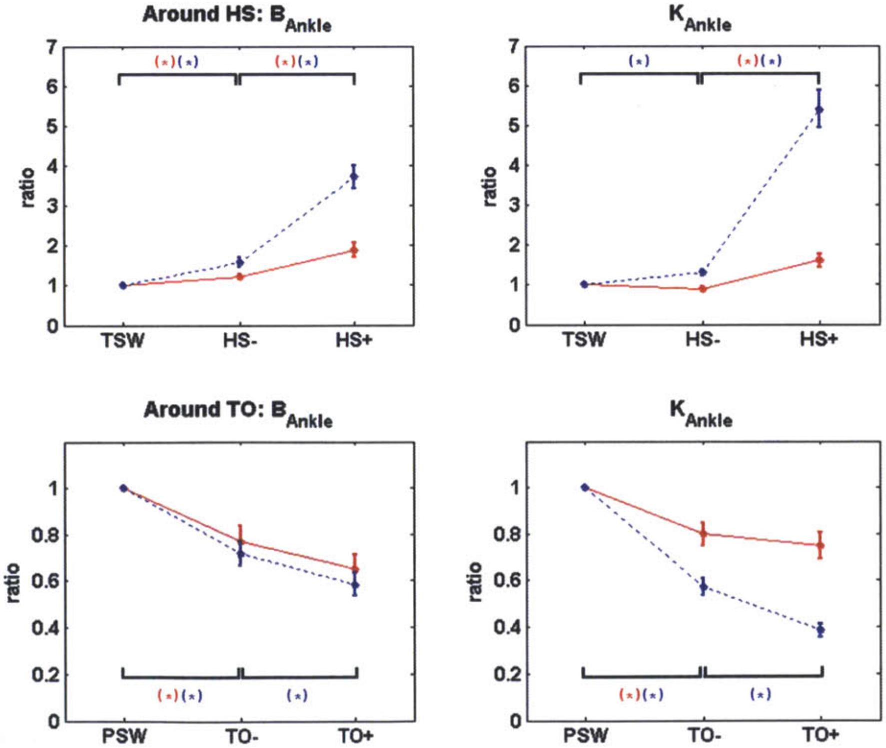

Figure 4.17: Ankle impedance increase ratios around HS and TO. The same format as in Figure 4.16.

First, B_{Ankle} and K_{Ankle} at HS$^+$ were substantially higher than at HS$^-$ and at TSW for both DOFs. Especially, B_{Ankle} and K_{Ankle} at HS$^-$ in the IE direction were significantly higher than at TSW. The increase of B_{Ankle} at HS$^-$ in the DP direction was less than in the IE direction, although statistically significant. No statistical change was observed for K_{Ankle} in the DP direction between TSW and HS$^-$.

Second, B_{Ankle} and K_{Ankle} at TO$^-$ were substantially lower than at PSW for both DOFs. In the IE direction, B_{Ankle} and K_{Ankle} at TO$^+$ further decreased than at TO$^-$, while no statistical difference was found for the DP direction.

4.7.7 Effect of Time-Scaling in Impedance Estimation around Heel-Strike and Toe-Off

Although simulation studies verified the small effect of time-scaling on impedance estimation, larger errors due to time-scaling may occur around HS and TO, because both are two key events between the stance and swing phases of the gait cycle. Especially HS is often described as a discrete event.

To address this issue, I compared two sets of ankle parameters, one estimated based on normalized realizations and the other one based on original realizations (no time-scaling). In average of all subjects, less than 6% errors between two sets were observed, which are statistically not significantly different (Table 4.5 and Figure 4.18).

Table 4.5: Parameter estimation with and without time-scaling.

Dir.	Parameters \ Phase	HS$^-$	HS$^+$	TO$^-$	TO$^+$
IE	B_{Ankle}	0.97	0.99	0.95	0.94
	K_{Ankle}	1.00	0.98	0.99	0.96
DP	B_{Ankle}	1.02	1.04	1.01	0.97
	K_{Ankle}	1.01	0.97	1.01	0.95

The ratio of parameter values estimated with time-scaling to without time-scaling was presented. All values showed no significant difference (p>0.05).

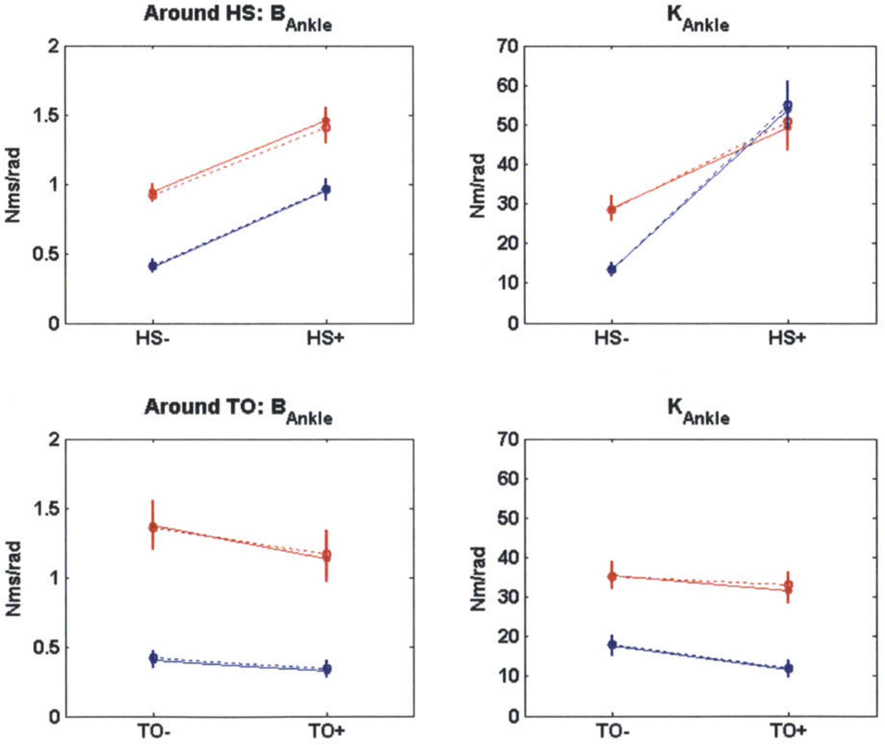

Figure 4.18: Effect of time-scaling in estimation of ankle parameters around HS and TO. 1st row: around HS, 2nd row: around TO. Solid and dotted red line: estimates without time-scaling and with scaling, respectively, in the DP direction. Solid and dotted blue line: estimates without time-scaling and with scaling, respectively, in the IE direction.

4.7.8 Discussion

Transient dynamic ankle impedance from final to initial stages of stance phase during walking (PSW~EST) on a treadmill was well characterized by the modified ensemble-based linear time-varying system identification method.

All healthy young subjects participated in this study could walk on a treadmill with the robot for about 15 minutes with no discomfort or muscle fatigue. Walking for 13 minutes with mild perturbations generated ensemble sets with more than 500 realizations. Even after the outlier rejection by 3 different criteria (temporal, spatial, and neurophysiological), the number of realizations was more than 450, which enabled robust identification of ankle impedance with possibly noisy measurements. Low variability of stride, stance, and swing durations (CV less than 0.03, 0.04, and 0.06, respectively) also justified the use of an ensemble-based approach.

The effect of mild random perturbations used in the study was very low, causing only the increase of muscle activation less than 0.5% MVC for all measured muscles. Simulation studies on the effect of time-scaling (normalization) also supported the approach to normalize all realizations to the mean stance or swing duration. We may alternatively run ensemble-based system identification on original data without time-scaling by introducing sub-ensemble approach [63, 111]. This approach requires construction of several sub-ensemble sets based on reference points, i.e., HS, TO, and the mid of swing phase. As shown in section 4.7.7, around HS and TO, there was no statistical difference in impedance identification, whether original or time-scaled data was used. On the other hand, setting the reference point for the mid of swing phase needs care. It can be set based on swing duration or joint kinematics (ankle and/or knee angle), and identification results may vary depending on which reference point is used, which is not an issue when all realizations are normalized to the same length.

IRFs were accurately estimated with the correlation-based system identification method in the time-domain. When averaged across all realizations, VAF_{output} was very high (>87%) and e_{output} was very small ($\leq 1^{\circ}$) for both DOFs, validating the accuracy of IRF estimation.

The lag size was set as 200 *ms*, since IRFs in all conditions settled close to zero within 200 *ms*. In addition, a causal filter was used, because admittance of the ankle was identified based on torque inputs and resulting angular displacement outputs, rather than impedance, which involves an acausal representation of joint mechanics [112].

Estimated IRFs were successfully approximated with a 2nd order model with inertia, damping, and stiffness to identify time-varying ankle parameters. VAF_{IRF} in the swing phase was higher than 95% for both DOFs. In PSW and EST when the foot had contact with the ground, VAF_{IRF} was lower than the swing phase, but still close to or higher than 90%. Ankle parameters may be directly derived from frequency response functions (FRF), calculated from IRFs with discrete Fourier transform. However, the short lag length of IRF limits the resolution and lowest identifiable FRF. Zero padding can be a solution to increase the resolution of FRFs, but this operation may also introduce noisy responses in the frequency domain.

Several interesting time-varying ankle behaviors were found in both DOFs across all 10 subjects. First, $I_{Ankle+Abot}$ was relatively constant across 5 sub-gait phases in both DOFs, and its variability was substantially lower than that of B_{Ankle} and K_{Ankle}. Only the value at

PSW in the DP direction was statistically different from the rest sub-phases. This is because some subjects showed high inertia in PSW. More investigation for these subjects is required.

At the end of the stance phase (PSW), B_{Ankle} and K_{Ankle} decreased to the level comparable to other sub-swing phases (ISW~TSW). According to previous work [54], B_{Ankle} and K_{Ankle} in the DP direction in the terminal stance (TST) phase were 0.038Nms/rad/kg and 4.6 Nm/rad/kg, respectively. These values are much higher than PSW values identified in this study. Substantial decrease of B_{Ankle} and K_{Ankle} matches well with decreased activation of plantarflexors (SOL, GAS, and PL) from the end of TST to PSW. In swing phase, both parameters remained relatively constant, in contrast to the finding in stance phase [54], where both damping and stiffness value increase throughout the stance phase.

Substantial increase of B_{Ankle} and K_{Ankle} was observed in EST after HS. More close investigation around HS revealed that B_{Ankle} and K_{Ankle} in the IE direction and B_{Ankle} in the DP direction actually started to increase just before HS, while K_{Ankle} in the DP direction increased right after HS. This finding is important evidence of "pre-tuning" for shock-absorption, one essential factor to maintain the stability of human walking. For example, the increase of ankle impedance increase will help exert a torque on the shank in the sagittal plane by the action of placing the foot and transferring body weight to it. That torque will act to move the knee out of hyperextension into the flexed position most appropriate for absorbing the kinetic energy of the descending body mass.

Another interesting finding is that B_{Ankle} and K_{Ankle} in EST, especially K_{Ankle}, increased more rapidly in the IE direction. Increased muscle activation of TA and PL, which are antagonistic pair in the frontal plane, can contribute to impedance increase right after HS.

This co-contraction mechanism is known to serve as an efficient way to increase mechanical impedance of the joint [86]. However, this is not enough to explain more and rapid increase of B_{Ankle} and K_{Ankle} in the IE direction than the DP direction, since TA and PL also contribute to DP impedance.

One possible explanation is the "lock" of the ankle joint in the frontal plane when HS occurs. The subtalar joint, which is responsible for IE movements, locks with eversion [113] and it has been known that the subtalar joint immediately goes from inversion to eversion right after HS [114, 115]. In addition, the mortise of the ankle, which is the space formed by the top of talus and the lower ends of the tibia and the fibula, locks in the frontal plane at the moment of the heel-strike. Another explanation is the stiffness increase due to the compression of soft tissues. Whatever its origin, substantial increase of ankle impedance in the frontal plane will help lateral stability from the moment of HS to the loading response.

The comparison of ankle parameters (B_{Ankle} and K_{Ankle}) around HS and TO with and without time-scaling of realizations showed negligible effect of the time-scaling for impedance identification.

The nominal trajectory (z_o) used in this study was obtained from all realizations from 14 minutes of walking. However, it has been known that walking is not completely random, and even in walking less than 10 minutes, long-range correlations in stride duration was observed, implying that the stride duration at any time depends on the stride duration at remote previous times [116, 117].

To evaluate the variability of impedance identification due to the variability of the nominal trajectory, a jackknife resampling method was used. In detail, first the whole ensemble set was splitted into 10 subsets, then for each of 10 iterations, one subset was removed from the whole ensemble set and other 9 sets were used to construct a new nominal trajectory. Ten iterations with different nominal trajectories provided a distribution for IRF estimates and parameter approximates ($I_{Ankle+Abot}$, B_{Ankle} , K_{Ankle}).

To compare parameters obtained by the resampling method and the original method using all realizations, statistical analyses (paired t-tests) were performed for each parameter and for each sub-gait phase on the pooled data from all 10 subjects. The ratio of parameter values from the resampling method to the original method was calculated and its statistical significance was evaluated (Table 4.6 and Figure 4.19).

Table 4.6: Parameter estimation by resampling of the nominal trajectory vs. by original method.

Dir.	Phase Parameters	PSW	ISW	MSW	TSW	EST
IE	$I_{Ankle+Abot}$	1.01	0.95*	0.93*	0.97	0.99
	B_{Ankle}	0.95	0.98	1.07	1.07	1.06
	K_{Ankle}	1.04	0.88	0.83	0.99	0.92
DP	$I_{Ankle+Abot}$	1.02	0.96	0.96	0.95	0.98
	B_{Ankle}	0.99	0.99	1.05	1.05	1.02
	K_{Ankle}	1.04	0.92	0.92	0.87	0.88

The ratio of parameter values from the resampling method to the original method was presented. Asterisks (*) denote significant difference ($p<0.05$).

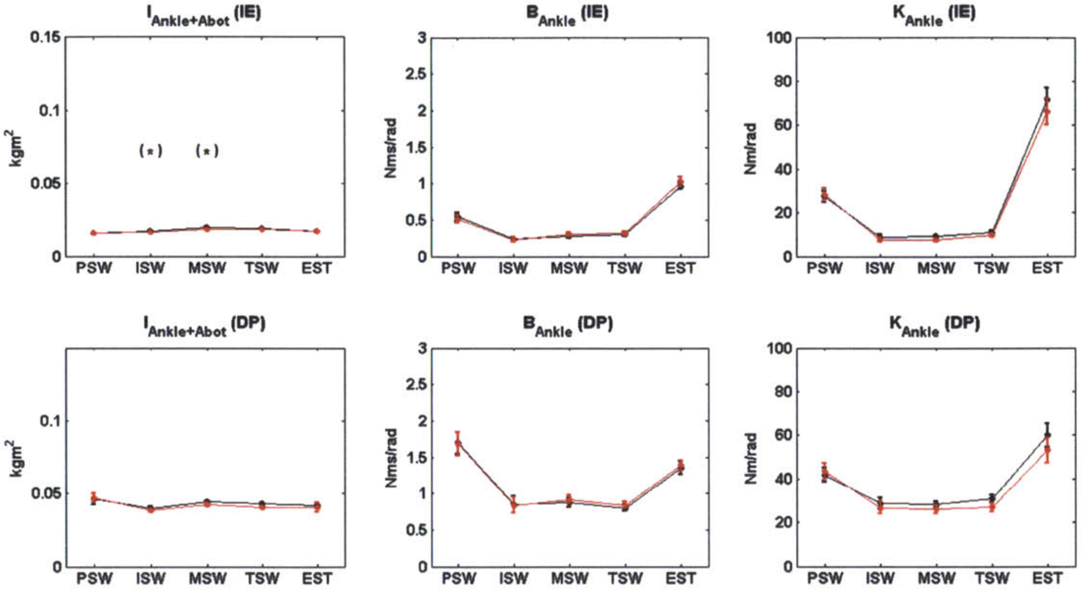

Figure 4.19: Time-varying ankle parameters in sub-gait phases. Red line: estimation based on the resampling method, black line: estimation based on the original method. 1st row: IE direction, 2nd row: DP direction.

No statistical difference between two measures was observed except $I_{Ankle+Abot}$ at ISW and MSW, which was expected mainly due to very low variability of inertia estimates. This finding supports the current method of calculating z_o with no further consideration of the effect of long-range correlation.

Chapter 5

Conclusion

5.1 Ankle Mechanical Impedance of Young Healthy Subjects: "Internally Complicated, but Externally Simple"

The human ankle joint is an intricate combination of the talocrural joint, the subtarlar joint, and the inferior tibiofibular joint, supported by 4 ligaments. The combination of these bones allows movements in multiple DOFs through the action of multiple muscles and tendons. The anatomical axes of the ankle joint do not intersect, are far from orthogonal, and even change with ankle movement.

Ankle muscles are activated either voluntarily by neural commands from the brain or reflexively through intra-muscular or inter-muscular feedback [10]. Both of voluntary and reflex actions contribute to ankle mechanical impedance, more specifically to intrinsic and reflex component of impedance, respectively [49].

Even with the internally complicated neuromusculoskeletal behavior of the ankle, ankle impedance of young healthy subjects has shown externally simple behaviors, consistent across most subjects, at least in the context of this experiment. These simple behaviors are expected to be very advantageous in many applications.

When ankle impedance is described in both the sagittal and frontal planes, interaction or coupling between different DOFs is substantially small, although non-negligible, over a wide frequency range and at different levels of muscle activation. In other words, generated ankle torques in the DP (IE) direction have small effect on ankle motions in the IE (DP) direction, or vice versa. Furthermore, ankle impedance in each DOF can be well approximated with a 2nd order model with inertia, damping, and stiffness, both under steady-state and time-varying conditions.

Another simple behavior of the ankle of young healthy subjects is its energetic passivity. The ankle of young healthy subjects in all measurement conditions was close to the energetically passive system.

Most subjects showed a highly linear relationship between muscle activation and ankle impedance in all movement directions in the 2D-space, even though joint stiffness is determined not only by muscle generated stiffness but also by kinematic stiffness due to nonlinear musculo-tendon kinematics.

Above findings will be a great help in controlling the mechanical device that interacts with the lower-extremity. First, when small coupling between 2 DOFs is neglected, we may design an independent controller for the sagittal and frontal planes. Second, we can guarantee the coupled stability of physical interaction between the human and the robot by making the robot behave as energetically passive system. Third, based on the highly linear relationship between muscle activation and impedance, we may use EMG sensors and other kinematics sensors to predict ankle impedance, while a wearable robot is used as an actuator for other purposes. This approach may also be used to estimate ankle mechanical impedance when direct identification is not available such as impedance during the mid- and terminal stance phase of the gait.

Externally simple characteristics of young healthy subjects will also serve as a baseline to explore ankle mechanical impedance of older and neurologically impaired subjects, whose biomechanical and neurological properties may be altered with aging and impairments. Based on several characteristic measures presented in this thesis, the severity of pathological behaviors of the joint can be quantified by calculating its deviation from the norm as a result of disorders.

5.2 Comparison of Characterization Methods

Three different characterization methods were presented in this thesis to study ankle impedance in different conditions. This chapter compares the three methods and briefly describes pros and cons of each method.

The first method described in Chapter 2 provides accurate nonlinear torque and angle relationship (vector field) over the wide ROM, from which we can directly calculate local stiffness at any point in the displacement field. On the other hand, other two methods using random perturbations can only provide information around the initial set position. For example, to get stiffness information at 15° dorsiflexed and 15° plantarflexed ankle positions using the second method, two separate measurements with different initial set positions are required, while the same information can be derived from a single measurement based on the first method. The limitation of the first method is that it can only provide stiffness information, but not damping, inertia or higher order dynamics of the ankle in multi-DOF.

The second method described in Chapter 3 quantifies dynamic properties of the ankle joint, not available from the first method. The use of mild random perturbations, due to its random nature, enables reliable measurements even in high muscle activation conditions with minimal likelihood of voluntary reactions. In addition, simple rotational operations provide fast computation of the anisotropy of ankle impedance around the initial set position as a function of frequency. However, impedance in opposite directions cannot be distinguished with this method because perturbations are applied around the initial set position, and all measurements in both directions are used for impedance identification. Thus, to identify impedance in both of opposite directions, separate measurements with different nominal ankle positions are required. For example, stiffness in dorsiflexion and plantarflexion directions can be identified with 2 separate measurements with different nominal ankle positions, one with dorsiflexed and the other with plantarflexed.

The third method presented in Chapter 4 characterizes transient or time-varying dynamic behavior of the ankle, not available from other two static or time-invariant methods. The same random perturbations in the second method are used to minimize involvement of voluntary reactions during time-varying motor functions, walking in this study. However, since the estimation is performed both across the time-axis as well as realizations of the ensemble set, longer measurements to collect hundreds of realizations are required for the reliable impedance identification.

Since each method has its own advantages and limitations, a proper method should be selected for different applications. Even when multiple methods should be used together, different types of measurements can be completed in a relatively short time using the same experimental setup. For example in this study, the same experimental setup including the

Anklebot was used across all three types of studies. While most of the experiment time was consumed for setting up the experiment, actual running time for each measurement was considerably less than the setup time, even in the walking experiment for transient impedance identification. Hence, the combination of all different methods using the same experimental setup can be a good package to better characterize the joint mechanical impedance.

5.3 Future Work

There are several interesting and important areas of investigation for future research.

First, from the studies of steady-state static and dynamic ankle impedance, a characteristic "tilted peanut" shape of ankle impedance in IE–DP space and its relationship to muscle activation were identified. In addition, several distinctive transient behaviors of ankle impedance in both DOFs were observed consistently across subjects. Although simple explanations were provided in this thesis, rigorous modeling studies based on reported biomechanical properties of the ankle will help better understanding of ankle impedance, which may be utilized in further simulation studies.

Second, as mentioned before, if predicted ankle impedance from sensor data (EMG and kinematics) is accurate enough to replace direct identification, the ankle robot can be used as an actuator for other purpose such as subject training or rehabilitation. More studies under different measurement conditions, both time-invariant and time-varying, will provide richer data sets to find a mapping, possibly dynamic and nonlinear, relating EMG and kinematics to the corresponding ankle impedance.

Third, the methods presented in this thesis are intended to be sufficiently general to be applicable to any multi-joint system or single joint having multiple DOFs. For example, multi-variable impedance of the knee and ankle or the hip and knee can be studied to understand interaction dynamics between joints. The wrist is a good example of single joint multi-DOF system, which has 3 DOFs to be studied.

5.4 Implication for Neuro-rehabilitation

The demand for lower-extremity rehabilitation for people with neurological disorders is growing as the number of patients is increasing apace with the aging population. Every year, about 795,000 Americans have a new or recurrent stroke [118]. This number corresponds to the fact that someone in the US has a stroke every 40 seconds. An estimated 764,000 Americans children and adults currently have cerebral palsy [119] . In addition in the US, about 250,000~350,000 people have been diagnosed with multiple sclerosis (MS) [120], and 250,000 people have spinal cord injuries, and approximately 11,000 new injuries occur every year [121]. These diseases cause severe damage to the neuromuscular system of the human body and alter mechanical properties of joint mechanical impedance that directly affects motor behaviors, including lower-extremity functions. Many of these persons have significant gait impairments including at the ankle, which causes abnormal walking patterns such as drop foot, excessive inversion, crouched gait, toe walking, and so on.

While several consistent characteristics of ankle impedance were observed in young healthy subjects, we may expect significantly different characteristics for neurologically impaired patients due to altered neuromuscular properties. A prerequisite for effective neuro-rehabilitation is an accurate diagnosis of pathological behaviors, and our characterization methods can be well used for this purpose.

In fact, a preliminary study with 4 neurologically impaired patients (3 stroke and 1 MS) was performed at the Providence Veteran Affairs Medical Center (RI, USA) after obtaining an approval of Institutional Review Board. Static ankle impedance was characterized in relaxed muscles following the same experimental procedure and analysis methods used in young healthy subjects [122].

Interestingly, 2 of 4 patients (AO1 and AO2) showed substantial non-passive behavior (non-zero curls) even when fully relaxed. The non-passive behavior was observed in both affected and unaffected sides, which can be only attributed to unbalanced inter-muscular feedback between different DOFs. This is in contrast to results obtained in young healthy subjects that were conservative everywhere. If the damage to descending neural pathways affects peripheral neural networks and causes unbalanced inter-muscular feedback accordingly, that could account for these non-zero curls.

Another interesting observation was that 2 patients (AO1 and AO2) showing non-passive behavior exhibited highly asymmetric anisotropy of ankle impedance between affected and unaffected sides (Figure 5.1). Asymmetric ankle impedance may require a more complex control scheme to guarantee balance, postural stabilization and joint coordination during locomotion. Further study is needed to verify any correlation between curl components and the amount of symmetry of the impedance structure.

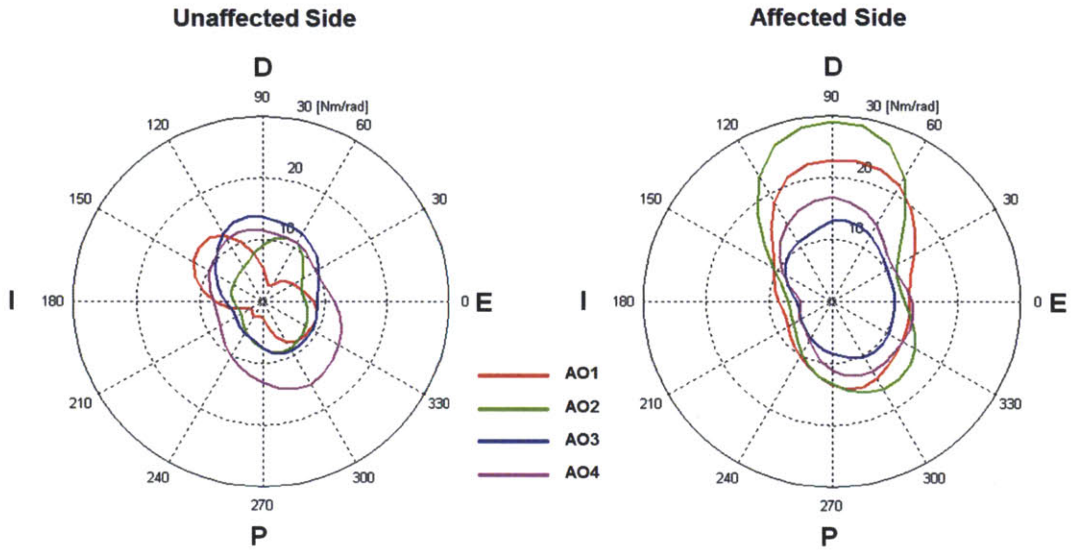

Figure 5.1: Anisotropy of static ankle mechanical impedance of neurologically impaired patients. Left: unaffected side, Right: affected side. Outbound and inbound results were averaged.

Although only static component of ankle impedance was characterized for a small number of patients, this study sufficiently shows the possibilities of characterization methods introduced in this thesis to be used for the neuro-rehabilitation application.

The preliminary study indicated that externally simple behaviors observed from young healthy subjects may not be valid any more for people with neurological disorders. Thus, multi-DOF studies can become more important in clinical studies to characterize pathological behaviors, which cannot be attained from multiple single-DOF studies.

With more rigorous studies for patients having neurological disorders, we anticipate that the suggested characterization methods will provide a quantitative measure to better diagnose impairments and understand lower-extremity functions of patients, and eventually to design strategies to rehabilitate them.

Appendix A: Thin-Plate Spline Smoothing with Generalized Cross Validation

As described in section 2.4.1, given a set of n data points ($P_i = (x_i, y_i), i = 1,2,\ldots,n$) in $\Re^2$ and n vectors $z = (z_1, z_2, \ldots, z_n)$, where z_i corresponds to the z value at point P_i, a weighted combination of TPS centered about each data point together with an affine transformation gives the interpolation function (f) (Eq. (A.1)) that minimizes bending energy E_b represented as a quadratic form (Eq. (A.2).

$$f(x,y) = a_0 + a_1 x + a_2 y + \sum_{i=1}^{n} w_i U(|P_i - (x,y)|)$$

$$U(r) = r^2 \log r^2, \quad U(0) = 0 \tag{A.1}$$

$$E_b = \iint_{\Re^2} \left(\left(\frac{\partial^2 f}{\partial x^2} \right)^2 + 2\left(\frac{\partial^2 f}{\partial x \partial y} \right) + \left(\frac{\partial^2 f}{\partial y^2} \right)^2 \right) \tag{A.2}$$

where x and y represent angular displacements (θ_{IE} and θ_{DP} respectively), and $f(x,y)$ is the corresponding torque value (either τ_{IE} or τ_{DP}). The weighting factor $W = (w_1, w_2, \ldots, w_n)$ and coefficients for the affine transformation $D = (a_0, a_1, a_2)$ can easily be calculated by matrix operations (Eq. (A.3)).

$$\begin{bmatrix} z_1 \\ z_2 \\ \vdots \\ z_n \\ 0 \\ 0 \\ 0 \end{bmatrix} = \left[\begin{array}{cccc|ccc} 0 & U(r_{12}) & \cdots\cdots & U(r_{1n}) & 1 & x_1 & y_1 \\ U(r_{21}) & 0 & \cdots\cdots & U(r_{2n}) & 1 & x_2 & y_2 \\ \vdots & \vdots & \ddots & \vdots & \vdots & \vdots & \vdots \\ U(r_{n1}) & U(r_{n2}) & \cdots\cdots & 0 & 1 & x_n & y_n \\ \hline 1 & 1 & & 1 & & & \\ x_1 & x_2 & \cdots\cdots & x_n & & 0 & \\ y_1 & y_2 & & y_n & & & \end{array}\right] \begin{bmatrix} w_1 \\ w_2 \\ \vdots \\ w_n \\ a_0 \\ a_1 \\ a_2 \end{bmatrix} \tag{A.3}$$

where r_{ij} is the distance between P_i and P_j.

For a fixed smoothing parameter λ, the smoothing function TPS (f_λ) is the minimizer of E_{tps} (Eq. (A.4)).

$$E_{tps} = \frac{1}{n}\sum_{i=1}^{n}(z_i - f(x_i,y_i)) + \lambda\iint_{\Re^2}\left(\left(\frac{\partial^2 f}{\partial x^2}\right)^2 + 2\left(\frac{\partial^2 f}{\partial x \partial y}\right) + \left(\frac{\partial^2 f}{\partial y^2}\right)^2\right)dxdy \tag{A.4}$$

In a matrix form, this equation can be represented as (Eq. (A.5)).

$$E_{tps} = \frac{1}{n}\|Z - PD - KW\|^2 + \lambda W^T KW, \qquad (P'W = 0) \tag{A.5}$$

The weighting factor $W = (w_1, w_2, \ldots, w_n)$ and coefficients $D = (a_0, a_1, a_2)$ of function f_λ can be solved using a least squares approach using QR decomposition of P (Eq. (A.6)). Details of this solution can be found in [71].

$$P = (Q_1 : Q_2)\begin{pmatrix} R \\ 0 \end{pmatrix}$$

$$W = Q_2(Q_2^T K Q_2 + \lambda I)^{-1} Q_2^T Z$$

$$D = R^{-1} Q_1^T (Z - KQ_2\gamma) \tag{A.6}$$

where, Q_1 and Q_2 are $n \times 3$ and $n \times (n-3)$ unitary matrices, respectively.

Finding the optimal smoothing parameter (λ^*) is a nonlinear regression problem of minimizing mean squared error $R(\lambda)$ between the estimate (f_λ) and the underlying function (f) (Eq. (A.7)).

$$\begin{aligned} & z_i = f(x_i, y_i) + \varepsilon_i \\ & R(\lambda) = \frac{1}{n}\sum_{i=1}^{n}(f_\lambda(x_i, y_i) - f(x_i, y_i))^2 \\ & \lambda^* = \arg\min_{\lambda} R(\lambda) \end{aligned} \tag{A.7}$$

where z_i are measured data, $f(x_i, y_i)$ an underlying smooth surface, $f_\lambda(x_i, y_i)$ an estimate, and ε_i a white noise process.

However, we cannot calculate $\lambda^* = \arg\min_{\lambda} R(\lambda)$ directly since it involves an unknown function $f(x_i, y_i)$. According to Craven and Wahba [123], the minimizer of the GCV function $V(\lambda)$ defined by Eq. (A.8) also minimizes $R(\lambda)$ for large n (providing reliable estimates of λ for $n > 25$).

$$V(\lambda) = \frac{\frac{1}{n}\left\|(I - A(\lambda)Z)\right\|^2}{\left[\frac{1}{n}Tr(I - A(\lambda))\right]^2} \tag{A.8}$$

where Z is the measured displacement vector and A is an influence matrix that relates Z and estimates vector f_λ (Eq. (A.9)).

$$
\begin{aligned}
&(f_\lambda(x_1,y_1),\cdots,f_\lambda(x_n,y_n))^T = A(\lambda)(z_1,\cdots,z_n)^T \\
&A(\lambda) = I - n\lambda Q_2(Q_2{}^T(K + n\lambda I)Q_2)^{-1}Q_2{}^T
\end{aligned}
\tag{A.9}
$$

Thus, the optimal smoothing parameter λ^* can be calculated by finding the minimizer of $V(\lambda)$ consisting of the measurement vector (Z) and the influence matrix (A) (Eq. (A.10)).

$$
\lambda^* = \arg\min_{\lambda} V(\lambda) \tag{A.10}
$$

Full descriptions of the GCV algorithms can be found in [71, 123].

Appendix B: Definition of Spling-like Property

From physical system theory, a spring is defined as an elastic energy-storage element characterized by a relation between generalized force and generalized displacement such that the integral of force with respect to displacement is mechanical work. The relation between force and displacement may be nonlinear or even discontinuous. A neuromuscular system is defined as spring-like if its force-length (or torque-angle) behavior permits the definition a scalar potential function ($E_p(\boldsymbol{q})$) of its length (or angle) (Eq. (B.1)) .

$$E_p(\boldsymbol{q}) = \int \boldsymbol{f}(\boldsymbol{q})^T \, d\boldsymbol{q} \tag{B.1}$$

where $\boldsymbol{f}$ and $\boldsymbol{q}$ denote force and displacement vectors, respectively. By definition, force is the gradient of the potential field (Eq. (B.2)), and the curl of a gradient is zero (Eq. (B.3)). A necessary and sufficient condition for the vector field $\boldsymbol{f}$ to be spring-like is that its curl is zero. Zero curl means that stiffness is symmetric (Eq. (B.4)).

$$\boldsymbol{f} = \nabla_q E_p(\boldsymbol{q}) \tag{B.2}$$

$$\nabla \times \boldsymbol{f} = \nabla \times \nabla_q E_p(\boldsymbol{q}) = 0 \tag{B.3}$$

$$\frac{\partial f_j}{\partial q_i} = \frac{\partial f_i}{\partial q_j}, \quad \forall i, j \tag{B.4}$$

Appendix C: Simulation of Vector Field Approximation

To validate our vector field approximation method based on approximating each vector component as a scalar field, two different datasets were simulated: one approximately conservative, the other an approximately rotational field. Artificial data were generated by sampling points in these conservative and rotational fields and adding noise with magnitude comparable to that observed in real experiments.

These data were approximated using our method, and the estimated field was decomposed into conservative and rotational components to check how well the method can detect curl components both when they are present and when they are not. For this purpose, paired t-tests were performed on the total vector field and the decomposed fields. Simulation results verified that our methods worked well whether the field has curl or not (Figure C.1)

In case (a), the conservative field was statistically indistinguishable from the total field and the rotational field is not significantly different from zero ($p \gg 0.05$). Conversely, in case (b), the conservative field was not significantly different from zero and the rotational field was statistically indistinguishable from the total field ($p \gg 0.05$).

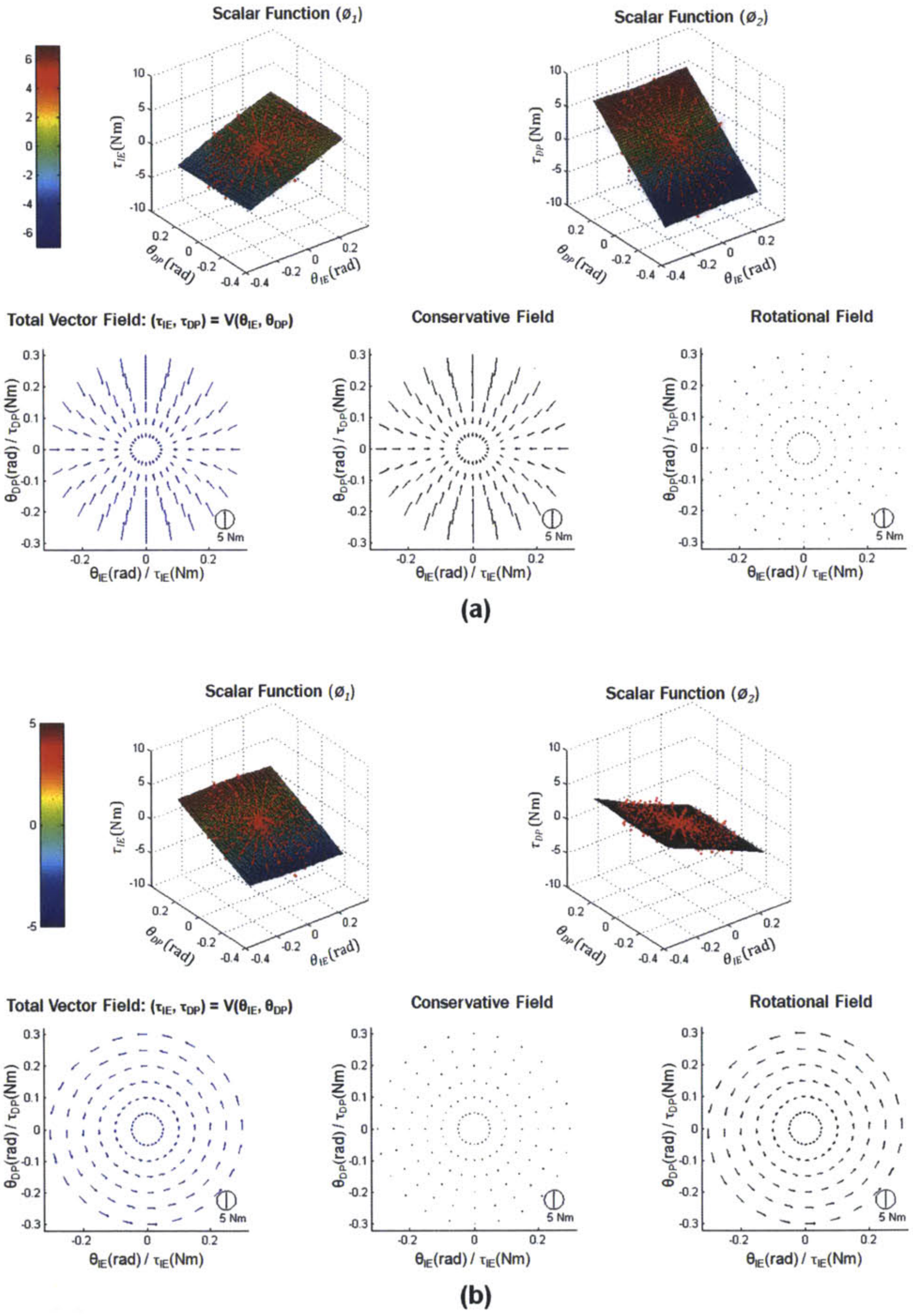

Figure C.1: Verification of our method using artificially generated noisy data. A conservative field (a) and a rotational field (b). Artificial data (depicted as point sets in 24 directions) and the corresponding approximated field (consisting of two TPS surface estimates (ϕ_1, ϕ_2) (top row) as well as the total vector field and decomposed fields are presented (bottom row).

Appendix D: Linear Time-Invariant Multi-Input Multi-Output Stochastic Identification

Linear time-invariant Multi-input, multi-output (MIMO) nonparametric system identification methods based on spectral analysis are described. When the time history of 2 inputs $x=(x_1,x_2)$ and 2 outputs $y=(y_1,y_2)$ are given, each element of transfer matrix ($\boldsymbol{H}(f)=[H_{11}\,H_{12};H_{21}\,H_{22}]$) (Eq. (D.1)) can be calculated from input auto- and cross-spectral density and input-output cross-spectral density (Eq. (D.2)).

$$\begin{bmatrix} y_1 \\ y_2 \end{bmatrix} = \begin{bmatrix} H_{11}(f) & H_{12}(f) \\ H_{21}(f) & H_{22}(f) \end{bmatrix} \begin{bmatrix} x_1 \\ x_2 \end{bmatrix} \tag{D.1}$$

$$\boldsymbol{H}(f)=\frac{1}{1-{\gamma_{x1x2}}^2}\begin{bmatrix} \dfrac{P_{x1y1}}{P_{x1x1}}\left(1-\dfrac{P_{x1x2}P_{x2y1}}{P_{x2x2}P_{x1y1}}\right) & \dfrac{P_{x2y1}}{P_{x2x2}}\left(1-\dfrac{P_{x2x1}P_{x1y1}}{P_{x1x1}P_{x2y1}}\right) \\ \dfrac{P_{x1y2}}{P_{x1x1}}\left(1-\dfrac{P_{x1x2}P_{x2y2}}{P_{x2x2}P_{x1y2}}\right) & \dfrac{P_{x2y2}}{P_{x2x2}}\left(1-\dfrac{P_{x2x1}P_{x1y2}}{P_{x1x1}P_{x2y2}}\right) \end{bmatrix} \tag{D.2}$$

where P_{ab} denotes cross power spectral density between a and b, and ${\gamma_{x1x2}}^2$ is the ordinary coherence function between x_1 and x_2 defined as (Eq. (D.3)):

$${\gamma_{x1x2}}^2=\frac{\left|P_{x1y1}\right|^2}{P_{x1x1}P_{x2x2}} \tag{D.3}$$

Partial coherence indicates linear dependency between input and output after removing the effects of other inputs. For a 2 inputs and 2 outputs system, a partial coherence matrix ($\boldsymbol{\Omega}^2$) is given by Eq. (D.4).

$$\mathbf{\Omega}^2 = \begin{bmatrix} \mathbf{\Omega}_{11}{}^2 & \mathbf{\Omega}_{12}{}^2 \\ \mathbf{\Omega}_{21}{}^2 & \mathbf{\Omega}_{22}{}^2 \end{bmatrix} = \begin{bmatrix} \dfrac{\left|P_{x1y1}P_{x2x2} - P_{x2y1}P_{x1x2}\right|^2}{P_{x2x2}P_{x2x2}P_{x1x1}P_{y1y1}(1-\gamma_{x2x1}{}^2)(1-\gamma_{x2y1}{}^2)} & \dfrac{\left|P_{x2y1}P_{x1x1} - P_{x1y1}P_{x2x1}\right|^2}{P_{x1x1}P_{x1x1}P_{x2x2}P_{y1y1}(1-\gamma_{x1x2}{}^2)(1-\gamma_{x1y1}{}^2)} \\ \dfrac{\left|P_{x1y2}P_{x2x2} - P_{x2y2}P_{x1x2}\right|^2}{P_{x2x2}P_{x2x2}P_{x1x1}P_{y2y2}(1-\gamma_{x2x1}{}^2)(1-\gamma_{x2y2}{}^2)} & \dfrac{\left|P_{x2y2}P_{x1x1} - P_{x1y2}P_{x2x1}\right|^2}{P_{x1x1}P_{x1x1}P_{x2x2}P_{y2y2}(1-\gamma_{x1x2}{}^2)(1-\gamma_{x1y2}{}^2)} \end{bmatrix} \tag{D.4}$$

Appendix E: Representations of Directional Variation of Mechanical Impedance

The directional variation of ankle mechanical impedance was represented in polar coordinates (direction dependent map), which describe the magnitude of impedance for each movement direction in the IE–DP space. On the other hand, stiffness ellipse describes the trajectory of restoring torque vectors when the joint is displaced along the unit circle in the IE–DP space (Eq. (E.1)). In fact, one representation can be derived from the other one, and vice versa. To illustrate two different impedance representations, three examples of joint stiffness matrices are defined as below:

$$\begin{bmatrix} \tau_{IE} \\ \tau_{DP} \end{bmatrix} = \begin{bmatrix} K_{11} & K_{12} \\ K_{21} & K_{22} \end{bmatrix} \begin{bmatrix} \theta_{IE} \\ \theta_{DP} \end{bmatrix}, \quad \boldsymbol{K} = \begin{bmatrix} K_{11} & K_{12} \\ K_{21} & K_{22} \end{bmatrix} \tag{E.1}$$

Example 1: $\boldsymbol{K} = \begin{bmatrix} 10 & 0 \\ 0 & 20 \end{bmatrix}$

Example 2: $\boldsymbol{K} = \begin{bmatrix} 10 & 0 \\ 0 & 30 \end{bmatrix}$

Example 3: $\boldsymbol{K} = \begin{bmatrix} 10 & -5 \\ -5 & 30 \end{bmatrix}$

For each example, two different stiffness representations are simulated and shown (Figure E.1~ Figure E.3).

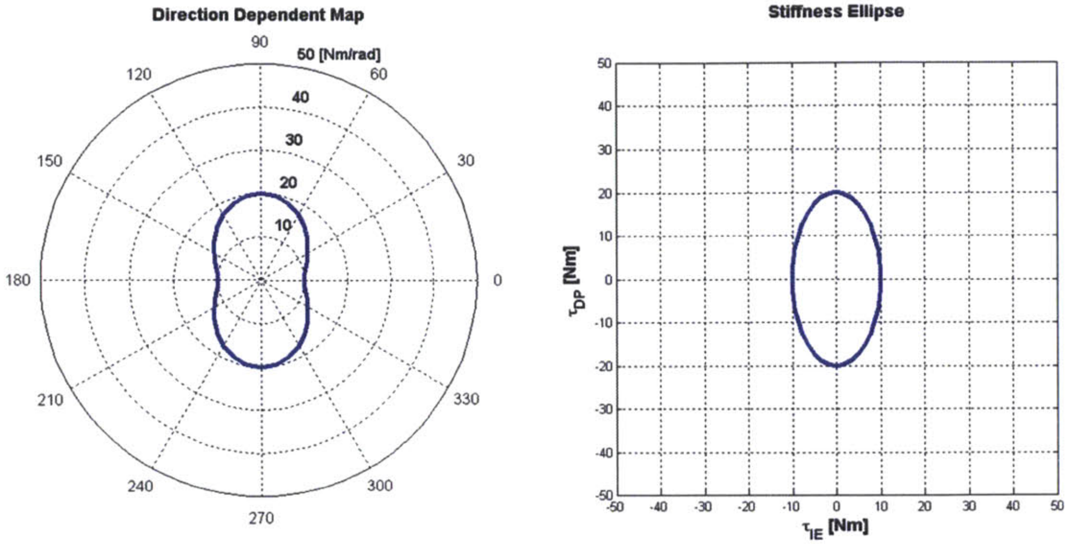

Figure E.1: Example 1. Ratio between K_{11} and K_{22} is 1:2.

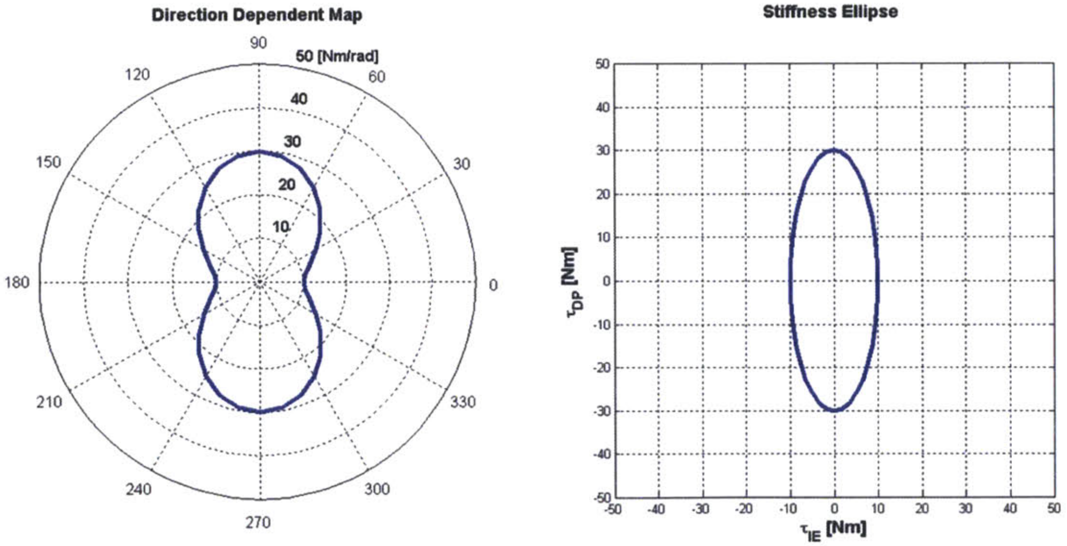

Figure E.2: Example 1. Ratio between K_{11} and K_{22} is 1:3.

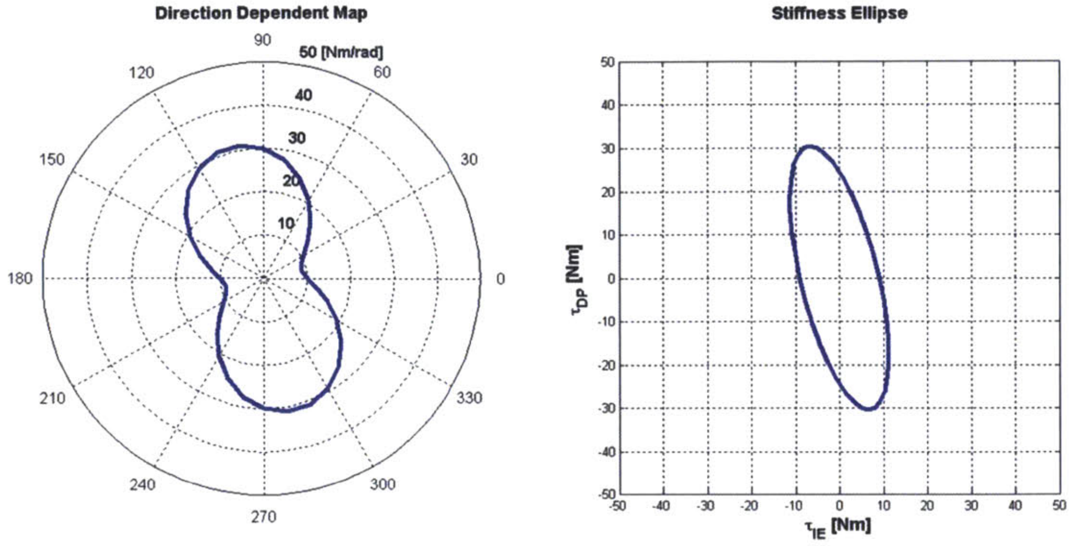

Figure E.3: Example 3. Off-diagonal components of the stiffness matrix are non-zero.

Directions of principal eigenvectors of the stiffness ellipse match with major and minor principal axes of the direction dependent map.

Appendix F: Resonance and Anti-Resonance Behavior of the Shoe Bracket

Identified ankle impedance showed resonance and anti-resonance behaviors over about 30 Hz (Figure 3.12). To investigate whether this is real biomechanical property of the human ankle, an additional test was performed using a physical mockup loosely resembling the human leg. The mockup consisted of the wooden thigh, shank, foot, and a connecting joint made of rubber. The same shoe used in human experiments was worn on the wooden foot, and the knee brace was installed over the wooden thigh and shank. Then, the robot was attached to the knee brace and the bracket of the shoe (Figure F.1 (left)).

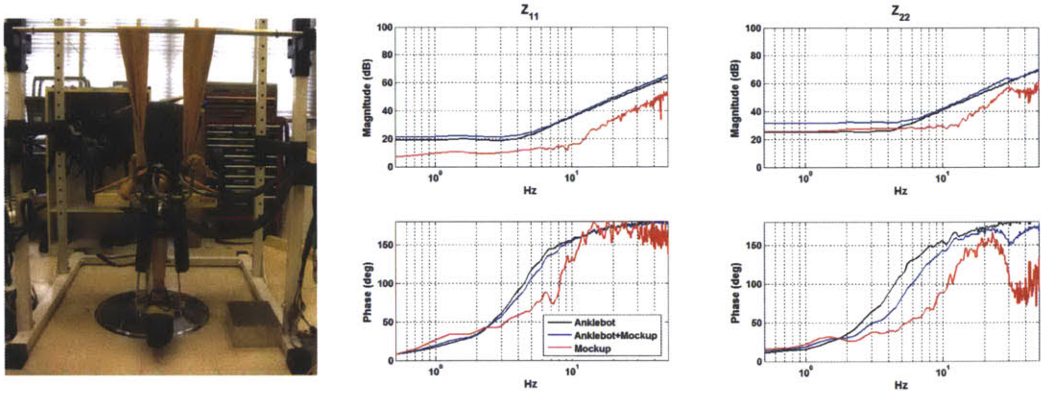

Figure F.1: Resonance and anti-resonance behavior of the shoe bracket. Black: Anklebot, Blue: Anklebot + Mockup, Red: Mockup.

Mechanical impedance of the mockup in joint coordinates was identified following the same procedure used in human subjects. Magnitude response over about 30 Hz and phase response over about 20 Hz were similar to those observed in human subjects (Figure F.1

(right)). Although not included, similar resonance and anti-resonance behavior was observed when the bracket was directly connected to the wooden block and measurement was performed without the shoe. In conclusion, the observed resonance and anti-resonance behavior was originated from the shoe bracket not from the ankle.

Appendix G: Directional Variation of Dynamic Ankle Impedance of Individual Subject

Directional variation of dynamic ankle impedance was represented both by the direction dependent map and ellipse representation. Results of individual subjects under relaxed muscles are shown in Figure G.1 ~ Figure G.4, and results under active muscles are provided in Figure G.5 ~ Figure G.12.

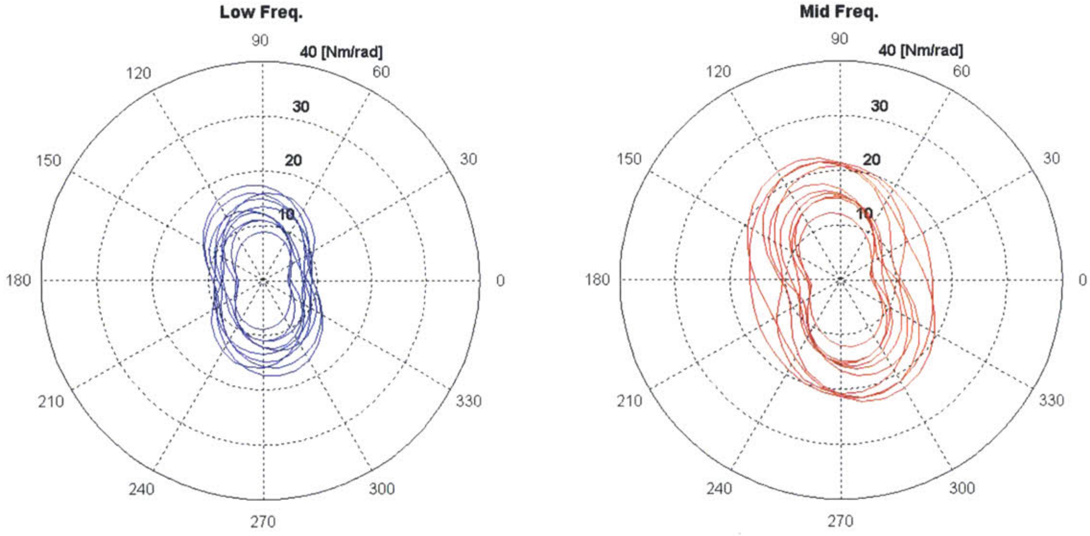

Figure G.1: Anisotropy of dynamic ankle impedance in seated posture. Left: low-frequency impedance, right: mid-frequency impedance

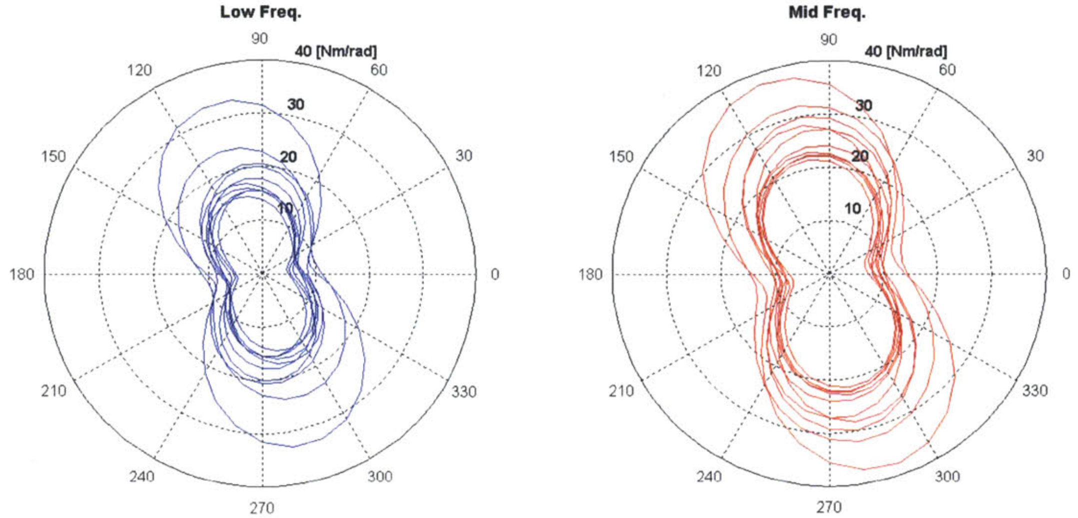

Figure G.2: Anisotropy of dynamic ankle impedance in standing posture.

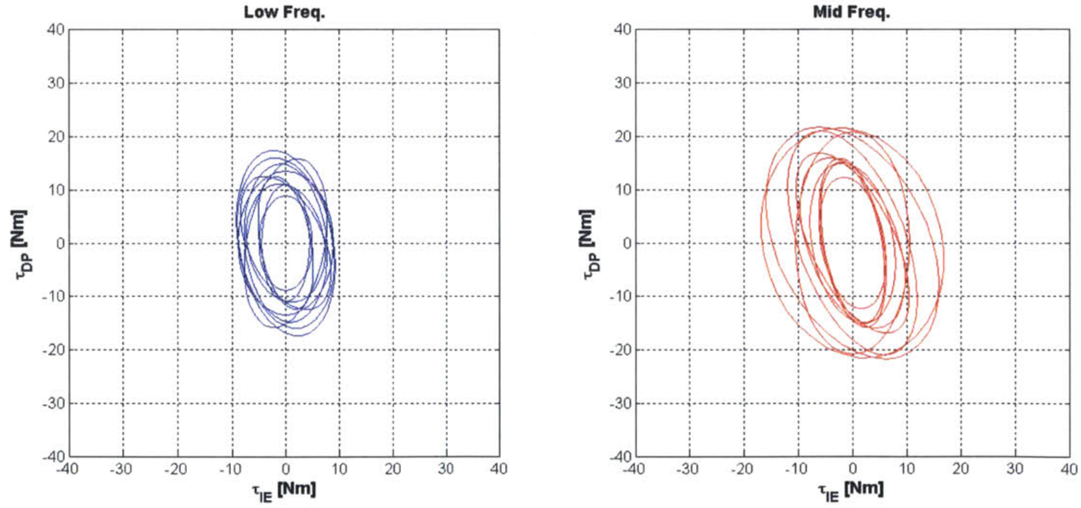

Figure G.3: Ellipse representation of dynamic ankle impedance in seated posture.

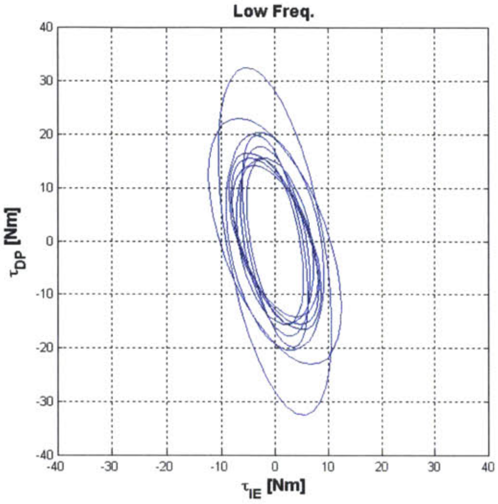

Figure G.4: Ellipse representation of dynamic ankle impedance in standing posture.

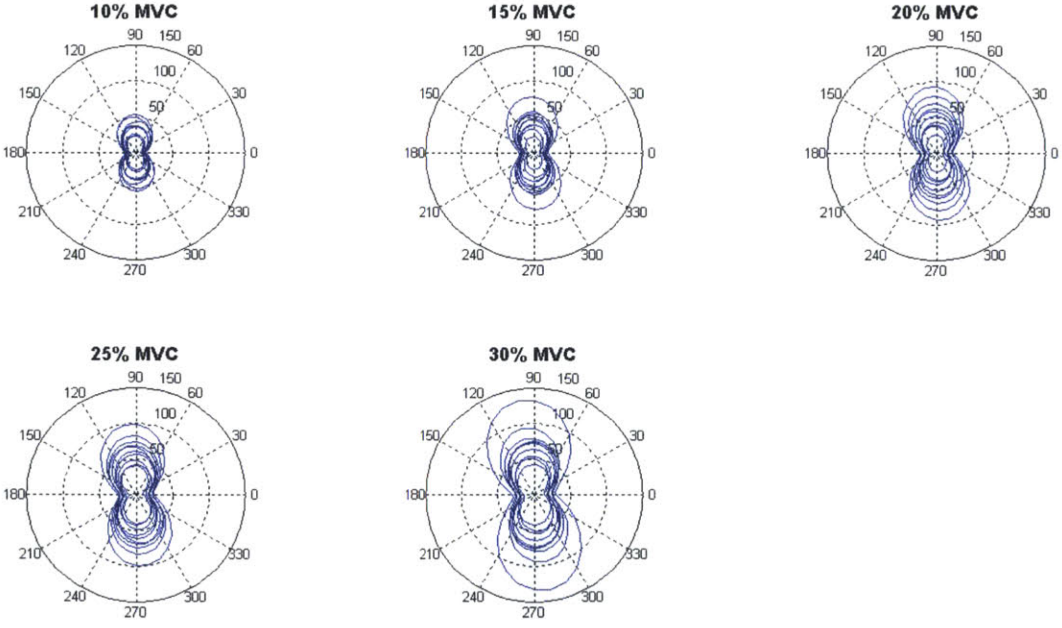

Figure G.5: Anisotropy of dynamic ankle impedance in the TA study (Low-frequency impedance). Unit: Nm/rad.

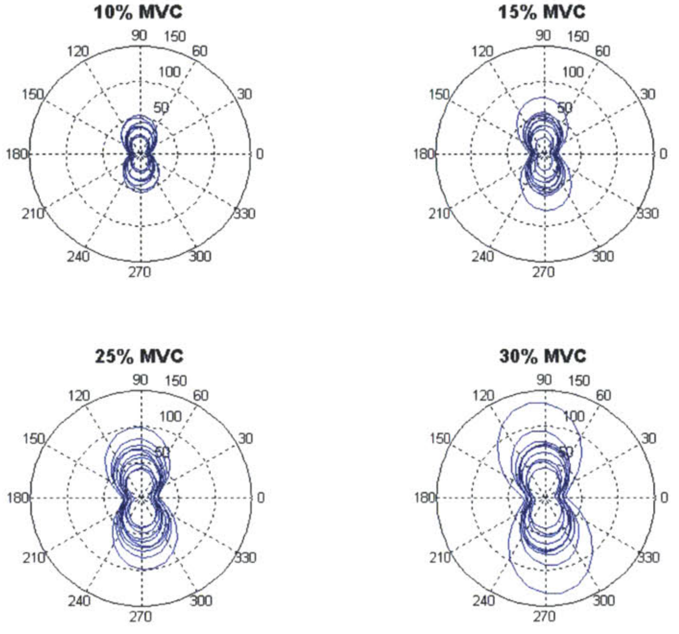

Figure G.6: Anisotropy of dynamic ankle impedance in the TA study (Mid-frequency impedance).

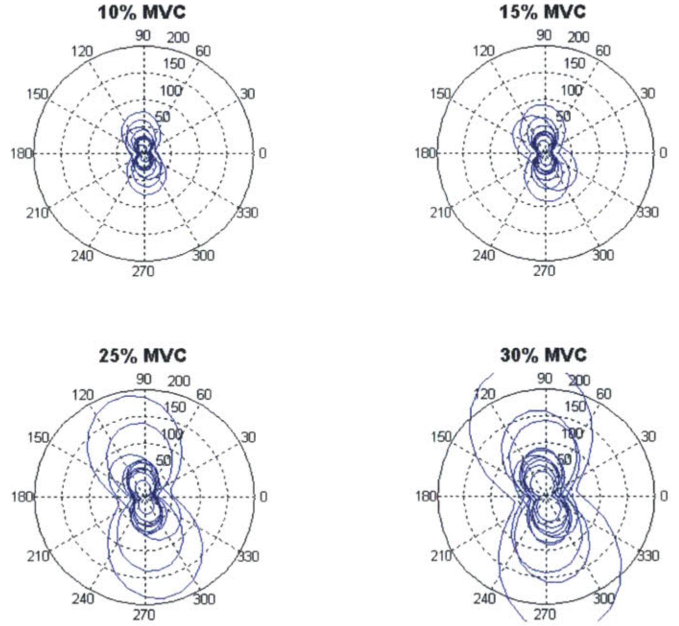

Figure G.7: Anisotropy of dynamic ankle impedance in the SOL study (Low-frequency impedance).

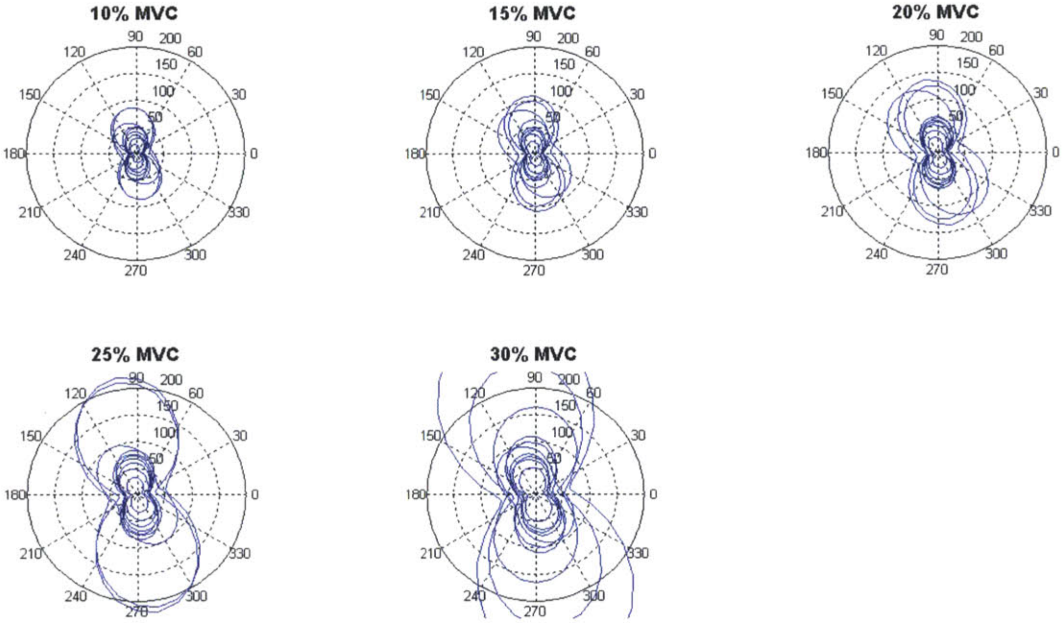

Figure G.8: Anisotropy of dynamic ankle impedance in the SOL study (Mid-frequency impedance).

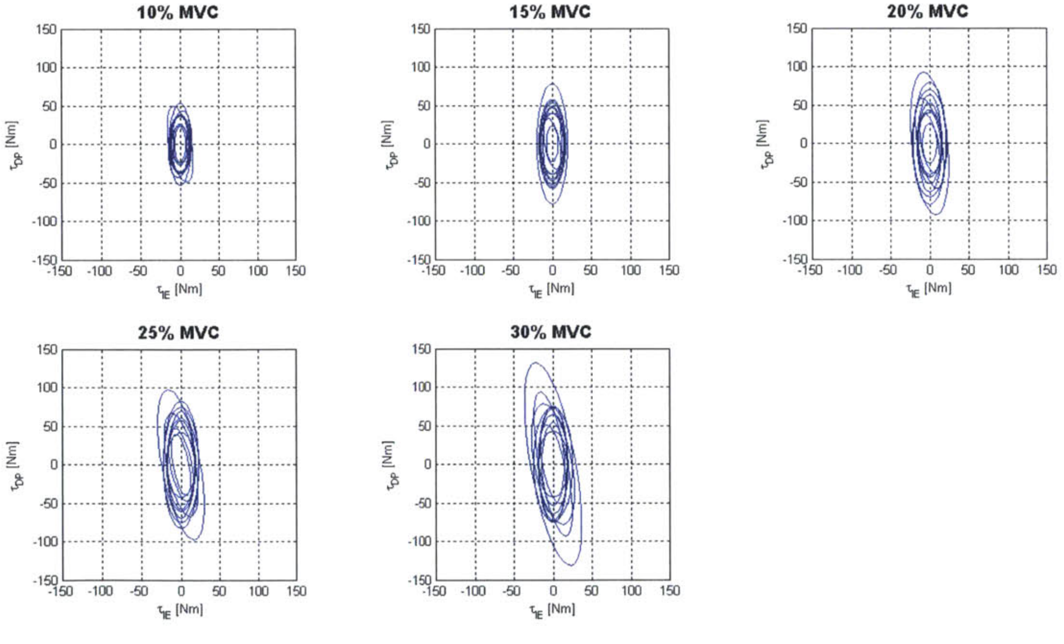

Figure G.9: Ellipse representation of dynamic ankle impedance in the TA study (Low-frequency impedance).

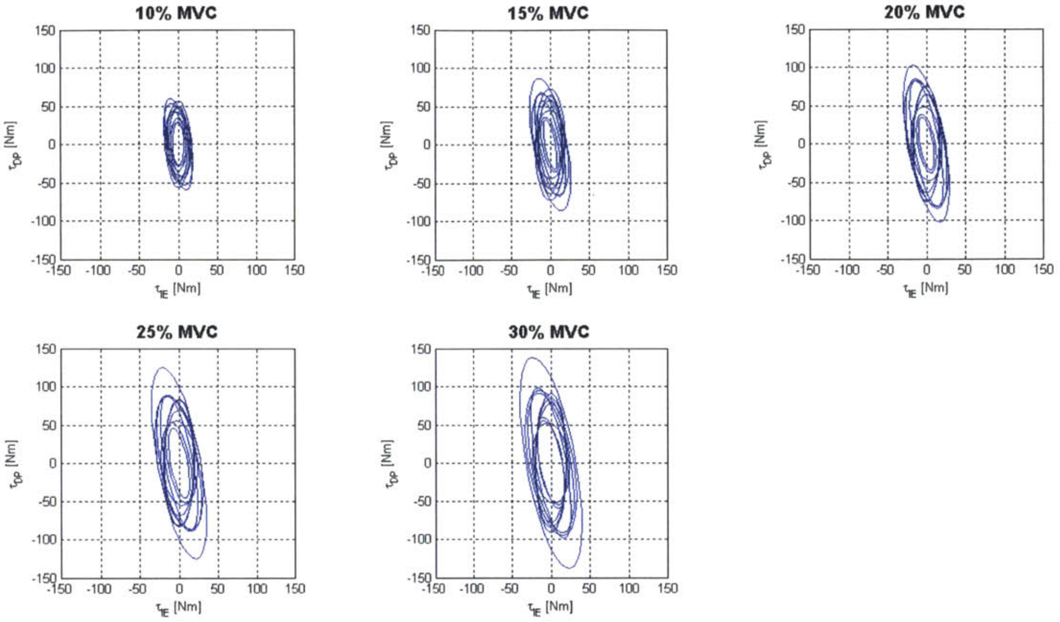

Figure G.10: Ellipse representation of dynamic ankle impedance in the TA study (Mid-frequency impedance).

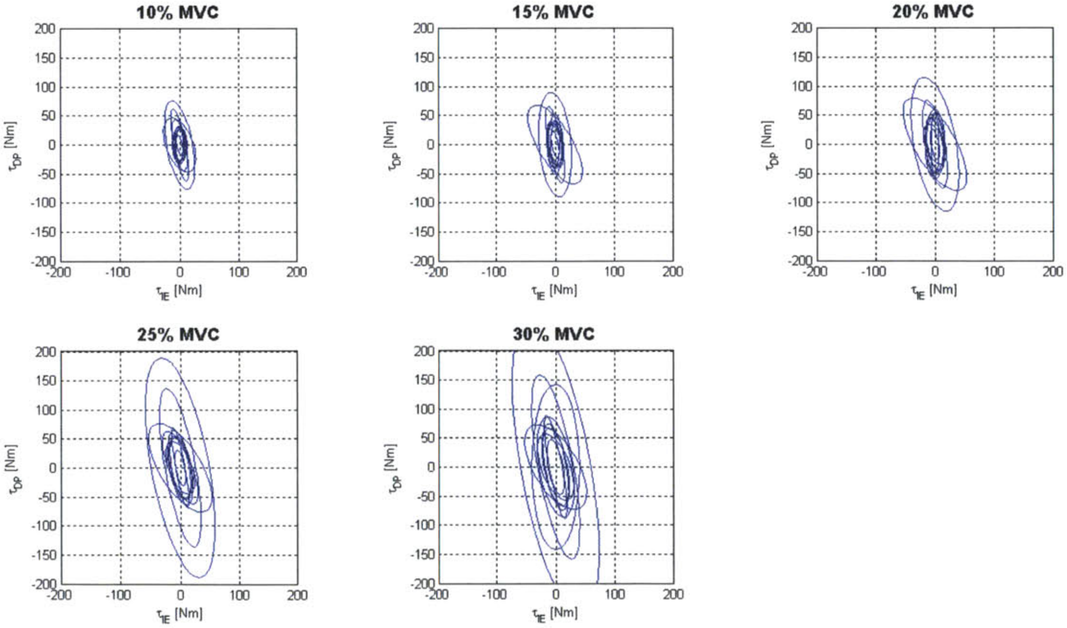

Figure G.11: Ellipse representation of dynamic ankle impedance in the SOL study (Low-frequency impedance).

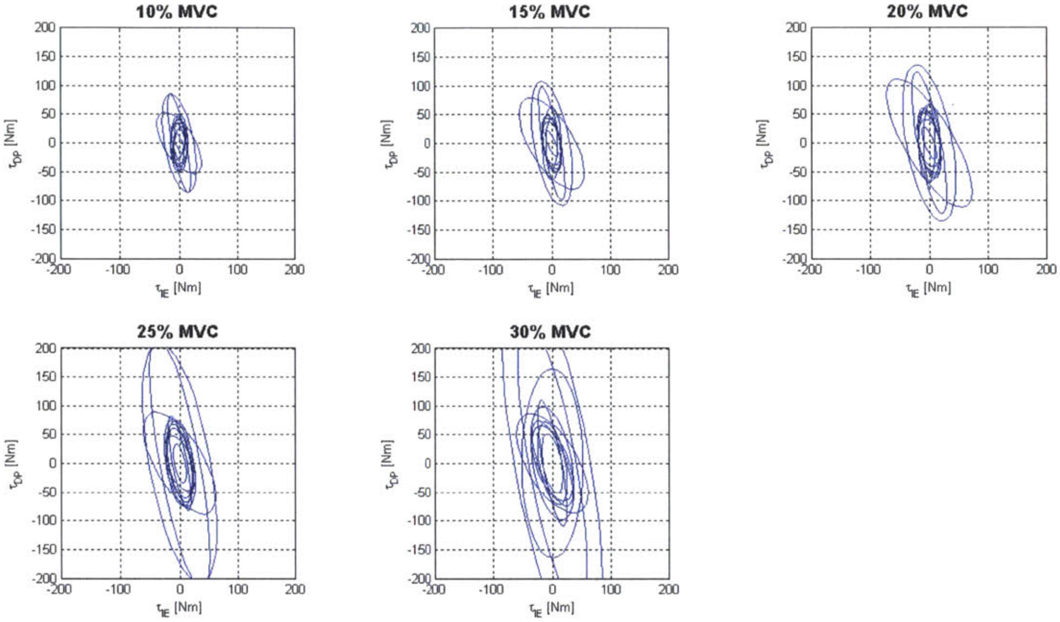

Figure G.12: Ellipse representation of dynamic ankle impedance in the SOL study (Mid-frequency impedance).

Appendix H: Effect of Kinematic Stiffness

Increased activation of muscles around a joint does not guarantee that the corresponding joint stiffness will also increase. A confounding factor arises from the nonlinear kinematic relation between joint angle and muscle length, $l = l(\theta_{DP}, \theta_{IE}) = l(\boldsymbol{\theta})$.

The derivative of muscle length with respect to joint angle determines the moment arms of the muscle force about the joint, $r_{DP}(\boldsymbol{\theta}) = \partial l / \partial \theta_{DP}$ and $r_{IE}(\boldsymbol{\theta}) = \partial l / \partial \theta_{IE}$, and hence the relation between muscle force and the corresponding joint torques, $\tau_{DP} = r_{DP}(\boldsymbol{\theta}) f$ and $\tau_{IE} = r_{IE}(\boldsymbol{\theta}) f$. As indicated, in general the moment arms vary with joint angle. As a result, when the muscle generates force, part of the joint stiffness arises from this variable moment arm.

For example, DP stiffness is $K_{DP} = \partial \tau_{DP} / \partial \theta_{DP} = r_{DP}(\theta)(\partial f / \partial l)(\partial l / \partial \theta_{DP}) + (\partial r_{DP} / \partial \theta_{DP}) f$. The first term in this expression is the muscle stiffness times the square of the moment arm (as required for consistency of units). The second term is due to the nonlinear kinematics and is proportional to muscle force. Because of human endo-skeletal anatomy, for modest displacements of the joint from its neutral posture this "kinematic stiffness" is negative; the muscle-generated torque acts to move the limb in a direction that increases the muscle moment arm. Consequently, if the stiffness of muscle and passive tissues around the joint were constant, co-contraction of opposing muscles would act to decrease the joint stiffness. If sufficiently large muscle forces could be exerted, joint stiffness would become negative, i.e. statically unstable. This is conceptually similar to the Euler buckling of a column under compressive loading. Of course, muscle stiffness is not constant but is generally observed to increase with activation. However, unless muscle stiffness increases more rapidly with force than the "kinematic stiffness" decreases with force, co-contraction of opposing muscles will decrease net joint stiffness.

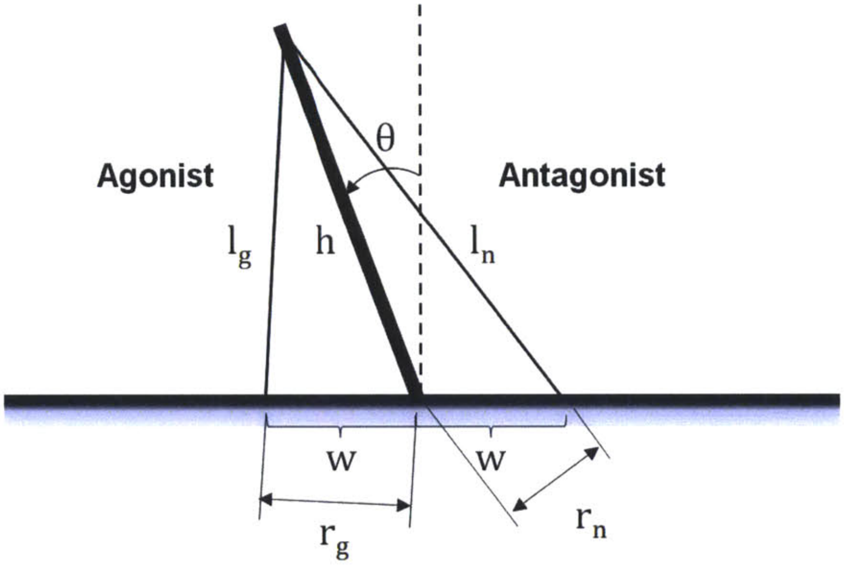

Figure H.1: A simple musculoskeletal model. Two identical muscles are depicted by the thin lines. Positive (negative) angles imply flexion (extension). The joint axis and the muscle origins lie on a straight line with each muscle origin at a distance w from the joint axis. The muscle insertions are each at a distance h axially along the bone (thick line) from the joint. The joint angle is denoted as θ and the muscle length for the agonist and antagonist is l_g and l_n, respectively.

An example may clarify the conditions under which negative joint stiffness may occur. Consider a single limb segment with two identical muscles (Figure H.1) having a linear force-length-activation relation with a constant stiffness as Eq. (H.1):

$$F_i = \begin{cases} u_i F_0 + k(l_i - l_0), & \text{if } F_i \geq 0 \\ 0 \quad , & \text{otherwise} \end{cases} \tag{H.1}$$

where $F_i \geq 0$ is muscle force (muscles pull and can't push), $u_i \geq 0$ is a dimensionless measure of neural activation, F_0 is a scaling constant with dimensions of force, k is muscle stiffness, l_i is muscle length and l_0 is muscle length at rest.

Muscle lengths (l_g and l_n) and moment arms (r_g and r_n) of agonist and antagonist muscles are derived from kinematic relations of the model (Eq. (H2) and Eq. (H3)). As θ increases from zero, r_g increases while r_n decreases. Note that $dl_g/d\theta$ is negative because increasing angle shortens the agonistic muscle.

$$\begin{aligned} l_g &= \sqrt{h^2 + w^2 - 2hw\sin(\theta)} \\ l_n &= \sqrt{h^2 + w^2 + 2hw\sin(\theta)} \end{aligned} \tag{H.2}$$

$$\begin{aligned} r_g &= -\frac{dl_g}{d\theta} = \frac{hw\cos(\theta)}{l_g} \\ r_n &= \frac{dl_n}{d\theta} = \frac{hw\cos(\theta)}{l_n} \end{aligned} \tag{H.3}$$

The net joint moment (τ) is as Eq. (H.4), and the torque restoring the limb to any posture within the range $-\pi/2 \leq \theta \leq \pi/2$ has the opposite sign, $\tau_{restoring} = -\tau$.

$$\tau = \tau_g - \tau_n = r_g F_g - r_n F_n = \frac{hw\cos(\theta)}{l_g} F_g - \frac{hw\cos(\theta)}{l_n} F_n \tag{H.4}$$

The net joint stiffness (K) is derived from Eq. (H.4), which has terms of two different types as explained above: the "kinematic stiffness" due to the variation of moment arms with joint angle, and the usual spring-like stiffness due to the variation of muscle force with muscle length (Eq. (H.5)).

$$
\begin{aligned}
K = \frac{\partial \tau_{restoring}}{\partial \theta} &= -\frac{\partial}{\partial \theta}(r_g F_g - r_n F_n) \\
&= -\frac{dr_g}{d\theta} F_g - r_g \frac{\partial F_g}{\partial l_g}\frac{dl_g}{d\theta} + \frac{dr_n}{d\theta} F_n + r_n \frac{\partial F_n}{\partial l_n}\frac{dl_n}{d\theta} \\
&= -\frac{dr_g}{d\theta} F_g + \frac{dr_n}{d\theta} F_n + (r_g{}^2 + r_n{}^2)k \\
&= -\gamma_g F_g + \gamma_n F_n + (r_g{}^2 + r_n{}^2)k \\
&= -\gamma_g \{u_g F_0 + k(l_g - l_0)\} + \gamma_n \{u_n F_0 + k(l_n - l_0)\} + (r_g{}^2 + r_n{}^2)k
\end{aligned}
\tag{H.5}
$$

where derivatives of moment arms (γ_g and γ_n) are as Eq. (H.6):

$$
\begin{aligned}
\gamma_g &= \frac{dr_g}{d\theta} = \frac{hw}{l_g}(-\sin(\theta) + \frac{hw}{l_g{}^2}\cos^2(\theta)) \\
\gamma_n &= \frac{dr_n}{d\theta} = -\frac{hw}{l_n}(\sin(\theta) + \frac{hw}{l_n{}^2}\cos^2(\theta))
\end{aligned}
\tag{H.6}
$$

Thus, the stiffness of each muscle contributes positive (stabilizing) joint stiffness. However, the "kinematic stiffness" may be negative and, in this case, it is.

Simulation results of this model are provided in Figure H.2, assuming $\tau = 0$ (both muscles are equally active) and $\theta = 0$. Parameters used in simulations are as follows: $F_0 = 5000N, k = 10000N/m, \quad w = 0.03m, h = 0.2m$.

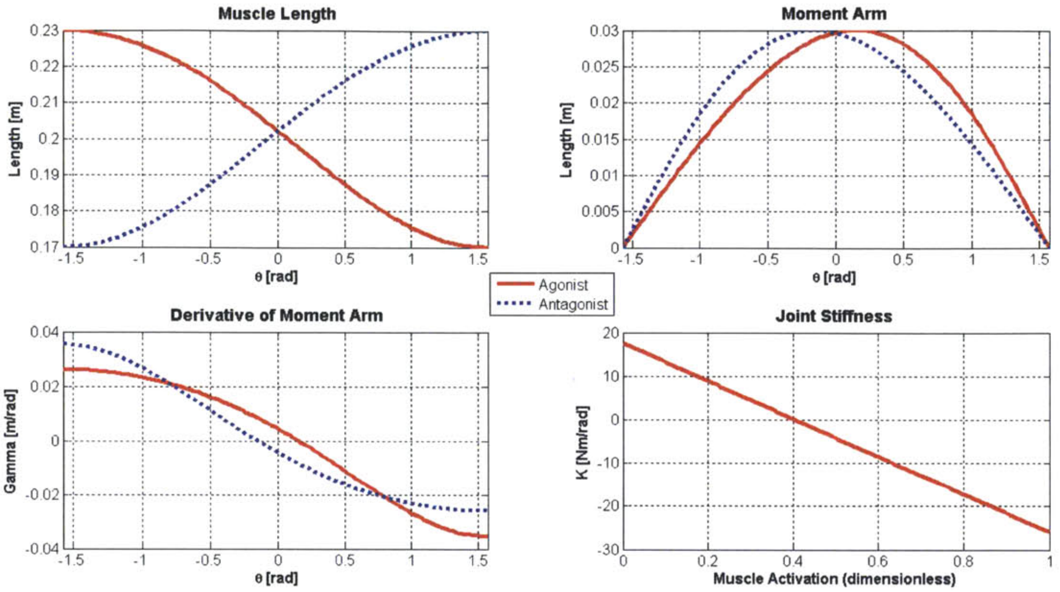

Figure H.2: Simulation results of a simple musculoskeletal model. Both antagonist muscles are equally active ($u_g = u_n, \tau = 0$), enabling investigation of joint stiffness at $\theta = 0$. Top left: muscle length vs. joint angle; Top right: moment arm; Bottom left: derivative of moment arm vs. joint angle; Bottom right: joint stiffness vs. muscle activation. If $u_g = u_n > 0.41$, the joint stiffness is negative.

Joint stiffness declines with muscle co-contraction and for sufficiently large muscle activation, joint stiffness becomes negative (Figure H.2 (bottom right)).

Even when a single muscle is considered (for example, the agonist, and K can be redefined as in Eq. (H.7), the effect of kinematic stiffness is still present. Compared to co-contraction of antagonistic muscles, the magnitude of the kinematic effect is smaller because the contribution of $\gamma_n u_n F_0$ in Eq. (H.5), which is negative, is absent in single muscle activation.

$$K = -\gamma_g \{u_g F_0 + k(l_g - l_0)\} + \gamma_n \{k(l_n - l_0)\} + ({r_g}^2 + {r_n}^2)k \qquad \text{(H.7)}$$

Appendix I: Temporal Distribution of Walking Data

Histograms of the stride duration, stance duration, and swing duration of each subject are provided in Figure I.1~Figure I.3.

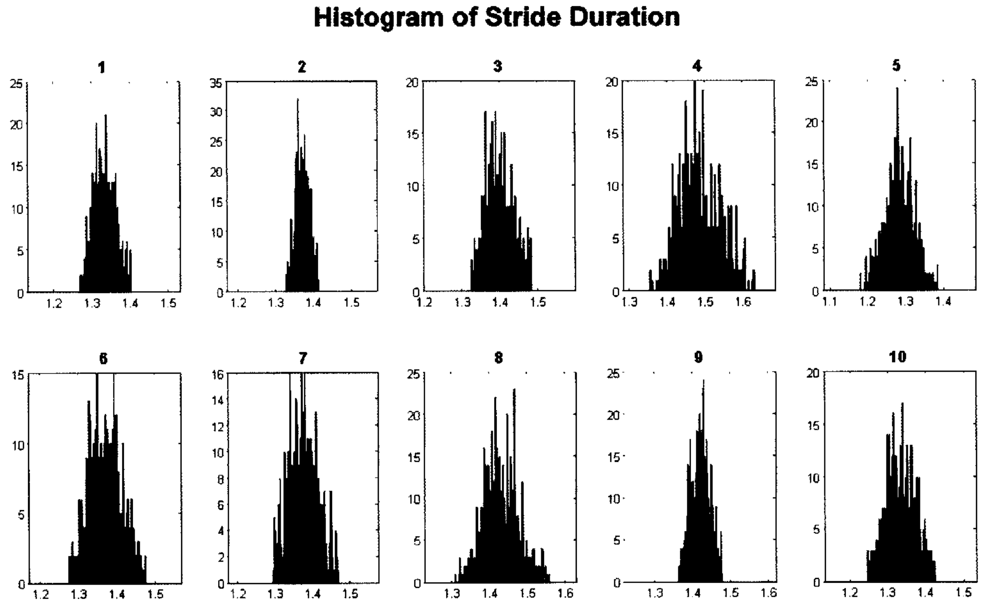

Figure I.1: Histogram of stride duration. The x-axis represents stride duration (unit: second), and y-axis denotes count. Each plot represents the result of individual subject.

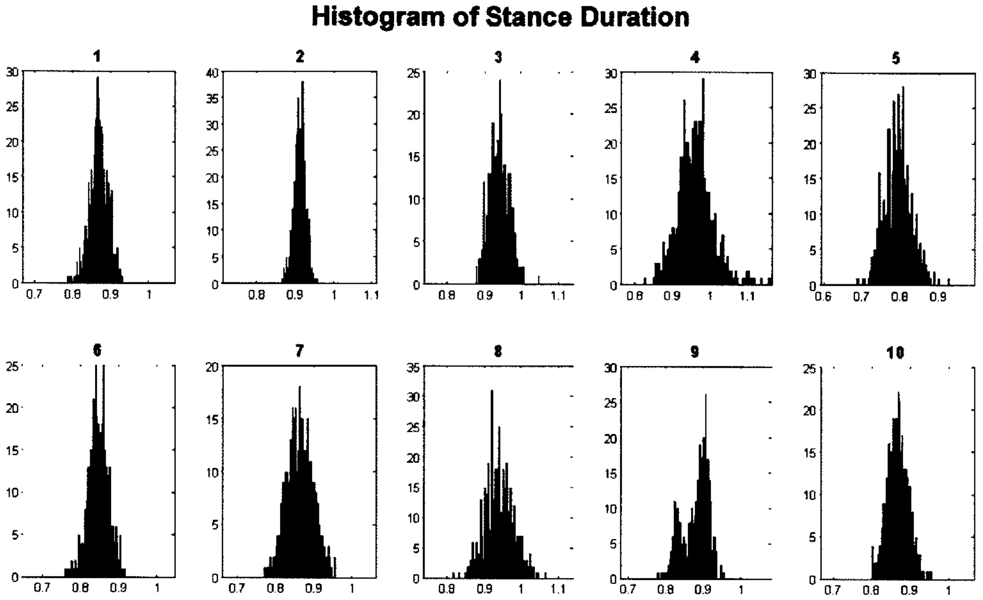

Figure I.2: Histogram of stance duration. The x-axis represents stance duration (unit: second).

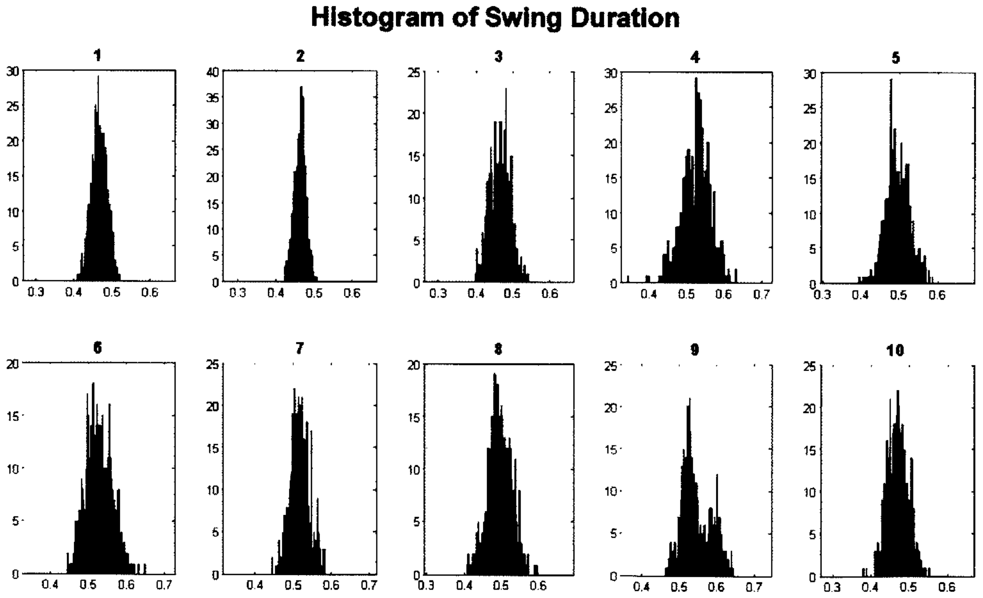

Figure I.3: Histogram of swing duration. The x-axis represents swing duration (unit: second).

Appendix J: Time-Varying Ankle Parameters in Sub-Gait Phases

Results of IRF estimates, 2nd order model approximates, reliability measures, and identified ankle parameters in 5 sub-gait phases of individual subject are provided in Figure J.1 ~ J.3.

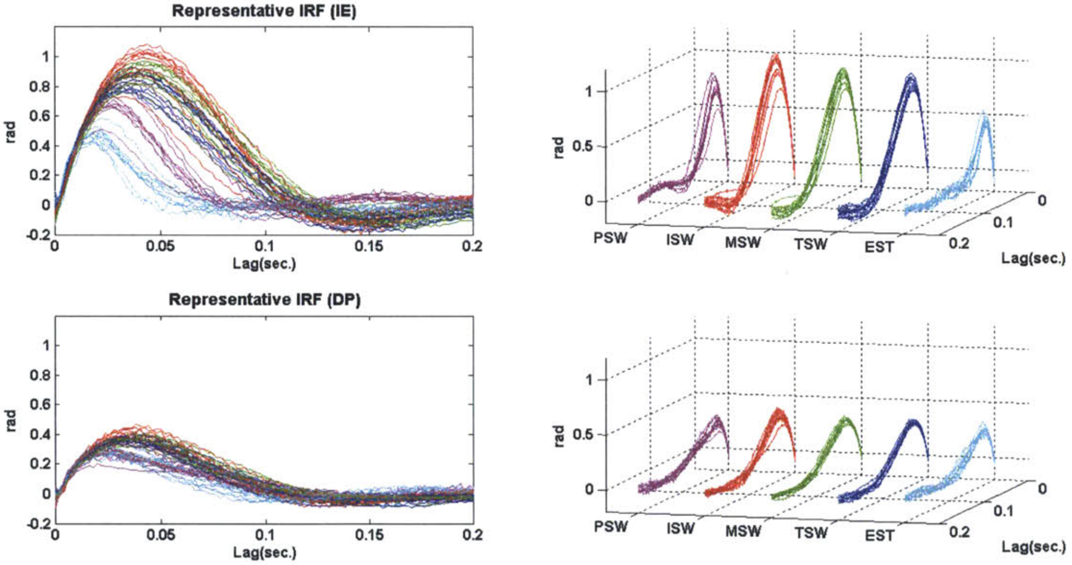

Figure J.1: IRF estimates of individual subject in sub-gait phases. 1st row: IE direction, 2nd row: DP direction. 1st column: 2D representation. 2nd column: 3D representation. Each plot represents the result of individual subject (magenta: PSW, red: ISW, green: MSW, blue: TSW, cyan: EST).

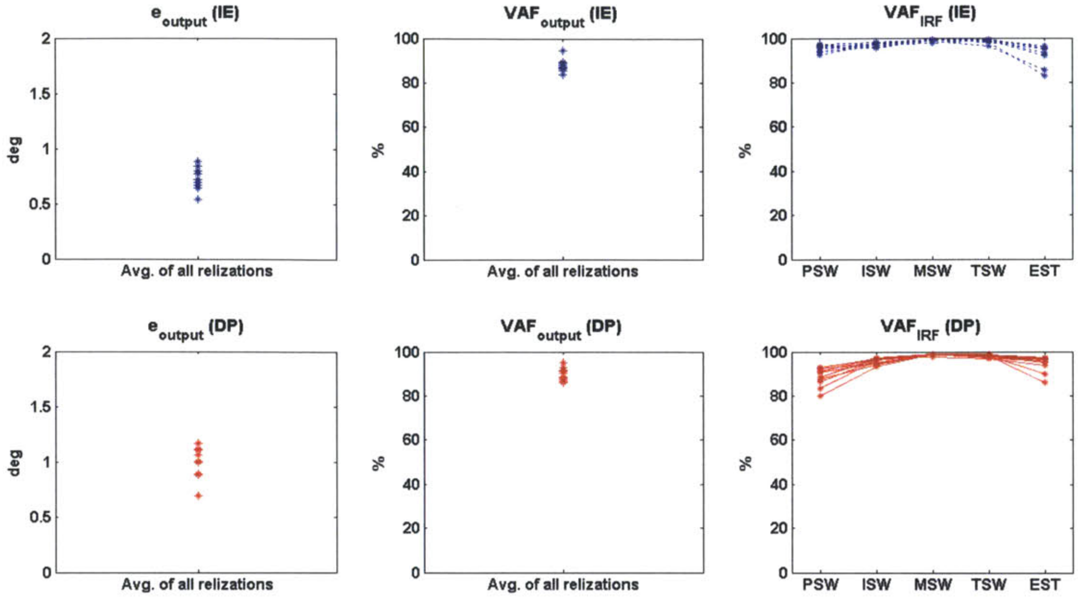

Figure J.2: Reliability measures for IRF estimation (VAF_{output} and e_{output}) and 2nd order model approximation (VAF_{IRF}) of individual subject. 1st row: IE direction, 2nd row: DP direction.

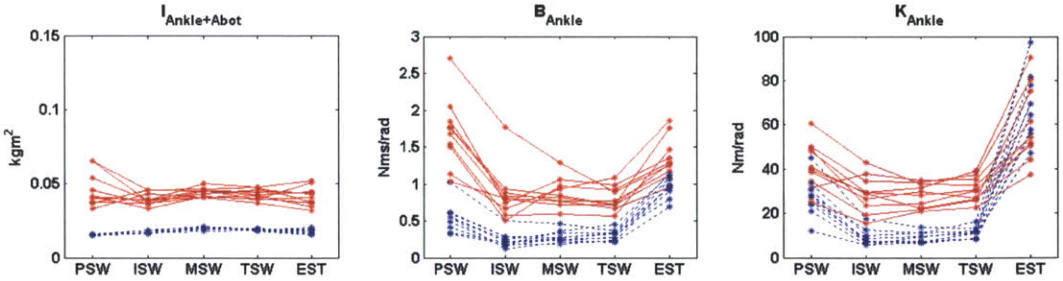

Figure J.3: Time-varying ankle parameters of individual subject in sub-gait phases. Solid red line: DP direction, dotted blue line: IE direction.

Parameter changes around HS and TO of individual subject are also provided in Figure J.4 and J.5.

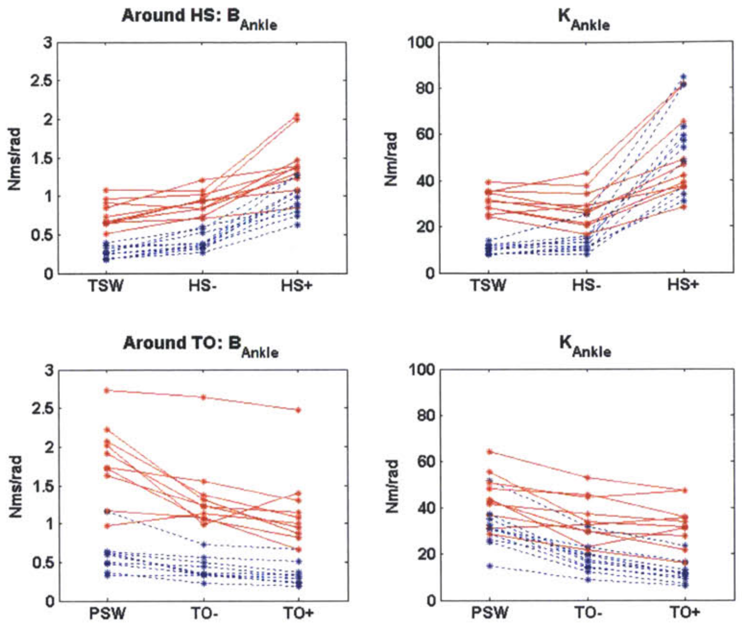

Figure J.4: Ankle parameter changes around HS and TO. 1st row: around HS, 2nd row: around TO.

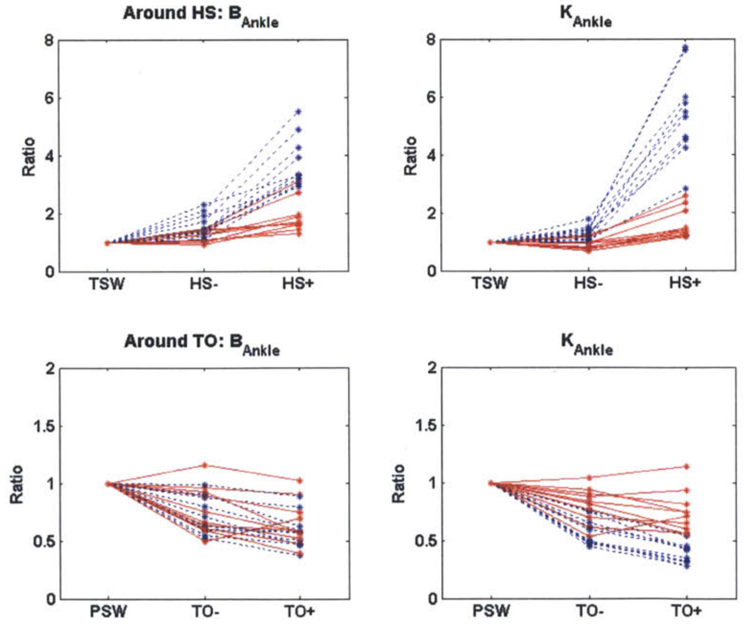

Figure J.5: Ankle impedance increase ratio around HS and TO. The same format as in Figure J.4.

Bibliography

[1] T. F. Novacheck, "The biomechanics of running," *Gait & Posture,* vol. 7, no. 1, pp. 77-95, Jan, 1998.

[2] J. Perry, "Gait Analysis: Normal and Pathologic Functions," *Slack Inc., New Jersey*, 1992.

[3] P. DeVita, J. Helseth, and T. Hortobagyi, "Muscles do more positive than negative work in human locomotion," *Journal of Experimental Biology,* vol. 210, no. 19, pp. 3361-3373, Oct 1, 2007.

[4] D. A. Winter, "Energy Generation and Absorption at the Ankle and Knee during Fast, Natural, and Slow Cadences," *Clinical Orthopaedics and Related Research*, no. 175, pp. 147-154, 1983.

[5] T. F. Winters, J. R. Gage, and R. Hicks, "Gait Patterns in Spastic Hemiplegia in Children and Young-Adults," *Journal of Bone and Joint Surgery-American Volume,* vol. 69A, no. 3, pp. 437-441, Mar, 1987.

[6] A. Lamontagne, F. Malouin, and C. L. Richards, "Contribution of passive stiffness to ankle plantarflexor moment during gait after stroke," *Archives of Physical Medicine and Rehabilitation,* vol. 81, no. 3, pp. 351-358, Mar, 2000.

[7] S. Siegler, G. D. Moskowitz, and W. Freedman, "Passive and Active Components of the Internal Moment Developed About the Ankle Joint during Human Ambulation," *Journal of Biomechanics,* vol. 17, no. 9, pp. 647-652, 1984.

[8] N. Hogan, and P. C. Breedveld, "The physical basis of analogies in physical system models," *The Mechatronics Handbook: Mechatronic Systems, Sensors, and Actuators. CRC Press,* vol. 2nd Ed., no. Chapter 16, 2008.

[9] S. K. Charles, "It's All in the Wrist: A Quantitative Characterization of Human Wrist Control," *MIT Ph.D Thesis*, 2008.

[10] N. Hogan, "The Mechanics of Multi-Joint Posture and Movement Control," *Biological Cybernetics,* vol. 52, no. 5, pp. 315-331, 1985.

[11] F. A. Mussa-Ivaldi, N. Hogan, and E. Bizzi, "Neural, mechanical, and geometric factors subserving arm posture in humans," *J Neurosci,* vol. 5, no. 10, pp. 2732-43, Oct, 1985.

[12] H. I. Krebs, L. Dipietro, S. Levy-Tzedek *et al.*, "A paradigm shift for rehabilitation robotics," *IEEE Engineering in Medicine and Biology Magazine,* vol. 27, no. 4, pp. 61-70, Jul-Aug, 2008.

[13] L. Q. Zhang, G. Wang, T. Nishida *et al.*, "Hyperactive tendon reflexes in spastic multiple sclerosis: measures and mechanisms of action," *Arch Phys Med Rehabil,* vol. 81, no. 7, pp. 901-9, Jul, 2000.

[14] S. G. Chung, E. van Rey, Z. Q. Bai *et al.*, "Biomechanic changes in passive properties of hemiplegic ankles with spastic hypertonia," *Archives of Physical Medicine and Rehabilitation,* vol. 85, no. 10, pp. 1638-1646, Oct, 2004.

[15] M. M. Mirbagheri, H. Barbeau, M. Ladouceur *et al.*, "Intrinsic and reflex stiffness in normal and spastic, spinal cord injured subjects," *Exp Brain Res,* vol. 141, no. 4, pp. 446-59, Dec, 2001.

[16] A. M. Dollar, and H. Herr, "Lower extremity exoskeletons and active orthoses: Challenges and state-of-the-art," *IEEE Transactions on Robotics,* vol. 24, no. 1, pp. 144-158, Feb, 2008.

[17] C. H. Barnett, and J. R. Napier, "The Axis of Rotation at the Ankle Joint in Man - Its Influence Upon the Form of the Talus and the Mobility of the Fibula," *Journal of Anatomy,* vol. 86, no. 1, pp. 1-&, 1952.

[18] M. Nordin, and V. H. Frankel, "Basic biomechanics of the musculoskeletal system," *Lippincott Williams & Wilkins; 3 edition*, 2001.

[19] H. I. Krebs, N. Hogan, M. L. Aisen *et al.*, "Robot-Aided Neurorehabilitation," *IEEE Transactions on Rehabilitation Engineering,* vol. 6, no. 1, pp. 75-87, Mar, 1998.

[20] H. Gomi, and M. Kawato, "Equilibrium-point control hypothesis examined by measured arm stiffness during multijoint movement," *Science,* vol. 272, no. 5258, pp. 117-120, Apr 5, 1996.

[21] T. Flash, and F. Mussaivaldi, "Human Arm Stiffness Characteristics during the Maintenance of Posture," *Experimental Brain Research,* vol. 82, no. 2, pp. 315-326, 1990.

[22] H. Gomi, and M. Kawato, "Human arm stiffness and equilibrium-point trajectory during multi-joint movement," *Biological Cybernetics,* vol. 76, no. 3, pp. 163-171, Mar, 1997.

[23] E. de Vlugt, A. C. Schouten, and F. C. T. van der Helm, "Closed-loop multivariable system identification for the characterization of the dynamic arm compliance using continuous force disturbances: a model study," *Journal of Neuroscience Methods,* vol. 122, no. 2, pp. 123-140, Jan 30, 2003.

[24] J. J. Palazzolo, M. Ferraro, H. I. Krebs *et al.*, "Stochastic estimation of arm mechanical impedance during robotic stroke rehabilitation," *IEEE Transactions on Neural Systems and Rehabilitation Engineering,* vol. 15, no. 1, pp. 94-103, Mar, 2007.

[25] E. J. Perreault, R. F. Kirsch, and A. M. Acosta, "Multiple-input, multiple-output system identification for characterization of limb stiffness dynamics," *Biological Cybernetics,* vol. 80, no. 5, pp. 327-337, May, 1999.

[26] P. H. Chang, and S. H. Kang, "Stochastic estimation of human arm impedance under nonlinear friction in robot joints: A model study," *Journal of Neuroscience Methods,* vol. 189, no. 1, pp. 97-112, May 30, 2010.

[27] D. J. Bennett, J. M. Hollerbach, Y. Xu *et al.*, "Time-Varying Stiffness of Human Elbow Joint during Cyclic Voluntary Movement," *Experimental Brain Research,* vol. 88, no. 2, pp. 433-442, Feb, 1992.

[28] L. Q. Zhang, and W. Z. Rymer, "Simultaneous and nonlinear identification of mechanical and reflex properties of human elbow joint muscles," *IEEE Transactions on Biomedical Engineering,* vol. 44, no. 12, pp. 1192-1209, Dec, 1997.

[29] F. Popescu, J. M. Hidler, and W. Z. Rymer, "Elbow impedance during goal-directed movements," *Experimental Brain Research,* vol. 152, no. 1, pp. 17-28, Sep, 2003.

[30] H. I. Krebs, B. T. Volpe, D. Williams *et al.*, "Robot-aided neurorehabilitation: A robot for wrist rehabilitation," *IEEE Transactions on Neural Systems and Rehabilitation Engineering,* vol. 15, no. 3, pp. 327-335, Sep, 2007.

[31] D. Formica, S. K. Charles, L. Zollo *et al.*, "The passive stiffness of the wrist and forearm," *Journal of Neurophysiology,* vol. 108, no. 4, pp. 1158-1166, Aug, 2012.

[32] A. H. Hansen, D. S. Childress, S. C. Miff *et al.*, "The human ankle during walking: implications for design of biomimetic ankle prostheses," *Journal of Biomechanics,* vol. 37, no. 10, pp. 1467-1474, 2004.

[33] D. A. Winter, A. E. Patla, S. Rietdyk *et al.*, "Ankle muscle stiffness in the control of balance during quiet standing," *Journal of Neurophysiology,* vol. 85, no. 6, pp. 2630-2633, Jun, 2001.

[34] R. B. Davis, and P. A. De Luca, "Gait characterization via dynamic joint stiffness," *Gait & Posture,* vol. 4, no. 3, pp. 224-231, 1996.

[35] M. Gunther, and R. Blickhan, "Joint stiffness of the ankle and the knee in running," *Journal of Biomechanics,* vol. 35, no. 11, pp. 1459-1474, Nov, 2002.

[36] S. D. Lark, J. G. Buckley, S. Bennett *et al.*, "Joint torques and dynamic joint stiffness in elderly and young men during stepping down," *Clinical Biomechanics,* vol. 18, no. 9, pp. 848-855, Nov, 2003.

[37] K. Shamaei, and A. M. Dollar, "On the Mechanics of the Knee during the Stance Phase of the Gait," *In Proc. IEEE International Conference on Rehabilitation Robotics (ICORR2011),* 2011.

[38] M. L. Latash, and V. M. Zatsiorsky, "Joint Stiffness - Myth or Reality," *Human Movement Science,* vol. 12, no. 6, pp. 653-692, Dec, 1993.

[39] E. J. Rouse, R. D. Gregg, L. J. Hargrove *et al.*, "The Difference between Stiffness and Quasi-stiffness in the Context of Biomechanical Modeling," *IEEE Transactions on Biomedical Engineering,* vol. 60, no. 2, pp. 562-568, 2013.

[40] L. Q. Zhang, G. Nuber, J. Butler *et al.*, "In vivo human knee joint dynamic properties as functions of muscle contraction and joint position," *Journal of Biomechanics,* vol. 31, no. 1, pp. 71-76, Jan, 1998.

[41] S. Pfeifer, H. Vallery, M. Hardegger *et al.*, "Model-Based Estimation of Knee Stiffness," *IEEE Transactions on Biomedical Engineering,* vol. 59, no. 9, pp. 2604-2612, Sep, 2012.

[42] B. Koopman, E. F. van Asseldonk, and H. van der Kooij, "In vivo measurement of human knee and hip dynamics using MIMO system identification," *In Proc. 32nd Annual*

International IEEE Engineering in Medicine and Biology Society (EMBC2010) vol. 2010, pp. 3426-9, 2010.

[43] I. W. Hunter, and R. E. Kearney, "Dynamics of Human Ankle Stiffness - Variation with Mean Ankle Torque," *Journal of Biomechanics,* vol. 15, no. 10, pp. 747-752, 1982.

[44] R. E. Kearney, and I. W. Hunter, "Dynamics of Human Ankle Stiffness - Variation with Displacement Amplitude," *Journal of Biomechanics,* vol. 15, no. 10, pp. 753-756, 1982.

[45] R. E. Kearney, and I. W. Hunter, "System-Identification of Human Joint Dynamics," *Critical Reviews in Biomedical Engineering,* vol. 18, no. 1, pp. 55-87, 1990.

[46] P. L. Weiss, R. E. Kearney, and I. W. Hunter, "Position Dependence of Ankle Joint Dynamics .1. Passive Mechanics," *Journal of Biomechanics,* vol. 19, no. 9, pp. 727-735, 1986.

[47] P. L. Weiss, R. E. Kearney, and I. W. Hunter, "Position Dependence of Ankle Joint Dynamics .2. Active Mechanics," *Journal of Biomechanics,* vol. 19, no. 9, pp. 737-751, 1986.

[48] R. E. Kearney, R. B. Stein, and L. Parameswaran, "Identification of intrinsic and reflex contributions to human ankle stiffness dynamics," *IEEE Transactions on Biomedical Engineering,* vol. 44, no. 6, pp. 493-504, Jun, 1997.

[49] M. M. Mirbagheri, H. Barbeau, and R. E. Kearney, "Intrinsic and reflex contributions to human ankle stiffness: variation with activation level and position," *Experimental Brain Research,* vol. 135, no. 4, pp. 423-436, Dec, 2000.

[50] M. Lortie, and R. E. Kearney, "Identification of physiological systems: estimation of linear time-varying dynamics with non-white inputs and noisy outputs," *Medical & Biological Engineering & Computing,* vol. 39, no. 3, pp. 381-390, May, 2001.

[51] D. Ludvig, T. S. Visser, H. Giesbrecht *et al.*, "Identification of Time-Varying Intrinsic and Reflex Joint Stiffness," *IEEE Transactions on Biomedical Engineering,* vol. 58, no. 6, pp. 1715-1723, Jun, 2011.

[52] R. F. Kirsch, and R. E. Kearney, "Identification of time varying stiffness dynamics of the human ankle joint during an imposed movement," *Experimental Brain Research,* vol. 114, no. 1, pp. 71-85, Mar, 1997.

[53] J. B. Macneil, R. E. Kearney, and I. W. Hunter, "Identification of Time-Varying Biological-Systems from Ensemble Data," *IEEE Transactions on Biomedical Engineering,* vol. 39, no. 12, pp. 1213-1225, Dec, 1992.

[54] E. J. Rouse, L. J. Hargrove, E. J. Perreault *et al.*, "Estimation of Human Ankle Impedance during Walking Using the Perturberator Robot," *In Proc. 4th International IEEE Biomedical Robotics and Biomechatronics Conference*, pp. 373-378, 2012.

[55] S. J. Rydahl, and B. J. Brouwer, "Ankle stiffness and tissue compliance in stroke survivors: A validation of myotonometer measurements," *Archives of Physical Medicine and Rehabilitation,* vol. 85, no. 10, pp. 1631-1637, Oct, 2004.

[56] T. Kobayashi, A. K. L. Leung, Y. Akazawa *et al.*, "Quantitative measurement of spastic ankle joint stiffness using a manual device: A preliminary study," *Journal of Biomechanics,* vol. 43, no. 9, pp. 1831-1834, Jun 18, 2010.

[57] J. Harlaar, J. G. Becher, C. J. Snijders *et al.*, "Passive stiffness characteristics of ankle plantar flexors in hemiplegia," *Clinical Biomechanics,* vol. 15, no. 4, pp. 261-270, May, 2000.

[58] A. Saripalli, and S. Wilson, "Dynamic ankle stability and ankle orientation," *In Proceedings of the 7th symposium on footwear biomechanics*, 2005.

[59] S. M. Zinder, K. P. Granata, D. A. Padua *et al.*, "Validity and reliability of a new in vivo ankle stiffness measurement device," *Journal of Biomechanics,* vol. 40, no. 2, pp. 463-467, 2007.

[60] J. Mizrahi, Y. Ramot, and Z. Susak, "The dynamics of the subtalar joint in sudden inversion of the foot," *J Biomech Eng,* vol. 112, no. 1, pp. 9-14, Feb, 1990.

[61] A. Roy, H. I. Krebs, C. T. Bever *et al.*, "Measurement of passive ankle stiffness in subjects with chronic hemiparesis using a novel ankle robot," *Journal of Neurophysiology,* vol. 105, no. 5, pp. 2132-2149, May, 2011.

[62] A. Roy, H. I. Krebs, D. J. Williams *et al.*, "Robot-Aided Neurorehabilitation: A Novel Robot for Ankle Rehabilitation," *IEEE Transactions on Robotics,* vol. 25, no. 3, pp. 569-582, Jun, 2009.

[63] H. Lee, and N. Hogan, "Investigation of Human Ankle Mechanical Impedance during Locomotion using a Wearable Ankle Robot," *In Proc. 2013 IEEE International Conference on Robotics and Automation*, pp. 2636-2641, 2013.

[64] H. Lee, P. Ho, M. A. Rastgaar *et al.*, "Multivariable static ankle mechanical impedance with relaxed muscles," *Journal of Biomechanics,* vol. 44, no. 10, pp. 1901-1908, Jul 7, 2011.

[65] H. Lee, H. I. Krebs, and N. Hogan, "A Novel Characterization Method to Study Multivariable Human Joint Mechanical Impedance," *In Proc. 4th International IEEE Biomedical Robotics and Biomechatronics Conference*, pp. 1524-1529, 2012.

[66] H. Lee, S. Wang, and N. Hogan, "Relationship between Ankle Stiffness Structure and Muscle Activation," *In Proc. 34th Annual International IEEE Engineering in Medicine and Biology Society (EMBC2012)* pp. 4879-4882, 2012.

[67] H. Lee, P. Ho, M. A. Rastgaar *et al.*, "Multivariable static ankle mechanical impedance with active muscles," *IEEE Transaction on Neural Systems and Rehabilitation Engineering,* accepted.

[68] H. Lee, and N. Hogan, "Linear Time-Varying Identification of Ankle Mechanical Impedance during Human Walking," *In Proc. ASME Dynamic Systems and Control Conference (DSCC2012)*, pp. 1-6, 2012.

[69] H. Lee, T. Patterson, J. Ahn *et al.*, "Static Ankle Impedance in Stroke and Multiple Sclerosis: A Feasibility Study," *In Proc. 33rd Annual International IEEE Engineering in Medicine and Biology Society (EMBC2011)* pp. 8523-8526, 2011.

[70] F. L. Bookstein, "Principal Warps - Thin-Plate Splines and the Decomposition of Deformations," *IEEE Transactions on Pattern Analysis and Machine Intelligence,* vol. 11, no. 6, pp. 567-585, Jun, 1989.

[71] G. Wahba, *Spline models for observational data*, Philadelphia, Pa.: Society for Industrial and Applied Mathematics, 1990.

[72] P. M. Rack, and D. R. Westbury, "The short range stiffness of active mammalian muscle and its effect on mechanical properties," *J Physiol,* vol. 240, no. 2, pp. 331-50, Jul, 1974.

[73] F. A. Mussaivaldi, "From Basis Functions to Basis Fields - Vector Field Approximation from Sparse Data," *Biological Cybernetics,* vol. 67, no. 6, pp. 479-489, Oct, 1992.

[74] D. H. Odonoghue, "Treatment of Injuries to Athlethes," *Saunders Company, Philadelphia,* 1984.

[75] N. Rijnveld, and H. I. Krebs, "Passive wrist joint impedance in flexion-extension and abduction-adduction," *In Proc. 2007 IEEE 10th International Conference on Rehabilitation Robotics,* vol. Vols 1 and 2, pp. 43-47, 2007.

[76] N. Hogan, "On the Stability of Manipulators Performing Contact Tasks," *IEEE Journal of Robotics and Automation,* vol. 4, no. 6, pp. 677-686, Dec, 1988.

[77] J. Lorentzen, M. J. Grey, C. Crone *et al.*, "Distinguishing active from passive components of ankle plantar flexor stiffness in stroke, spinal cord injury and multiple sclerosis," *Clinical Neurophysiology,* vol. 121, no. 11, pp. 1939-1951, Nov, 2010.

[78] A. d'Avella, and E. Bizzi, "Shared and specific muscle synergies in natural motor behaviors," *Proceedings of the National Academy of Sciences of the United States of America,* vol. 102, no. 8, pp. 3076-3081, Feb 22, 2005.

[79] G. Torres-Oviedo, and L. H. Ting, "Subject-Specific Muscle Synergies in Human Balance Control Are Consistent Across Different Biomechanical Contexts," *Journal of Neurophysiology,* vol. 103, no. 6, pp. 3084-3098, Jun, 2010.

[80] A. M. Taylor, E. A. Christou, and R. M. Enoka, "Multiple features of motor-unit activity influence force fluctuations during isometric contractions," *Journal of Neurophysiology,* vol. 90, no. 2, pp. 1350-1361, Aug, 2003.

[81] R. Merletti, and P. J. Paker, *Electromyography: Physiology, Engineering, and Non-Invasive Applications*: Wiley, 2004.

[82] S. G. Rugg, R. J. Gregor, B. R. Mandelbaum *et al.*, "In vivo moment arm calculations at the ankle using magnetic resonance imaging (MRI)," *Journal of Biomechanics,* vol. 23, no. 5, pp. 495-501, 1990.

[83] S. S. Lee, and S. J. Piazza, "Inversion-eversion moment arms of gastrocnemius and tibialis anterior measured in vivo," *Journal of Biomechanics,* vol. 41, no. 16, pp. 3366-70, Dec 5, 2008.

[84] N. Hogan, "Mechanical Impedance of Single- and Multi-Articular System," *In: J.Winters and S.Woo (eds.) Multiple Muscle Systems: Biomechanics and Movement Organization, Springer-Verlag, New York*, pp. 149-164, 1990.

[85] R. Shadmehr, and M. A. Arbib, "A Mathematical-Analysis of the Force-Stiffness Characteristics of Muscles in Control of a Single Joint System," *Biological Cybernetics,* vol. 66, no. 6, pp. 463-477, Apr, 1992.

[86] N. Hogan, "Adaptive-Control of Mechanical Impedance by Coactivation of Antagonist Muscles," *IEEE Transactions on Automatic Control,* vol. 29, no. 8, pp. 681-690, 1984.

[87] N. Hogan, "Skeletal Muscle Impedance in the Control of Motor Actions," *Journal of Mechanics in Medicine and Biology,* vol. 2, no. 3-4, pp. 359-373, Sep-Dec, 2002.

[88] D. Rancourt, and N. Hogan, "The Biomechanics of Force Production," *Progress in Motor Control: A Multidisciplinary Perspective,* vol. 629, pp. 645-661, 2009.

[89] A. Lundberg, "Kinematics of the Ankle and Foot Invivo Roentgen Stereophotogrammetry - Introduction," *Acta Orthopaedica Scandinavica,* vol. 60, pp. 1-26, 1989.

[90] J. E. Colgate, and N. Hogan, "Robust-Control of Dynamically Interacting Systems," *International Journal of Control,* vol. 48, no. 1, pp. 65-88, Jul, 1988.

[91] N. Hogan, "Impedance Control - an Approach to Manipulation .1. Theory," *Journal of Dynamic Systems Measurement and Control-Transactions of the ASME,* vol. 107, no. 1, pp. 1-7, 1985.

[92] N. Hogan, "Impedance Control - an Approach to Manipulation .3. Applications," *Journal of Dynamic Systems Measurement and Control-Transactions of the ASME,* vol. 107, no. 1, pp. 17-24, 1985.

[93] N. Hogan, "Impedance Control - an Approach to Manipulation .2. Implementation," *Journal of Dynamic Systems Measurement and Control-Transactions of the ASME,* vol. 107, no. 1, pp. 8-16, 1985.

[94] E. K. Antonsson, and R. W. Mann, "The Frequency Content of Gait," *Journal of Biomechanics,* vol. 18, no. 1, pp. 39-47, 1985.

[95] K. R. Acharya, G. F. Harris, S. A. Riedel *et al.*, "Force Magnitude and Spectral Frequency Content of Heel Strike during Gait," *Images of the Twenty-First Century, Pts 1-6,* vol. 11, pp. 826-827, 1989.

[96] J. Bendat, and A. Piersol, "Random Data: Analysis and Measurement Process," *4th edition, Wiley*, 2010.

[97] P. D. Welch, "The use of fast fourier transform for the estimation of power spectra: a method based on time averaging over short, modified periodograms," *IEEE Transactions on Audio and Electroacoustics,* vol. 15, pp. 70-73, 1967.

[98] E. Colgate, and N. Hogan, "An Analysis of Contact Instability in Terms of Passive Physical Equivalents," *Proceedings - 1989 IEEE International Conference on Robotics and Automation, Vol 1-3*, pp. 404-409, 1989.

[99] E. Colgate, "The Control of Dynamically Interacting Systems " *PhD Dissertation at the Massachusetts Institute of Technology (MIT)*, 1988.

[100] J. J. E. Slotine, and W. Li, *Applied nonlinear control*, Englewood Cliffs, N.J.: Prentice Hall, 1991.

[101] J. F. Baumhauer, D. M. Alosa, P. A. F. H. Renstrom *et al.*, "A Prospective-Study of Ankle Injury Risk-Factors," *American Journal of Sports Medicine*, vol. 23, no. 5, pp. 564-570, Sep-Oct, 1995.

[102] E. Burdet, R. Osu, D. W. Franklin *et al.*, "A method for measuring endpoint stiffness during multi-joint arm movements," *Journal of Biomechanics*, vol. 33, no. 12, pp. 1705-1709, Dec, 2000.

[103] R. Zou, H. L. Wang, and K. H. Chon, "A robust time varying identification algorithm using basis functions," *Annals of Biomedical Engineering*, vol. 31, no. 7, pp. 840-853, Jul-Aug, 2003.

[104] S. Sanyal, S. L. Kukreja, E. J. Perreault *et al.*, "Identification of linear time varying systems using basis pursuit," *In Proc. 27th Annual International IEEE Engineering in Medicine and Biology Society (EMBC2005)* pp. 22-25, 2005.

[105] Z. Y. Shi, and S. S. Law, "Identification of linear time-varying dynamical systems using Hilbert transform and empirical mode decomposition method," *Journal of Applied Mechanics-Transactions of the Asme*, vol. 74, no. 2, pp. 223-230, Mar, 2007.

[106] D. Piovesan, P. DiZio, and J. R. Lackner, "A new time-frequency approach to estimate single joint upper limb impedance," *In Proc EMBC 2009 Annual International Conference of the Ieee Engineering in Medicine and Biology Society, Vols 1-20*, pp. 1282-1285, 2009.

[107] I. Khanna, A. Roy, M. M. Rodgers *et al.*, "Effects of unilateral robotic limb loading on gait characteristics in subjects with chronic stroke," *J Neuroeng Rehabil*, vol. 7, pp. 23, 2010.

[108] J. Duysens, M. Trippel, G. A. Horstmann *et al.*, "Gating and Reversal of Reflexes in Ankle Muscles during Human Walking," *Experimental Brain Research*, vol. 82, no. 2, pp. 351-358, 1990.

[109] R. B. Stein, and R. E. Kearney, "Nonlinear Behavior of Muscle Reflexes at the Human Ankle Joint," *Journal of Neurophysiology*, vol. 73, no. 1, pp. 65-72, Jan, 1995.

[110] R. Ritzmann, A. Kramer, M. Gruber *et al.*, "EMG activity during whole body vibration: motion artifacts or stretch reflexes?," *European Journal of Applied Physiology*, vol. 110, no. 1, pp. 143-151, Sep, 2010.

[111] H. Lee, and N. Hogan, "Linear Time-Varying Identification of Ankle Mechanical Impedance during Human Walking," *Proceedings of the ASME 2012 Dynamic Systems and Control Conference*, pp. 1-6, 2012.

[112] D. T. Westwick, and E. J. Perreault, "Estimates of acausal joint impedance models," *IEEE Trans Biomed Eng*, vol. 59, no. 10, pp. 2913-21, Oct.2012.

[113] A. L. Logan, and L. J. Rowe, *The Foot and Ankle: Clinical Applications*: Jones & Bartlett Learning, 1994.

[114] A. Arndt, P. Westblad, I. Winson *et al.*, “Ankle and subtalar kinematics measured with intracortical pins during the stance phase of walking,” *Foot & Ankle International,* vol. 25, no. 5, pp. 357-364, May, 2004.

[115] J. Perry, “Anatomy and biomechanics of the hindfoot,” *Clin Orthop Relat Res*, no. 177, pp. 9-15, Jul-Aug, 1983.

[116] J. M. Hausdorff, C. K. Peng, Z. Ladin *et al.*, “Is Walking a Random-Walk - Evidence for Long-Range Correlations in Stride Interval of Human Gait,” *Journal of Applied Physiology,* vol. 78, no. 1, pp. 349-358, Jan, 1995.

[117] J. M. Hausdorff, P. L. Purdon, C. K. Peng *et al.*, “Fractal dynamics of human gait: Stability of long-range correlations in stride interval fluctuations,” *Journal of Applied Physiology,* vol. 80, no. 5, pp. 1448-1457, May, 1996.

[118] A. S. Go, D. Mozaffarian, V. L. Roger *et al.*, “Heart disease and stroke statistics--2013 update: a report from the American Heart Association,” *Circulation,* vol. 127, no. 1, pp. e6-e245, Jan 1.

[119] http://cerebralpalsy.org/, “http://cerebralpalsy.org/about-cerebral-palsy/.”

[120] multiple-sclerosis.emedtv.com, “http://multiple-sclerosis.emedtv.com/multiple-sclerosis/multiple-sclerosis-statistics.html.”

[121] sci-info-pages, “http://www.sci-info-pages.com/facts.html.”

[122] H. Lee, T. Patterson, J. Ahn *et al.*, “Static Ankle Impedance in Stroke and Multiple Sclerosis: A Feasibility Study,” *2011 Annual International Conference of the IEEE Engineering in Medicine and Biology Society (EMBC)*, pp. 8523-8526, 2011.

[123] P. Craven, and G. Wahba, “Smoothing Noisy Data with Spline Functions - Estimating the Correct Degree of Smoothing by the Method of Generalized Cross-Validation,” *Numerische Mathematik,* vol. 31, no. 4, pp. 377-403, 1979.